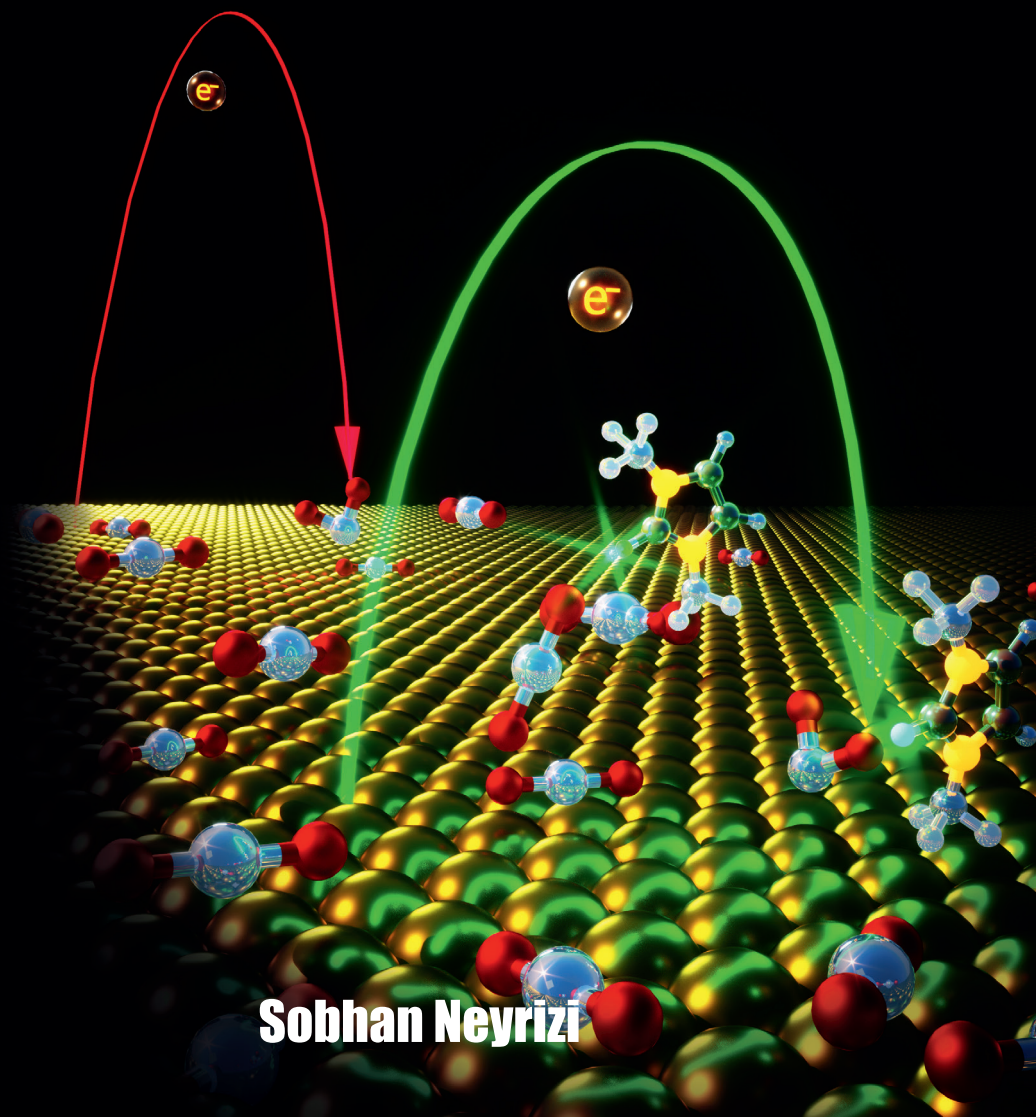


Imidazolium  
**co-catalysts**  
for efficient  
**electrochemical**  
reduction of  $\text{CO}_2$   
in acetonitrile



Sobhan Neyrizi



**IMIDAZOLIUM CO-CATALYSTS FOR EFFICIENT  
ELECTROCHEMICAL REDUCTION OF CO<sub>2</sub> IN  
ACETONITRILE**

*Sobhan Neyrizi*

**IMIDAZOLIUM CO-CATALYSTS FOR EFFICIENT  
ELECTROCHEMICAL REDUCTION OF CO<sub>2</sub> IN  
ACETONITRILE**

DISSERTATION

to obtain  
the degree of doctor at the University of Twente,  
on the authority of the rector magnificus,  
prof. dr. ir. A. Veldkamp,  
on account of the decision of the Doctorate Board  
to be publicly defended  
on Thursday 30 November 2023 at 14.45 hours

by

**Sobhan Neyrizi**

born on the 22nd of May, 1989  
in Ray, Iran

This dissertation has been approved by:

Promotor

prof.dr.ir. G. Mul

Co-promotor

dr. M.A. Hempenius

Cover design: Ella Maru studio

Printed by: Ridderprint

Lay-out: Sobhan Neyrizi

ISBN (print): 978-90-365-5912-6

ISBN (digital): 978-90-365-5913-3

URL: <https://doi.org/10.3990/1.9789036559133>

© 2023 Sobhan Neyrizi, The Netherlands. All rights reserved. No parts of this thesis may be reproduced, stored in a retrieval system or transmitted in any form or by any means without permission of the author. Alle rechten voorbehouden. Niets uit deze uitgave mag worden vermenigvuldigd, in enige vorm of op enige wijze, zonder voorafgaande schriftelijke toestemming van de auteur.

## Graduation Committee:

Chair / secretary: prof.dr. J.L. Herek

Promotor: prof.dr.ir. G. Mul  
University of Twente, TNW, Photocatalytic Synthesis

Co-promotor: dr. M.A. Hempenius  
University of Twente, TNW, Sustainable Polymer Chemistry

Committee Members: prof. dr. J. Huskens  
University of Twente, TNW, Molecular Nanofabrication

prof. dr. J. Lange  
University of Twente, TNW, Sustainable Process  
Technology

prof. dr. M.T.M. Koper  
Leiden University, Leiden Institute of Chemistry

prof. dr. P.J.A. Kenis  
University of Illinois Urbana-Champaign, Chemical and  
Biomolecular Engineering

dr. S. Er  
DIFFER

This thesis is dedicated to the memory of my father,  
**Qasem Neyrizi** (قاسم نيريزي), may his memory forever be a comfort and a blessing.





# Summary

The combustion of carbon-based fuels has led to the persistent accumulation of carbon dioxide (CO<sub>2</sub>) in the Earth's atmosphere, resulting in far-reaching climate changes. To address this pressing global issue, there is an urgent need for sustainable and efficient methods to harness CO<sub>2</sub> as an energy source, thus mitigating its environmental impact. One of the most promising approaches for CO<sub>2</sub> utilization is electrochemical reduction, often carried out in water due to its green and abundant nature. However, the intrinsic electrochemical reactivity of water presents challenges in this process

This PhD thesis explores the potential for improving carbon dioxide (CO<sub>2</sub>) reduction efficiency by transitioning from water-based electrochemical processes to non-aqueous media, using acetonitrile as a solvent. To enhance efficiency, imidazolium cations are introduced as co-catalysts and essential components of the electrolyte. The central aim of this work is to gain a fundamental understanding of the pivotal role of imidazolium cations in promoting non-aqueous electrochemical CO<sub>2</sub> reduction. Additionally, it investigates their potential in facilitating efficient electrochemical conversion across a variety of affordable transition metals. By analyzing the structure-activity relationship for imidazolium electrolyte cations, this research provides insights into the selection or synthesis of effective electrolyte cations to enhance non-aqueous electrochemical CO<sub>2</sub> reduction.

# Samenvatting

De verbranding van koolstofhoudende brandstoffen heeft geleid tot de aanhoudende ophoping van koolstofdioxide (CO<sub>2</sub>) in de atmosfeer van de aarde, met als gevolg ingrijpende klimaatveranderingen. Om dit urgente wereldwijde probleem aan te pakken, is er een dringende behoefte aan duurzame en efficiënte methoden om CO<sub>2</sub> als energiebron te benutten en daarmee de milieueffecten te verminderen. Een van de meest veelbelovende benaderingen voor CO<sub>2</sub>-gebruik is elektrochemische reductie, vaak uitgevoerd in water vanwege de groene en overvloedige aard ervan. De intrinsieke elektrochemische reactiviteit van water brengt echter uitdagingen met zich mee in dit proces.

Dit proefschrift verkent de mogelijkheden om de efficiëntie van de reductie van kooldioxide (CO<sub>2</sub>) te verbeteren door over te stappen van elektrochemische processen in water naar niet-waterige media, waarbij acetonitril als oplosmiddel wordt gebruikt. Om de efficiëntie te verbeteren, worden imidazoliumkationen geïntroduceerd als mede-katalysatoren en essentiële componenten van de elektrolyt. Het centrale doel van dit onderzoek is een fundamenteel begrip te verkrijgen van de cruciale rol die imidazoliumkationen spelen bij het bevorderen van elektrochemische CO<sub>2</sub>-reductie in niet-waterige omgevingen. Daarnaast onderzoekt het hun potentieel om efficiënte elektrochemische conversie te vergemakkelijken over een verscheidenheid aan betaalbare overgangsmetalen. Door de structuur-activiteitsrelatie voor imidazolium-elektrolytkationen te analyseren, biedt dit onderzoek inzicht in de selectie of synthese van effectieve elektrolytkationen om de niet-waterige elektrochemische CO<sub>2</sub>-reductie te verbeteren.

# Table of Contents

<b>Chapter 1:</b> CO <sub>2</sub> Reduction in Non-Aqueous Media: Advantages, Mechanism, and Promotional Effects of Imidazolium Cation .....	[9-15]
<b>Chapter 2:</b> Advancements in Non-Aqueous Electrochemical CO <sub>2</sub> Reduction: Design and Optimization of Experimental Protocols .....	[17-46]
<b>Chapter 3:</b> Unveiling the Role of Imidazolium Cations in Promoting Electrochemical CO <sub>2</sub> Reduction.....	[47-98]
<b>Chapter 4:</b> Investigating the Influence of C4, C5-Substituted Imidazolium Cations on Electrochemical CO <sub>2</sub> Conversion.....	[99-133]
<b>Chapter 5:</b> Exploring the Structure-Activity Relationship of Late-Transition Metal Catalysts in Imidazolium-Assisted Electrochemical CO <sub>2</sub> Reduction.....	[135-164]
<b>Chapter 6:</b> Exploring Electrochemical CO <sub>2</sub> Reduction Catalyzed by 2-Methylated Imidazolium: Insights from ATR-FTIR Spectroscopy.....	[165-188]
<b>Chapter 7:</b> Exploring the Influence of Electrolyte Identity on Non-Aqueous CO <sub>2</sub> Reduction: Impact of Alkyl Chain Length and Alkali Metal Cations.....	[189-200]
<b>Chapter 8:</b> Summary and Perspectives.....	[201-208]
<b>Appendix</b> .....	[209-212]
<b>References</b> .....	[213-220]
<b>Acknowledgments</b> .....	[221]
<b>Publications</b> .....	[222]



# **Chapter 1:**

## **CO<sub>2</sub> Reduction in Non-Aqueous Media: Advantages, Mechanism, and Promotional Effects of Imidazolium Cation**

## 1.1. Why electrochemical reduction of CO<sub>2</sub> and associated challenges

The electrochemical reduction of CO<sub>2</sub> (CO<sub>2</sub>RR), driven by electrical energy from renewable sources, holds significant promise in mitigating the escalating levels of atmospheric CO<sub>2</sub> and the resulting impact on Earth's climate. Moreover, such process presents an alternative avenue to traditional fossil resources as a sustainable carbon source<sup>9</sup>. To achieve efficient electrochemical CO<sub>2</sub> reduction, substantial advancements in catalyst properties<sup>10-12</sup>, electrode design (such as gas diffusion electrodes)<sup>13-15</sup>, and electrolyte composition<sup>16-18</sup> have been reported. However, several challenges still need to be addressed before the technology becomes commercially viable<sup>19-20</sup>, particularly in the context of aqueous electrolytes. These challenges encompass the low solubility of CO<sub>2</sub> in water<sup>21-23</sup>, the acidification of the electrolyte due to CO<sub>2</sub> dissolution (resulting in bicarbonate/carbonate formation and salt precipitation)<sup>24-26</sup>, the concurrent occurrence of the competing hydrogen evolution reaction<sup>27-28</sup>, and the instability of metal and metal oxide catalysts in acidic aqueous environments<sup>29-30</sup>.

## 1.2. CO<sub>2</sub> reduction in non-aqueous solvents

The electrochemical inertness of organic solvents, such as acetonitrile, presents potential solutions to alleviate some of the issues mentioned earlier with aqueous media<sup>21, 23, 31</sup>. Notably, CO<sub>2</sub> solubility in acetonitrile is approximately eight times higher than in water<sup>32</sup>, a critical parameter that promotes enhanced CO<sub>2</sub> utilization within the context of reactor design. The absence of water ensures a high selectivity towards CO<sub>2</sub> reduction products. This is further reinforced by the consideration of the broad electrochemical window (electrochemical stability) of organic media, as well as the fact that CO<sub>2</sub> becomes the sole redox-active species on the electrode-catalyst surface. For instance, acetonitrile and propylene carbonate have been reported to exhibit electrochemical windows of 6.1 V and 6.6 V, respectively<sup>33</sup>.

This extended electrochemical window provides ample room for accommodating diverse redox chemistries, a considerable advantage compared to the constraints posed by water as a solvent, with its electrochemical window typically around 2.06 V (the exact value may depend on the solution's pH).

The advantages discussed above have spurred investigations into CO<sub>2</sub> reduction in non-aqueous media, although the number of such studies is not as extensive as those conducted in aqueous media. By utilizing a two-layered carbon-free lead (Pb) gas diffusion electrode (GDE), Konig et al.<sup>34</sup> demonstrated a 53% Faradaic efficiency for oxalate production at a current density of approximately 80 mA/cm<sup>2</sup> and a potential of approximately -2.5 V vs. Ag/Ag<sup>+</sup>. Their study employed a 0.1 M tetraethylammonium tetrafluoroborate solution in acetonitrile as the electrolyte. In a different study, Tomita et al.<sup>35</sup> observed that for a Pt electrode, the main product was oxalic acid at a current density of 5 mA/cm<sup>2</sup> using a 0.1 M tetraethylammonium perchlorate acetonitrile-water mixture. However, an increase in water concentration led to a decrease in oxalic acid formation and an increase in formic acid production. At higher water concentrations, hydrogen evolution became dominant. Another study by Figueiredo et al.<sup>21</sup> reported CO as the primary product in wet acetonitrile using an ammonium-based electrolyte. The formation of CO, accompanied by formate and carbonate, was also reported by Christensen and Hamnett<sup>36</sup> using a 0.1 M tetrabutylammonium tetrafluoroborate solution in acetonitrile over an Au electrode. As we can observe, the performance of CO<sub>2</sub> reduction in non-aqueous media has exhibited significant variations dependent on factors such as the composition of the electrolyte, the nature of the electrode, and the availability of proton donors. For readers interested in an extensive review, a recent work by Reis et al.<sup>37</sup> offers a comprehensive overview of CO<sub>2</sub> electrochemical reduction studies in non-aqueous media.

### 1.3. Electron transfer and reaction intermediates mediated by imidazolium cations

From a mechanistic perspective, the initiation of CO<sub>2</sub> reduction has been argued to involve a first electron transfer to the CO<sub>2</sub> molecule<sup>19, 38</sup>. In the case of a metal electrode catalyst, this step follows CO<sub>2</sub> adsorption. The following central equation can be considered for CO<sub>2</sub> activation:



Due to the high reactivity and short lifespan of this intermediate, as identified by Bard et al.<sup>39</sup>, the predominant reaction and subsequent product distribution considerably depend on the nature of the electrode material<sup>40</sup>, the surrounding microenvironment<sup>41-42</sup>, and the availability of protons<sup>43</sup>. In situations involving low-proton aprotic media, numerous studies have documented the formation of CO, oxalate, and carbonate as the primary products. Additionally, in the presence of residual water, other products like hydrogen, glyoxalate, glycolic acid, glyoxylic acid, and formic acid have been observed in the reaction mixture<sup>44-48</sup>. The formation of CO in non-aqueous media has predominantly been linked to a disproportionation reaction. In this process, upon the second electron transfer to an adsorbed \*CO<sub>2</sub> intermediate, carbonate and CO are simultaneously generated in equimolar proportions. Oxalate, on the other hand, has been proposed to emerge from a self-coupling reaction of adsorbed \*CO<sub>2</sub> intermediates, while the presence of water has been suggested to drive the formation of formate<sup>31, 36</sup>. The first reaction stage mentioned in Eq. [1.1] requires a significantly negative standard potential, as reported to be -2.21 V vs. SCE on a mercury electrode in DMF solvent<sup>44</sup>. Recent work by Koper et al.<sup>49</sup> has even demonstrated the absence of CO<sub>2</sub> conversion in the absence of solvation effects that stabilize the negatively charged CO<sub>2</sub> intermediate. Without water as a potential



moderator for energy requirements during the initial electron transfer, the utilization of electrolyte cations to engineer the kinetics of CO<sub>2</sub> reduction appears to be a promising approach. Among the electrolyte cations, imidazolium cations have shown great promise for CO<sub>2</sub> reduction in both aqueous and non-aqueous media. Rosen et al. reported a 96% faradaic efficiency for CO formation on an Ag electrode in an ethyl methyl imidazolium-water mixture (18 mol % EMIM BF<sub>4</sub> in water) with a cell voltage of 1.5 Volts (+0.2 V overpotentials)<sup>50</sup>. Following this seminal work, various attempts have been made to utilize imidazolium-type molecules to enhance CO<sub>2</sub> reduction in non-aqueous media. Lau et al. employed C2-functionalized imidazolium cations to achieve an onset potential of around -2.0 V vs. Fc/Fc<sup>+</sup> for CO<sub>2</sub> reduction over an Ag electrode in acetonitrile<sup>8</sup>, and Atifi et al. reported the use of butyl methyl imidazolium hexafluorophosphate for the conversion of CO<sub>2</sub> to CO with 85% FE using a Bi electrode<sup>51</sup>. Sung et al. also demonstrated the improved efficiency of a molecular Lehn-type catalyst through the incorporation of imidazolium species into the secondary coordination sphere<sup>52</sup>.

Despite these efforts, the reported onset potentials and associated energy losses in imidazolium solutions remain relatively high. Moreover, the fundamental understanding of the function of imidazolium cations is limited, and several hypotheses regarding the promotion mechanism have been proposed. These hypotheses include: i) the coordination of the cation with the adsorbed CO<sub>2</sub> intermediate, the nature of which still requires clarification<sup>3, 50</sup>, ii) the suppression of the H<sub>2</sub> evolution reaction<sup>53-54</sup>, iii) the formation of an intermediate imidazolium carboxylate providing a low-energy pathway for the conversion of CO<sub>2</sub> to CO<sup>3-4, 55</sup>, or iv) the stabilization of the high-energy \*CO<sub>2</sub><sup>-</sup> intermediate (on Ag surfaces) through hydrogen bonding via the C4-H or C5-H functionality of C2-substituted imidazolium cations (**Figure 1.1**)<sup>8</sup>. However, different reaction conditions have been previously applied, including variations in applied salts (different anions and C2-substituted imidazolium cations) and variable water

content in solvent compositions, making it difficult to discriminate between these hypotheses and to properly assess the general function of the cations based solely on existing literature.

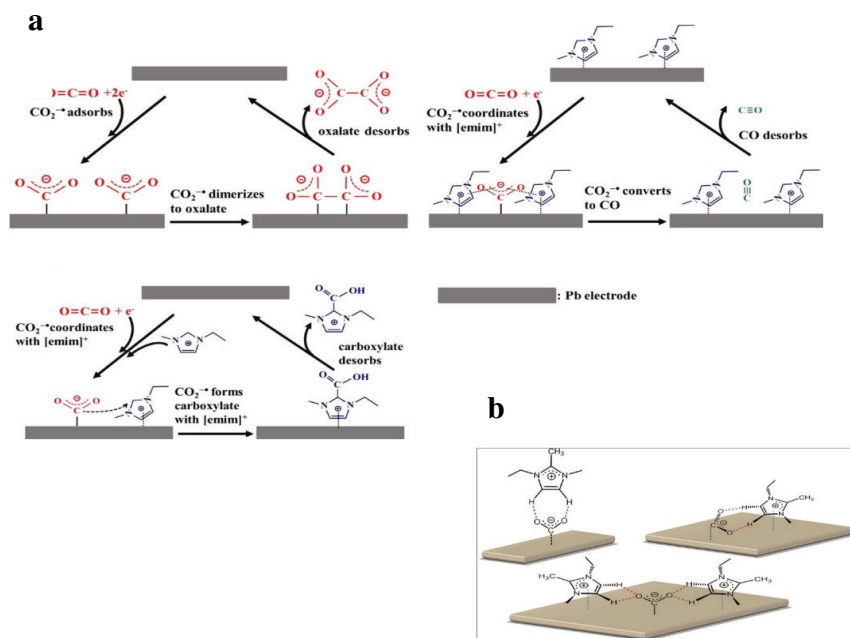


**Figure 1.1.** (a) Schematic representation of interactions involving imidazolium, as proposed by Kamet et al.<sup>3</sup> This includes cation coordination with adsorbed intermediates, carboxylation, and a side reaction leading to oxalate formation as a byproduct on a Pd electrode. (b) Proposed mechanism by Lau et al.<sup>8</sup> involving hydrogen bonding to adsorbed  $^*CO_2$  intermediate as the main mechanism for C2-methylated imidazolium on Ag electrode. These studies were conducted in an acetonitrile environment.

Unraveling the underlying role of these cations in  $CO_2$  reduction performance holds the potential to open new avenues for the efficient design of non-aqueous electrochemical  $CO_2$  reduction systems. This thesis embarks on a comprehensive investigation into the influence of imidazolium cations on the performance of (predominantly) Au electrodes in the electrochemical reduction of  $CO_2$  in non-aqueous media. Rigorous measures have been taken to maintain anhydrous conditions, mitigating the potential interference from water (**Chapter 2**). Au electrodes were chosen as a benchmark catalyst facilitating a systematic exploration. The research strategy involves a combination of synthetic methodologies, electrochemical

experiments, and Density Functional Theory (DFT) calculations aimed at providing deep insights into the promotional effect that imidazolium cations exert on CO<sub>2</sub> reduction. In particular, the influence of substituents at both C1, C3- and at the N1, N3- positions of the imidazolium ring on its catalytic performance will be scrutinized (**Chapters 3 and 4**). This analysis will shed light on the structure-activity relationships governing the impact of cations on CO<sub>2</sub> reduction. Expanding the investigation, the performance of anhydrous imidazolium-acetonitrile will be systematically examined on other electrode materials, including Ag, Zn, Cu, and Ni (**Chapter 5**). This broader exploration aims to understand the generality of the observed effects and the potential for cation-mediated enhancement across different catalysts. Furthermore, the performance of C2-methylated imidazolium cation will be investigated using in-situ FTIR spectroscopy (**Chapter 6**). Finally, the impact of the alkyl chain length of 1-alkyl-3-methyl imidazolium cations on their catalytic efficiency will be also discussed (**Chapter 7**).



## **Chapter 2:**

# **Advancements in Non-Aqueous Electrochemical CO<sub>2</sub> Reduction: Design and Optimization of Experimental Protocols**

## Summary

**Chapter 2** delves into an investigation of the applicability of common practices and experimental protocols for non-aqueous electrochemical CO<sub>2</sub> reduction. The chapter focuses on exploring the influence of widely used Ag/Ag<sup>+</sup> reference systems and metallic (such as Ag) counter electrodes, shedding light on the associated artifacts that arise when studying the CO<sub>2</sub> reduction process in non-aqueous media. Building upon the limitations of existing methods, a novel experimental protocol is developed to establish a robust approach. This work introduces key modifications that address two critical aspects: **a)** ensuring reliable potential recording for the working electrode, which serves as a vital parameter for assessing catalytic performance, and **b)** providing detailed steps to prepare and conduct experiments under anhydrous conditions.

## **Anhydrous Electrochemistry: Methods and Considerations**

The main objective of this study was to investigate the co-catalyzed reduction of CO<sub>2</sub> by imidazolium cations over Au electrodes in the absence of water. To ensure anhydrous conditions throughout our experiments, significant emphasis was placed not only on maintaining anhydrous conditions during preparation, but also throughout the entire course of the experiments. To achieve this, a detailed protocol was established and elaborated on in this section, which ensured relatively consistent water content (<50 ppm). This was essential to ensure the integrity of the results and prevent any interference from variations in water content on the performance and assessment of the reaction mechanism. Throughout this chapter, a model system consisting of 1,3-dimethyl imidazolium NTf<sub>2</sub> (**MM** NTf<sub>2</sub>) in anhydrous acetonitrile was employed to investigate the experimental approach. The performance of the **MM** cation in promoting CO<sub>2</sub> reduction will be discussed in detail in **Chapter 3**.

**Electrodes and reactor.** For each electrolysis measurement, the electrodes underwent an initial polishing process using sandpaper until a smooth and shiny surface was achieved. In the case of voltammetry electrodes, a polishing pad (Prosense, QVMF 1040) was moistened with ethanol and the electrode was gently polished for a duration of 4 minutes (no alumina was utilized on the polishing pad). Subsequently, the electrodes were thoroughly rinsed with Milli-Q water (Milli-Q® Reference, 18.2 MΩ, 5 ppb TCO, Merc) and subjected to a 10-minute sonication in 0.5 molar HNO<sub>3</sub>. Following this step, another round of sonication in ethanol was performed, concluding with a 10-minute sonication in HPLC grade acetonitrile (99.9%, Sigma Aldrich) to ensure the electrodes' cleanliness. It is important to note that the electrodes were always rinsed with Milli-Q water between each sonication step.

Noble electrodes such as Au underwent additional electrochemical cleaning (**Supporting Information Section III**) as necessary. However, general electrochemical cleaning as proposed

by some studies<sup>56</sup> for electrodes such as Cu resulted in poor electrochemical results with unassigned peaks (**Supporting Information Figures S2.7a-S2.7c**). Thus, it is recommended to avoid electrochemical cleaning with non-noble metals, and if necessary, rigorous sandpaper polishing (mechanical cleaning) should be applied.

The glass reactor, reference compartment, graphite rod, gas inlet, and gas outlet tubes underwent a thorough rinsing process using Milli-Q water, ethanol, and HPLC grade acetonitrile. Subsequently, the working electrode and all other reactor components were assembled, and the entire setup was sonicated for 2 sets of 5 minutes using HPLC grade acetonitrile. Following this step, the reactor was subjected to a continuous purge of super dry helium (Helium A/Zero Grade N4.6, Linde) for a duration of 30 minutes prior to the introduction of the electrolyte. In experiments involving CO<sub>2</sub>, a dryer (ZPure DS H<sub>2</sub>O, ChromRes) was employed to ensure the complete removal of moisture from the CO<sub>2</sub> inlet (Carbon Dioxide Food Grade, Linde) before it entered the reactor. This additional step ensured that the CO<sub>2</sub> supplied to the reactor was free from any residual moisture. **Figures S2.1** displays the results of SEM and EDX analysis from Ni and Au electrodes after the above-mentioned cleaning procedure. The surface appears to be sufficiently clean for being tested in electrochemical experiments.

**Counter electrode.** A graphite rod was chosen as the counter electrode to mitigate additional artifacts resulting from metal oxidation and subsequent deposition onto the working electrode. The choice of counter electrode plays a crucial role in the electrochemical CO<sub>2</sub> reduction process. **Figure 2.1** presents a comparison of chronoamperometry results for CO<sub>2</sub> reduction on an Au electrode using different counter electrodes: Au and Ag (**Figure 2.1a**) as well as graphite (**Figure 2.1b**). The results show that employing Au and Ag as counter electrodes leads to an increase in current, suggesting the occurrence of additional reactions. On the other hand, when graphite is used as the counter electrode, the performance of the CO<sub>2</sub> reduction remains stable,



with a consistent Faradaic efficiency for CO production. **Figure S2.8** further supports the influence of the counter electrode choice. It displays images of an Au voltammetry electrode before and after conducting linear sweep voltammetry (LSV) experiments for CO<sub>2</sub> reduction, with Ag employed as the counter electrode. The deposition of silver on the Au electrode during the experiment results in a noticeable transformation, resembling the appearance of silverish. However, when using graphite as the counter electrode, no significant changes in the electrode's appearance are observed after the voltammetry experiments. These observations emphasize the importance of selecting the appropriate counter electrode material in non-aqueous electrochemical CO<sub>2</sub> reduction studies to minimize unwanted side reactions and artifacts.

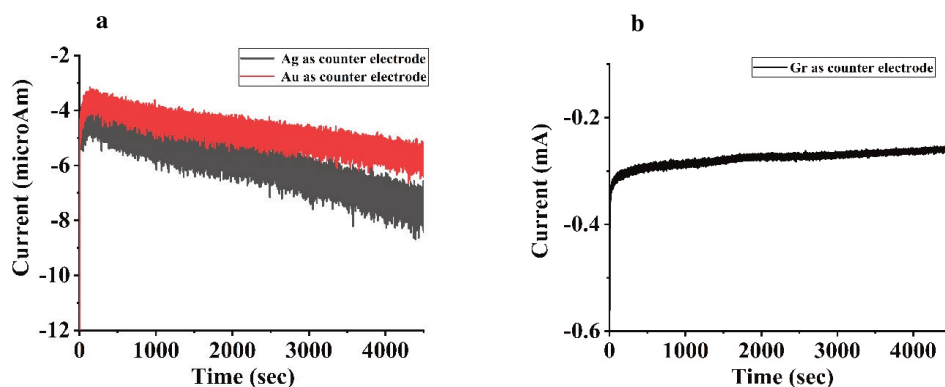


**Figure 2.1.** Chronoamperometry results for Au electrode under CO<sub>2</sub> purging with 0.5 mol% of MM NTf<sub>2</sub> as electrolyte in anhydrous acetonitrile. (a) with Au and Ag as counter electrode, and (b) with graphite as counter electrode. Both experiments were performed at -1.8 V vs. Ag/Ag<sup>+</sup>. The higher current observed for the experiment with graphite is due to the larger size of the working electrode (Au foil).

**Glassware to prepare electrolyte solutions.** All glassware intended for solution preparation underwent a thorough cleaning process. Firstly, the glassware was sonicated in Milli-Q water for a duration of 10 minutes. Following that, a subsequent round of sonication was conducted using ethanol for an additional 10 minutes. This ensured the removal of impurities or residues from the glass surfaces, ensuring a clean environment for solution preparation. After the cleaning process, the glassware was dried at a temperature of 200 degrees Celsius for a minimum of 2 hours, immediately transferred to the glove box antechamber while hot, where

it was subjected to five evacuation-N<sub>2</sub> refilling cycles before it was taken into the glove box. This ensured the complete elimination of any remaining moisture. The dried glassware was utilized for the preparation of electrolyte solutions and reference solutions using anhydrous acetonitrile. Electrolyte solutions always contained 0.5 molar percent of the electrolyte salt target to study. The electrolyte solutions were formulated to contain a target concentration of 0.5 molar percent of the electrolyte salt under investigation.

**Reference electrode and solution preparation.** In order to avoid the cross-contamination of the working solution with other organic cations, for each cation, a new reference solution was prepared for the electrochemical measurement. A reference solution always contained 0.1 mol% (0.02 molar) of Ag OTf with 0.4 mol% of the electrolyte subject to study (in total 0.5 molar percent of salt concentration in anhydrous acetonitrile)<sup>57</sup>. The reference solution was separated from the working solution by an ultrafine frit. Ag wire was used as the pseudo-reference electrode. The potential recorded versus the Ag reference electrode immersed in an electrolyte containing 0.02 molar silver salt in acetonitrile can be converted into the SHE scale by the following equation<sup>58</sup>:

$$E (\text{vs. Ag/Ag}^+) = +542 \text{ mV vs. SHE } (\pm 45 \text{ mV})$$

**Electrochemical measurements.** Solutions (electrolyte and reference solutions) were transferred with caution into the reactor with gas-tight syringes. Before solution injection, the reactor was washed twice with anhydrous acetonitrile (transferred from the glove box). After injection, the solutions were kept under He/CO<sub>2</sub> purging for 1hr to remove any remaining oxygen. Karl-Fischer titrations were performed to measure the water content from solutions inside the glove box and after the injection into the reactor. 48-55 ppm water was found for all solutions and it was confirmed that no water was introduced to the solutions upon transferring

from the glove box into the reactor. **Figure S2.9** illustrates the electrochemical set-up utilized in this study.

For recording potentials versus  $\text{Ag}/\text{Ag}^+$ , an Ag wire was used as the pseudo-reference electrode. 0.1 mol% Ag OTf in 0.1 mL anhydrous acetonitrile was always used as the reference solution and was separated from the working solution with an ASTM ultrafine frit. Working solutions always contained 0.5 mol% of the electrolyte and were all prepared inside the glove box.  $\text{NTf}_2$  was always used as the common electrolyte anion and anhydrous acetonitrile was the common solvent for all measurements. A graphite rod (99.99% Sigma Aldrich) was used as the counter electrode. Gas chromatography (Compact GC 4.0, Inter science) was used to analyze the gas products from the reactor. He was used as the carrier gas and the Pulsed Discharge Detector of the GC was calibrated for 1 to 100,000 ppm CO (Carbon Monoxide CP Grade N3.0, Linde). All electrochemical measurements were performed with a Biologic SP-300. RDE measurements were performed using a WaveVortex 10 Electrode Rotator (Pine research). **Figure 2.2** illustrates the sensitivity of our non-aqueous setup to the presence of water. The figure showcases the LSV (Linear Sweep Voltammetry) results obtained from the Ni electrode under He purge, with varying levels of residual water concentration. Notably, the findings reveal a discernible increase in the reductive current upon the introduction of water into the system in the potential range of -1.0 to -1.5 V, lower than required for reduction of  $\text{CO}_2$ . The reduction of  $\text{H}_2\text{O}$  becomes mass transfer limited in the range of -1.5 V to -2.0 V.

To ensure consistent hydrodynamics and minimize variations during linear sweep voltammetry (LSV) and electrolysis (EL) measurements, several parameters were kept constant. These parameters included maintaining a consistent reaction volume size, counter electrode size, and gas flow rate (5 ml/min). These measures were implemented to ensure reliable and meaningful comparisons of the apparent relative activities when studying different electrolytes or electrodes. Prior to any electrochemical measurement, it was ensured that a stable open-circuit

voltage was achieved. Reproducibility of measurements was checked to ensure reliable data. Due to its inherent activity for water reduction, a Nickel electrode was used to probe the impact of the presence of water experimentally.

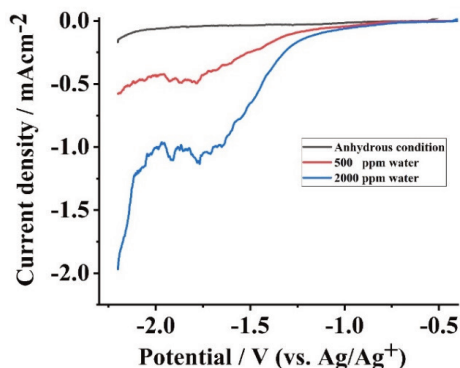


**Figure 2.2.** LSV results for a Ni electrode under He purge at varying levels of water content. Introducing 500 ppm (red) and 2000 ppm (blue) of water induces a noticeable increase in the reductive current within the same electrochemical window.

**Gas Analysis and Faradaic Efficiency Evaluation Method.** To evaluate Faradaic efficiency for a reaction, gas and liquid products were analyzed. For gas analysis, the GC was first calibrated for the relevant ppm's of CO and other potential products for CO<sub>2</sub> reduction. **Figure S2.4** shows examples of the calibration data for CO and H<sub>2</sub>. The pressure drop over the lines of the GC was taken into account for calculating CO concentration. The *flow in* was always contrasted with the *flow out* to ensure a leak-less experiment. Before electrolysis, a few sequences from the reactor were recorded to obtain the background with no reaction. After obtaining the background, electrolysis started and CO was detected (**Figure S2.5**). After GC measurement, the pressure drop was re-measured to ensure that the experimental conditions were the same as at the beginning of the electrolysis. Based on calibration measurements, CO ppm was evaluated and then converted to *mol* fraction by the use of GC pressure drop, lab temperature, and total volume of the gas. After electrolysis, the solution was always analyzed by NMR to inspect the presence of other possible products.

## Artifacts and Protocol for Potential Recording in Non-Aqueous Electrochemical CO<sub>2</sub> Reduction

In our preliminary approach to investigate non-aqueous CO<sub>2</sub> reduction through electrochemical measurements, we employed a three-electrode cell, a widely adopted configuration in electrochemical research, as extensively reported by previous researchers<sup>59-61</sup>. This configuration, as detailed in the previous section, involved the utilization of an Ag wire as the pseudo-reference electrode. For recording potentials relative to Ag/Ag<sup>+</sup>, a reference solution was employed, consisting of 0.1 mol% (0.02 molar) of Ag OTf with 0.4 mol% of the electrolyte under study. To maintain consistency, the salinity of the reference solution was matched with that of the working solution, thereby preventing salt transport induced by concentration potential between the compartments. To ensure proper separation between the reference solution and the working solution, we incorporated an ASTM ultrafine frit. Moreover, we chose to use a graphite counter electrode to mitigate any potential issues arising from metal deposition from a metallic counter electrode, which could interfere with the reaction mechanism under investigation at the working electrode.

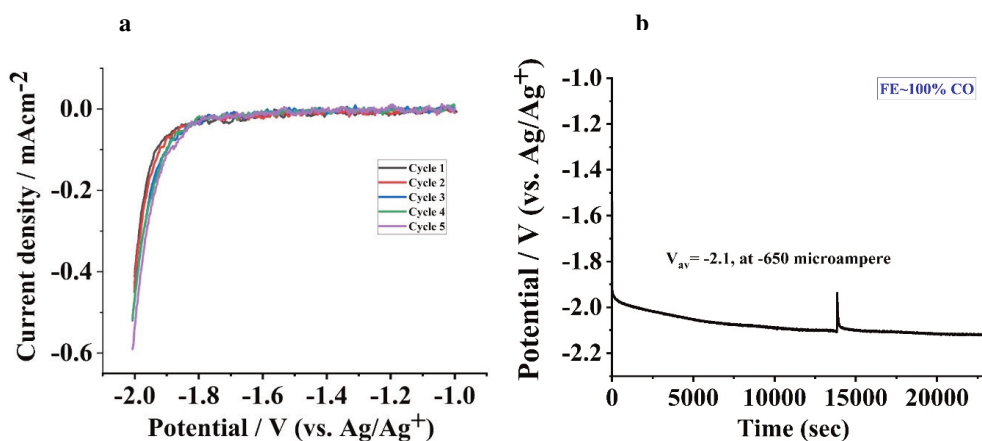


**Figure 2.3.** (a) Linear sweep voltammetry (LSV) results for CO<sub>2</sub> reduction on a Pt wire electrode in anhydrous acetonitrile. The electrolyte and co-catalyst used were 0.5 mol% of MM NTf<sub>2</sub>. Subsequent cycles are indicated by the corresponding numbers. (b) Electrolysis results for the same system demonstrating the consistent production of CO with 100% faradaic efficiency.

**Figure 2.3 (a)** illustrates the linear sweep voltammetry (LSV) results for CO<sub>2</sub> reduction at a Pt electrode using the three-electrode configuration described earlier. The electrolyte and co-catalyst utilized were 0.5 mol% of 1,3-dimethyl imidazolium bis(trifluoromethylsulfonyl)imide (MM NTf<sub>2</sub>). The detailed discussion on the role of MM cation and other imidazolium cations in CO<sub>2</sub> reduction will be presented in future chapters. In this context, the system serves to demonstrate the establishment of the experimental protocol.

From **Figure 2.3 (a)** we observed a slight increase in the reductive current for the Pt electrode with subsequent cycles. While these incremental changes may not be readily apparent in just two consecutive cycles (as shown in **Figure 2.4**), they become more noticeable when multiple cycles are overlapped, revealing an overall increase in the current.

**Figure 2.5** presents the EDX-SEM results obtained from the Pt electrode after electrolysis, as detailed in **Figure 2.3**. The SEM image highlights two distinct regions. In one of these regions, marked by spectrum 30, a dendritic structure is clearly observed. The corresponding EDX analysis in the top-right corner confirms the presence of Ag (43%), C (29%), and N (18%) elements in this region. Conversely, in the second region, represented by spectrum 31, no dendritic structure is evident. The EDX analysis from this region further supports the hypothesis

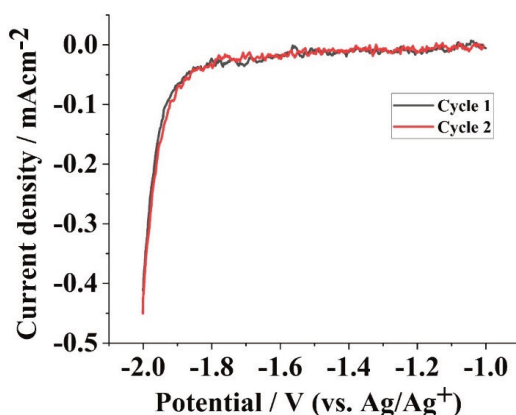


**Figure 2.4.** Overlapping the first two cycles of LSVs from Figure 2.3 for demonstration purposes.

that the presence of Ag, C, and N in spectrum 30 is specifically associated with the dendritic structure. It is worth noting that NHCs (parent N-heterocyclic compounds) have been documented for their ability to coordinate with metallic nanoparticles and heterogeneous metallic surfaces (as shown in the bottom left panel in **Figure 2.5**)<sup>62-64</sup>. Metal-NHC complexes have found applications in the fields of catalysis and biochemistry<sup>65</sup>. The results obtained from **Figures 2.3-2.5** allow us to propose a hypothesis that, upon applying a reductive potential, Ag particles from the reference solution and imidazolium compounds present in the working solution may form NHC-imidazole clusters on the surface of the Pt catalyst. However, a more detailed analytical and electrochemical study is required to determine the exact composition and coordination number of these clusters.

It is important to highlight that the observed surface coverage with Ag-MM species, as mentioned earlier, is attributed to the use of Ag NTf<sub>2</sub> reference solution, which reaches a maximum concentration of 20 ppm in the electrolyte solution if all Ag leaks from the reference solution compartment. Various reference capillaries, both commercially available and custom-made, were tested to investigate the possibility of preventing Ag leakage from the reference solution. Unfortunately, regardless of the type of frit used in the capillaries, the deposition of Ag was consistently observed. However, it is important to note that the extent of Ag deposition varied depending on factors such as the magnitude of the reductive potential applied and the duration of electrolysis.

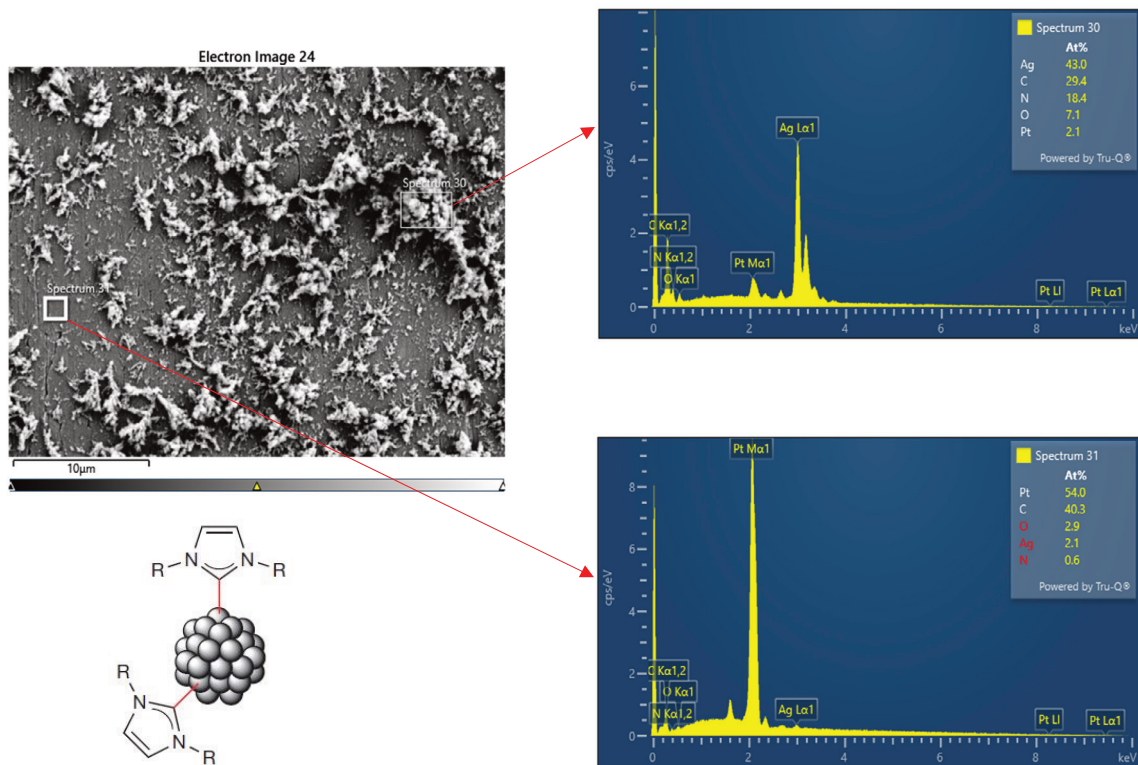


**Figure 2.5.** Scanning electron microscopy (SEM) results along with associated energy-dispersive X-ray spectroscopy (EDX) analysis of the Pt electrode investigated in Figure 2.3. The bottom left panel illustrates a schematic representation of the coordination of metal nanoparticles with NHC (N-heterocyclic compound) compounds, adapted from reference<sup>5</sup>.

To mitigate the challenge of reductive Ag deposition in electrolysis experiments, a novel protocol was developed and implemented in this study, which is illustrated in **Figures 2.6 and 2.7**. In this new approach, the initial step involved conducting all linear sweep voltammetry (LSV) measurements and electrolysis experiments using a graphite rod as both the counter and reference electrode (**Figure 2.6a**). A critical requirement of this protocol was that the size of the graphite counter electrode consistently exceeded that of the working electrode. Additionally, the applied current in the cell was deliberately restricted to the bulk concentration of the reactant, specifically CO<sub>2</sub> in acetonitrile. By adhering to these conditions, the undesired impacts of the counter electrode on the working electrode and its associated reaction were effectively minimized. In the second step of the protocol, once a stable electrochemical response was obtained using the two-electrode configuration, a reference solution containing



Ag NTf<sub>2</sub> salt, identical in composition to the previously described solution, was introduced into the reference capillary. This was followed by the recording of a single linear sweep voltammogram (LSV) using a three-electrode configuration. The setup involved an Ag wire as the pseudo-reference electrode, graphite as the counter electrode, and the working electrode being the Au foil (**Figure 2.6b**). Importantly, a four-electrode connection was utilized to measure the potentials of both the working electrode and the counter electrode relative to Ag/Ag<sup>+</sup>. Subsequently, the Ag solution was withdrawn from the capillary to minimize the potential impact of Ag-imidazolium deposition on the working electrode. In the third step, the potential recorded versus Ag/Ag<sup>+</sup> in the second step is contrasted with the potential recorded versus graphite in the first step (**Figure 2.7a**). This comparison allows for the alignment of the previously recorded potential versus graphite with respect to the Ag/Ag<sup>+</sup> reference using the following equation:

$$E_{\text{vs. Ag/Ag}^+} = E_{\text{vs. graphite}} + \Delta E \quad [\text{eq. 2.1}]$$

This alignment step ensures the accurate calibration of the potential recorded versus graphite as a function of potential ( $\Delta E$ ) with respect to the Ag/Ag<sup>+</sup> reference, enabling reliable comparison and analysis of the electrochemical data. Finally, in the last step, the cell potential recorded in the three-electrode configuration was compared to that of the two-electrode configuration to examine the overlap between the two profiles obtained in steps 1 and 2 (**Figure 2.7b**). This comparison aimed to ensure the absence of any artifacts or anomalous effects arising from the presence of the Ag salt reference solution. By assessing the consistency and agreement between the cell potentials obtained from both configurations, the reliability and validity of the experimental data were verified, further confirming the effectiveness of the developed protocol in mitigating potential issues associated with reductive Ag deposition during electrolysis experiments. Furthermore, **Figure 2.7c** presents the scanning electron microscopy (SEM) results along with energy-dispersive X-ray spectroscopy (EDX) analysis of the Au foil used as

the working electrode in the aforementioned showcase experiment. Contrasting the results of SEM-EDX analysis from the Au electrode with those from the Pt working electrode in **Figure 2.5** provides supporting evidence for the efficiency of the experimental protocol devised in this work. Specifically, no evidence of Ag deposition is observed, reinforcing the accuracy of the potentials recorded in steps 1 and 2 as described earlier.

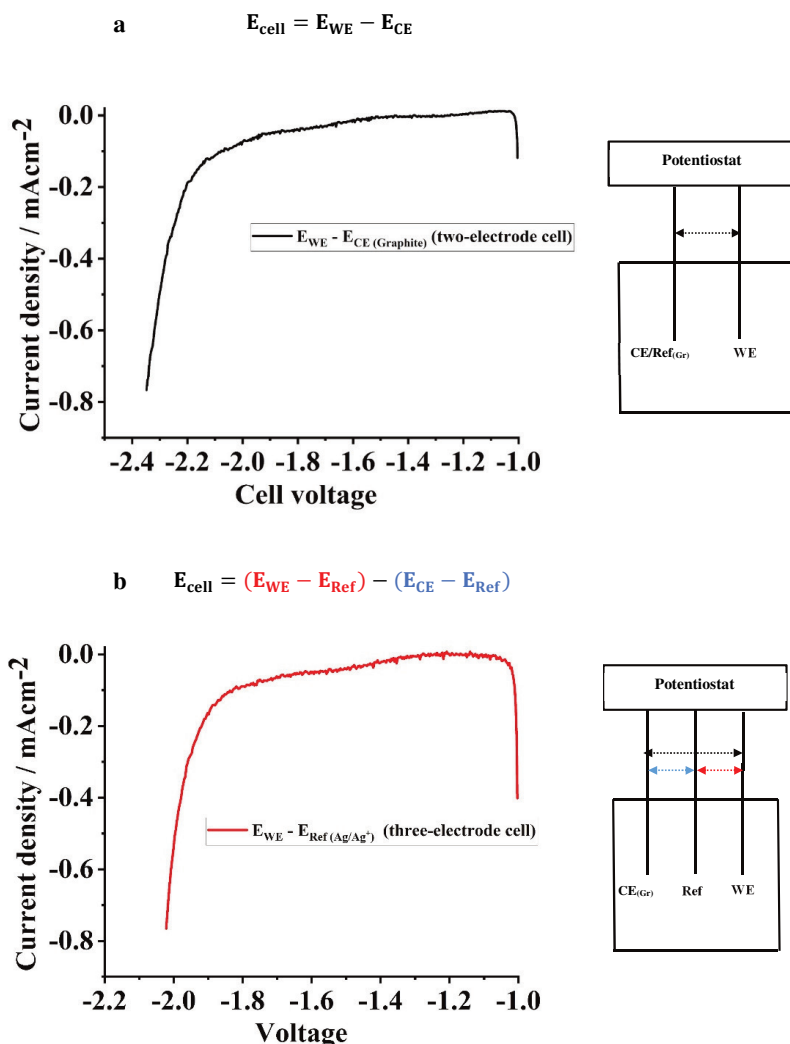


**Figure 2.6** . Illustrating the protocol devised for acquiring electrochemical data in non-aqueous  $\text{CO}_2$  reduction. **(a)** Stage 1: Potential recorded using a two-electrode configuration with a graphite rod serving as both the reference and counter electrode. **(b)** Stage 2: Introduction of a reference solution containing 0.1 mol% of  $\text{Ag NTf}_2$  to the reference capillary. LSV measurement is conducted in a three-electrode configuration, with an Au foil as the working electrode. The potentials of both the working and counter electrodes are recorded relative to  $\text{Ag}/\text{Ag}^+$  using a four-electrode connection to the potentiostat. The electrolyte employed is 0.5 mol% of MM  $\text{NTf}_2$ .

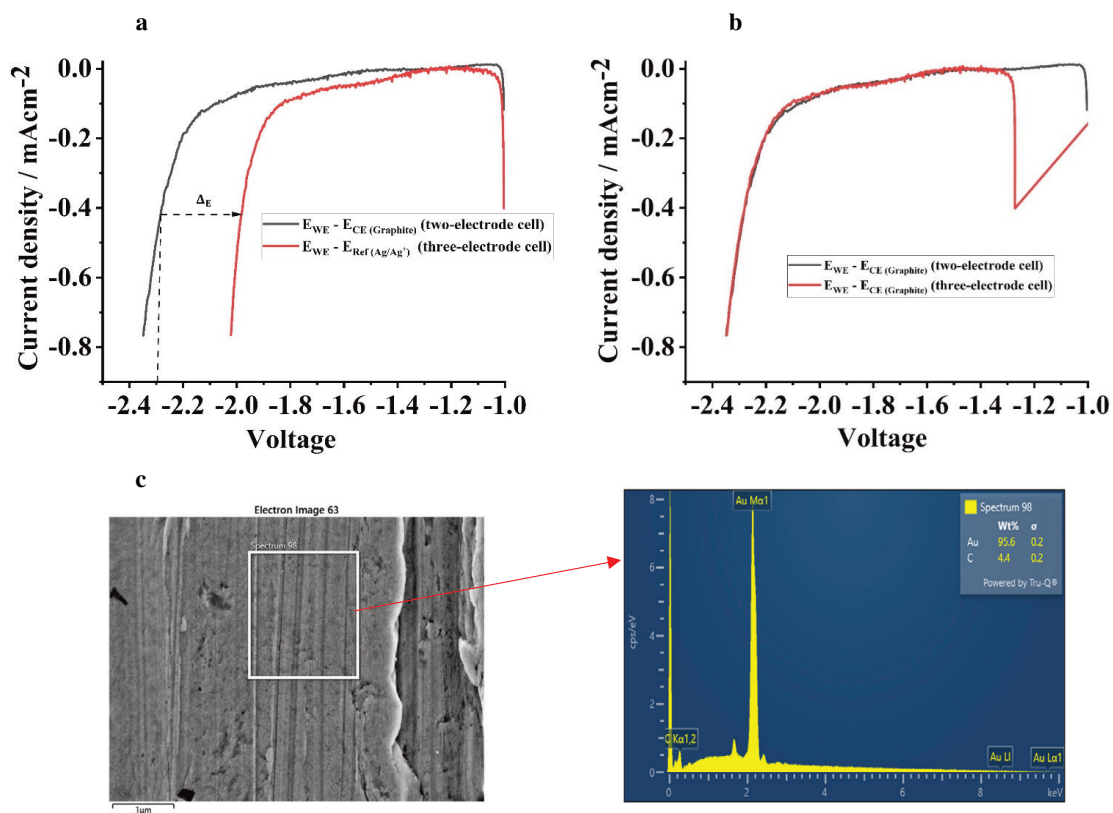


**Figure 2.7** . Illustrating the protocol devised in this study for acquiring electrochemical data in non-aqueous CO<sub>2</sub> reduction. (a) Stage 3: Conversion of the potentials recorded versus graphite in step 1 to the corresponding potentials versus Ag/Ag<sup>+</sup> by comparing the profiles obtained in steps 1 and 2. Note that each potential may require a specific calibration constant ( $\Delta E$ ). (b) Stage 4: Verification of the protocol's accuracy by assessing the overlap of cell potentials obtained in steps 1 and 2. Any deviation between the two profiles could indicate potential interference from Ag leakage- see Figures 2.8-2.9.(c) SEM-EDX analysis providing evidence of a Ag free experiment performed following the devised protocol in this study.

**Figures 2.8 and 2.9** investigate the sensitivity of our devised protocol to Ag impurities.

Deviations in the LSV results recorded in stage 3 suggest interference from Ag leakage and potential Ag deposition (**Figure 2.8**). Subsequent SEM-EDX analysis (**Figure 2.9**) provides further evidence of Ag deposition. These findings demonstrate the capability of our protocol to detect and identify the interference from Ag (or other metals) deposition during electrochemical LSV experiments.

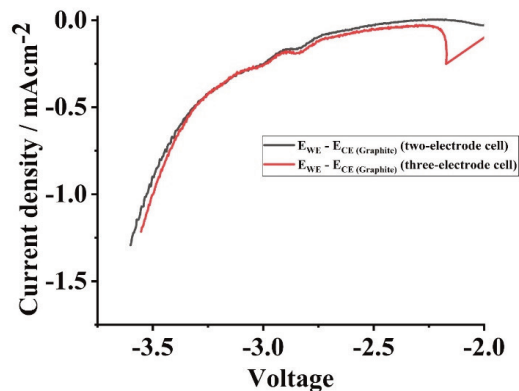


**Figure 2.8.** Sensitivity of the devised protocol for acquiring electrochemical data in non-aqueous CO<sub>2</sub> reduction. Deviations in the current-potential profiles recorded in stage 3 indicates the possible Ag deposition during the calibration stage, see Figure 2.9.

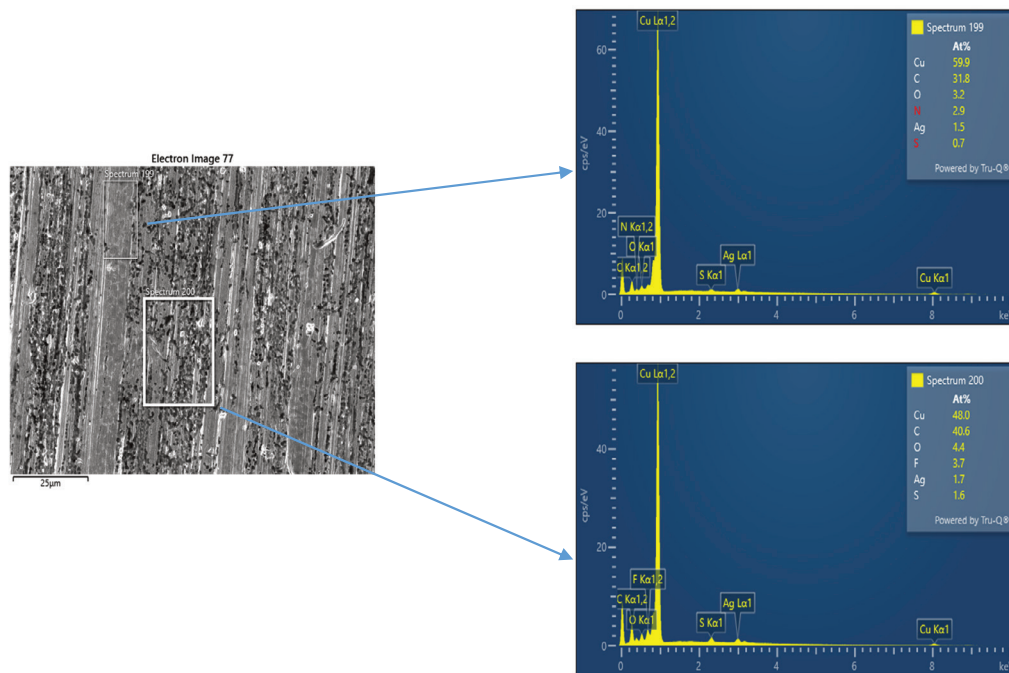


**Figure 2.9.** Sensitivity of the devised protocol for acquiring electrochemical data in non-aqueous CO<sub>2</sub> reduction. SEM-EDX analysis providing evidence of Ag deposition arising from Ag leakage in stage 3.

The significant implications of conducting electrochemical experiments accurately are further illustrated by comparing the electrolysis results obtained when potentials are recorded versus Ag/Ag<sup>+</sup> reference electrode and when our devised protocol is applied (**Figure 2.10**).

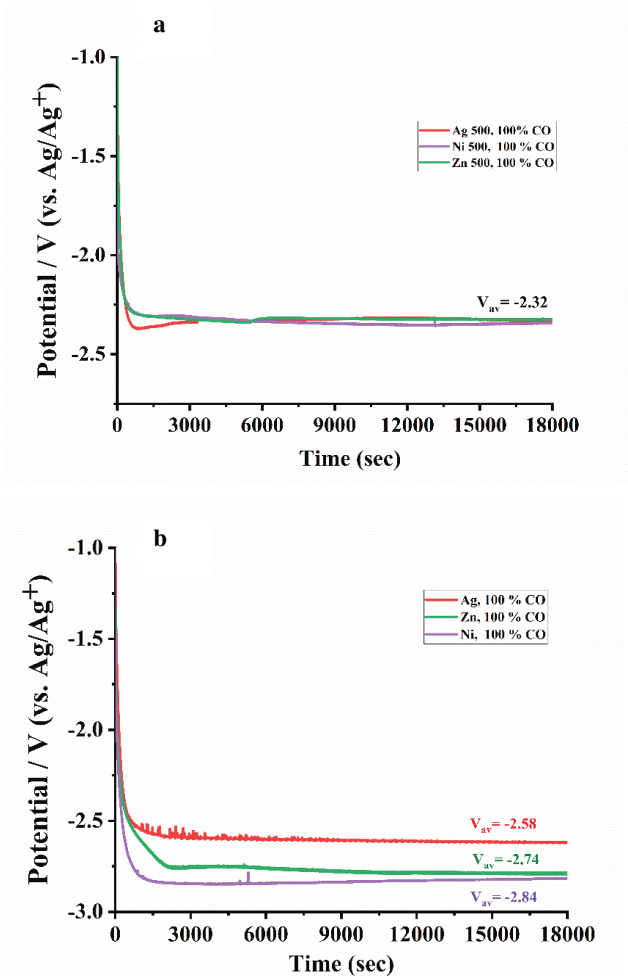


**Figure 2.10.** Electrolysis results for CO<sub>2</sub> reduction at -1 mA/cm<sup>2</sup> using Ag, Ni, and Zn electrodes in anhydrous acetonitrile. The electrolyte consisted of 0.5 mol% of MM NTf<sub>2</sub>. a, The reference solution contained 0.1 mol% (0.02 molar) of Ag OTf, and an Ag wire served as the pseudo-reference electrode. b, Potentials were corrected using the experimental protocol devised in this study, relative to the Ag/Ag<sup>+</sup> reference.

**Figure 2.10a** depicts the experimental results for three catalysts (Ni, Ag and Zn) where 0.1 mol% (0.02 molar) of Ag OTf was added to the reference capillary, with an Ag wire serving as the reference electrode. The corresponding electrodes are labeled as Ag 500, Ni 500, and Zn 500. In contrast, **Figure 2.10b** shows the results obtained when the electrolysis experiments were conducted according to the protocol devised in this study. Interestingly, there are no noticeable differences in the activity of Ni, Zn, and Ag catalysts for CO<sub>2</sub> reduction when Ag OTf is consistently used as the reference solution (Ni 500, Ag 500, and Zn 500). However, when the reference solution is removed from the capillary and our protocol is applied to perform electrolysis, the differences between the three catalysts become evident. We also note that all three electrodes display more negative overpotentials for the same current density as compared to Ag 500, Ni 500 and Zn 500. After conducting EDX-SEM analysis on the electrode surfaces following electrolysis (**Supporting Information Figure S2.2**), it was observed that Ag, carbon, and oxygen were present. This finding is reminiscent of the situation observed for the Pt electrode, as shown in **Figure 2.5**. It is important to note that the concentration of Ag in the reactor was 20 ppm at maximum, indicating that the deposition of Ag alone cannot account for the improved overpotentials observed for Ni 500, Ag 500, and Zn 500 electrodes compared to the situation when Ag OTf was not used. Therefore, we can conclude that the similar catalytic performance observed for Ni 500, Ag 500, and Zn 500 can be attributed to a modified catalytic behavior associated with Ag-MM deposition during the electrolysis process.

While EDX-SEM analysis for electrodes used in **Figure 2.9b** did not show any evidence of Ag deposition, carbon, nitrogen, and oxygen species were still present for all three catalysts (**Supporting Information Figure S2.3**). This observation implies the potential deposition of carbonyl and MM cation during electrolysis. Our experiment with the Zn electrode for 100 hours of electrolysis (**Figure S2.3c**) showed a very slight shift in the overpotential that could always be compensated by the gradual addition of MM cation. In line with the EDX-SEM

analysis, this observation allows us to assume the gradual deposition of cations over the electrode surface during prolonged electrolysis experiments.

In conclusion, the experiments described above show that anhydrous conditions can be assessed easily by noting a reduction potential which is significantly lower than required for the reduction of  $\text{CO}_2$ , while the deposition of Ag can be prevented using the described protocol for measurement of the reference potential.





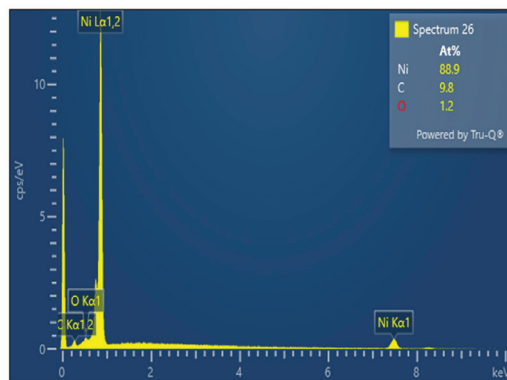
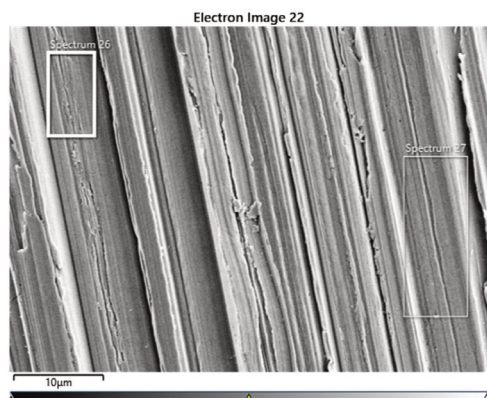
# Supporting Information

## Table of Contents

- I- Results of EDX-SEM analysis**
- II- GC analysis and calibration**
- III- Electrochemical cleaning**
- IV- The effect of counter electrode**
- V- Set-up**

## I- Results of EDX-SEM analysis

a



b

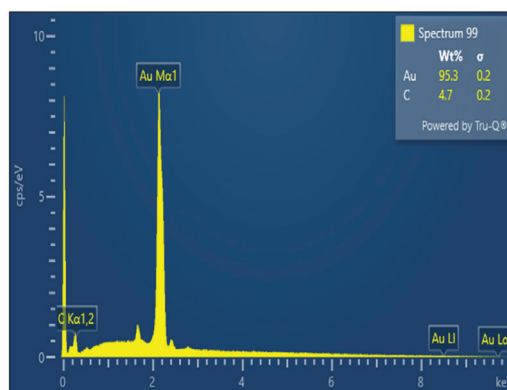
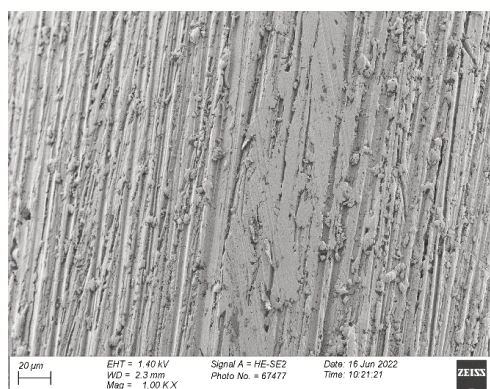


**Figure S2.1.** The results of scanning electron microscopy (SEM) in conjunction with the associated energy-dispersive X-ray spectroscopy (EDX) analysis from (a) Ni and (b) Au electrodes after undergoing the cleaning procedure described in the main text.

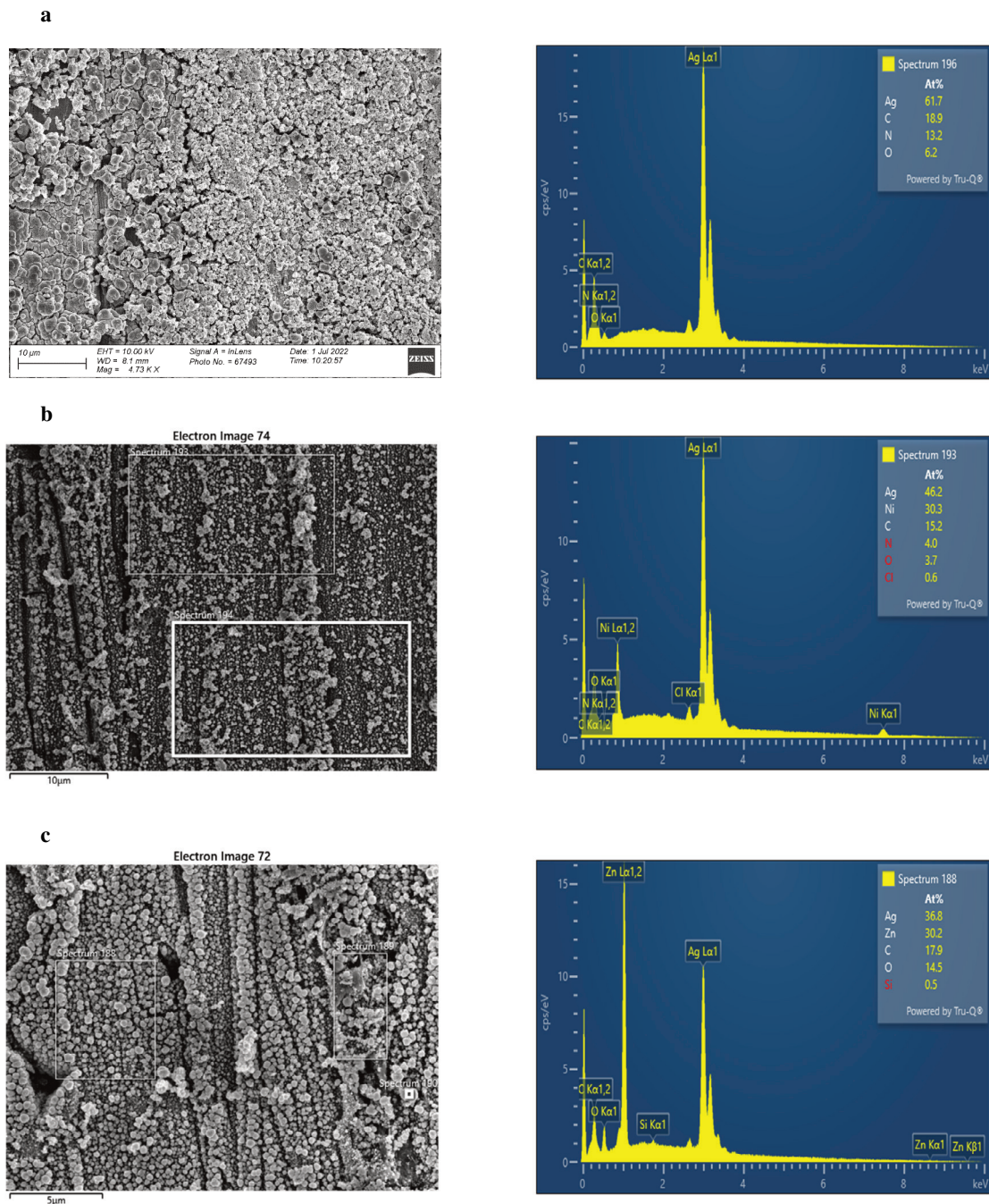


**Figure S2.2.** The results of scanning electron microscopy (SEM) in conjunction with the associated energy-dispersive X-ray spectroscopy (EDX) analysis from (a) Ag 500 , (b) Ni 500, and (c) Zn 500 electrodes after 5 hrs of CO<sub>2</sub> electrolysis. Ag OTf was used as reference solution.

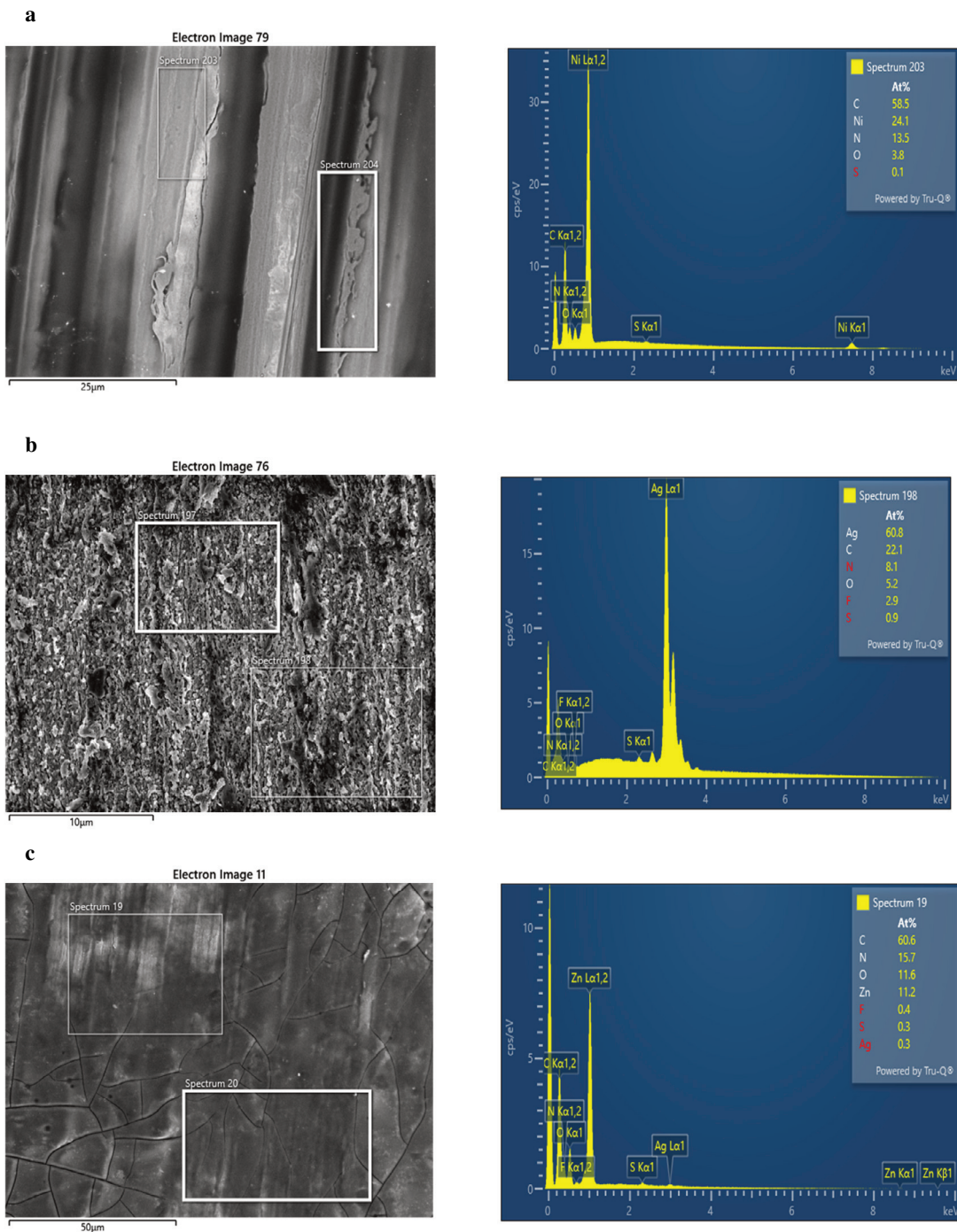


**Figure S2.3.** The results of scanning electron microscopy (SEM) in conjunction with the associated energy-dispersive X-ray spectroscopy (EDX) analysis from (a) Ni, (b) Ag, and (c) Zn electrodes after 3 hrs (Ni), 5 hrs (Ag) and 100 hrs (Zn) of CO<sub>2</sub> electrolysis. The protocol devised in this study was applied to perform the experiments.

## II- GC analysis and calibration

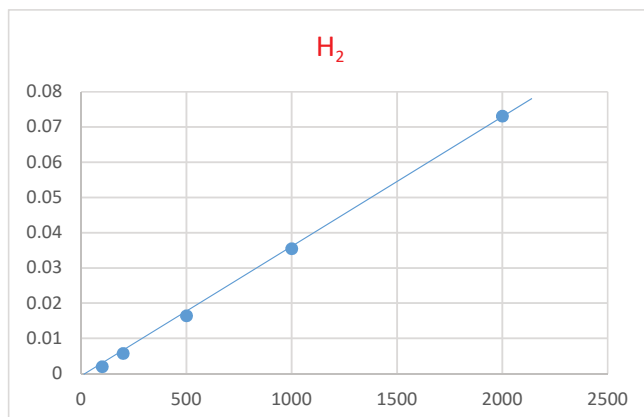
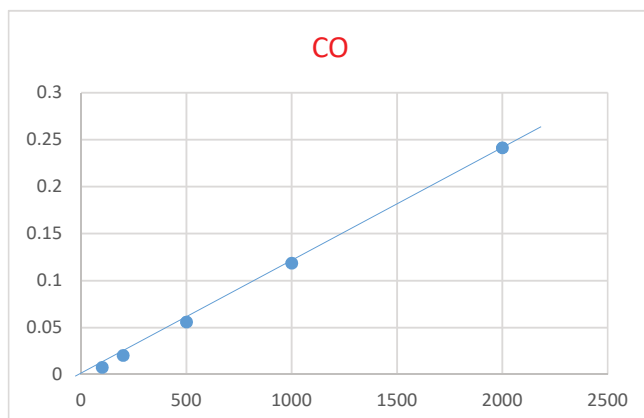


**Figure S2.4.** Calibration of the GC for H<sub>2</sub> and CO.

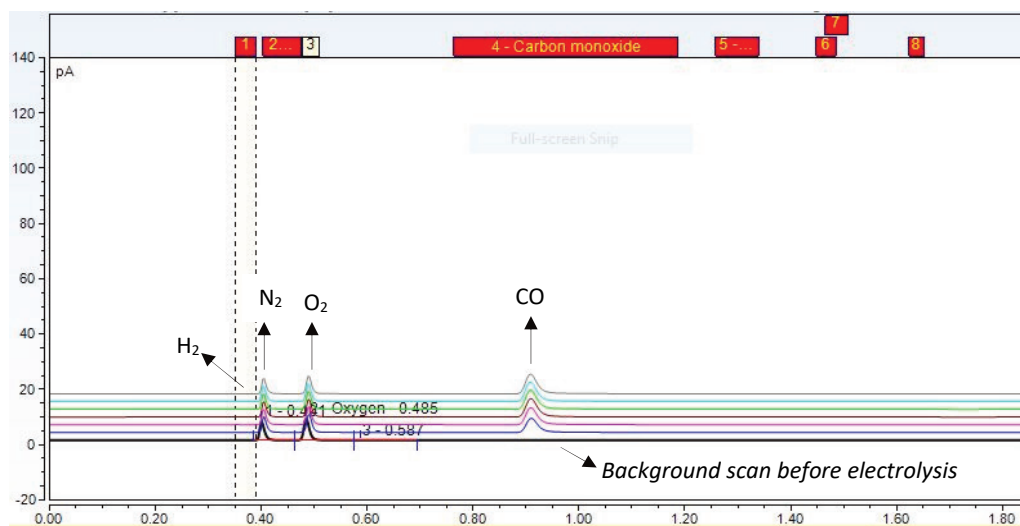


**Figure S2.5.** Subsequent sequences of the GC for detection of the products for CO<sub>2</sub> reduction. The black line is the background obtained before electrolysis. In this example CO is the only product. The electrolyte was 0.5 mol% MM NTf<sub>2</sub> in anhydrous MeCN.

### III- Electrochemical cleaning

For noble electrodes such as Au, an electrochemical cleaning procedure was employed after the electrolysis experiments as follows: After sonication in 0.5 molar  $\text{HNO}_3$ , the electrode was subjected to electrochemical washing in a 0.1 molar  $\text{H}_2\text{SO}_4$  aqueous solution. The electrochemical cleaning process involved the recording of cyclic voltammograms (CVs) with 20 cycles at a scan rate of 1 V/sec, followed by 10 cycles at 100 mV/sec within the voltage range of 0.2 to 1.5 V versus Ag/AgCl. **Figure S2.6** provides an illustration of the electrochemical cleaning procedure for the Au electrode. The cleaning process was continued until repeatable cycles were achieved.

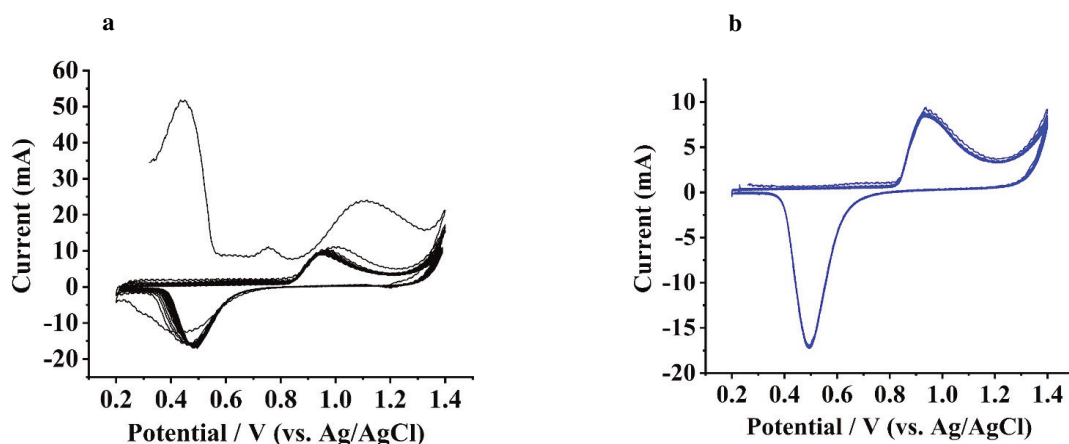


**Figure S2.6.** Electrochemical cleaning of Au electrode in a 0.1 molar  $\text{H}_2\text{SO}_4$  aqueous solution. **(a)** The first 20 cycles demonstrate the gradual attainment of repeatable cycles. The initial cycle displays a noticeable oxidation peak, indicating the removal of carbon species from the electrode surface, which was previously exposed to  $\text{CO}_2$  electrolysis experiments. **(b)** Subsequent cycles exhibit consistent and repeatable behavior. The electrochemical cleaning process was conducted immediately after  $\text{CO}_2$  electrolysis in a 0.5 mol% MM  $\text{NTf}_2$  electrolyte solution in anhydrous MeCN.

However, electrochemical cleaning for non-noble metals such as Cu resulted in poor electrochemical behavior. **Figure S2.7a** illustrates the cleaning results of a Cu electrode, which does not exhibit a reversible reduction and oxidation cycle as observed for the Au electrode. Comparatively, **Figures S2.7b and S2.7c** present the cyclic voltammetry results for Au and Cu

electrodes, respectively, after the electrochemical cleaning process. In the case of the Cu electrode, a noticeable unassigned peak is observed during the reduction cycle, while the Au electrode exhibits the expected behavior of a clean electrode.

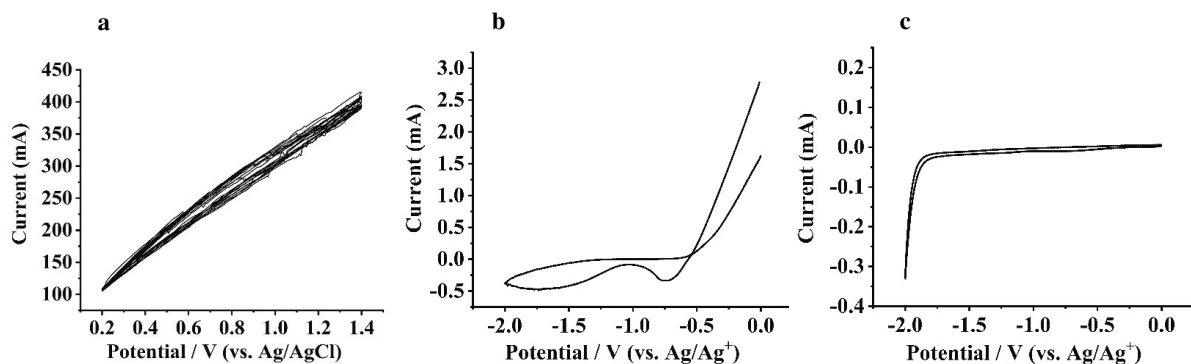


**Figure S2.7.** (a) Electrochemical cleaning of Cu electrodes in a 0.1 molar H<sub>2</sub>SO<sub>4</sub> aqueous solution. b and c, Cyclic voltammetry in CO<sub>2</sub> saturated anhydrous acetonitrile for Cu (b) and Au (c) electrodes after electrochemical cleaning. 0.5 mol% MM NTF<sub>2</sub> was added as supporting electrolyte.



#### IV- The effect of counter electrode

a



b



**Figure S2.8.** Au voltammetry electrode before (a) and after (b) voltammetry experiments under CO<sub>2</sub> purging with Ag as the counter electrode. The deposition of silver is visibly observed after the voltammetry experiments. The supporting electrolyte used was 0.5 mol% MM NTF<sub>2</sub>.

## V- Set-up

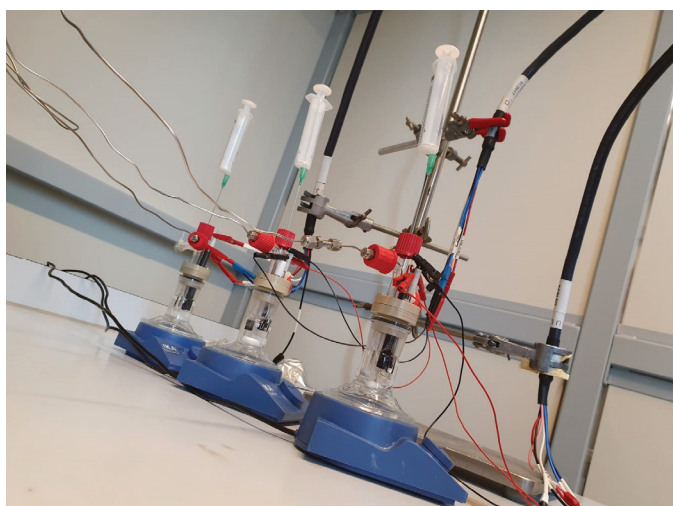
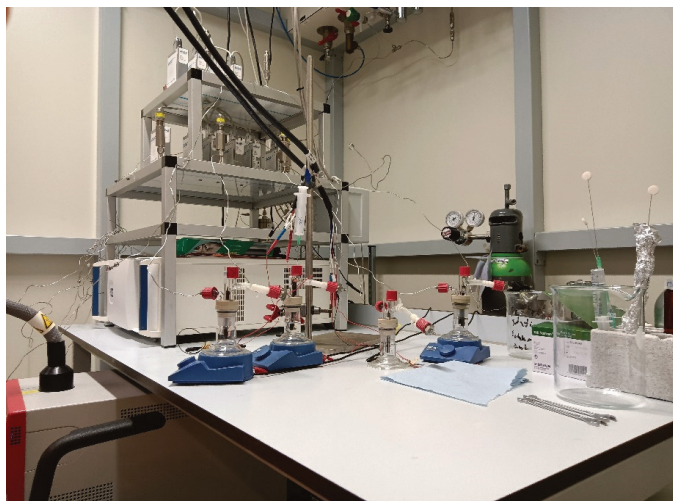
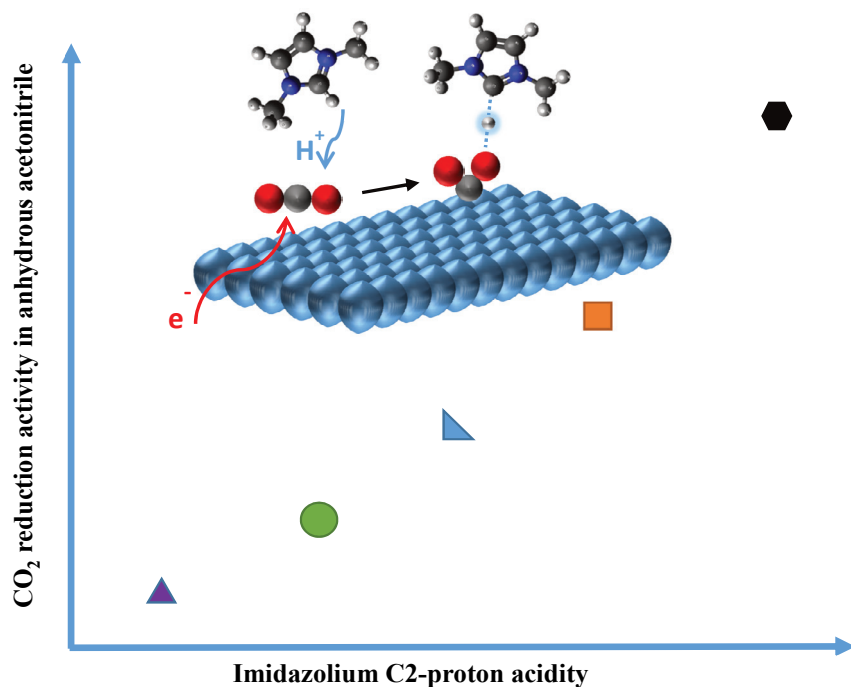


**Figure S2.9.** Experimental set-up designed for conducting electrochemical CO<sub>2</sub> reduction under anhydrous conditions. Solutions were consistently transferred from the glove box and injected into the reactors while maintaining a continuous purge of super dry He or CO<sub>2</sub> gas inlet.

## Chapter 3:

# Unveiling the Role of Imidazolium Cations in Promoting Electrochemical CO<sub>2</sub> Reduction

Proposed concerted pathway in the electrochemical reduction of CO<sub>2</sub>



*This chapter is partially based on:* S. Neyrizi, J. Kiewiet, M. A. Hempenius, G. Mul, What It Takes for Imidazolium Cations to Promote Electrochemical Reduction of CO<sub>2</sub>. ACS Energy Lett. 2022, 7, 3439–3446.

## Summary

In this chapter, it is first demonstrated that the combination of imidazolium cations with anhydrous media (dry acetonitrile) leads to unprecedentedly low overpotential for CO<sub>2</sub> conversion over conventional electrodes (such as Au foil) with 100% Faradaic efficiency for CO production. Modification of N<sub>1</sub> and N<sub>3</sub> functionality of imidazolium cation shows a direct correlation between the performance for CO<sub>2</sub> reduction in anhydrous media and C<sub>2</sub>-H acidity of the cation. Based on NMR analyses, DFT calculations, and isotopic labeling study, showing an inverse kinetic isotope effect, it is demonstrated that the mechanism involves a concerted coupled proton-electron transfer with a partial proton transfer to the electrode-adsorbed CO<sub>2</sub> intermediate.

## Introduction

Imidazolium cations have been shown to enhance the performance of electrode catalysts for CO<sub>2</sub> reduction in aqueous and also in non-aqueous media- for more details see **Chapter 1**. However, their underlying role and the reason for their enhanced performance over other electrolyte cations remain unclear.

In this chapter, the objective is to develop a comprehensive understanding of the mechanisms underlying the effectiveness of imidazolium cations in facilitating CO<sub>2</sub> reduction. To accomplish this, Au electrode and anhydrous acetonitrile were chosen as a model system for conducting a systematic investigation into how the molecular structure of imidazolium compounds influences their performance in electrochemical CO<sub>2</sub> reduction.

Regarding improvements in kinetics in non-aqueous media through the use of imidazolium cations, previous studies have reported an onset potential of approximately ~ -0.4 V vs SHE for CO formation, albeit with the presence of 10 to 500 mM H<sub>2</sub>O<sup>66</sup>. Lau et al. reported onset potentials around -2.0 V vs. Fc/Fc<sup>+</sup> when utilizing a C2-methylated imidazolium cation in acetonitrile<sup>8</sup>. Here it is found that the systematic chemical modification of the imidazolium cations under well-controlled anhydrous media leads to an onset potential of around -0.8 V vs. Ag/Ag<sup>+</sup> (~ -0.258 V vs. SHE) which shows significant improvements over previous studies. Furthermore, the performance of the imidazolium cation is proved to be in strong correlation with the acidity of the C2-H bond, demonstrating the kinetic relevance of proton donation through isotopic labeling experiments. Finally, complementary DFT calculations are conducted to support the findings, confirming that a concerted coupled electron-proton transfer mechanism with partial proton transfer is the most likely operative mechanism.

The demonstrated mechanism provides guidelines for improvement in the energy efficiency of non-aqueous electrochemical CO<sub>2</sub> reduction by a tailored design of electrolyte cations.

## Results and discussion

**Figure 3.1 a** shows linear sweep voltammetry (LSV) for the Au disk electrode immersed in such anhydrous acetonitrile containing 0.5 mol% of 1,3-dimethyl imidazolium NTf<sub>2</sub> (**MM** NTf<sub>2</sub>) introducing a purge of He or CO<sub>2</sub> in a small conventional, undivided electrochemical cell. The absence of a noticeable faradaic current within the potential window of -1.8 to -2.2 V vs. Ag/Ag<sup>+</sup> in the absence of CO<sub>2</sub>, demonstrates the stability of the imidazolium cation against electrochemical conversion, which is also confirmed by NMR analysis. In the presence of CO<sub>2</sub>, significant current can be observed, assigned to the conversion of CO<sub>2</sub> to CO. Such currents are not observed when other types of cations (Cesium NTf<sub>2</sub> and tetraethylammonium NTf<sub>2</sub>) are dissolved in acetonitrile (**Figure 3.1 b**). Thus, the unique ability of imidazolium cations in promoting the reduction of CO<sub>2</sub> in anhydrous media is demonstrated. Performing the experiment in a rotating disc electrode configuration (**Figures 3.1 c and 3.1 d**), minimizing mass transfer limitations, demonstrates that the onset potential for CO<sub>2</sub> activation in anhydrous **MM**-acetonitrile electrolyte is around -0.8 V vs. Ag/Ag<sup>+</sup> (~ -0.258 V vs. SHE (± 45 mV), see also experimental details in **Chapter 2**). To the best of our knowledge, this onset potential is the lowest ever reported for activation of CO<sub>2</sub> in non-aqueous electrolytes.

Chronopotentiometry at -10 mA/cm<sup>2</sup> shows high stability in the performance for the production of CO in the **MM**-acetonitrile electrolyte with 100% Faradaic efficiency (FE) (**Figure 3.1 e**, for the procedure used to evaluate Faradaic efficiencies see experimental protocols in **Chapter 2**). NMR analyses confirm that after electrolysis, **MM** NTf<sub>2</sub> and acetonitrile remain unchanged (see **Figures S3.31 to S3.33**). It should be mentioned that the products formed in the presence of other cations such as tetrabutylammonium NTf<sub>2</sub> are mainly hydrogen and methane (**Figure S3.1**), showing that not only activity (on-set potential) but also selectivity (FE) is favorably tuned by the imidazolium cation. Upon switching the CO<sub>2</sub> flow to He, the concentration of CO decreases gradually while the cell potential increases. Using 10 mL of the **MM**-acetonitrile

electrolyte it took  $\sim 90$  mins to minimize the CO concentration (**Figure 3.1 f**). The gradual decrease in CO level after switching the flow of CO<sub>2</sub> to He is due to the high solubility of CO<sub>2</sub> in MM-acetonitrile electrolyte<sup>67-68</sup>. As described in **Chapter 2**, the water content was 55 ppm at maximum for all experiments; this water fraction might result in the formation of carboxylate species<sup>6,66</sup>; however, the analysis did not provide any evidence of the presence of such species.

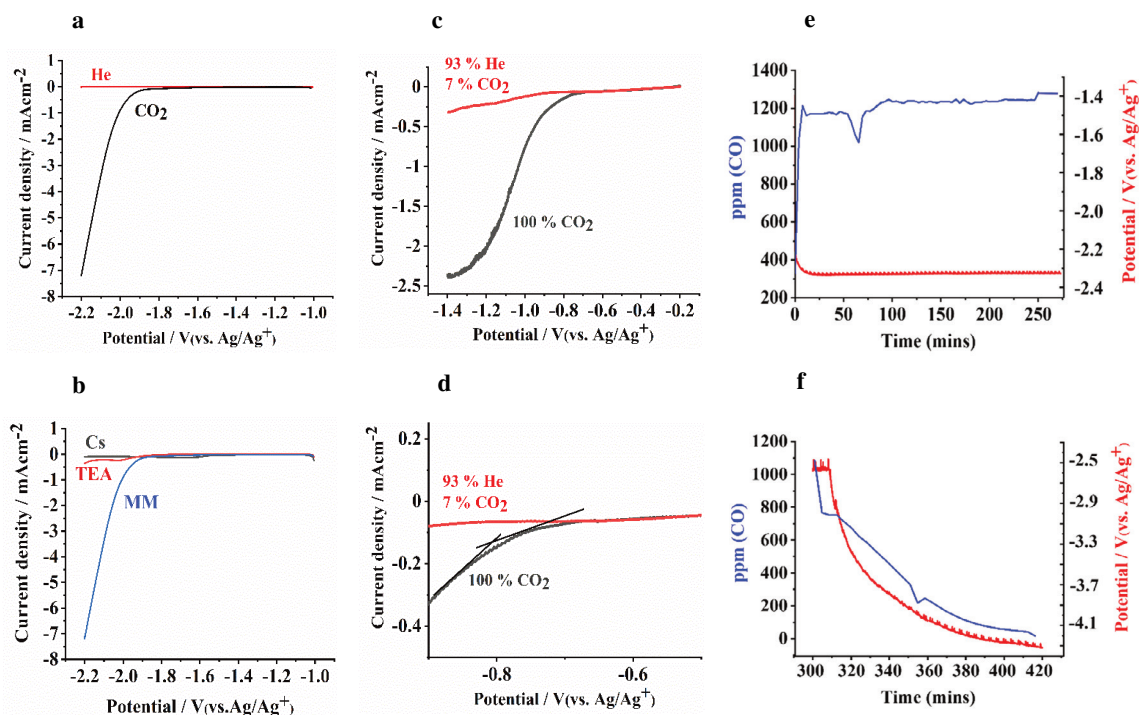


**Figure 3.1. The co-catalytic activity of imidazolium cation for electrochemical CO<sub>2</sub> reduction in acetonitrile (<50 ppm water).** (a) LSV with 0.5 mol% of 1,3-dimethyl imidazolium MM NTf<sub>2</sub>: under He (red) and CO<sub>2</sub> (black) atmosphere in quiescent solution. (b) LSVs for Au disk electrode in CO<sub>2</sub> saturated acetonitrile with 0.5 mol% of MM NTf<sub>2</sub> (blue), TEA NTf<sub>2</sub> (red) and Cs<sup>+</sup> NTf<sub>2</sub> (black) electrolyte. (c) LSVs with 0.5 mol% of MM NTf<sub>2</sub> with rotating Au disk electrode at 2000 rpm. Red was recorded with 7% CO<sub>2</sub> partial pressure. Black was recorded with CO<sub>2</sub> saturated acetonitrile. (d) The zoomed-in potential region from c to highlight the onset potential under CO<sub>2</sub> purging. (e) Chronopotentiometry at -10 mA/cm<sup>2</sup> and constant CO production with 0.5 mol% MM NTf<sub>2</sub> under 5 ml/min CO<sub>2</sub> purging [1.2 bars] and normal stirring conditions using an Au foil electrode (blue), the potential remains stable during electrolysis and Faradaic efficiency for CO was 100%. f, CO (ppm) level in GC after switching the flow from CO<sub>2</sub> to He. WE potential increases with switching flow to He which shows a higher overpotential for the same current density in the absence of CO<sub>2</sub> as the reactant.

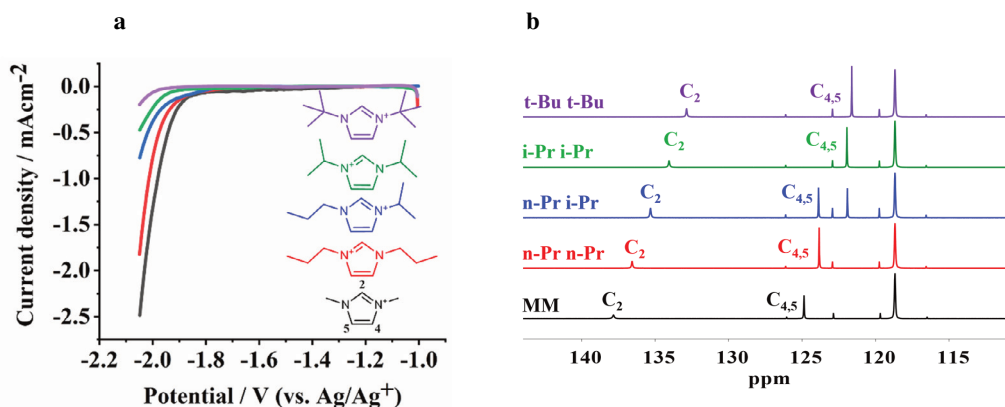


**Figure 3.2.** (a) LSVs with 0.5 mol% of: 1,3-dimethylimidazolium NTf<sub>2</sub> (**MM**), 1,3-dipropylimidazolium NTf<sub>2</sub> (**n-Pr n-Pr**), 1-propyl-3-isopropyl imidazolium (**n-Pr i-Pr**), 1,3-diisopropylimidazolium (**i-Pr i-Pr**), and 1,3-di-*tert*-butylimidazolium (**t-Bu t-Bu**) in CO<sub>2</sub>-saturated acetonitrile. (b) Comparison of <sup>13</sup>C NMR spectra for five cations, recorded in CD<sub>3</sub>CN.

To investigate the influence of imidazolium cations on CO<sub>2</sub> reduction in anhydrous conditions, several analogs of the **MM** cation were synthesized and their performance in the electrochemical reduction of CO<sub>2</sub> was evaluated using voltammetry. **Figure 3.2 a** shows LSVs for **MM**, 1,3-dipropylimidazolium (**n-Pr n-Pr**), 1-propyl-3-isopropylimidazolium (**n-Pr i-Pr**), 1,3-diisopropylimidazolium (**i-Pr i-Pr**) and 1,3-di-*tert*-butylimidazolium (**t-Bu t-Bu**) using an Au electrode in CO<sub>2</sub>-saturated acetonitrile. The structural variation of the imidazolium cation clearly affects the achievable current density. For example at -2 V (vs. Ag/Ag<sup>+</sup>), the current density for **t-Bu t-Bu** is lowered by a factor of 10 in comparison to the **MM** analog. Further, chronoamperometry at -1.8 V (vs. Ag/Ag<sup>+</sup>) shows that in the presence of 0.5 mol % of **MM** 3 times more charge is transferred to CO<sub>2</sub>, yielding CO (**Figure S3.2**), than achieved with the same amount of **t-Bu t-Bu**.

**Figure 3.2 b** shows <sup>13</sup>C NMR spectra for 5 cations. **MM** displays the largest chemical shift (ppm) among all cations for all three carbons of the ring [C2, C4, and C5]. VDD charge analysis of the cations also shows a more positive charge for the C2-proton and C4, C5-protons of the **MM** cation in comparison to other cations; which is in agreement with the trend obtained with <sup>13</sup>C NMR spectra (for VDD charge analysis see **Figure S3.8**). The differences in chemical shifts



in  $^{13}\text{C}$  NMR and VDD charge analysis show that the electron density is a function of the substitution, which also affects the C2-H acidity. pKa calculations/measurements in acetonitrile from previous studies also demonstrate a trend in the acidity for **MM** (32.5), **i-Pr i-Pr** (33.6), and **t-Bu t-Bu** (34.1) cations<sup>69-70</sup>, which is also in agreement with the trend obtained with  $^{13}\text{C}$  NMR spectra (**Table S3.1**). Interestingly, and most importantly, the electron density of the imidazolium cation translates to higher or lower performance in the electrochemical reduction of  $\text{CO}_2$ , showing an almost linear trend between  $^{13}\text{C}$  peak position (**Figure 3.2 b**) and current density in the reduction of  $\text{CO}_2$ , as schematically indicated in the graphical abstract of this chapter.

With the establishment of this structure-activity relationship, the focus now shifts to understanding *how imidazolium promotes  $\text{CO}_2$  reduction in anhydrous media*. To address this, the significance of the C2-proton was first compared to that of the C4- and C5-protons of the imidazolium ring. In the literature discussing electrochemical  $\text{CO}_2$  reduction, it is well-known that the rate-determining step (RDS) is the first electron transfer from the electrode to adsorbed  $\text{CO}_2$ <sup>19,39</sup>. According to previous studies, the Au electrode surface facilitates the initial electron transfer to  $\text{CO}_2$ , resulting in the formation of a high-energy  $^*\text{CO}_2^-$  intermediate<sup>71-72</sup>. DFT calculations revealed a notable  $\sim 70$  kcal/mol difference in free energy between the adsorbed  $^*\text{CO}_2^-$  ( $\text{Au-CO}_2^-$ ) and the solvated  $\text{CO}_2^-$  radical ( $\text{CO}_2^-$  (sol)), confirming the hypothesis of adsorption-induced electron transfer ( $^+\text{CO}_2 + \text{e}^- = ^*\text{CO}_2^-$ ) in acetonitrile (**Supporting Information Section V**). The structure-activity relationship developed in this work suggests that ring-protons H2, H4, and H5 may play a role in promoting the kinetics by stabilizing the  $^*\text{CO}_2^-$  intermediate. While the trend in NMR chemical shifts for C2 is more pronounced than for C4 or C5 (**Figure 3.2 b**), it remains inconclusive which ring proton is involved in stabilizing the  $^*\text{CO}_2^-$  intermediate. To investigate further, DFT calculations were employed to compare the stability of  $^*\text{CO}_2^-$  when interacting with the C2-proton (*configuration i*) or C4- and C5-protons

(*configuration ii*) of the MM cation (**Figure 3.3**). *Configuration i* exhibited a gain of 4 kcal/mol compared to *configuration ii*. Surface charge density and differential VDD charge analysis (**Figure 3.3** bottom part, also see **Supporting Information Figure S3.10**) indicate that *configuration i* with the C2-proton leads to a more uniform charge distribution (noted by the red and blue color densities). Additionally, the activity of MM was compared to that of 2-methylated MM (**2-Me MM**) to shed light on the role of the C2-proton (**Figure S3.3**). The substantial decrease in current density observed for **2-Me MM** compared to **MM** suggests that the C2-proton is most effective in promoting the reduction of CO<sub>2</sub>.

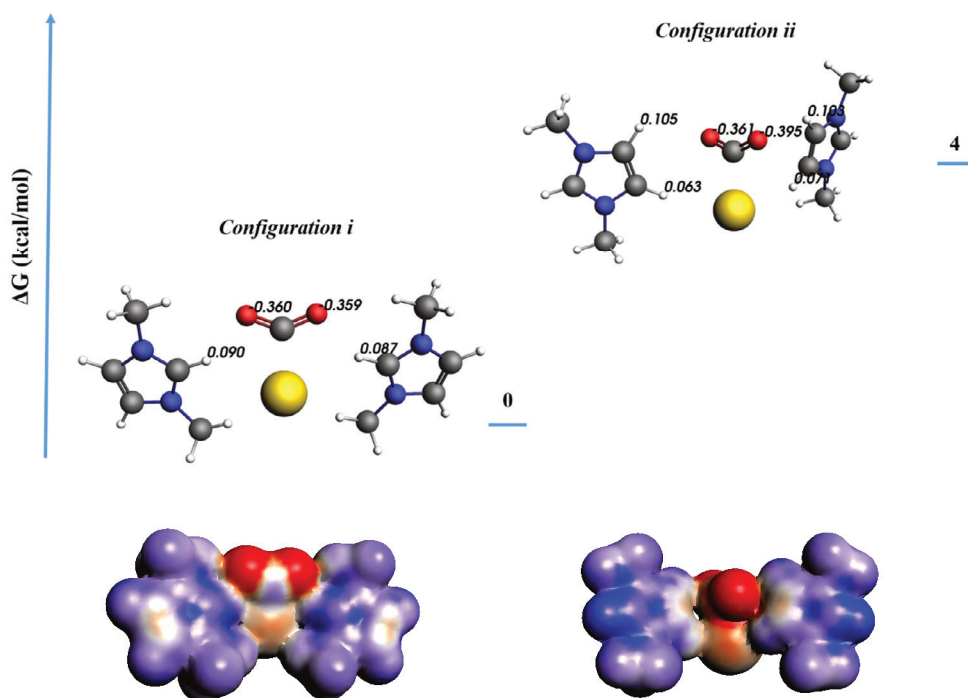


**Figure 3.3.** 4 kcal/mol energy is gained when C-2 proton is brought into interaction with  $^*\text{CO}_2^-$  (*configuration i* vs *configuration ii*). This extra energy gain can be understood in terms of a more uniform charge distribution. VDD charges are shown for the oxygen atoms of  $^*\text{CO}_2^-$  and involved C2-, C4-, and C5- protons (for differential charge analysis see Supporting Information Figure S3.10). Surface charge densities (on COSMO surface) are constructed and are depicted below each relevant configuration.

We will now investigate how the C2-proton affects the reduction of CO<sub>2</sub>. *Pathway i* (**Figure 3.4 a**) considers electron transfer to the cation to form a cation radical as proposed by Wang, et al.<sup>4</sup>. For this pathway, the reduced cation acts as an initiator and reduces CO<sub>2</sub> through a nucleophilic attack to form an imidazolium-CO<sub>2</sub> adduct (**Supporting Information Scheme S3.1**). After the nucleophilic attack, the C2-proton is transferred via an isomerization step, which is considered the rate-determining step (RDS). However, DFT calculations for the isomerization step do not show any noticeable difference in the activation energy for several selected cations (**Supporting Information Section VII**). Besides, *pathway i* implies an electrochemical response in the absence of CO<sub>2</sub> (the electron transfer to the imidazolium cation), which is not observed in **Figure 3.1**. If an initial electron transfer to the imidazolium cation were the case, the same onset potentials would be observed for the reduction of the cation (CVs under He purging) and reduction of CO<sub>2</sub> (CVs under CO<sub>2</sub> purging). This situation is typical when pyridinium-type molecules are used as the promoter but this is not the case with imidazolium cations. (For more arguments see **Supporting Information Section VIII**).

Thus, even though the mechanism proposed in *pathway i* might be considered in homogeneous solution electron transfer reactions, Au catalyzed surface transformation appears to follow another mechanism. *Pathway ii* (**Figure 3.4 b**) depicts the initial electron transfer to CO<sub>2</sub> upon its adsorption. Upon electron transfer, the imidazolium cation donates its C2-proton to the negatively charged \*CO<sub>2</sub><sup>-</sup> being formed on the Au surface. Such a charge transfer is also confirmed by differential charge analysis from the interaction between MM and \*CO<sub>2</sub><sup>-</sup> (**Figure 3.3, Supporting Information Figure S3.10**). This pathway highlights a concerted coupled electron-proton transfer (CEPT) mechanism. For this mechanism, the first electron transfer should be still rate-determining, and this was confirmed with the obtained Tafel slope of 119 mV/dec (**Supporting Information Figure S3.4**). CEPT reactions are of significant importance

because they can bypass high-energy intermediates present in sequential PT and ET steps and generally occur with lower reaction barriers (**Figure 3.4 c**)<sup>73-75</sup>.

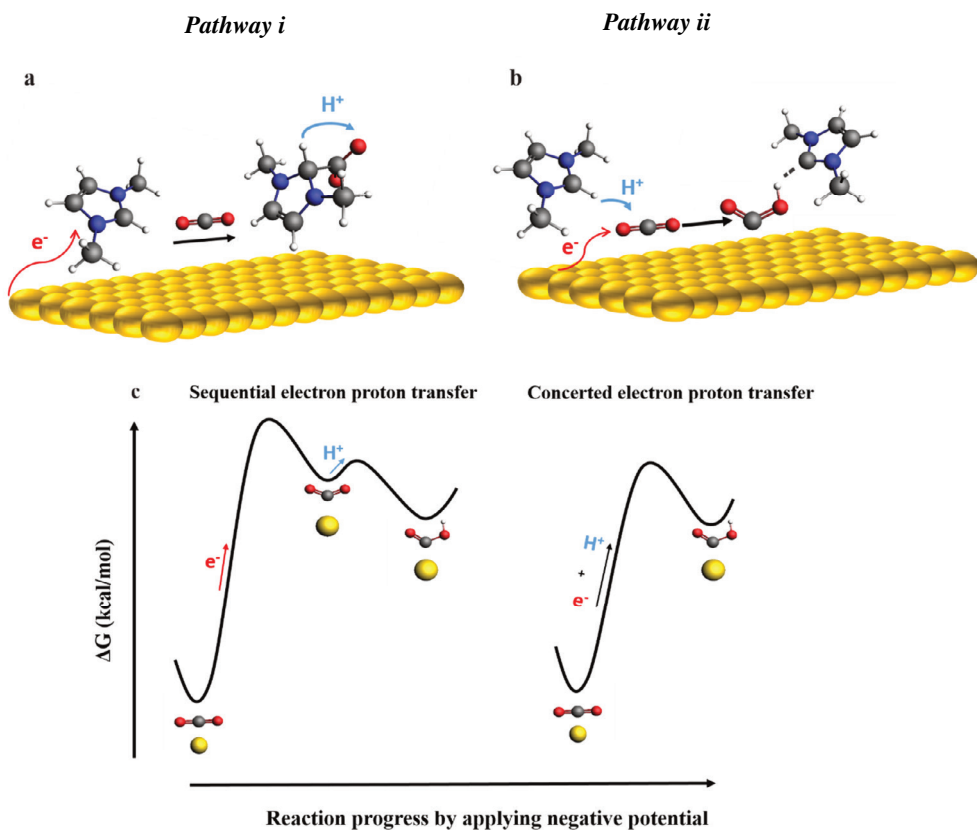


**Figure 3.4.** (a) *Pathway i* depicts an initial electron transfer to MM cation followed by a sequential PT-ET to  $CO_2$ . (b) *Pathway ii* (proposed in this work) depicts the concerted mechanism in which a bidirectional ET (from Au electrode) and PT (from C2-proton of MM cation) leads to a lower energy barrier. **c**, shows a schematic of the energy diagram for step-wise and concerted pathways.

For a CEPT mechanism, an  $^*(\text{OC})\text{O}\cdots\text{H}$  intermediate develops during the rate-determining step. To determine the kinetic significance of the  $^*(\text{OC})\text{O}\cdots\text{H}$  intermediate, the difference in frequencies between O-H and deuterated O-D of the adsorbed intermediate was first calculated ( $\Delta\sigma_{\text{in}}$ , to be  $964\text{ cm}^{-1}$  (in these calculations, complete covalent O-H and O-D bond formation were considered), which is larger than the difference in frequency of the C-H and C-D bonds in the imidazolium cations ( $(\Delta\sigma)_{\text{Gs}}=837\text{ cm}^{-1}$ ) (see **Supporting Information Section IX**). This difference in differential frequencies leads to a larger difference in the  $\Delta\text{ZPE}$  (zero-point energy) of the transition state than in the  $\Delta\text{ZPE}$  in the ground state, suggesting an inverse kinetic isotope effect (iKIE,  $\frac{k_{\text{H}}}{k_{\text{D}}} = 0.735$ ) when a covalent bond character is considered (see **Figure 3.5 a**). Thus, from frequency calculations, it is predicted that for a CEPT mechanism deuterium substitution at the C2 position of the imidazolium cation should result in a higher current density (lower activation energy) in the reduction of  $\text{CO}_2$ . The inverse kinetic isotope effect was indeed experimentally identified when performing the reduction of  $\text{CO}_2$  in an RDE setup ( $\frac{k_{\text{H}}}{k_{\text{D}}} = 0.89$ , **Figure 3.5 b** and **Supporting Information Figure S3.5**). The deuterated version of MM shows significantly larger current densities, with an 18% deviation between the calculated, and experimentally determined iKIE. This deviation can be rationalized in the context of a partial proton transfer in the concerted mechanism (see also **Supporting Information Section X** for extra notes on iKIE) and there is still an opportunity to further improve performance by optimizing the  $^*(\text{OC})\text{O}^{\delta-}\cdots\delta^+\text{H-C2}$  bond in the transition state, lowering the energy of the transition state.

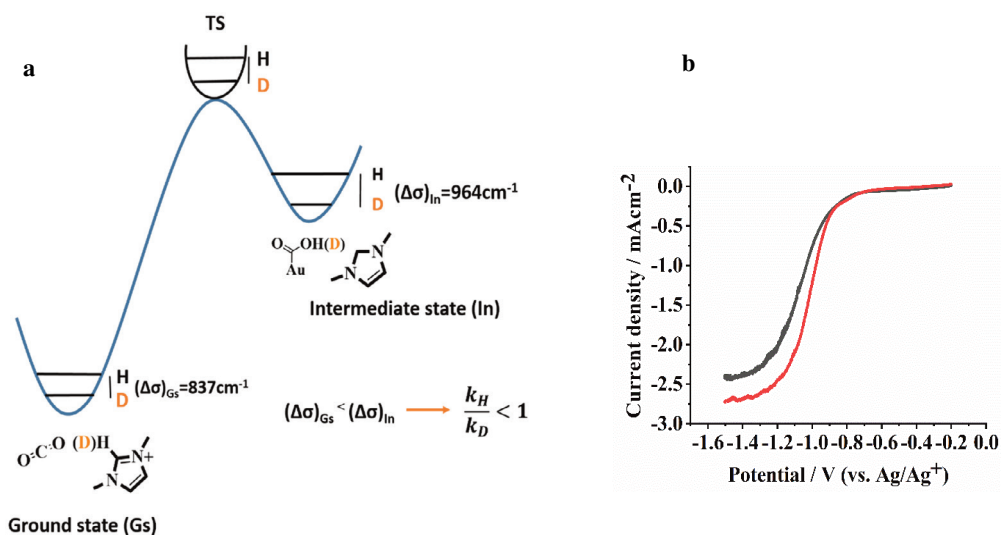


**Figure 3.5.** (a) DFT calculation for a CEPT rate-determining step for **MM** co-catalyzed  $\text{CO}_2$  reduction in anhydrous acetonitrile. (b) LSVs recorded using Au rotating disk electrode (2000 rpm) with **MM** and **deuterated MM** in  $\text{CO}_2$  saturated acetonitrile showing an experimental inverse kinetic isotope effect, for quantification of iKIE see Supporting Information Figure S3.5.

## Conclusion

This study demonstrated a correlation between the C2-H acidity of imidazolium cations and the achievable current density in the reduction of  $\text{CO}_2$  under anhydrous conditions. This correlation was established by modifying the functionality of the molecule at the N1 and N3 positions. The inverse kinetic isotope effect and Tafel analysis showed that the rate-determining step involves a concerted coupled electron-proton transfer with a partial proton transfer, which leaves room for even further optimizing the molecular structure. What we have not assessed in the present study, is the interaction of the conjugated base of the imidazolium cation (carbene) with the electrode. *N*-Heterocyclic carbenes (NHCs) readily bind transition metals by  $\sigma$ -donation<sup>5</sup>, and recently their great affinity for electrode surfaces such as Au has been shown<sup>76</sup>. The relevance of such interaction for performance in the electrochemical reduction of  $\text{CO}_2$  needs to be assessed for electrodes of different binding energies.

# Supporting Information

## Table of Contents

- I. Materials
- II. Electrochemical data
- III. VDD charge analysis of cations
- IV.  $^{13}\text{C}$  NMR chemical shifts (ppm) of imidazolium NTf<sub>2</sub> salts in CD<sub>3</sub>CN
- V. Stability of  $^*\text{CO}_2^-$  vs free  $\text{CO}_2$  anion radical in acetonitrile
- VI. Interaction of C2-proton and C4, C5-protons of MM with  $\text{Au-CO}_2^-$
- VII. Activation energy analysis for isomerization step
- VIII. Notes on the initial act of the electrode
- IX. Inverse kinetic isotope effect estimated from frequency calculations
- X. Extra notes on inverse kinetic isotope effect
- XI. Synthetic procedures
- XII. Copies of  $^1\text{H}$ ,  $^{13}\text{C}$ , and  $^{19}\text{F}$  NMR spectra
- XIII. Computational methods

## I. Materials

Gold (Au) voltammetry electrodes (3.0 mm diameter, 99.95%) were purchased from Prosense. Gold wire (0.025 mm diameter, 99.99 %) for electrolysis experiments were supplied by Sigma Aldrich. Anhydrous acetonitrile (99.8%), acetonitrile (ReagentPlus, 99%), dichloromethane (puriss p.a. ACS reagent  $\geq 99.9\%$ ), diethyl ether (anhydrous, ACS reagent,  $\geq 99.0\%$ ), tetraethylammonium bis(trifluoromethylsulfonyl)imide (97%) and tetrabutylammonium bis(trifluoromethylsulfonyl)imide (99%), bis(trifluoromethane)sulfonimide lithium salt (99%), silver trifluoromethanesulfonate ( $\geq 99\%$ ), deuterium oxide (99.9 atom % D), acetonitrile- $d_3$  ( $\geq 99.8$  atom % D), 1,3-diisopropylimidazolium chloride (97%) and 1,3-di-*tert*-butylimidazolium tetrafluoroborate (97%) were obtained from Sigma-Aldrich. Acetonitrile- $d_3$  (99.8 atom % D) for electrolysis experiments, Cs bis(trifluoromethylsulfonyl)imide (98%) , and 1-iodopropane (99%) were obtained from Acros Organics. 1-Isopropylimidazole (98%) was obtained from abcr GmbH, Karlsruhe. 1,3-Dimethylimidazolium bis(trifluoromethylsulfonyl)imide (99%), 1-methyl-3-pentyl imidazolium bis(trifluoromethylsulfonyl)imide (99%), and 1,3-dipropylimidazolium bis(trifluoromethylsulfonyl)imide (98%) were purchased from Iolitec Ionic Liquids Technologies GmbH. Milli-Q water was taken from a Milli-Q Advantage A10 Water Purification System, Millipore (18 M $\Omega$ .cm). 1,3-Di-*tert*-butylimidazolium tetrafluoroborate and 1,3-diisopropylimidazolium chloride were anion exchanged for NTf<sub>2</sub> and were transferred to the glove box after vacuum drying.



## II. Electrochemical data

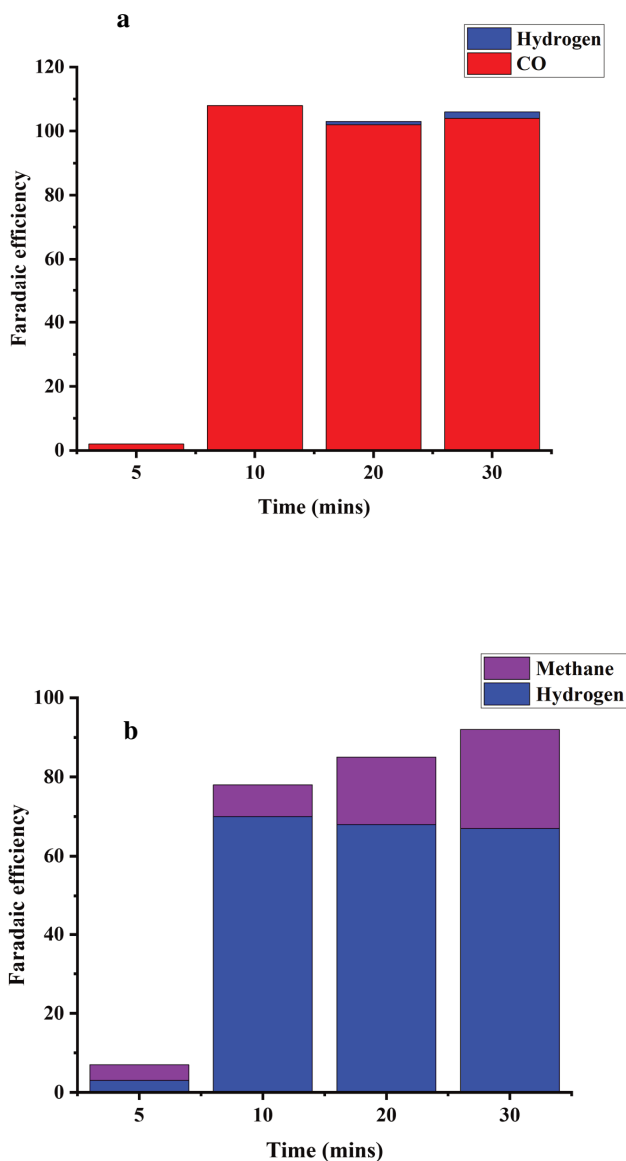


**Figure S3.1. Comparison of the performance for CO<sub>2</sub> reduction with 1.5 mol% of 1-methyl-3-pentyl imidazolium (PM) and 1.5 mol% of tetrabutylammonium (TBA) cations in anhydrous acetonitrile. (a) Electrolysis with PM NTf<sub>2</sub> at 18 mA/cm<sup>2</sup> shows ~100 % FE for CO production at an average voltage of -2.58 V vs. Ag/Ag<sup>+</sup>. (b) Electrolysis with TBA NTf<sub>2</sub> at 18 mA/cm<sup>2</sup> results in lower performance for both selectivity and productivity: H<sub>2</sub> was the main product with an average voltage of -3.3 V vs. Ag/Ag<sup>+</sup>. Electrolysis measurements were performed over the Au foil electrode in a two-compartment cell under normal stirring conditions and applying a flow of 5 mL CO<sub>2</sub>/min.**

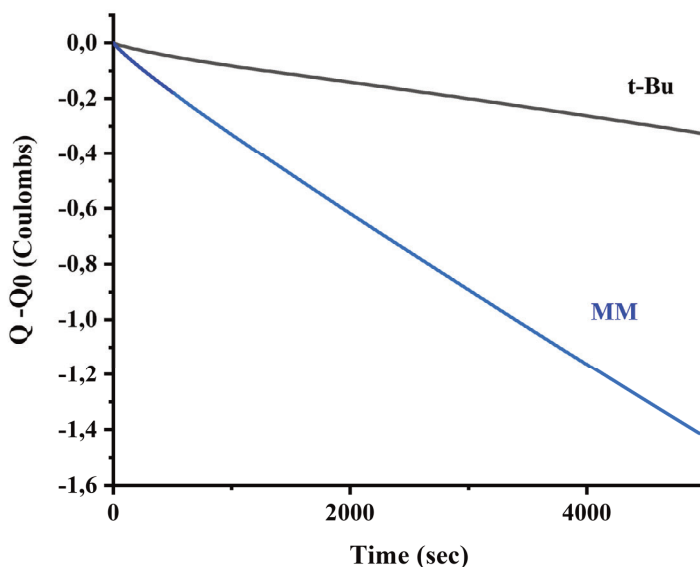


**Figure S3.2. Comparisons of the stable electrochemical activity of MM and t-Bu for CO<sub>2</sub> reduction.** The charges transferred in the presence of 0.5 molar % of MM NTf<sub>2</sub> and 0.5 molar % of t-Bu NTf<sub>2</sub>. The potential was constant at -1.8 V vs. Ag/Ag<sup>+</sup>, and the reactor was purged with 5 mL/min CO<sub>2</sub>. The stability of t-Bu NTf<sub>2</sub> was also checked after chronoamperometry (Figures S3.34 to S3.36).

$$\begin{aligned}
 (\Delta q_{CO_2} - \Delta q_{He})_{MM} / (\Delta q_{CO_2} - \Delta q_{He})_{t-Bu} &= -0.53203 \text{ coulombs/hr} / -0.16742 \text{ coulombs/hr} \\
 &= 3.177
 \end{aligned}$$

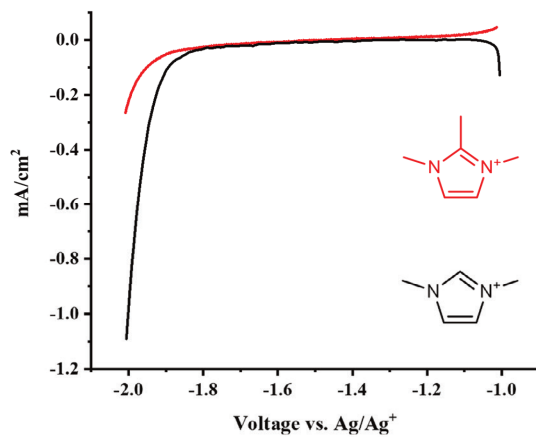


**Figure S3.3. Importance of the C2-proton in determining CO<sub>2</sub> reduction activity.** Comparison of CO<sub>2</sub> reduction activity for the MM cation with that of the 2-methylated MM cation. LSVs were recorded in CO<sub>2</sub> saturated acetonitrile at an Au disk electrode.

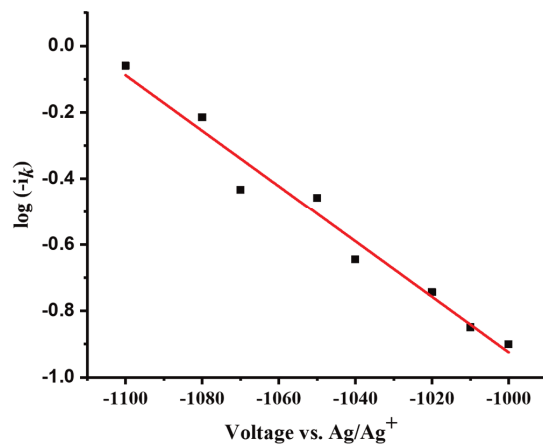


**Figure S3.4. Tafel analysis for  $\text{CO}_2$  reduction in anhydrous MM-acetonitrile.** The Koutecky-Levich equation was used to obtain kinetic currents ( $-i_k$  in mA) within the linear region of the current-potential profile using the RDE set up at different rpms.

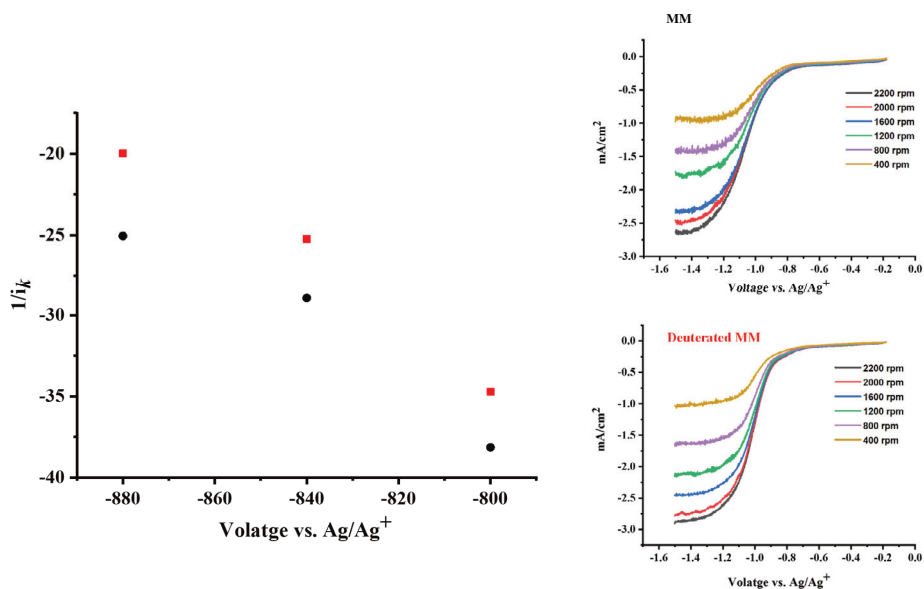


**Figure S3.5. The determination of the inverse kinetic isotope effect for CO<sub>2</sub> reduction in anhydrous imidazolium-acetonitrile.** The Koutecky-Levich equation was used to obtain kinetic currents ( $i_k$  in mA) for both MM and **deuterated MM** with the RDE set up at different rpms (**right**). Kinetic currents at low overpotentials were used to evaluate the inverse kinetic isotope effect (**left**).

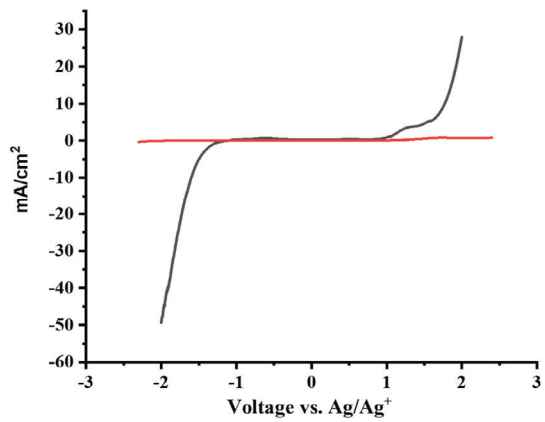


**Figure S3.6. Electrochemical window of MM-acetonitrile vs MM-water.** LSVs for Au disk electrode under the purge of He in water with 0.5 mol% of MM Cl (**red**) and in acetonitrile with 0.5 mol% of MM NTf<sub>2</sub>.

For all LSV measurements, the experiments were repeated to determine reproducibility. For each cation two LSVs are compared as follows.

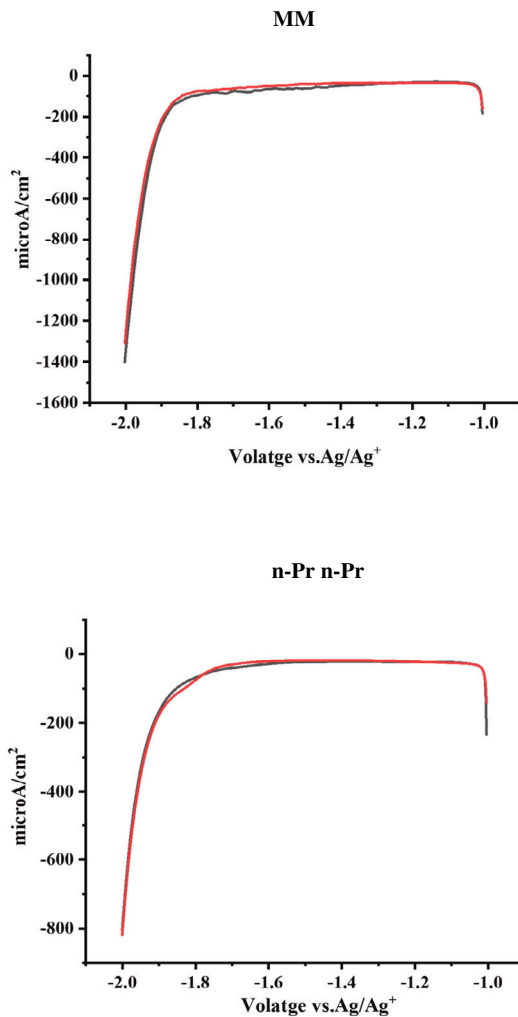


**Figure S3.7 a. Reproducibility of LSVs for the activity of imidazolium cations for CO<sub>2</sub> reduction in anhydrous acetonitrile.** LSVs with 0.5 mol% of imidazolium salts in CO<sub>2</sub> saturated anhydrous acetonitrile at Au disk electrode.

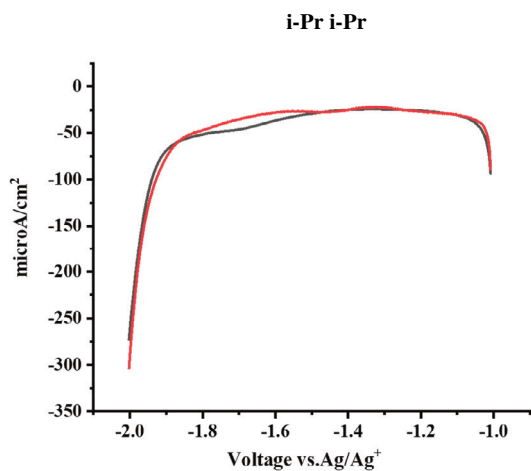
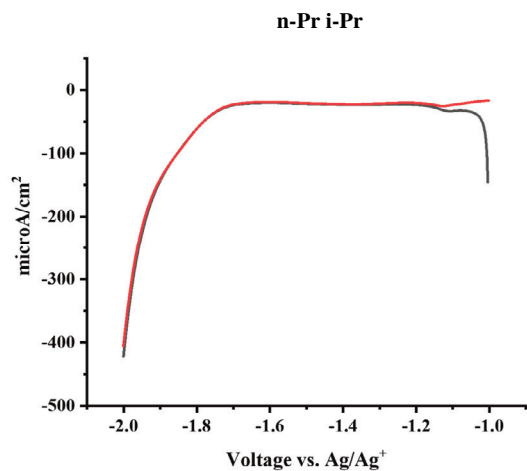
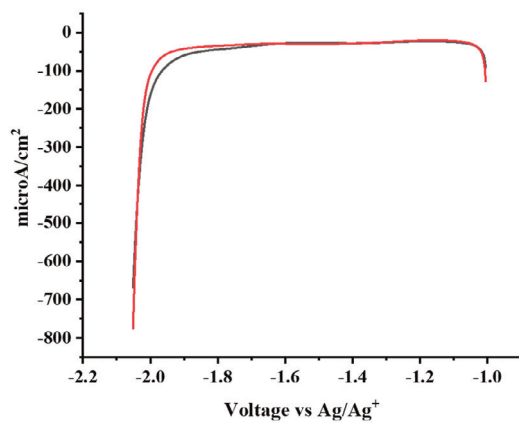


**Figure S3.7 b. Reproducibility of LSVs for the activity of imidazolium cations for CO<sub>2</sub> reduction in anhydrous acetonitrile.** LSVs with 0.5 mol% of imidazolium salts in CO<sub>2</sub> saturated anhydrous acetonitrile at Au disk electrode.



### t-Bu t-Bu



### 2-Me MM

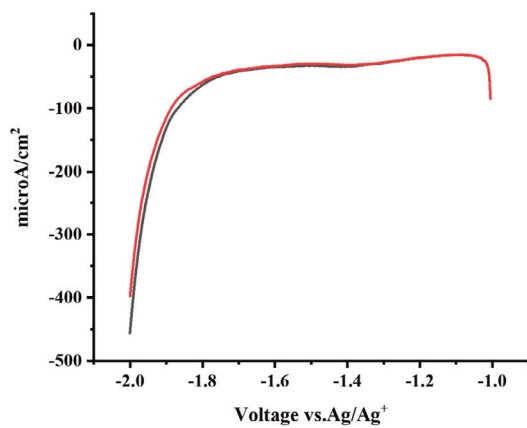


**Figure S3.7 c. Reproducibility of LSVs for the activity of imidazolium cations for CO<sub>2</sub> reduction in anhydrous acetonitrile. LSVs with 0.5 mol% of imidazolium salts in CO<sub>2</sub> saturated anhydrous acetonitrile at Au disk electrode.**

### III. VDD charge analysis of cations

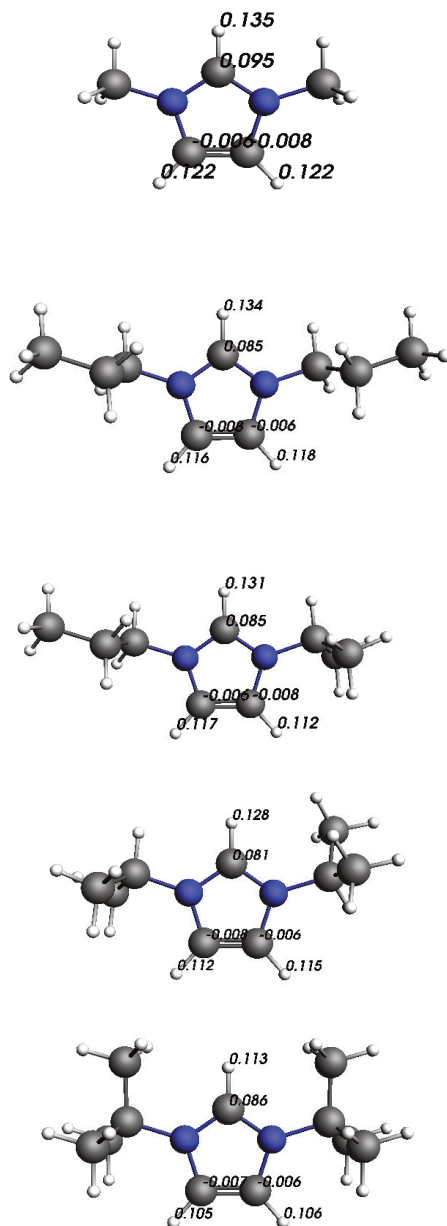
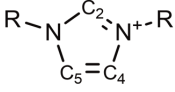


Figure S3.8. VDD charge analysis for imidazolium cations in acetonitrile.

#### IV. $^{13}\text{C}$ NMR chemical shifts (ppm) of imidazolium NTf<sub>2</sub> salts in CD<sub>3</sub>CN

**Table S3.1.**  $^{13}\text{C}$  NMR chemical shifts (ppm) of imidazolium NTf<sub>2</sub> salts in CD<sub>3</sub>CN and their activity for CO<sub>2</sub> reduction in acetonitrile.

	C-2	C-4 + C-5	Current density at -2 V vs. Ag/Ag <sup>+</sup>
Methyl Methyl	137.85	124.88	-1370
<i>n</i> -Propyl <i>n</i> -Propyl	136.59	123.85	-780
<i>i</i> -Propyl <i>n</i> -Propyl	135.33	121.93, 123.89	-385
<i>i</i> -Propyl <i>i</i> -Propyl	134.07	121.96	-245
<i>t</i> -Butyl <i>t</i> -Butyl	132.88	121.63	-65

## V. Stability of $^*CO_2^-$ vs the free $CO_2^-$ anion radical in acetonitrile

To evaluate the energy gain for  $CO_2^-$  radical anion upon its binding with Au atom we calculated the formation energy for  $Au-^*CO_2^-$  and  $CO_2^-$  in acetonitrile and used the following equations:

$$G(^*CO_2^-)_{MeCN} = G(Au-CO_2^-)_{MeCN} - G(Au)_{MeCN}$$
$$\Delta G_{ads} = G(^*CO_2^-)_{MeCN} - G(CO_2^-)_{MeCN} = 60.99 \text{ kcal/mol}$$

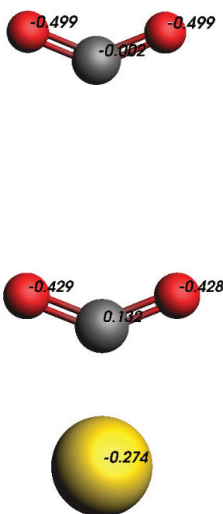


**Figure S3.9. VDD charges for geometry optimized  $^*CO_2^-$  and  $CO_2^-$  in acetonitrile.** Upon binding Au atom a more uniform charge distribution is obtained. The formation energy of  $\sim 70$  kcal/mol highlights the greater stability of  $^*CO_2^-$  versus  $CO_2^-$ .

## VI. Interaction of C2-proton and C4, C5-protons of MM with Au- CO<sub>2</sub><sup>-</sup>

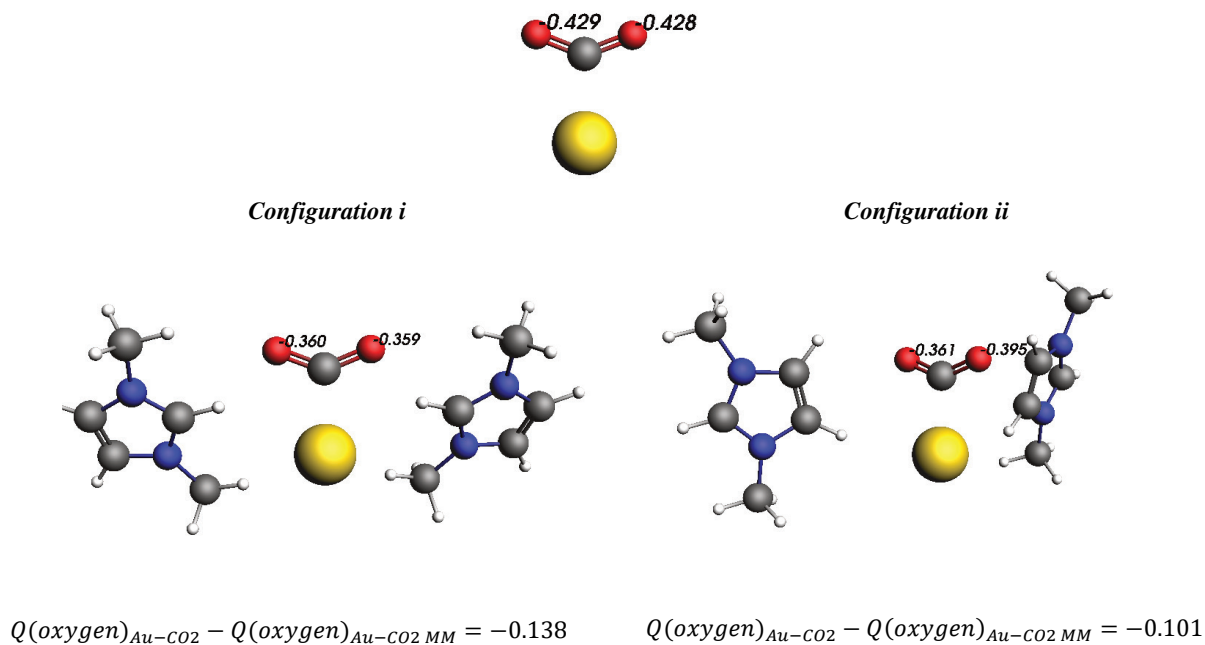
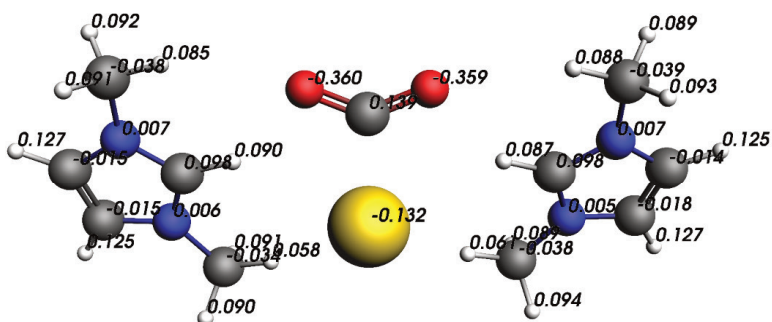


**Figure S3.10. Differential VDD charge analysis for \*CO<sub>2</sub><sup>-</sup> in interaction with two possible configurations of the MM cation.** Equations depict the charge difference between oxygen atoms in free Au-CO<sub>2</sub><sup>-</sup> (top) and Au-CO<sub>2</sub><sup>-</sup> in interaction with MM cations (bottom). Full VDD charges are provided in Figure S3.11.

### Configuration i



### Configuration ii

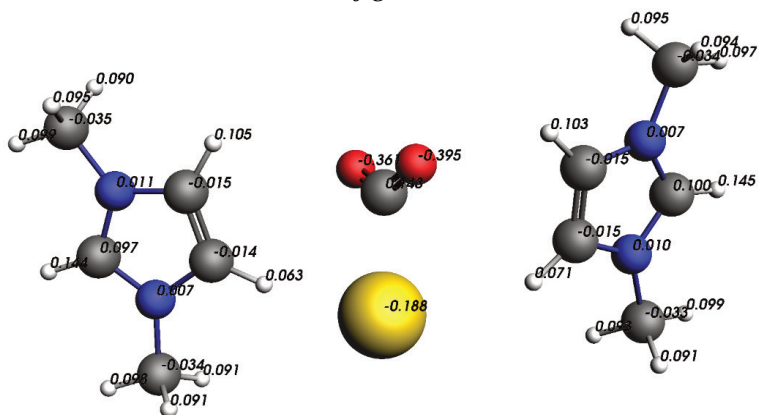
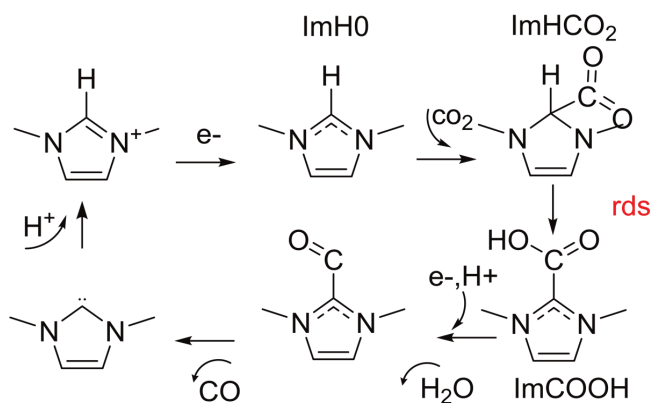


**Figure S3.11.** Charge distribution upon the interaction of  $^*\text{CO}_2^-$  and MM cation with two possible configurations. In *configuration i* C2-proton is pointed towards  $^*\text{CO}_2^-$  and in *configuration ii* C4- and C5-protons are positioned towards  $^*\text{CO}_2^-$ . Full VDD charges are depicted.

## VII. Analysis of the activation energy for isomerization step

To investigate the proton transfer as the RDS in the isomerization step proposed by Wang et al.<sup>4</sup> (Scheme S3.1), we performed the activation energy analysis for three cations: **MM**, **n-Pr**, and **i-Pr**.



**Scheme S3.1. Step-wise electron-proton transfer to CO<sub>2</sub> mediated by imidazolium cation.** Catalytic cycle proposed by Wang, et al.<sup>4</sup> for cation mediated sequential electron-proton transfer to CO<sub>2</sub>. Proton transfer in the isomerization from ImHCO<sub>2</sub> adduct to ImCOOH was proposed as the rate-determining step.

The following steps were considered to evaluate the activation energy:

- Geometries for cations (*compounds i* in **Figure S3.12**), reduced cations **ImH0** (*compounds ii* in **Figure S3.12**), **ImHCO<sub>2</sub>** adducts (*compounds iii* in **Figure S3.12**), and intermediates **ImCOOH** (*compounds iv* in **Figure S3.12**) were optimized step-wise. **Figure S3.12** shows the geometry optimized for all 4 compounds for **MM**, **n-Pr**, and **i-Pr** cations.
- In order to find an initial guess for the transition state, we performed a potential energy surface scan (PES) for proton transfer proposed in the isomerization step (from *compound iii* to *compound iv*).

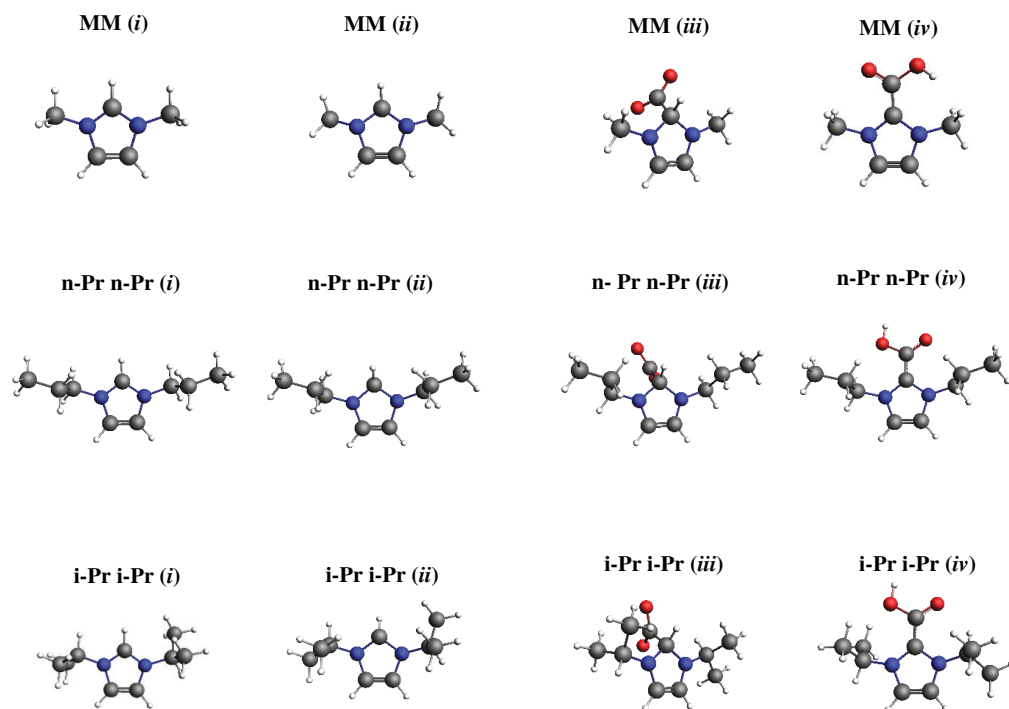
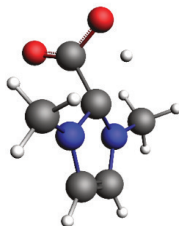


**Figure S3.12.** Optimized geometry for cations (i), reduced cations ImH0 (ii), ImHCO<sub>2</sub> adduct (iii), and intermediates ImCOOH (iv) for three cations: MM, n-Pr n-Pr, i-Pr i-Pr. The energy was considered converged when the change in energy was smaller than  $10^{-5}$  Hartree.

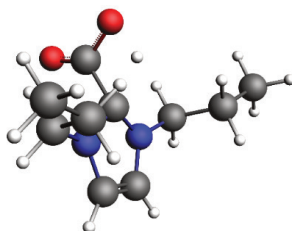
- c) To make sure that the initial guess for the transition state from step **b** is positioned at a saddle point, we performed an extra transition state search with frequency calculations. The initial guess from step **b** was taken as the initial geometry for this calculation<sup>77</sup>. Geometries obtained for transition states are depicted in **Figure S3.13**. While PES was performed for multiple coordinates, for all cations the negative eigenvalue occurs for the vibration along the proton transfer.



**MM TS**



**n-Pr n-Pr TS**



**i-Pr i-Pr TS**

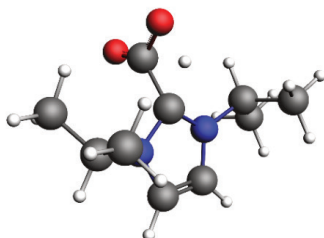


**Figure S3.13.** Transition state (TS) structures for the proton transfer in the isomerization step according to the electron-proton transfer mechanism proposed in scheme S3.1.

d) After finding the transition state, we obtained the reaction path with the intrinsic reaction coordinate (IRC) analysis<sup>78-79</sup>. With the IRC, the analysis starts at a transition state and slides down the hill towards the adjacent local minimum at either side of the transition state. The IRC analysis gives full information about the pathway as well as the height of the barrier in the reaction<sup>80</sup>. For all three cations, the isomerization reaction is found to be endothermic and *compound iii* and *compound iv* are found as the stationary points for the reactants and products, respectively. Thus, the isomerization with proton transfer as the reaction coordinate remains the preferred pathway from *compound iii* to *compound iv* for all three cations. **Table S3.2** reports the barrier height for all three cations. No noticeable difference is found for the three cations in terms of activation energy. This is in striking contrast with our electrochemical results and challenges the idea of isomerization as a rate-determining step.

**Table S3.2. Activation energy for proton transfer in the isomerization step**

Cation	$\Delta G^\ddagger$
MM	46.11
n-Pr n-Pr	46.066
i-Pr i-Pr	46.098

### VIII. Notes on the initial act of the electrode

As argued in the article a first electron transfer to the imidazolium cation violates the role of the heterogeneous catalyst and the electrode turns into an electron supplier with some affinity for a given cation. That is similar to what has been proposed for the pyridinium chemistry at electrodes such as Pt<sup>81-82</sup>. For CO<sub>2</sub> reduction with pyridinium as a molecular electro-catalyst, the cation first reduces to form a radical active form, and with the follow-up electron-proton transfers, CO<sub>2</sub> is reduced to products such as methanol and formic acid. The CV profile for such a system shows the same onset potential for the reduction of the cation and the reduction of CO<sub>2</sub> (**Figure S3.14 a**). This implies that the first electron transfer to pyridinium is involved in the initial stages of the mechanism. However, with imidazolium, there is a significant difference between the onset potential for the reduction of the cation and the onset potential for the reduction of CO<sub>2</sub> (**Figure S3.14 b**). Even with seven times higher concentrations of MM compared to CO<sub>2</sub>, we did not observe cation reduction in the potential region in which CO<sub>2</sub> reduction occurs. This observation challenges the idea of the first electron transfer to imidazolium as an initial step, otherwise, similar to pyridinium chemistry we would observe the same onset potentials for the reduction of the cation and the reduction of CO<sub>2</sub>. Indeed, a proposed mechanism for imidazolium-assisted electrochemical CO<sub>2</sub> reduction should consider the role of the electrode catalyst in adsorbing CO<sub>2</sub> and facilitating electron transfer to adsorbed CO<sub>2</sub>.

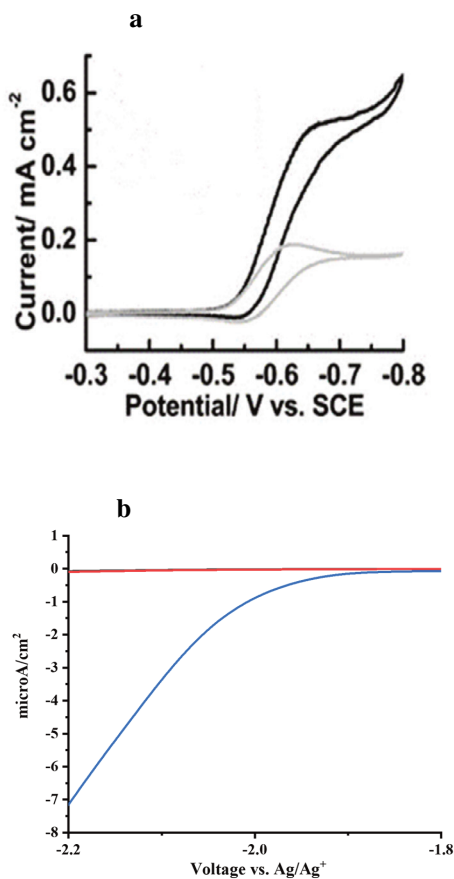


**Figure S3.14.** (a) CVs of pyridinium reduction under Ar (gray) and CO<sub>2</sub> (black) at a Pt disk electrode in 0.5 M KCl aqueous electrolyte. (b) LSVs for a Au disk electrode in acetonitrile with 0.5 mol% (red) and 1 mol% (black) of MM NTf<sub>2</sub> during He purging. (blue) is LSV with 0.5 mol% of MM under CO<sub>2</sub> purging. CO<sub>2</sub> solubility in our reactor condition is 0.14 mol%. (a) was reproduced with permission.

## IX. Inverse kinetic isotope effect estimated from frequency calculations

To evaluate the kinetic isotope effect, we calculated IR frequencies for hydrogenated and deuterated MM cations. These frequencies were compared with those of Au-COOH and Au-COOD as intermediates. Differences in ZPEs were calculated as follows:

$$\frac{k_H}{k_D} = \frac{Ae^{-E_a(H)/RT}}{Ae^{-E_a(D)/RT}}$$

$$E_a(D) = \frac{1}{2}hc [\bar{\nu}(OD) - \bar{\nu}(C_2D)]$$

$$E_a(H) = \frac{1}{2}hc [\bar{\nu}(OH) - \bar{\nu}(C_2H)]$$

$$\frac{k_H}{k_D} = e^{\frac{hc}{2RT} [(\bar{\nu}(OD) - \bar{\nu}(OH)) - (\bar{\nu}(C_2D) - \bar{\nu}(C_2H))]}$$

$$\frac{k_H}{k_D} = 0.735, \quad \frac{k_D}{k_H} = 1.36$$

## X. Extra notes on the inverse kinetic isotope effect

While for most coupled electron-proton transfer reactions a normal KIE effect ( $k_H/k_D > 1$ ) is expected<sup>73, 83-84</sup>, the inverse KIE (iKIE) observed in this work highlights a unique feature of the imidazolium-mediated anhydrous CO<sub>2</sub> reduction. The observed inverse kinetic isotope effect shares similarities with the proton transfer in catalytic reactions involving the formation of low-barrier hydrogen bonds (LBHBs). In catalytic reactions associated with LBHBs, a weak hydrogen bond in the ground state becomes a low barrier hydrogen bond (strong and short-distance hydrogen bond) in the transition state<sup>85-87</sup>. LBHBs are mostly observed in non-protic solvents. The energy released in forming the LBHB then contributes to lowering the activation barrier for the reaction<sup>85</sup>. In another word, this energy release can explain the preference for the CEPT pathway over the sequential pathway in anhydrous media (**Figure 3.4**). Developing the strong hydrogen bonds between negatively charged oxygen of \*CO<sub>2</sub><sup>δ-</sup> and δ<sup>+</sup>H-C2 of MM in the transition state, thus, should have caused the inverse KIE observed in this work.

## XI. Synthetic procedures

**NMR Characterization.** 400 MHz  $^1\text{H}$ , 100 MHz  $^{13}\text{C}$ , and 376 MHz  $^{19}\text{F}$  NMR spectra were recorded on a Bruker Avance III 400 NMR spectrometer in  $\text{CD}_3\text{CN}$ . Solvent residual signals with chemical shifts of 1.94 ppm ( $^1\text{H}$  NMR) and 118.69 ppm ( $^{13}\text{C}$  NMR) were used as references.

**1-Isopropyl-3-propylimidazolium iodide.** A 250 mL round bottom flask equipped with a magnetic stirring bar and reflux condenser was charged with 1-isopropylimidazole (5.185 g, 47.0 mmol) and  $\text{NaHCO}_3$  (1.5 eq., 70.5 mmol, 5.92 g). Acetonitrile (100 mL) and 1-iodopropane (2 eq., 94 mmol, 16.0 g, 9.2 mL) were added and the mixture was stirred at 50 °C for 1 week under  $\text{N}_2$ . Acetonitrile was removed under vacuum and the residue was dissolved in  $\text{CH}_2\text{Cl}_2$  (50 mL). The  $\text{CH}_2\text{Cl}_2$  solution was separated from the formed salts which were subsequently washed with some  $\text{CH}_2\text{Cl}_2$ . Under stirring, diethyl ether (150 mL) was added to the combined  $\text{CH}_2\text{Cl}_2$  solutions under stirring to precipitate the imidazolium iodide product. The flask was placed in a refrigerator overnight. The  $\text{CH}_2\text{Cl}_2$ /ether layer was removed and the liquid residue was washed with diethyl ether (50 mL) which was also removed. The residue was dried under a slow flow of  $\text{N}_2$  and subsequently under vacuum (6 mbar, then 0.01 mbar), yielding 1-isopropyl-3-propylimidazolium iodide as a colorless liquid (12.77 g, 97%).

$^1\text{H}$  NMR ( $\text{CD}_3\text{CN}$ , 400 MHz):  $\delta$  (ppm) = 0.90 (t,  $\text{CH}_3$ , 3H), 1.52 (d,  $\text{CH}_3$ , 6H), 1.88 (m,  $\text{CH}_2$ , 2H), 4.17 (t, N- $\text{CH}_2$ , 2H), 4.66 (m, CH, 1H), 7.51 (s, H-4 or H-5, 1H), 7.57 (s, H-4 or H-5, 1H), 9.23 (H-2, s, 1H).  $^{13}\text{C}$  NMR ( $\text{CD}_3\text{CN}$ , 100 MHz):  $\delta$  (ppm) = 11.31 ( $\text{CH}_2\text{CH}_3$ ), 23.58 ( $\text{CH}_3$ ), 24.51 ( $\text{CH}_2$ ), 52.07 (N- $\text{CH}_2$ ), 54.19 (CH), 121.99 (C-4 or C-5), 123.75 (C-4 or C-5), 136.29 (C-2).

**Counterion exchange.** The following procedure was used to convert 1-isopropyl-3-propylimidazolium iodide, 1,3-diisopropylimidazolium chloride and 1,3-di-*tert*-butylimidazolium tetrafluoroborate into the corresponding  $\text{NTf}_2$  salts. The imidazolium iodide, chloride, or tetrafluoroborate (18.65 mmol) was dissolved in  $\text{CH}_3\text{CN}$  (20 mL). To this solution,  $\text{Li NTf}_2$  (20.52 mmol, 1.1 eq.) was added as a solid. Milli-Q water (20 mL) was added and the

mixture was stirred overnight. CH<sub>3</sub>CN was removed by a flow of N<sub>2</sub> flow. The resulting mixture was extracted three times with CH<sub>2</sub>Cl<sub>2</sub>. The combined organic layers were washed once with Milli-Q water to remove the last traces of lithium salts, dried on Na<sub>2</sub>SO<sub>4</sub>, evaporated to dryness using a rotary evaporator, and further dried under vacuum (6 mbar, then 0.01 mbar). 1-Isopropyl-3-propylimidazolium NTf<sub>2</sub> and 1,3-diisopropylimidazolium NTf<sub>2</sub> were obtained as colorless liquids, 1,3-di-*tert*-butylimidazolium NTf<sub>2</sub> as a white solid, in yields of 99%.

**1-Isopropyl-3-propylimidazolium bis(trifluoromethylsulfonyl)imide.** <sup>1</sup>H NMR (CD<sub>3</sub>CN, 400 MHz): δ (ppm) = 0.92 (t, CH<sub>3</sub>, 3H), 1.51 (d, CH<sub>3</sub>, 6H), 1.87 (m, CH<sub>2</sub>, 2H), 4.09 (t, *N*-CH<sub>2</sub>, 2H), 4.59 (m, CH, 1H), 7.41 (s, H-4 or H-5, 1H), 7.48 (s, H-4 or H-5, 1H), 8.51 (H-2, s, 1H). <sup>13</sup>C NMR (CD<sub>3</sub>CN, 100 MHz): δ (ppm) = 11.17 (CH<sub>2</sub>CH<sub>3</sub>), 23.18 (CH<sub>3</sub>), 24.37 (CH<sub>2</sub>), 52.52 (*N*-CH<sub>2</sub>), 54.55 (CH), 116.57 (CF<sub>3</sub>), 119.76 (CF<sub>3</sub>), 121.93 (C-4 or C-5), 122.94 (CF<sub>3</sub>), 123.89 (C-4 or C-5), 126.13 (CF<sub>3</sub>), 135.33 (C-2). <sup>19</sup>F NMR (CD<sub>3</sub>CN, 376 MHz): δ (ppm) = -80.09 (s, CF<sub>3</sub>).

**1,3-Diisopropylimidazolium bis(trifluoromethylsulfonyl)imide.** <sup>1</sup>H NMR (CD<sub>3</sub>CN, 400 MHz): δ (ppm) = 1.51 (d, CH<sub>3</sub>, 12H), 4.58 (m, CH, 2H), 7.47 (s, H-4+H-5, 2H), 8.53 (H-2, s, 1H). <sup>13</sup>C NMR (CD<sub>3</sub>CN, 100 MHz): δ (ppm) = 23.18 (CH<sub>3</sub>), 54.58 (CH), 116.57 (CF<sub>3</sub>), 119.76 (CF<sub>3</sub>), 121.96 (C-4+C-5), 122.94 (CF<sub>3</sub>), 126.13 (CF<sub>3</sub>), 134.07 (C-2). <sup>19</sup>F NMR (CD<sub>3</sub>CN, 376 MHz): δ (ppm) = -80.08 (s, CF<sub>3</sub>).

**1,3-Di-*tert*-butylimidazolium bis(trifluoromethylsulfonyl)imide.** <sup>1</sup>H NMR (CD<sub>3</sub>CN, 400 MHz): δ (ppm) = 1.62 (s, C(CH<sub>3</sub>)<sub>3</sub>, 18H), 7.57 (s, H-4+H-5, 2H), 8.42 (H-2, s, 1H). <sup>13</sup>C NMR (CD<sub>3</sub>CN, 100 MHz): δ (ppm) = 30.10 (CH<sub>3</sub>), 61.56 (CH), 116.57 (CF<sub>3</sub>), 119.75 (CF<sub>3</sub>), 121.63 (C-4+C-5), 122.94 (CF<sub>3</sub>), 126.13 (CF<sub>3</sub>), 132.88 (C-2). <sup>19</sup>F NMR (CD<sub>3</sub>CN, 376 MHz): δ (ppm) = -80.17 (s, CF<sub>3</sub>).

**1,3-Dimethyl-2,4,5-trideuteroimidazolium bis(trifluoromethylsulfonyl)imide.** A mixture of 1,3-dimethylimidazolium bis(trifluoromethylsulfonyl)imide (5.0 g, 13.25 mmol), D<sub>2</sub>O (6.0 mL, 0.332 mol) and triethylamine (0.1 mL, 0.72 mmol) was stirred at 65 °C for four days under N<sub>2</sub>. After cooling, D<sub>2</sub>O and Et<sub>3</sub>N were removed under vacuum, fresh D<sub>2</sub>O (6.0 mL) and triethylamine (0.1 mL, 0.72 mmol) were added, and stirring at 65 °C was continued for another four days. After a total of six heating-evaporation cycles, D<sub>2</sub>O and Et<sub>3</sub>N were removed under vacuum and the liquid residue was dissolved in CH<sub>2</sub>Cl<sub>2</sub> and dried on Na<sub>2</sub>SO<sub>4</sub>. The dichloromethane was evaporated on a rotary evaporator, the residue was redissolved in 20 mL dichloromethane, passed through a regenerated cellulose membrane filter (pore size 0.2 μm) to remove traces of solids, and then dried under vacuum (6 mbar, then 0.01 mbar), yielding 1,3-dimethyl-2,4,5-trideuteroimidazolium bis(trifluoromethylsulfonyl)imide as a colorless liquid



(4.65 g, 92 %).  $^1\text{H}$  NMR spectroscopy revealed a conversion of C2-H into C2-D of 97.7 % and of C4-H+C5-H into C4-D+C5-D of 94.1%.

$^1\text{H}$  NMR ( $\text{CD}_3\text{CN}$ , 400 MHz):  $\delta$  (ppm) = 3.81 (s, N- $\text{CH}_3$ , 6H). Trace signals at  $\delta$  = 7.31 (s, H-4+H-5) and  $\delta$  = 8.35 (s, H-2) were visible in the spectrum.  $^{13}\text{C}$  NMR ( $\text{CD}_3\text{CN}$ , 100 MHz):  $\delta$  (ppm) = 37.01 (N- $\text{CH}_3$ ), 116.47 ( $\text{CF}_3$ ), 119.66 ( $\text{CF}_3$ ), 121.63 (C-4+C-5), 122.85 ( $\text{CF}_3$ ), 124.17, 124.48, 124.67, 124.79 (C-4+C-5), 126.03 ( $\text{CF}_3$ ), 137.23, 137.56, 137.89 (C-2).  $^{19}\text{F}$  NMR ( $\text{CD}_3\text{CN}$ , 376 MHz):  $\delta$  (ppm) = -80.18 (s,  $\text{CF}_3$ ).

## XII. Copies of $^1\text{H}$ , $^{13}\text{C}$ and $^{19}\text{F}$ NMR spectra

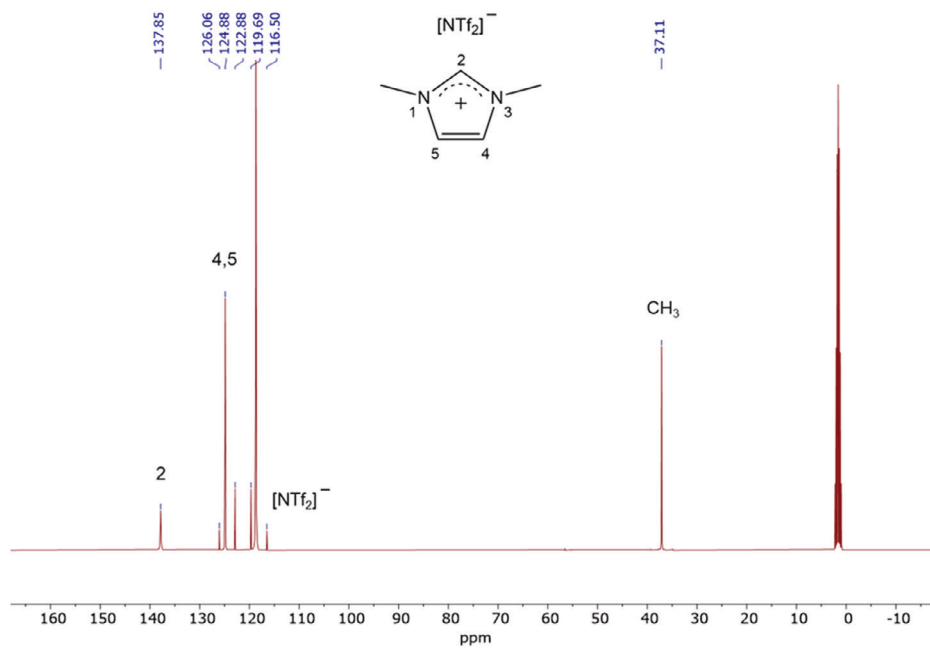


**Figure S3.15.**  $^{13}\text{C}$  NMR spectrum of 1,3-dimethylimidazolium bis(trifluoromethylsulfonyl)imide in  $\text{CD}_3\text{CN}$ .

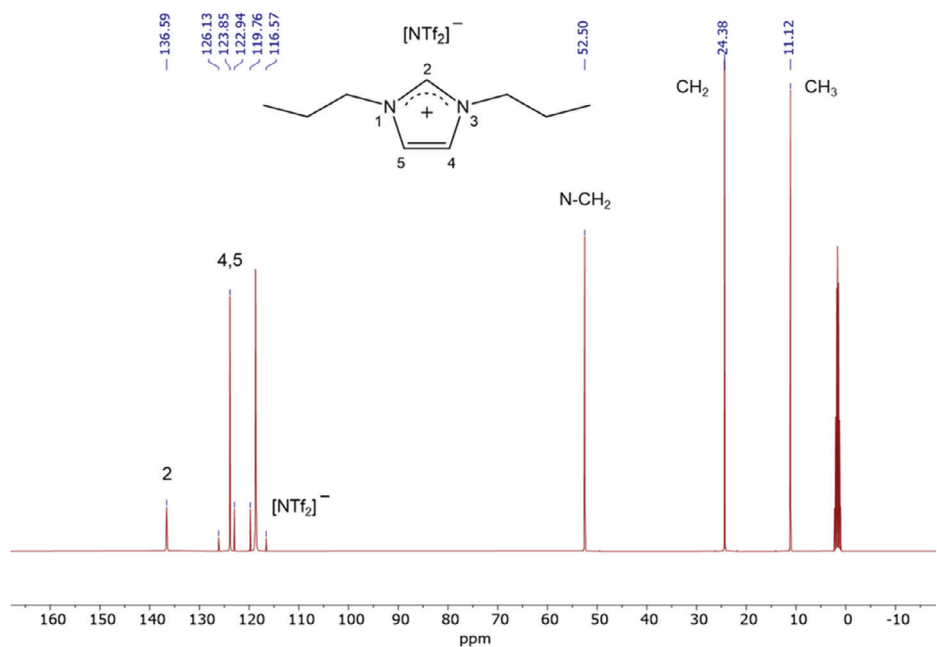


**Figure S3.16.**  $^{13}\text{C}$  NMR spectrum of 1,3-dipropylimidazolium bis(trifluoromethylsulfonyl)imide in  $\text{CD}_3\text{CN}$ .

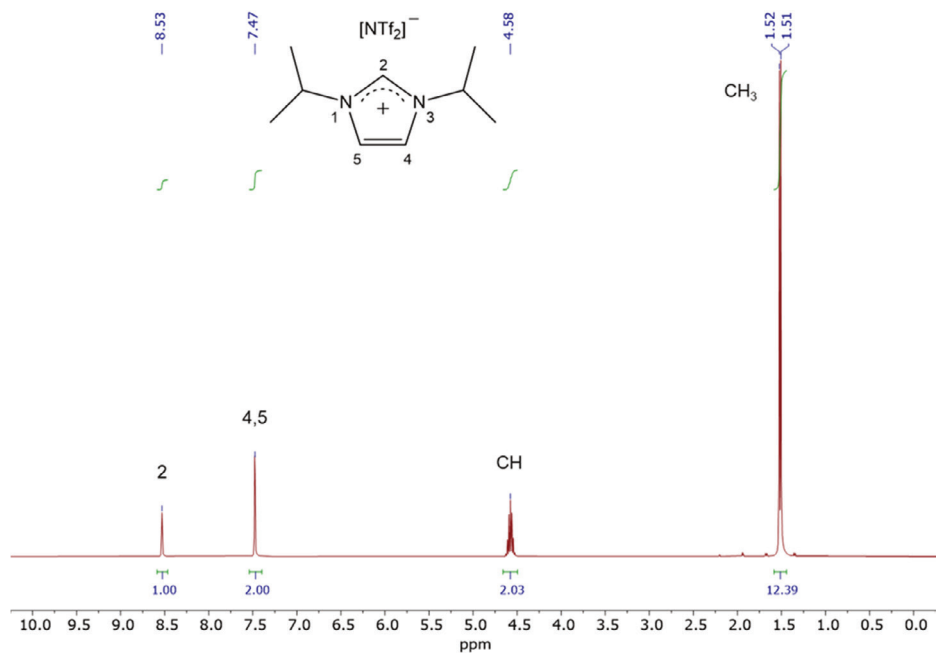


**Figure S3.17.**  $^1\text{H}$  NMR spectrum of 1,3-diisopropylimidazolium bis(trifluoromethylsulfonyl)imide in  $\text{CD}_3\text{CN}$ .

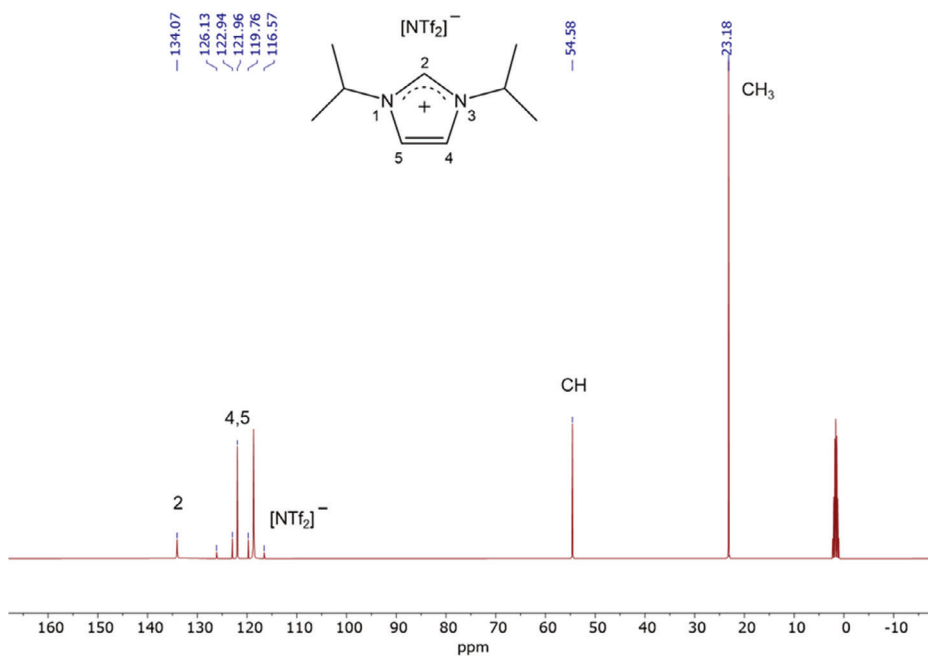


**Figure S3.18.**  $^{13}\text{C}$  NMR spectrum of 1,3-diisopropylimidazolium bis(trifluoromethylsulfonyl)imide in  $\text{CD}_3\text{CN}$ .

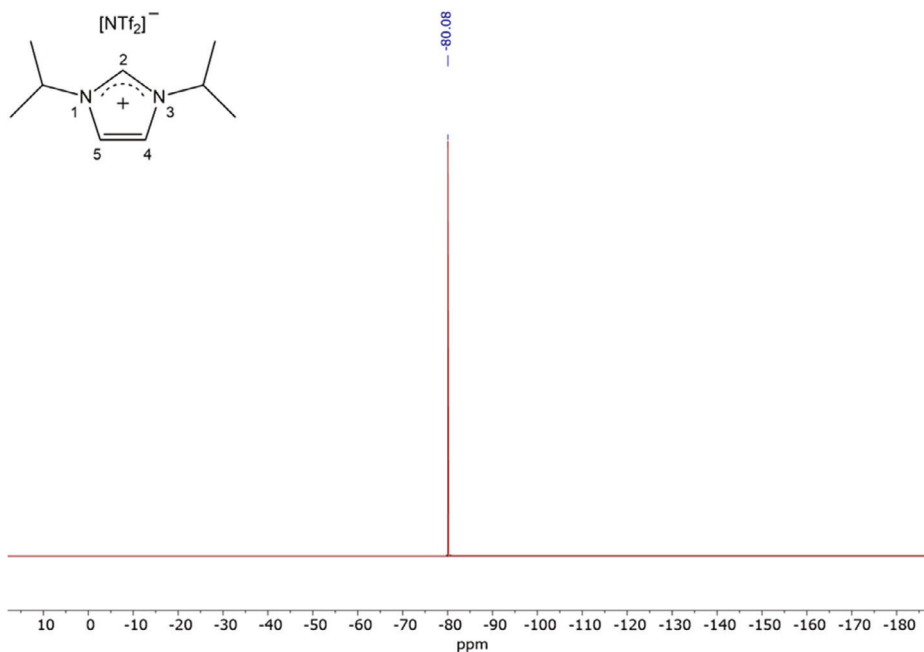


**Figure S3.19.**  $^{19}\text{F}$  NMR spectrum of 1,3-diisopropylimidazolium bis(trifluoromethylsulfonyl)imide in  $\text{CD}_3\text{CN}$ .

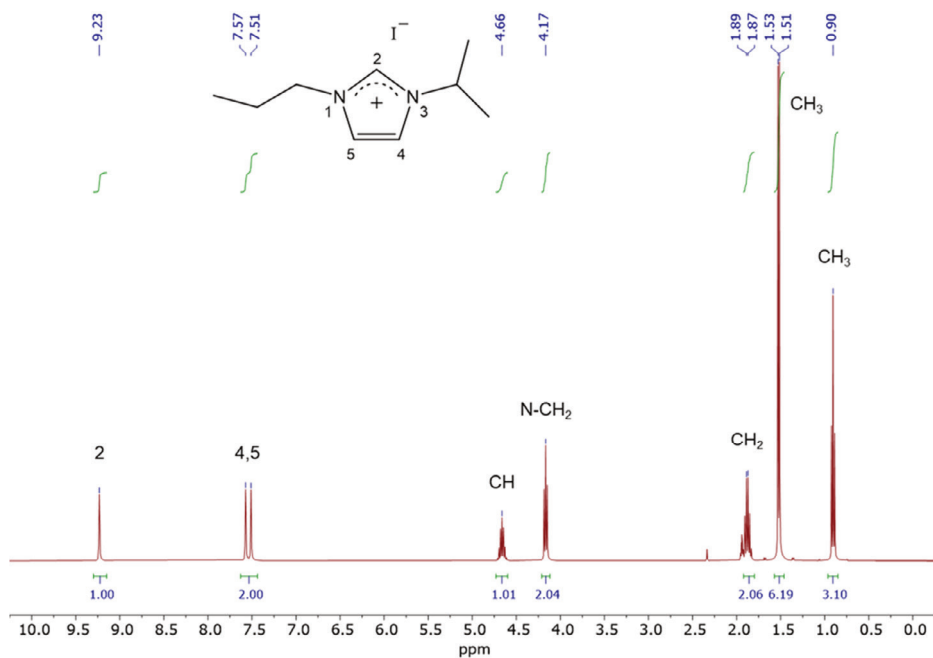


**Figure S3.20.** <sup>1</sup>H NMR spectrum of 1-propyl-3-isopropylimidazolium iodide in CD<sub>3</sub>CN.

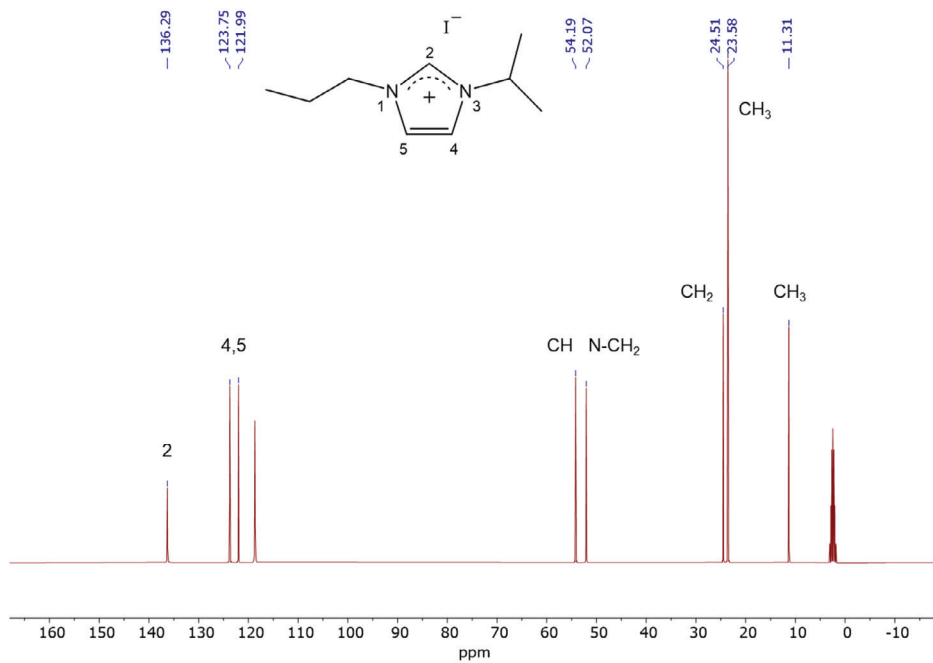


**Figure S3.21.** <sup>13</sup>C NMR spectrum of 1-propyl-3-isopropylimidazolium iodide in CD<sub>3</sub>CN

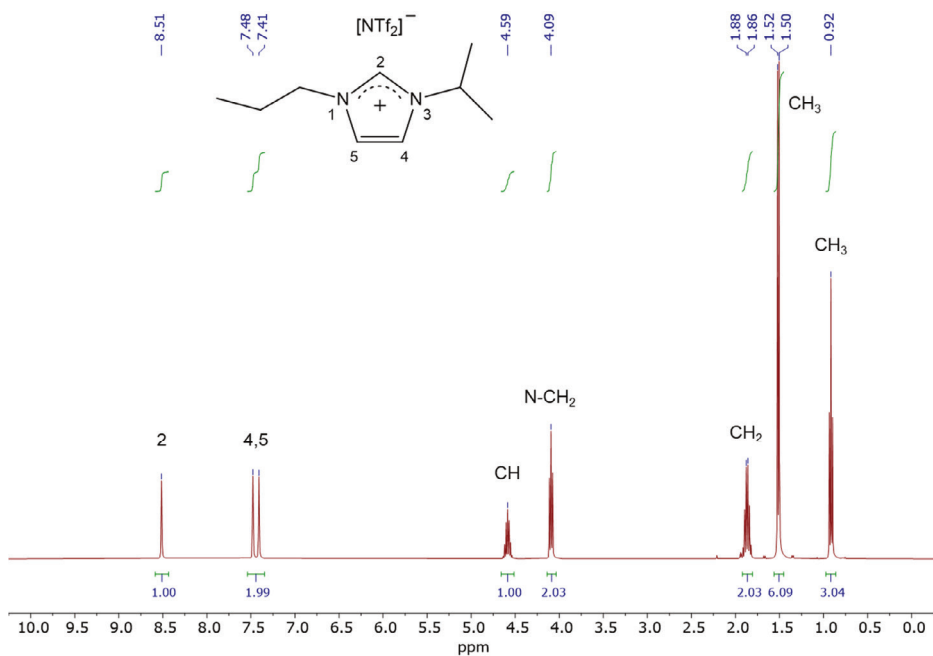


**Figure S3.22.**  $^1\text{H}$  NMR spectrum of 1-propyl-3-isopropylimidazolium bis(trifluoromethylsulfonyl)imide in  $\text{CD}_3\text{CN}$ .

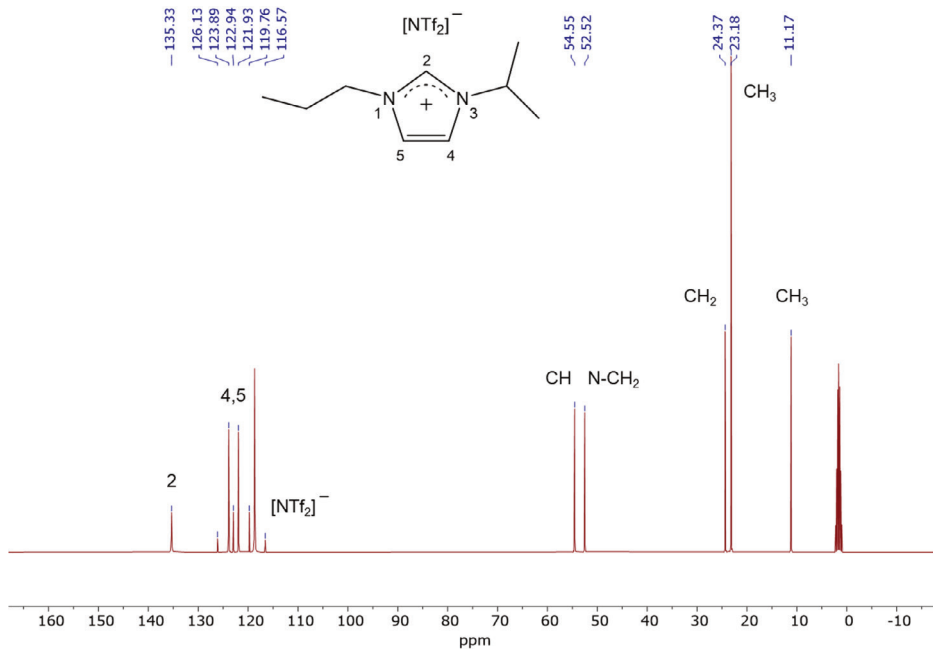


**Figure S3.23.**  $^{13}\text{C}$  NMR spectrum of 1-propyl-3-isopropylimidazolium bis(trifluoromethylsulfonyl)imide in  $\text{CD}_3\text{CN}$ .

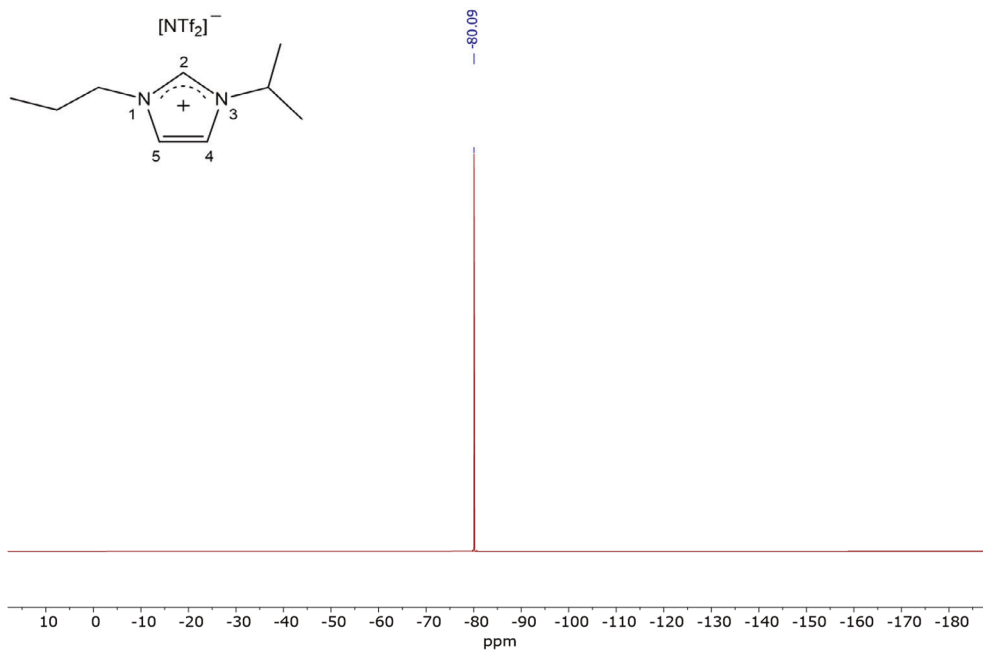


**Figure S3.24.**  $^{19}\text{F}$  NMR spectrum of 1-propyl-3-isopropylimidazolium bis(trifluoromethylsulfonyl)imide in  $\text{CD}_3\text{CN}$ .

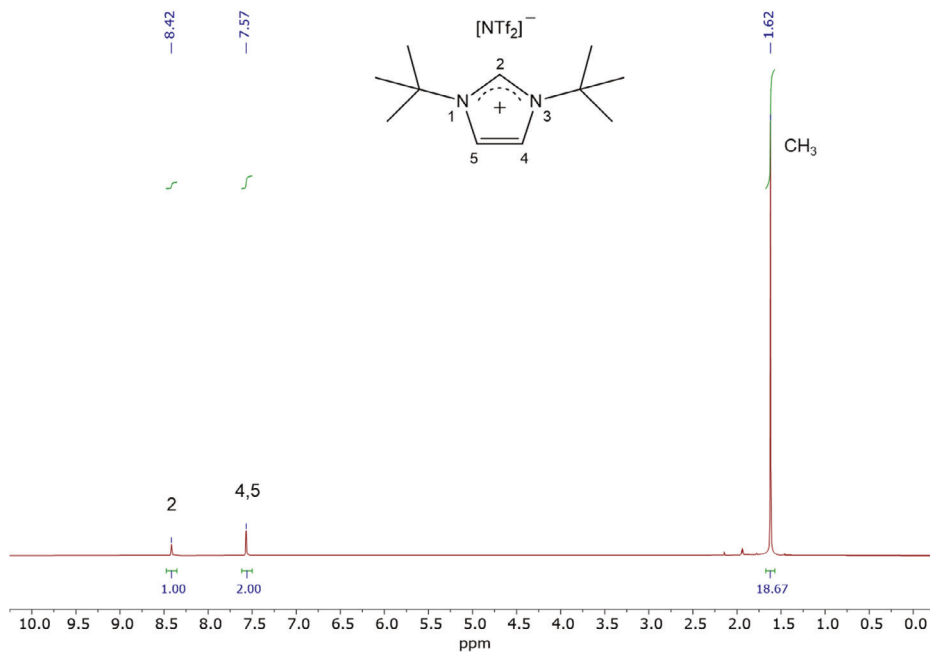


**Figure S3.25.**  $^1\text{H}$  NMR spectrum of 1,3-di-*tert*-butylimidazolium bis(trifluoromethylsulfonyl)imide in  $\text{CD}_3\text{CN}$ .

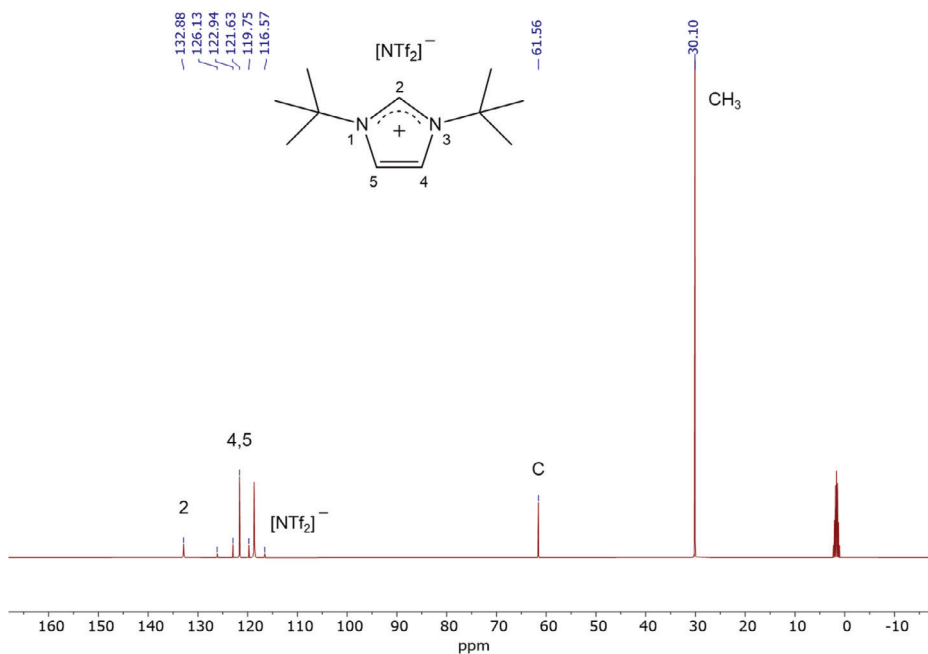


**Figure S3.26.** <sup>13</sup>C NMR spectrum of 1,3-di-*tert*-butylimidazolium bis(trifluoromethylsulfonyl)imide in CD<sub>3</sub>CN.

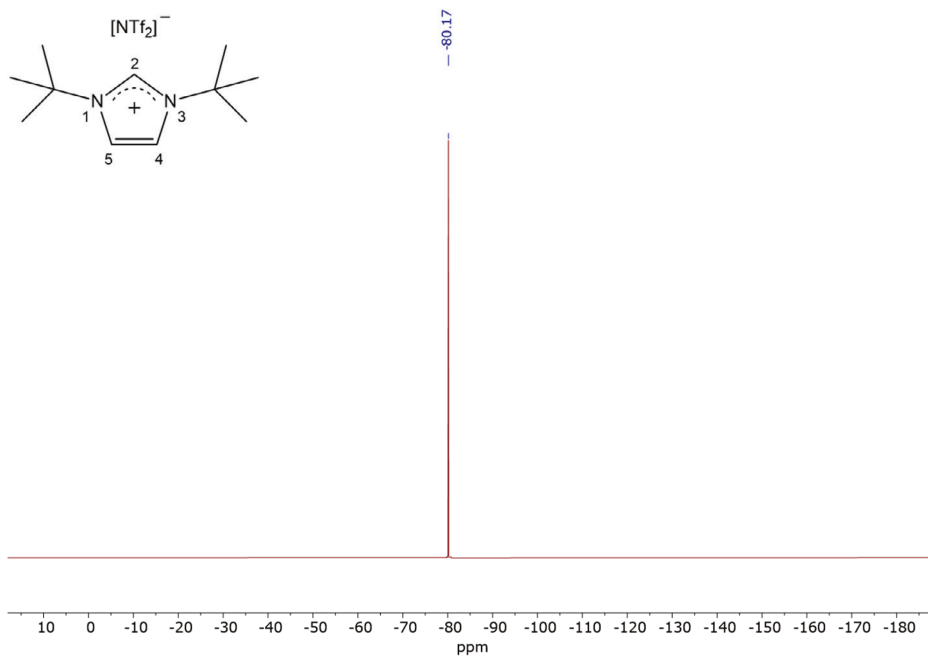


**Figure S3.27.** <sup>19</sup>F NMR spectrum of 1,3-di-*tert*-butylimidazolium bis(trifluoromethylsulfonyl)imide in CD<sub>3</sub>CN.



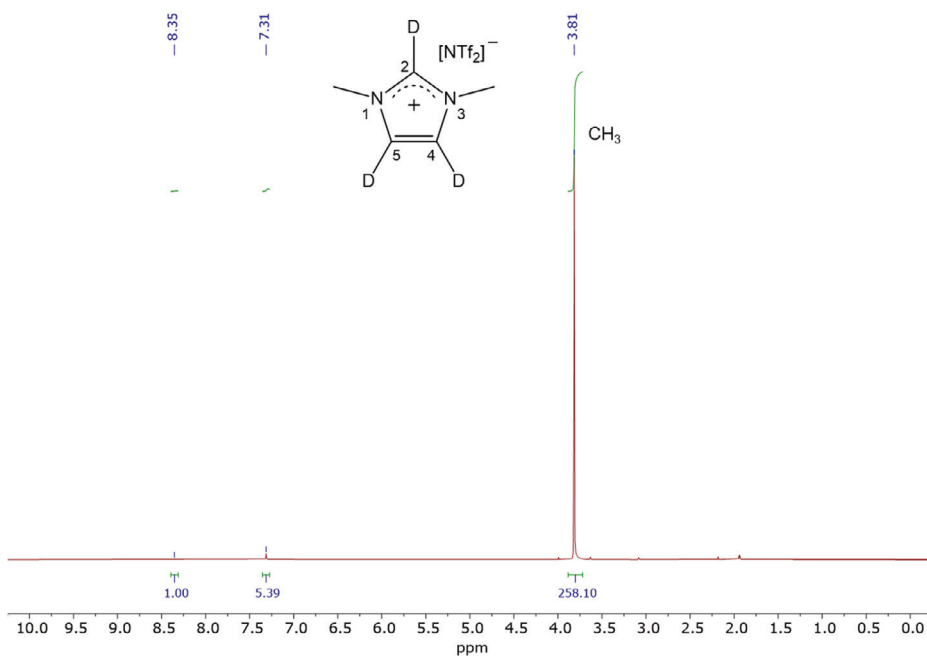


**Figure S3.28.**  $^1\text{H}$  NMR spectrum of 1,3-dimethyl-2,4,5-trideuterioimidazolium bis(trifluoromethylsulfonyl)imide in  $\text{CD}_3\text{CN}$ .

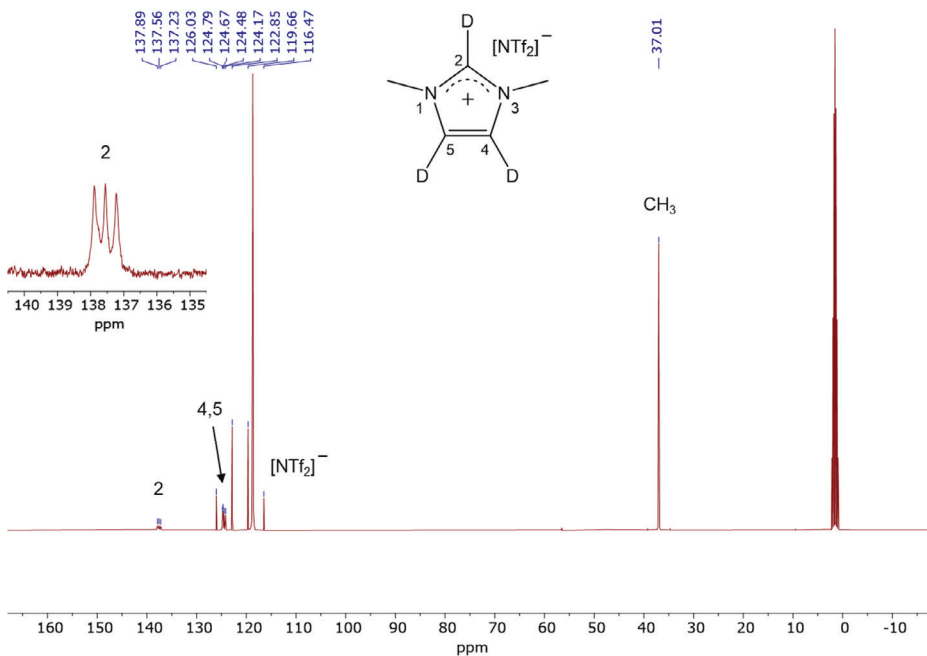


**Figure S3.29.**  $^{13}\text{C}$  NMR spectrum of 1,3-dimethyl-2,4,5-trideuterioimidazolium bis(trifluoromethylsulfonyl)imide in  $\text{CD}_3\text{CN}$ .

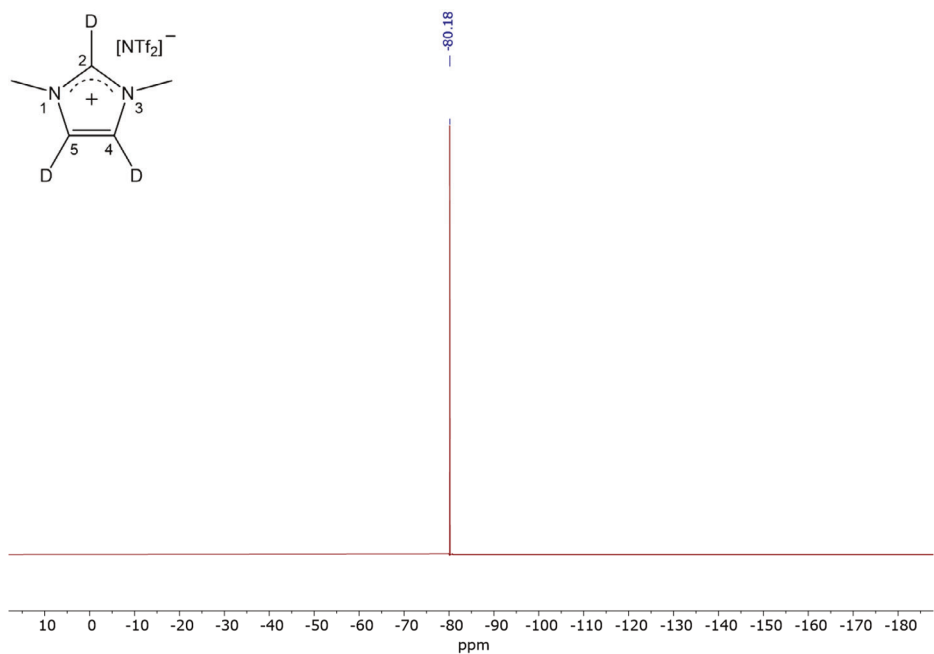


**Figure S3.30.** <sup>19</sup>F NMR spectrum of 1,3-dimethyl-2,4,5-trideuteroimidazolium bis(trifluoromethylsulfonyle)imide in CD<sub>3</sub>CN.

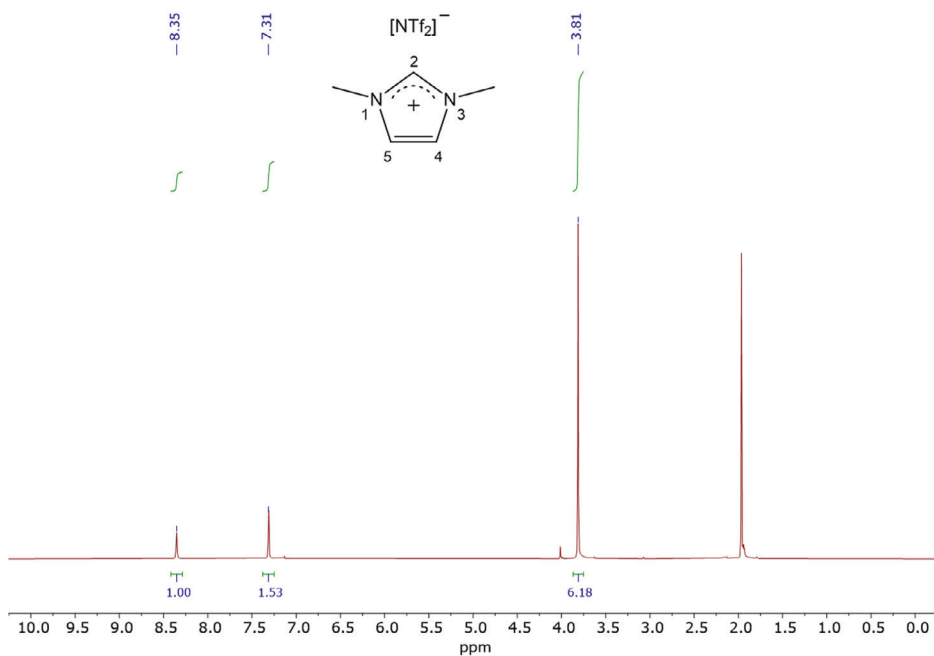


**Figure S3.31.** <sup>1</sup>H NMR spectrum of 1,3-dimethylimidazolium bis(trifluoromethylsulfonyle)imide in CD<sub>3</sub>CN. The spectrum is from the MM-acetonitrile after 5 hrs. of electrolysis (Figure 3.1e).

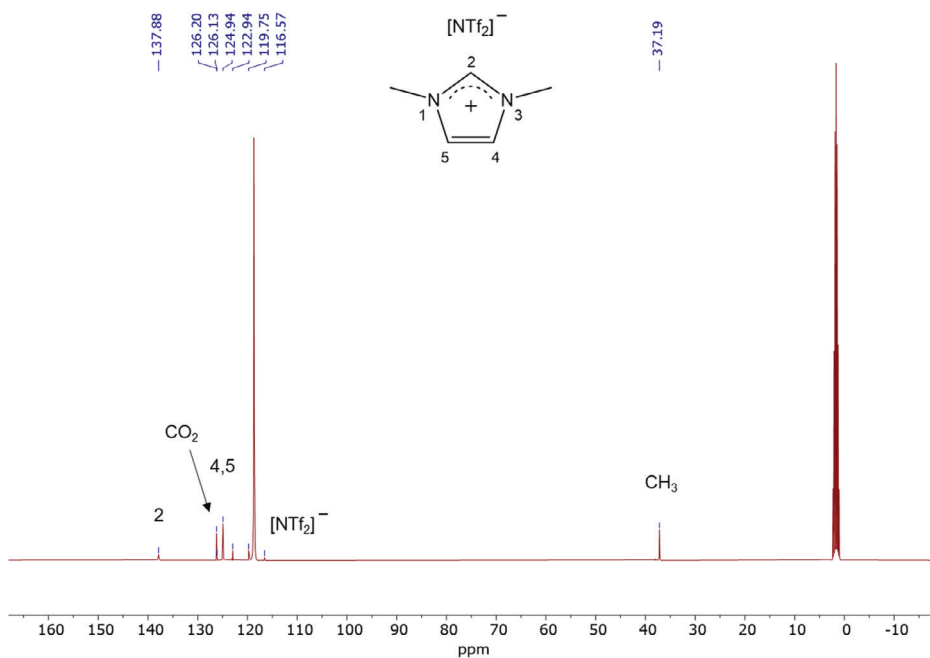


**Figure S3.32.** <sup>13</sup>C NMR spectrum of 1,3-dimethylimidazolium bis(trifluoromethylsulfonyl)imide in CD<sub>3</sub>CN. The spectrum is from the MM-acetonitrile after 5 hrs. of electrolysis (Figure 3.1e). CO<sub>2</sub> peak appears as a result of CO<sub>2</sub> absorption by MM-acetonitrile.

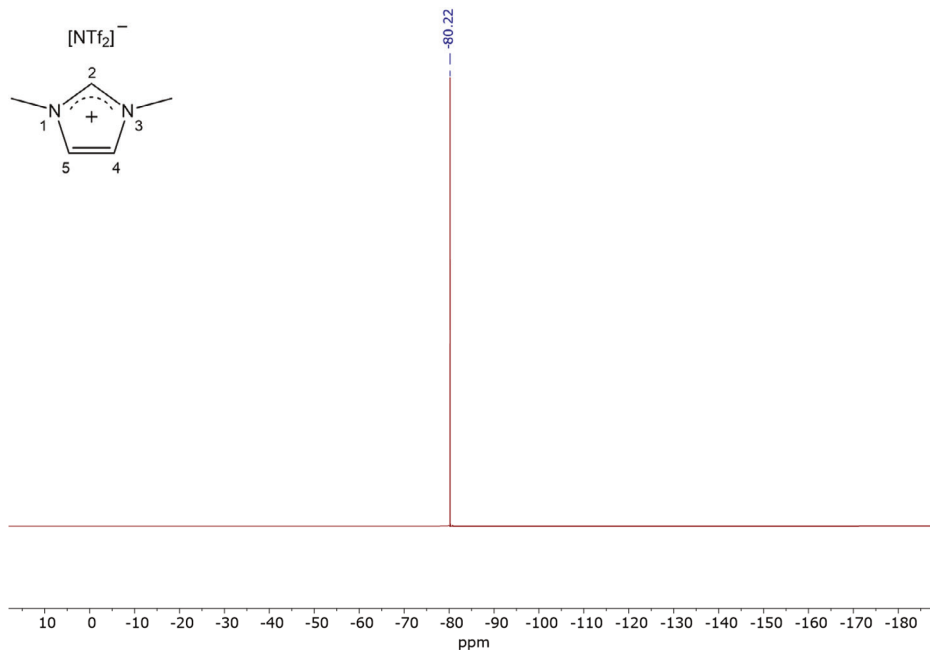


**Figure S3.33.** <sup>19</sup>F NMR spectrum of 1,3-dimethylimidazolium bis(trifluoromethylsulfonyl)imide in CD<sub>3</sub>CN. The spectrum is from the MM-acetonitrile after 5 hrs. of electrolysis (Figure 3.1e).

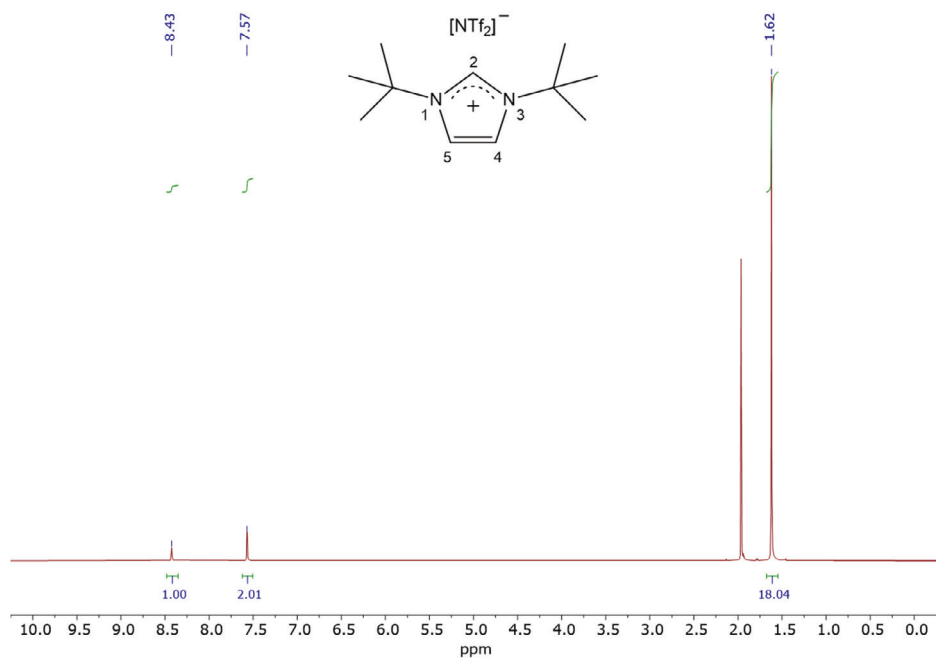


**Figure S3.34.**  $^1\text{H}$  NMR spectrum of 1,3-di-*tert*-butylimidazolium bis(trifluoromethylsulfonyl)imide in  $\text{CD}_3\text{CN}$ . The spectrum is from the *t*-Bu-acetonitrile after 1.5 hrs. of chronoamperometry at  $-1.8$  V vs.  $\text{Ag}/\text{Ag}^+$  (Figure S3.2).

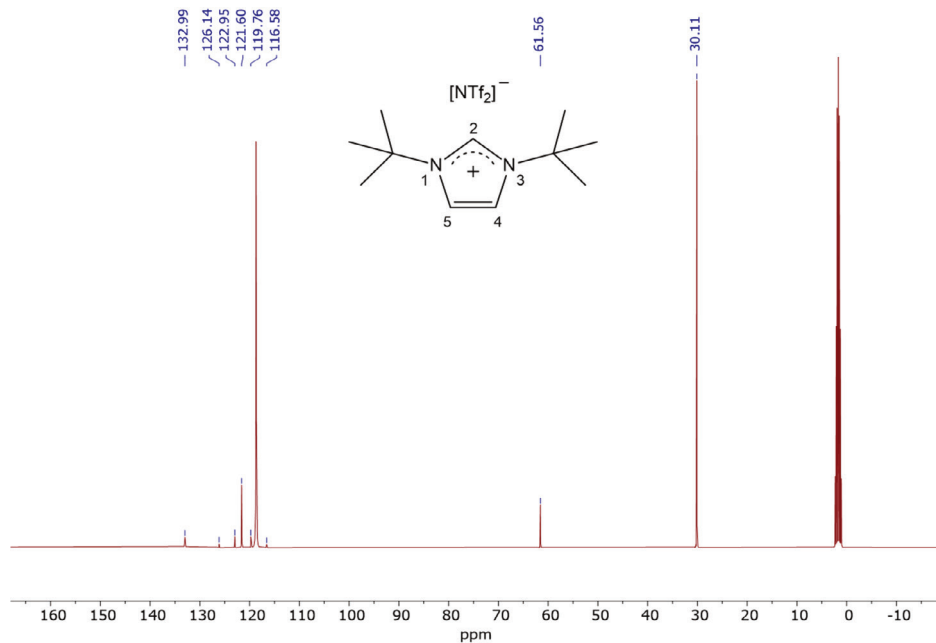


**Figure S3.35.**  $^{13}\text{C}$  NMR spectrum of 1,3-di-*tert*-butylimidazolium bis(trifluoromethylsulfonyl)imide in  $\text{CD}_3\text{CN}$ . The spectrum is from the *t*-Bu-acetonitrile after 1.5 hrs. of chronoamperometry at  $-1.8$  V vs.  $\text{Ag}/\text{Ag}^+$  (Figure S3.2).

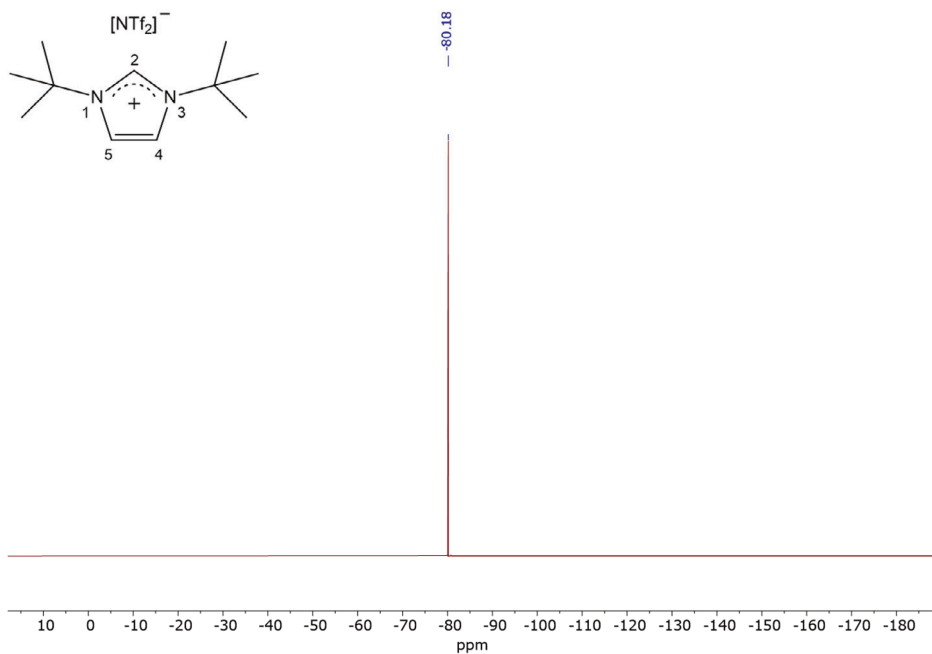


**Figure S3.36.**  $^{19}\text{F}$  NMR spectrum of 1,3-di-*tert*-butylimidazolium bis(trifluoromethylsulfonyl)imide in  $\text{CD}_3\text{CN}$ . The spectrum is from the *t*-Bu-acetonitrile after 1.5 hrs. of chronoamperometry at  $-1.8$  V vs.  $\text{Ag}/\text{Ag}^+$  (Figure S3.2).

### **XIII. Computational methods**

DFT calculations were performed with the Amsterdam density functional program<sup>80</sup>. B3LYP was used as a hybrid exchange-correlation functional<sup>88</sup> together with Grimme's DFT-D3 dispersion correction with Becke-Johnson damping (BJ)<sup>89</sup>. For all atoms, a Slater-type basis set of triple zeta valence quality with two polarization functions was used (TZ2P)<sup>90</sup>. For all calculations, scalar relativistic effects using the ZORA (zeroth-order regular approximation) formalism were included. For calculations including gold atoms, spin-orbit coupling was considered. Calculations were always performed with no frozen core (an all-electron basis set) with a "very good" numerical quality. All calculations were performed with a conductor-like screening model (COSMO) to account for solvent effects (acetonitrile).

## **Chapter 4:**

### **Investigating the Influence of C4, C5-Substituted Imidazolium Cations on Electrochemical CO<sub>2</sub> Conversion**

## Summary

In **Chapter 3** it was found that the acidity of the C-2 protons of imidazolium cations play a key role in co-catalyzing the reduction of CO<sub>2</sub> at the Au electrode. In this chapter we will extend the library of cations for which the acidity is modified by C4,C5-substituents. Three remarkable results will be extensively discussed. First, the 1,3,4,5-tetramethyl imidazolium (**TetraMe**) cation unsurprisingly exhibits a higher overpotential requirement for CO<sub>2</sub> reduction compared to **MM**. This outcome finds concurrence with both the <sup>13</sup>C carbon NMR data and the Voronoi Deformation Density (VDD) charge analysis, both indicating an escalated positive charge density linked with the C2-H2 of **MM** cation.

Furthermore, a surprising observation emerges from the divergent behavior exhibited by the **MM** cation and the 1,3-dimethyl-4,5-diphenyl imidazolium (**DiPh**) cation in chronoamperometry measurements for CO<sub>2</sub> reduction. Notably, while the required potential increases with the **MM** cation, it leads to an overall enhanced performance for the **DiPh** cation. The improved performance of **DiPh** in steady-state electrolysis experiments aligns with its higher acidity, as verified through VDD charge analysis and pKa determination. However, this result contrasts with the LSV findings, which indicate a more negative onset potential for CO<sub>2</sub> reduction with the bulkier **DiPh** cation. We tentatively explain this observation by differences in hydrophobicity – the **MM** cation is less hydrophobic, and therefore more susceptible to interactions with residual water within the surface boundary layer – causing the time-dependent formation of adsorbed species after deprotonation, as previously proposed in the literature. These adsorbed species could potentially exert an influence on the CO<sub>2</sub> reduction under steady-state conditions, resulting in a higher overpotential for the **MM** cation. The final observation is the notably lower onset potential observed for the 1,3-dimethyl-4,5-dichloro imidazolium (**DiCl**) cation, compared to the **MM** cation. This observation is consistent with the higher C2-H2 positive charge density for **DiCl**. However, chronoamperometry measurements for the **DiCl**



cation yielded inconclusive results, necessitating further investigation. Thus, elucidating the difference in behavior between these cations remains a challenge.

## Introduction

According to the findings in **Chapter 3**, 1,3-dimethyl imidazolium cation was found to display the highest activity among the five cations investigated. Here, we will broaden the parameter space by focusing on the effect of C4 and C5-substituents. Imidazolium cations are conjugated acids of N-heterocyclic carbenes (NHCs) (**Figure 4.1. a**). For NHCs, the electronic features and consequently the conjugated acidity are controlled via electron donating or electron withdrawing characteristics of substituents at the N1, N3, or C4, C5 positions (**Figure 4.1. b**). In **Chapter 3**, we tuned the acidity of the imidazolium cation by altering the substituents at the N1 and N3 positions, affecting the C2 proton acidity and interaction with surface adsorbed CO<sub>2</sub>. So far, we have excluded steric effects, which could play a role if substituents become too bulky. This steric influence on the reactivity of C2-H is perceived to be much less by substitutions at the C4 and C5 positions<sup>5,91</sup>. Besides, feasible synthetic routes are available for introducing various substituents at the C4 and C5 positions during construction of the imidazole ring.

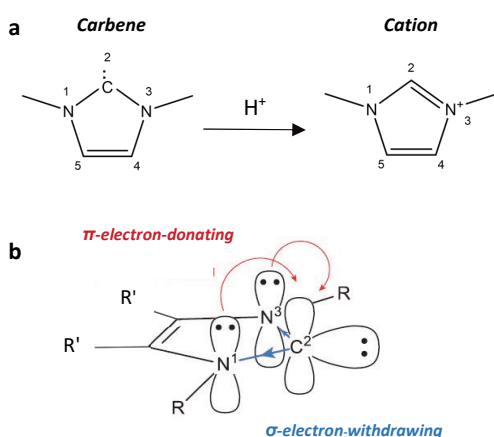


**Figure 4.1.** (a) Structure of 1,3-dimethyl imidazole-2-ylidenes (**left**) and its conjugate acid 1,3-dimethyl imidazolium cation (**right**). The acidity of the imidazolium cation is in direct relation with the basicity of the free carbene. (b) The electronic features of C2-carbene are tuned via substituents at N1, N3(R) and C4,C5 (R') positions.

## Results and discussion

To modify the electronic features of the C2-H2 of imidazolium cation carbon, we synthesized four cations: 1,3-dimethyl-4,5-dichloro imidazolium (**DiCl**), 1,3,4,5-tetramethyl imidazolium (**TetraMe**), 1,3-dimethyl-4,5-diphenyl imidazolium (**DiPh**) and 1,3-dimethyl-4,5-di(4-methoxy) diphenyl (**DiMeOP**). The structure of the cations is shown in **Figure 4.2**. The activity of these cations will be compared to that of **MM** cation as our benchmark co-catalyst. **Figure 4.3** summarizes the  $^{13}\text{C}$  NMR results for all cations studied in this chapter, aiming at providing insights into the charge density of C2-proton for cations of the same functional family. For a detailed discussion on acidity trends among these cations, please refer to **Supporting Information Section VI**.

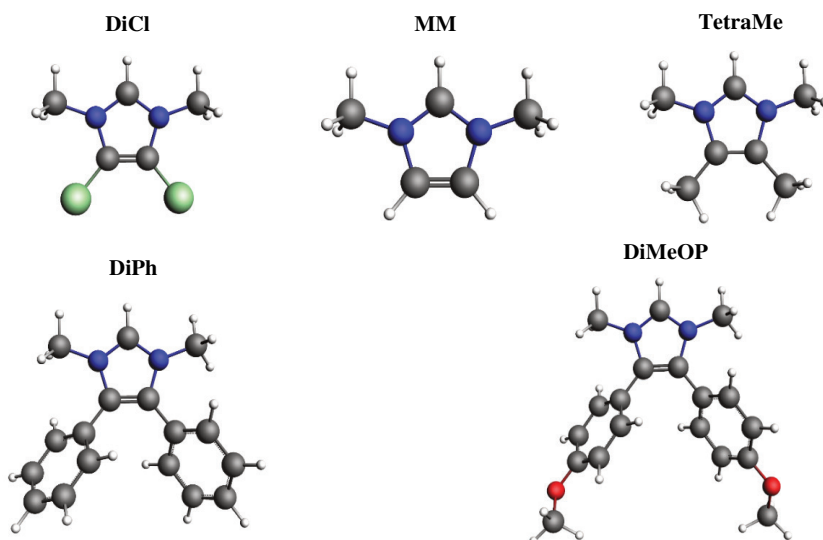


**Figure 4.2.** Imidazolium cations synthesized in this work for investigating electrochemical reduction of  $\text{CO}_2$  in anhydrous acetonitrile.

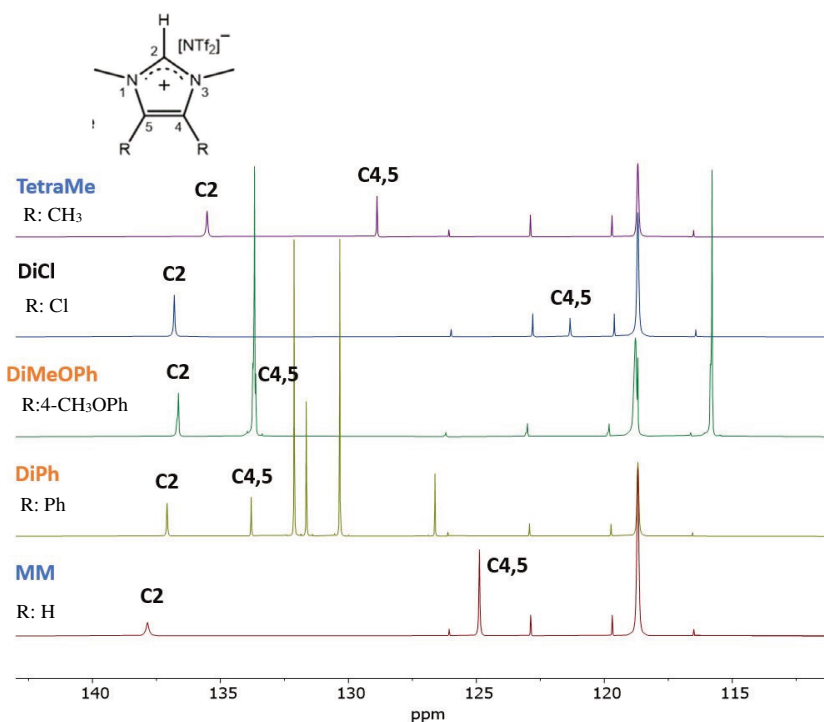


**Figure 4.3.** <sup>13</sup>C NMR spectra of the five cations investigated in this chapter. Refer to **Figure 4.2** for the molecular structures of the cations. Cations with similar functional group arrangements are indicated by the same color.

**Figure 4.4** (left) displays the LSVs recorded for **MM** and **TetraMe** cations under a CO<sub>2</sub> atmosphere. The LSV results uncover a slightly higher apparent activity for CO<sub>2</sub> reduction associated with the **MM** cation, although the distinction appears marginal. This observation is substantiated by the VDD charge analysis map depicted in **Figure 4.4** (right). Comparatively, **MM** is characterized as a more electron-deficient cation than **TetraMe**. As a result, **TetraMe** is expected to display reduced acidity at the C2-H position, aligning with the anticipated lower activity. Electrolysis at -1 mA/cm<sup>2</sup> under CO<sub>2</sub> purge conditions demonstrated a 100% FE for CO formation with both cations when employed under the same salinity. For **MM**, achieving the same FE coincided with a reduction of the requisite reductive potential by 90 mV. This reduction is consistent with outcomes derived from the LSV results, the electron density map, and the <sup>13</sup>C NMR analysis (**Figure 4.3**, indicated by blue letters).

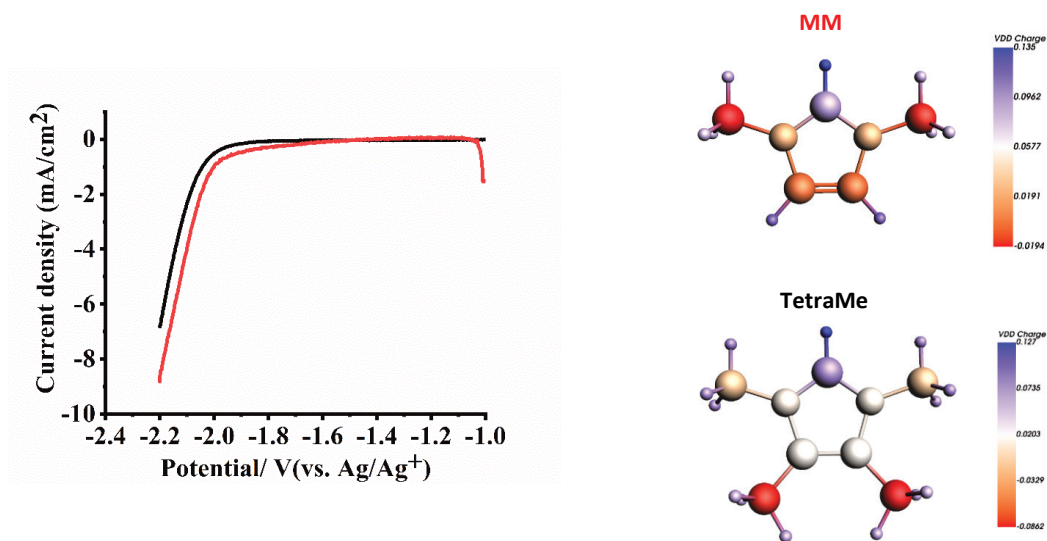


**Figure 4.4.** (left) The comparison of LSVs for 0.5 mol% **MM-NTf<sub>2</sub>** (red) and **TetraMe-NTf<sub>2</sub>** (black) for CO<sub>2</sub> reduction in anhydrous acetonitrile. (right) Electron density map (from VDD charge analysis) which shows **MM** is more electron poor, thus a more acidic cation.

Next, we proceed to a comparison of the results concerning the diphenyl-substituted groups. LSV results for **DiPh** and **DiMeOPh** cations under CO<sub>2</sub> atmosphere are presented in **Figure 4.5** (left). Concurrently, **Figure 4.5** (right) exhibits the electron density maps calculated for these two cations. The outcomes of the calculated charge analysis align with the <sup>13</sup>C NMR findings depicted in **Figure 4.3** (indicated by orange letters). These results suggest a reduced co-catalytic activity for the **DiMeOPh** cation in comparison to the **DiPh** cation, owing to its increased electron richness. This is well-confirmed by the LSV results which shows a lower apparent activity for the diphenyl methoxy substituted imidazolium cation.

While comparing outcomes within the same functional groups can be straightforward, assessing results across different functional families requires careful consideration. In **Figure 4.6** (left), we present the LSV results obtained from **MM** and **DiPh** cations during CO<sub>2</sub> reduction under consistent salinity conditions. Based on the electron density maps generated from DFT calculations (**Figure 4.6** right), it becomes apparent that **DiPh** displays a somewhat higher

positive charge within the imidazolium ring, with a slight increase in positive charge localized at the C2-H proton. This observation hints at the possibility of a more acidic character within the **DiPh** cation. To further explore this, we subjected the **DiPh** cation to exposure with the indenyl anion as an indicator base. Following this,  $^1\text{H}$  NMR spectroscopy was employed to quantitatively gauge the acidity of the **DiPh** cation (for additional information, refer to **Supporting Information Section V**). The analysis yielded a measured pKa value of 20.1 for **DiPh** in DMSO. Comparing this value with the reported pKa value for the **MM** cation in DMSO ( $\sim 22.0$ )<sup>70</sup> support the more acidic character of **DiPh** cation. Consequently, one might anticipate an increased activity for the **DiPh** cation; however, this expectation is not corroborated by the LSV results shown in **Figure 4.6**. Unexpectedly, we observe a significantly more negative onset potential for CO<sub>2</sub> reduction with the **DiPh** cation. To rationalize the unforeseen outcomes of the LSV results, we may consider the impact of cation bulkiness. It's apparent that the **DiPh** cation boasts a larger molecular size compared to the **MM** cation. The increased bulk of the **DiPh** cation could potentially influence the interaction between the cation and the Au electrode, as well as the surface-adsorbed CO<sub>2</sub> species. A similar adverse effect was also witnessed with the sizeable 1-nonyl-3-methyl (**NM**) imidazolium cation (as discussed in **Chapter 7**). Despite having only marginal acidity differences in comparison to the **MM** cation, a noticeable decrease in activity was observed with **NM** cation. To further validate the impact of cation size, future investigations should consider employing techniques such as impedance measurements and molecular simulations.

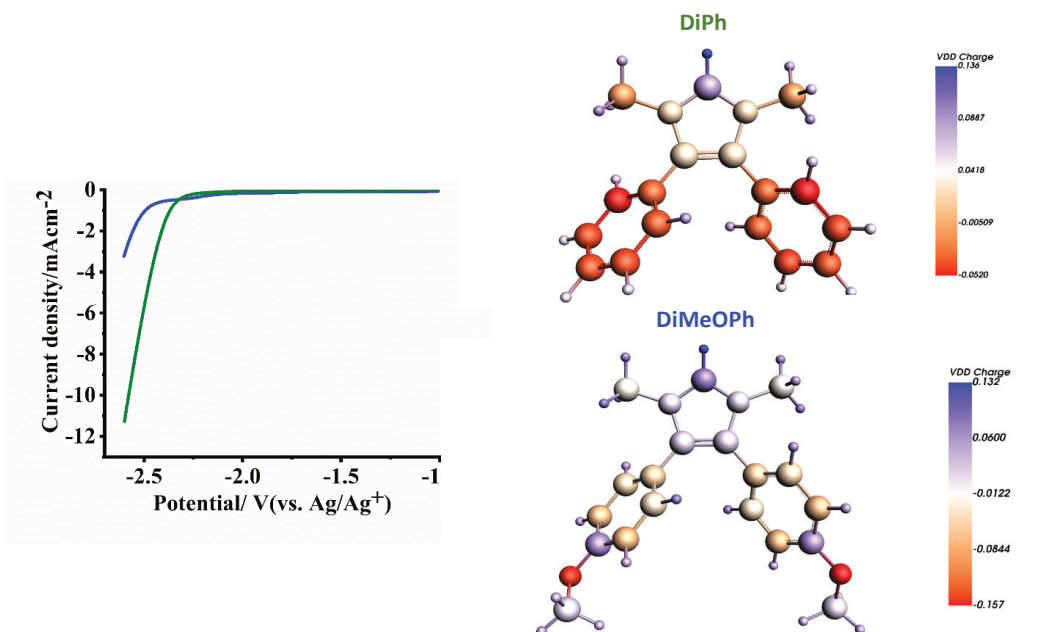


**Figure 4.5.** (left) The comparison of LSVs for 0.5 mol% **DiPh-NTf<sub>2</sub>** (olive) and **DiMeOPh-NTf<sub>2</sub>** (blue) for CO<sub>2</sub> reduction in anhydrous acetonitrile. (right) Electron density map (from VDD charge analysis) which shows **DiPh** as more electron poor, thus a more acidic cation.

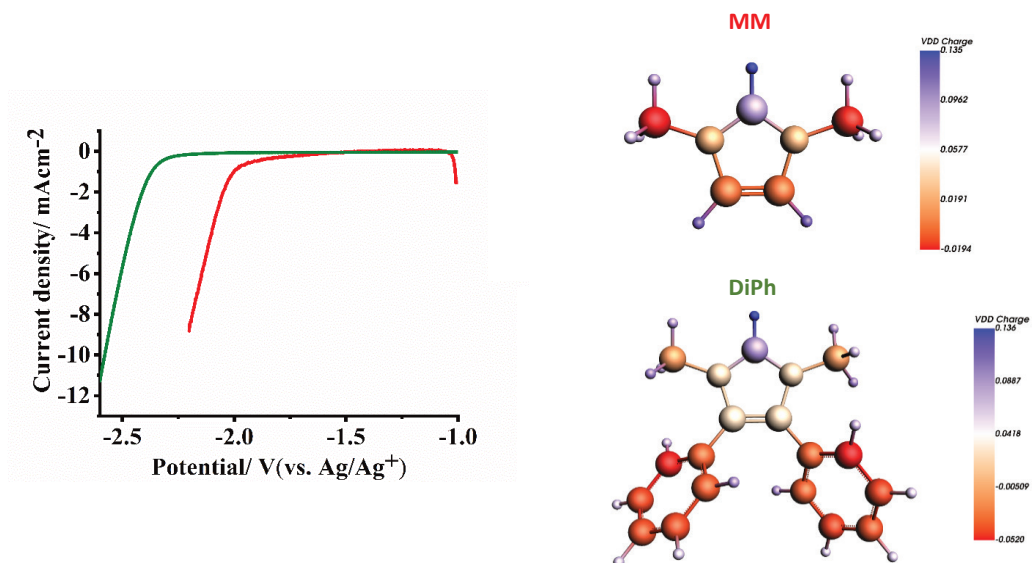


**Figure 4.6.** (left) The comparison of LSVs for 0.5 mol% **MM-NTf<sub>2</sub>** (red) and **DiPh-NTf<sub>2</sub>** (olive) for CO<sub>2</sub> reduction in anhydrous acetonitrile. (right) Electron density map (from VDD charge analysis) which shows that **DiPh** is slightly more electron poor. Stability of **DiPh-NTf<sub>2</sub>** after electrolysis was confirmed with NMR analysis (see Supporting Information **Figures S4.1-S4.3**)

**Figure 4.7** displays the outcomes of electrolysis experiments involving **MM** and **DiPh** cations. The data reveals two distinct patterns. In the initial 1000 seconds, the **MM** cation displays a lower overpotential, aligning with the findings from the LSV results. However, after this, the **MM** cation experiences a gradual rise in the needed overpotential before attaining a stable performance. In contrast, the phenyl-substituted cation demonstrates a decrease in overpotential over time. Notably, a crossover of the required potential for both cations becomes evident after approximately 1000 seconds of experimentation. Overall, the phenyl-substituted cation achieves the best performance, notably by lowering the necessary potential by around 250 mV.

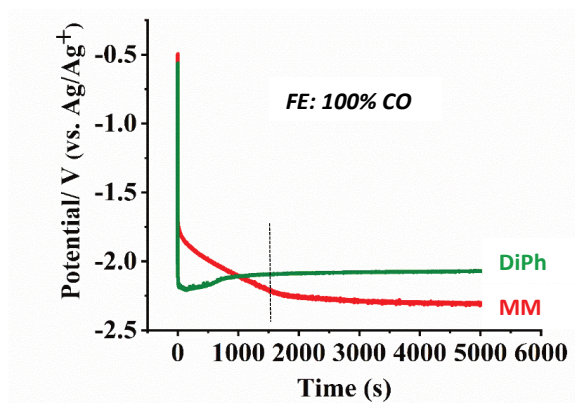


**Figure 4.7.** Electrolysis at  $-1 \text{ mA/cm}^2$  with 0.5 mol% **MM-NTf<sub>2</sub>** (red) and **DiPh-NTf<sub>2</sub>** (olive) for  $\text{CO}_2$  reduction in anhydrous acetonitrile. The dashed line indicated the time after which steady state is reached.

Phenyl substituents are indeed hydrophobic functionalities, and it is reasonable to expect that these substituents would hinder the association of water molecules with the cation residing in the double layer. Bi et al.<sup>92</sup> have demonstrated that hydrophobic ionic liquids can help keep water molecules away from negatively charged electrodes in humid conditions. Therefore, in the case of the **DiPh** cation, we can anticipate an effect from the reduced presence of residual water in the electric double layer (EDL) compared to cations such as **MM**. In our experiments, there is inevitably some residual water present in the electrolyte, typically up to 50 ppm, which is challenging to eliminate in an experimental setup open to the atmosphere. Considering the

hydrophobic nature of phenyl substituents and the presence of residual water in the electrolyte, it is plausible to propose that the stability and catalytic performance of the **MM** cation are influenced by the interaction between residual water and the cation in the electric double layer. We anticipate that the presence of residual water, which is more prevalent in the case of more hydrophilic cations like **MM**, will have an impact on the stability of the **MM** cation. This hypothesis is supported by the findings of Amit et al.<sup>6</sup>, who demonstrated that the reduction of water in the vicinity of the electrode surface can generate hydroxyl groups. These hydroxyl groups can subsequently lead to the deprotonation of nearby imidazolium cations as well as the potential decoration of the electrode with the conjugate base of the cation (**Figure 4.8**).

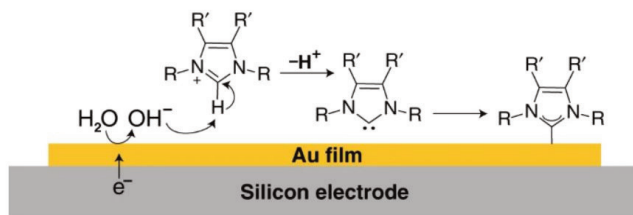


**Figure 4.8.** The deprotonation of imidazolium cation in presence of active surface hydroxyl group at the vicinity of the electrode. Proposed by Amit et al.<sup>6</sup>

As discussed by Amit et al., the extent of deprotonation and its impact on the cation's behavior will be influenced by the specific nature of the cation and the abundance of hydroxyl groups at the electrode surface. Taking this chemical understanding into account, the gradual increase in overpotential observed with the **MM** cation (**Figure 4.7**) can likely be attributed to the partial deactivation of the **MM** cation caused by the reduction of residual water in the electric double layer (EDL). It's also essential to acknowledge that the **MM** cation has consistently been a commercially available entity in this study, potentially subjected to different drying procedures compared to the rigorous processes applied to in-house synthesized cations like **DiPh**. Consequently, the likelihood of increased water presence on the electrode surface, accompanied by the **MM** cation, is a noteworthy consideration. It's worth noting that this hypothesis could



find stronger support through background experiments involving both cations at varying water levels. The results from **DiPh** and **MM** show that when the cation is acting as a co-catalyst the overpotential is not only dependent on the intrinsic kinetics of the co-catalyzed reaction but also on the stability of the cation and possible side reactions involving residual water. This will bring this notion that to gain a full picture of the performance, transient experiments (for example: LSVs) should always be complemented by steady-state experiments. It's noteworthy to acknowledge that while we have put forth the potential influence of residual water on the observed behavior of the **MM** and **DiPh** cations, an alternative explanation might also be considered. This alternative explanation suggests the potential for a mechanistic alteration in the reaction during steady-state experiments, specifically involving the **DiPh** cation. Notably, in the steady-state scenario, the **DiPh** cation demonstrates an improved performance compared to the **MM** cation, aligning with the expectations from our theory of C2-H acidity. However, at the moment, we lack any viable hypothesis that could be proposed for such a scenario.

The last experiment was aimed at the comparison between **MM** and **DiCl** cations. **Figure 4.9** shows the LSVs results under CO<sub>2</sub> atmosphere and the electron density map for both cations. Clearly, **DiCl** is an electron poor cation, and we would expect a higher activity compared with that for **MM**. This is confirmed by the LSV results and the electrolysis results for which a more positive overpotential up to +200 mVs is obtained by **DiCl** (**Figure 4.10**). However, electrolysis results did not show the expected amount of CO. Thus, we suspect the formation of other products or the degradation of the cation. Yet, <sup>13</sup>C NMR and <sup>1</sup>H NMR analysis after few hours of electrolysis did show neither any liquid product nor any evidence of the degradation of the cation (**Supporting Information, Figures S4.4-S4.6**).

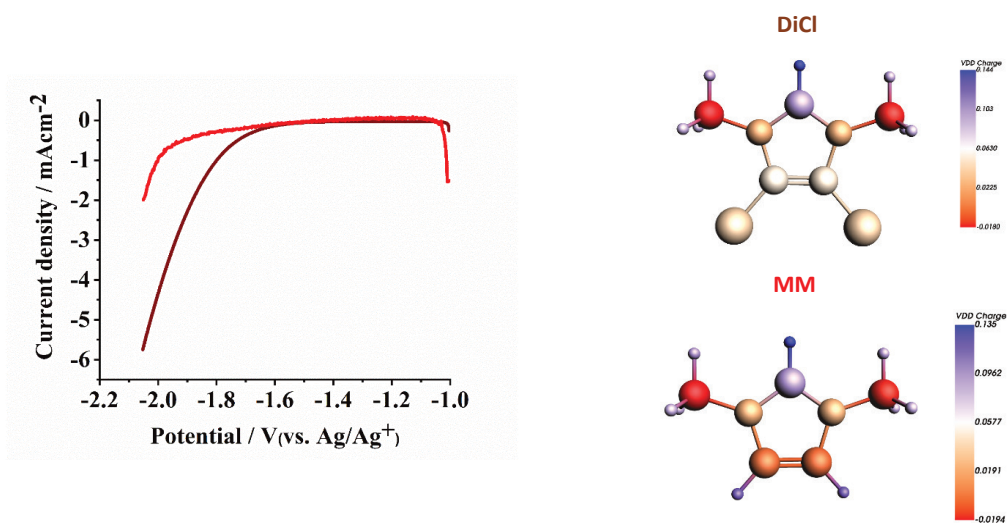


**Figure 4.9.** (left) The comparison of LSVs for 0.5 mol% **MM-NTf<sub>2</sub>** (red) and **DiCl-NTf<sub>2</sub>** (brown) for CO<sub>2</sub> reduction in anhydrous acetonitrile. (right) Electron density map (from VDD charge analysis) which shows that **DiCl** is a more electron poor cation.

The higher apparent activity, aligning with the stability of the cation, positions **DiCl** as a promising contender for the efficient activation of CO<sub>2</sub>. However, a more comprehensive analysis involving detailed GC and liquid analysis is necessary to investigate the potential formation of other products, when using a **DiCl** solution. Notably, the LSV results reveal a deviation in the apparent slope of the current-potential profile when compared to the **MM**, **TM**, **DiPh** and **DiMeOPh** cations investigated in this study. This observation prompts us to consider alternative mechanisms that could be contributing, possibly linked to the heightened acidic nature of the cation.

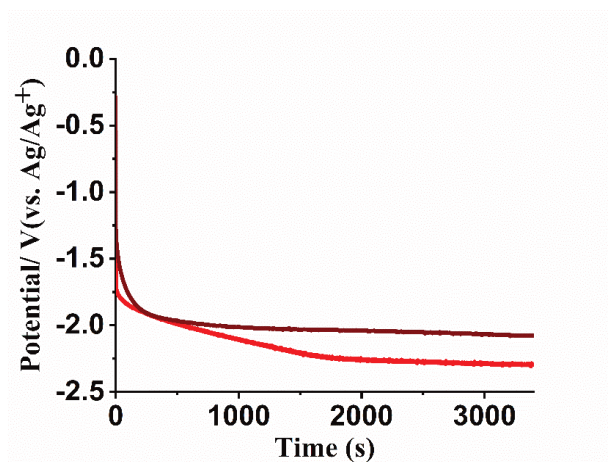


**Figure 4.10.** Electrolysis at  $-1 \text{ mA/cm}^2$  with 0.5 mol% **MM-NTf<sub>2</sub>** (red) and **DiCl-NTf<sub>2</sub>** (brown) for CO<sub>2</sub> reduction in anhydrous acetonitrile.

## Conclusion and outlook

In this chapter, our goal was to explore the impact of different substituents at the C4 and C5 positions on the performance of CO<sub>2</sub> activation. We observed that while comparing functionalities within the same family, such as **MM** and **TetraMe**, yielded straightforward results, the behavior of cations with substituents from different functional families, including alkyls, halides, and phenyls, varied significantly. This variation can be attributed to the high sensitivity of the electrocatalytic reaction to the immediate environment within the electric double layer. To gain a more comprehensive understanding of the factors influencing the performance of CO<sub>2</sub> activation, a systematic synthetic approach is required. For instance, within the phenyl substituent family, comparing different substituents at the para positions could provide valuable insights. Additionally, for highly electron-poor cations like 1,3-dimethyl-4,5-dichloro imidazolium, it is possible to observe changes in the mechanistic pathway.

In summary, when considering the impact of substituents, the following points should be considered:

- a) **Electronic Features:** Changing the electronic features of the cation ring can affect its acidity, potentially improving or diminishing catalytic activity, or even introducing new reaction pathways. This particularly might be of high relevance for highly acidic cations.
- b) **Bulkiness:** Different substituents can impact the bulkiness of the cation, which in turn affects the interfacial interaction of the cation with the catalyst and adsorbed CO<sub>2</sub>. Bulky cations may also obstruct active sites at the same surface concentration. To ensure a fair comparison, it is advisable to compare substituents within the same functional family that have similar bulkiness.
- c) **Hydrophobicity/Hydrophilicity:** The hydrophobic or hydrophilic nature of the cation can influence the stability and mechanism of the non-aqueous CO<sub>2</sub> conversion process, especially in the presence of residual water. The effect of water on cation chemistry depends on the cation's nature, and more acidic cations are more likely to experience significant impacts such as deprotonation and reaction with hydroxyl groups.
- d) **Intrinsic Electronic Effects:** The intrinsic electronic effects of the cation within the double layer can have an impact. Non-specific interactions with the electrode, including the image charge effect, can modify the electrostatic potential and the adsorption properties of the electrode for polar intermediates<sup>93-94</sup>. While these effects are expected to be similar for cations with the same charge density per volume<sup>94</sup>, they may differ for cations with significantly different bulkiness and charge density. Therefore, it is important to work with cations of similar bulkiness when studying specific chemical factors such as acidity.

# Supporting Information

## Table of Contents

- I. Copies of  $^1\text{H}$ ,  $^{13}\text{C}$ , and  $^{19}\text{F}$  NMR spectra
- II. Computational methods
- III. Materials
- IV. Synthetic procedures
- V. Determining the pKa of DiPh cation
- VI. Discussion of acidity trends in C4,C5-substituted cations

## I. Copies of $^1\text{H}$ , $^{13}\text{C}$ and $^{19}\text{F}$ NMR spectra

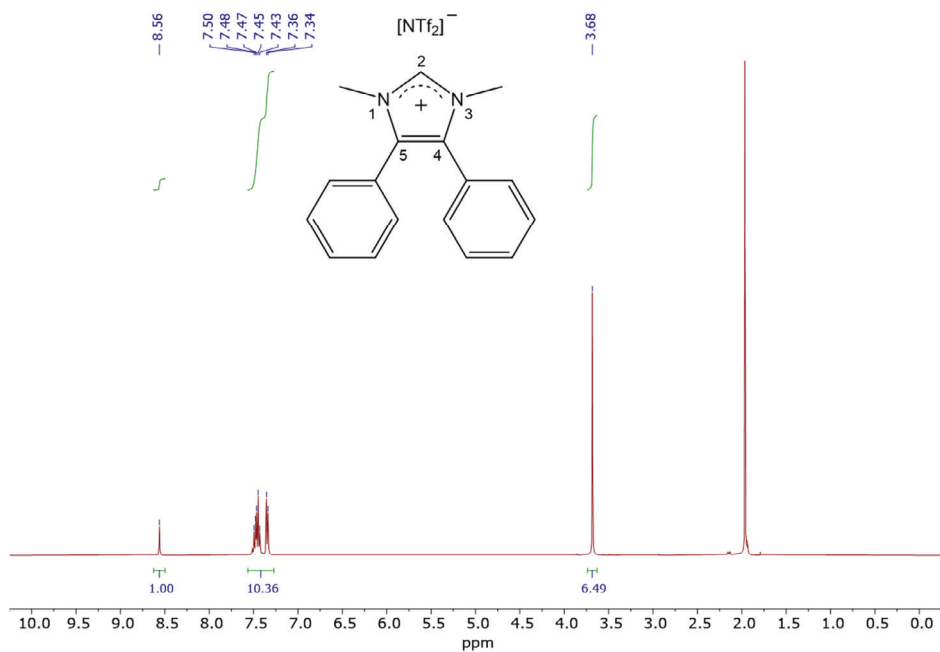


**Figure S4.1.**  $^1\text{H}$  NMR spectrum of 1,3-dimethyl-4,5-diphenylimidazolium bis(trifluoromethylsulfonyl)imide in  $\text{CD}_3\text{CN}$  after electrolysis.

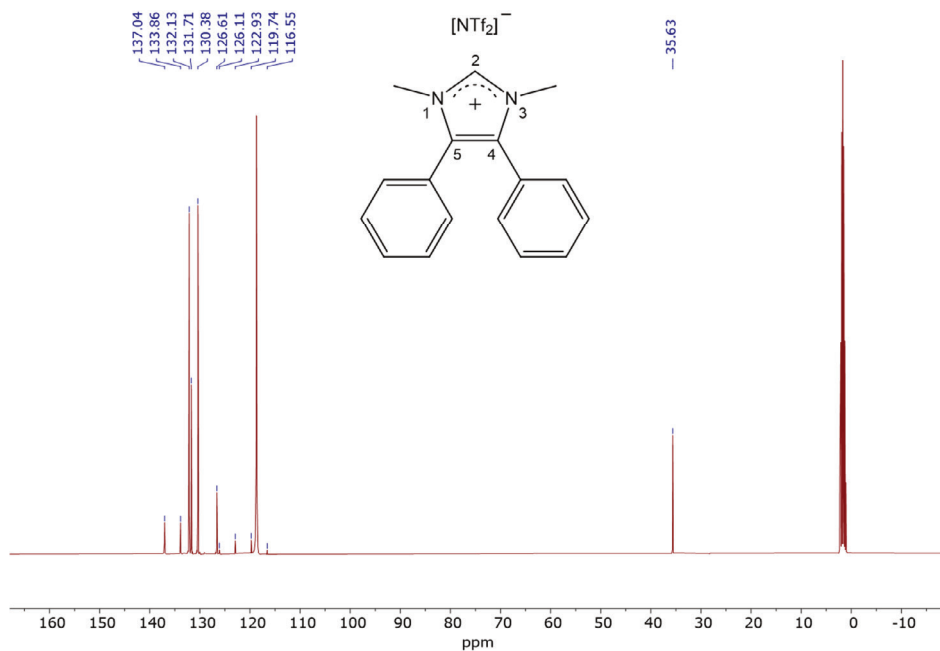


**Figure S4.2.**  $^{13}\text{C}$  NMR spectrum of 1,3-dimethyl-4,5-diphenylimidazolium bis(trifluoromethylsulfonyl)imide in  $\text{CD}_3\text{CN}$  after electrolysis.

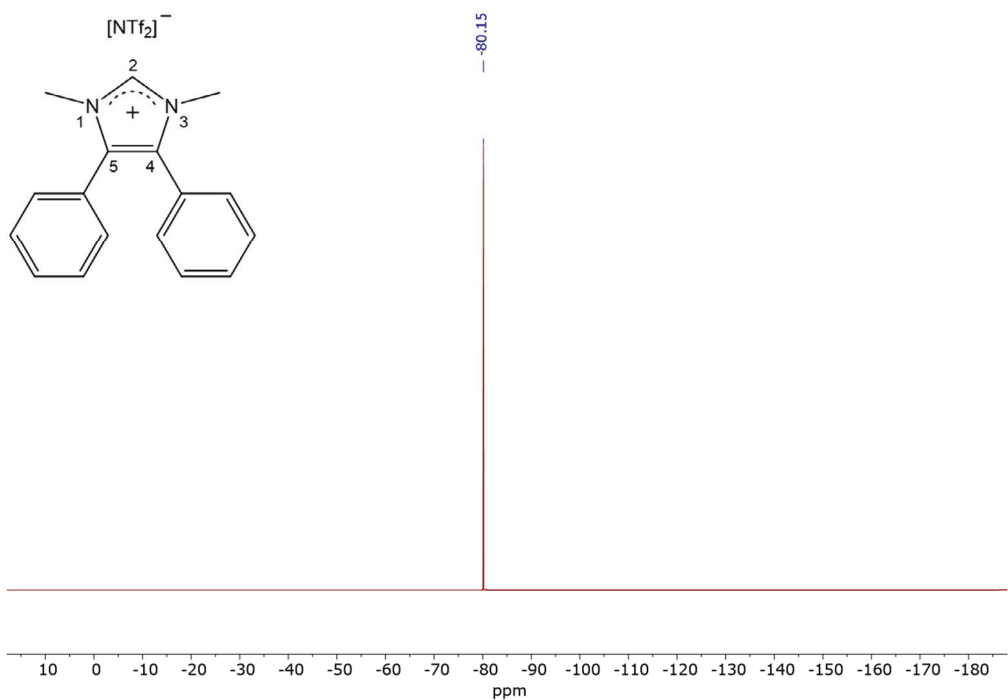


**Figure S4.3.**  $^{19}\text{F}$  NMR spectrum of 1,3-dimethyl-4,5-diphenylimidazolium bis(trifluoromethylsulfonyl)imide in  $\text{CD}_3\text{CN}$  after electrolysis.

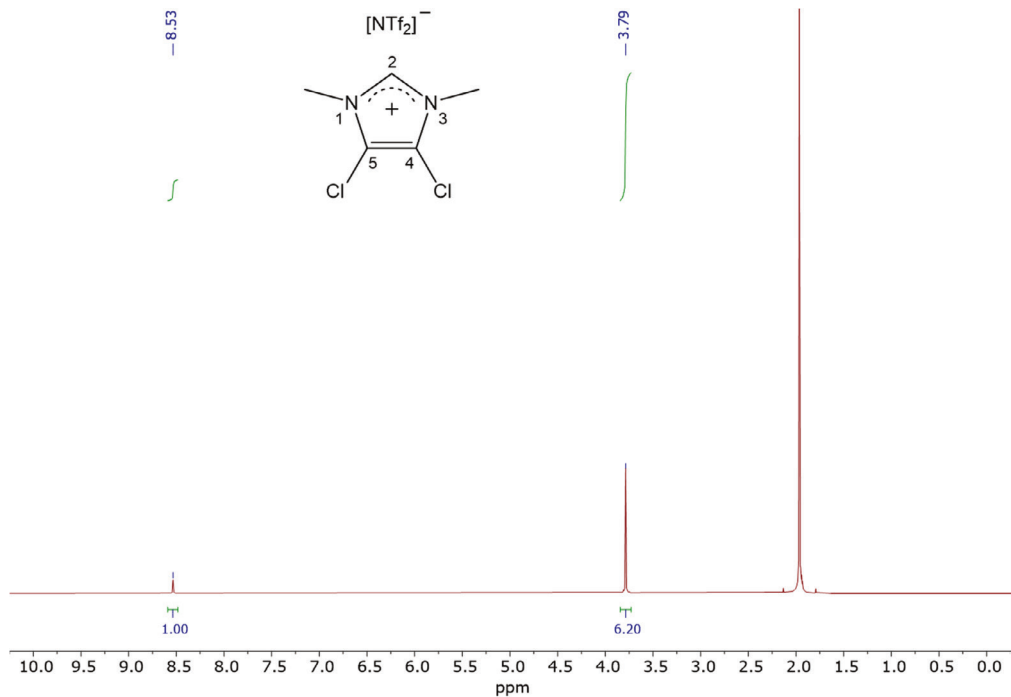


**Figure S4.4.**  $^1\text{H}$  NMR spectrum of 1,3-dimethyl-4,5-dichloroimidazolium bis(trifluoromethylsulfonyl)imide in  $\text{CD}_3\text{CN}$  after electrolysis.

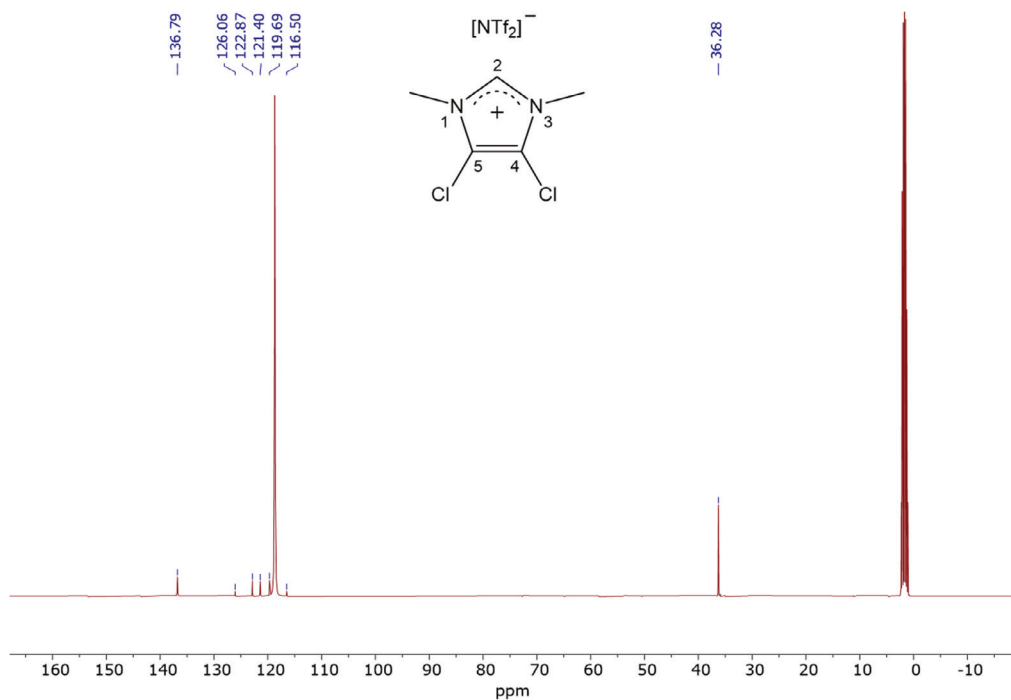


**Figure S4.5.**  $^{13}\text{C}$  NMR spectrum of 1,3-dimethyl-4,5-dichloroimidazolium bis(trifluoromethylsulfonyl)imide in  $\text{CD}_3\text{CN}$  after electrolysis.

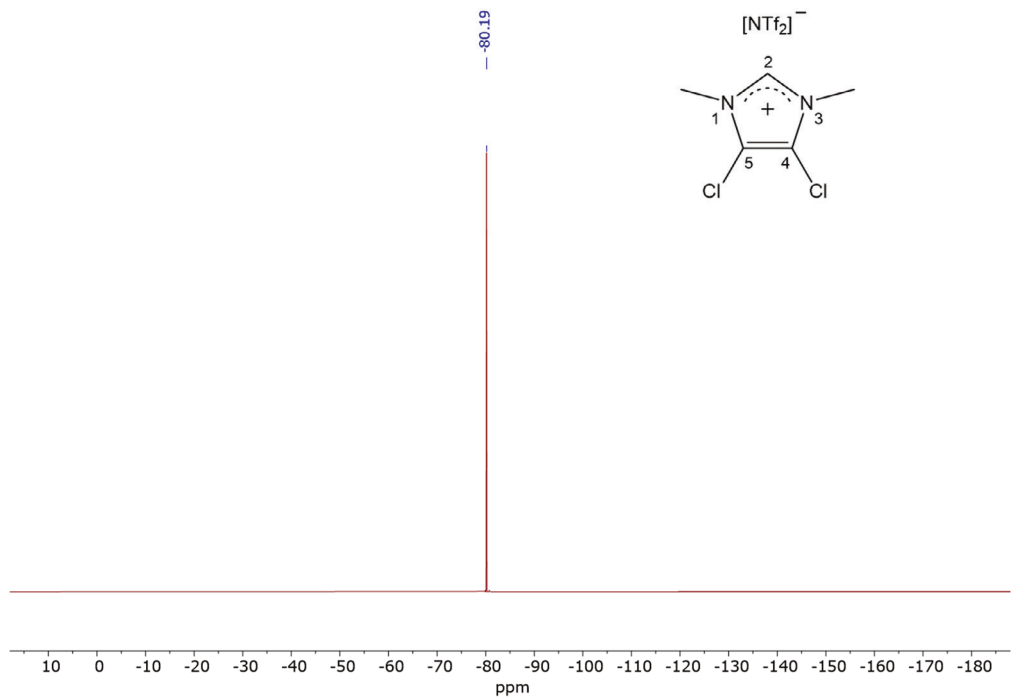


**Figure S4.6.**  $^{19}\text{F}$  NMR spectrum of 1,3-dimethyl-4,5-dichloroimidazolium bis(trifluoromethylsulfonyl)imide in  $\text{CD}_3\text{CN}$  after electrolysis.



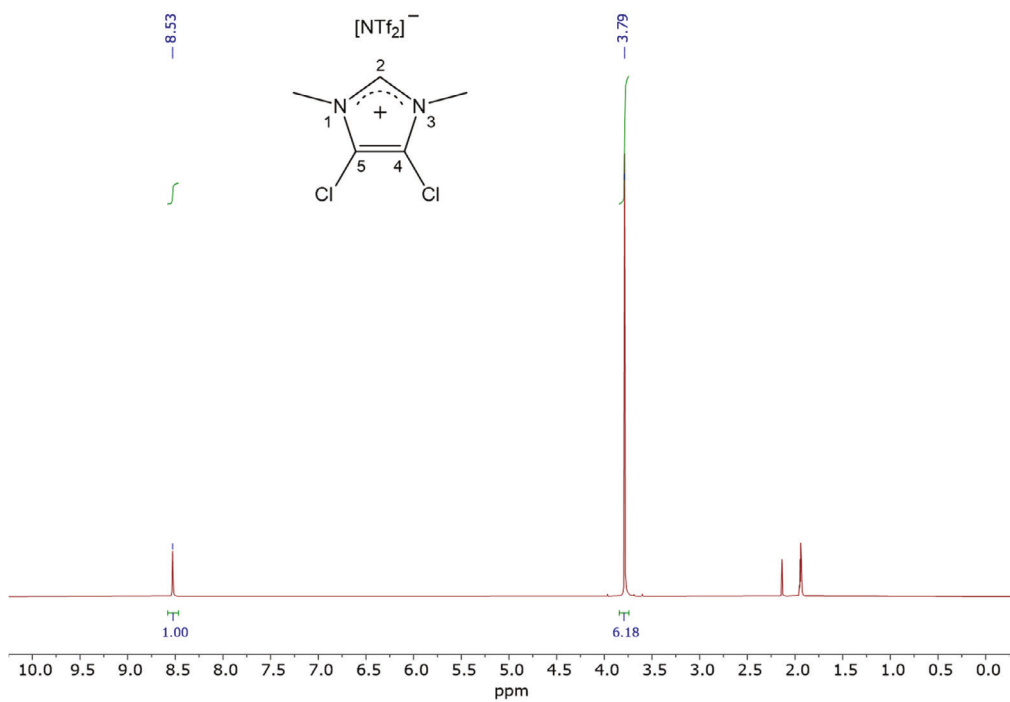


**Figure S4.7.**  $^1\text{H}$  NMR spectrum of 1,3-dimethyl-4,5-dichloroimidazolium bis(trifluoromethylsulfonyl)imide in  $\text{CD}_3\text{CN}$ .

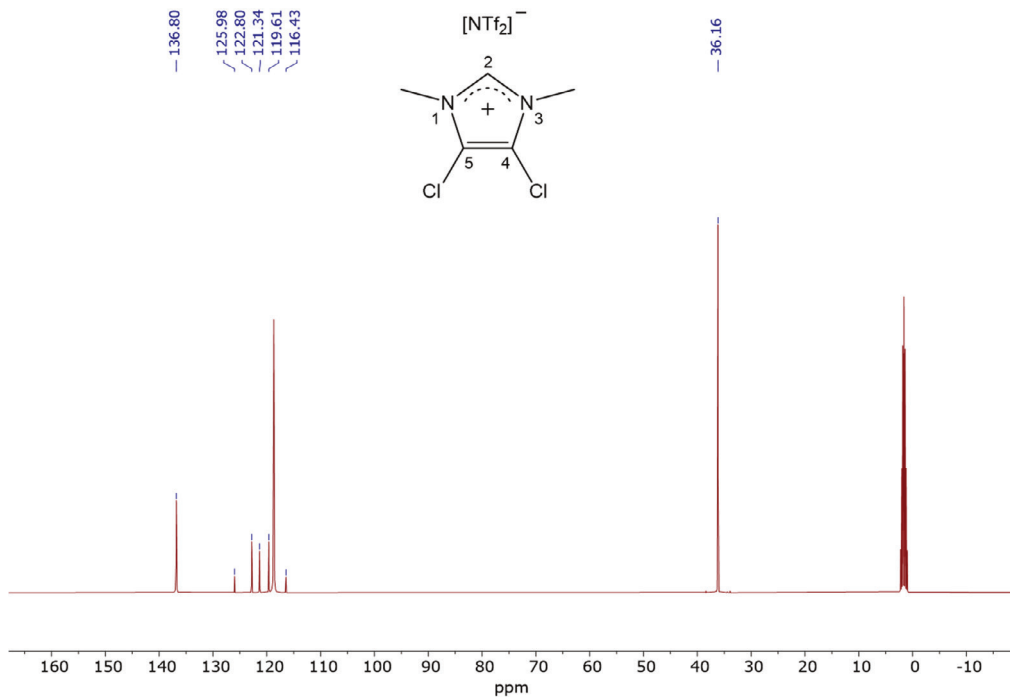


**Figure S4.8.**  $^{13}\text{C}$  NMR spectrum of 1,3-dimethyl-4,5-dichloroimidazolium bis(trifluoromethylsulfonyl)imide in  $\text{CD}_3\text{CN}$ .

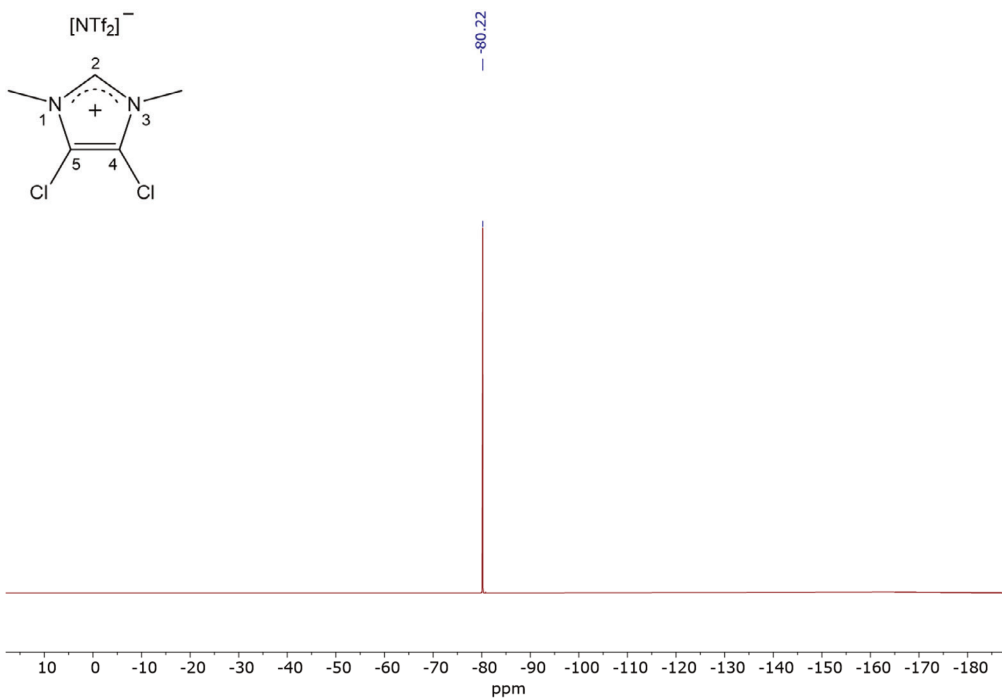


**Figure S4.9.**  $^{19}\text{F}$  NMR spectrum of 1,3-dimethyl-4,5-dichloroimidazolium bis(trifluoromethylsulfonyl)imide in  $\text{CD}_3\text{CN}$ .

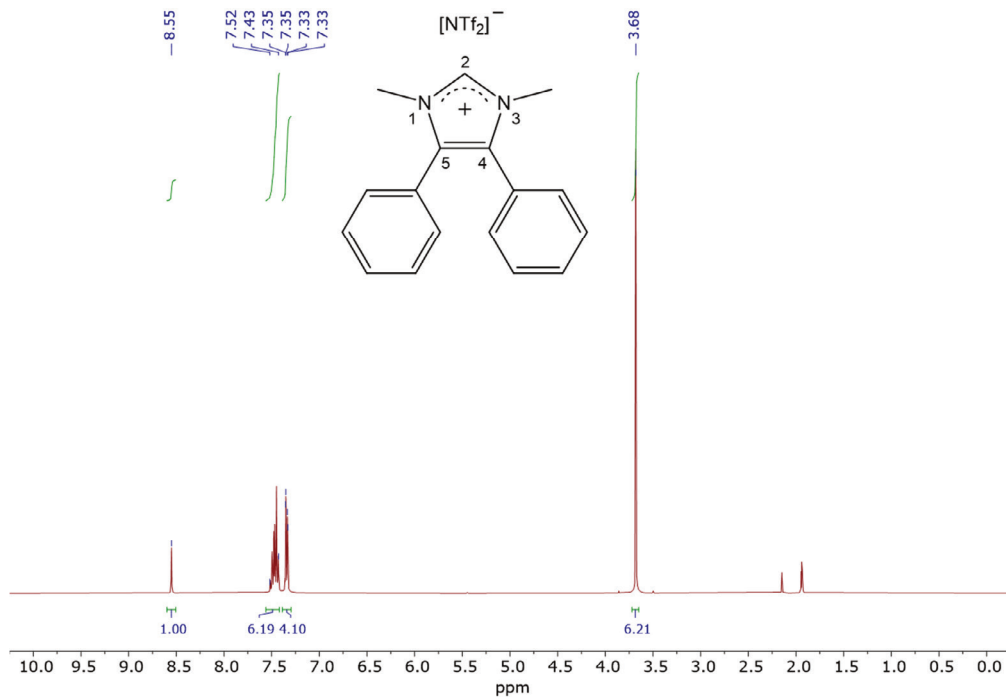


**Figure S4.10.**  $^1\text{H}$  NMR spectrum of 1,3-dimethyl-4,5-diphenylimidazolium bis(trifluoromethylsulfonyl)imide in  $\text{CD}_3\text{CN}$ .

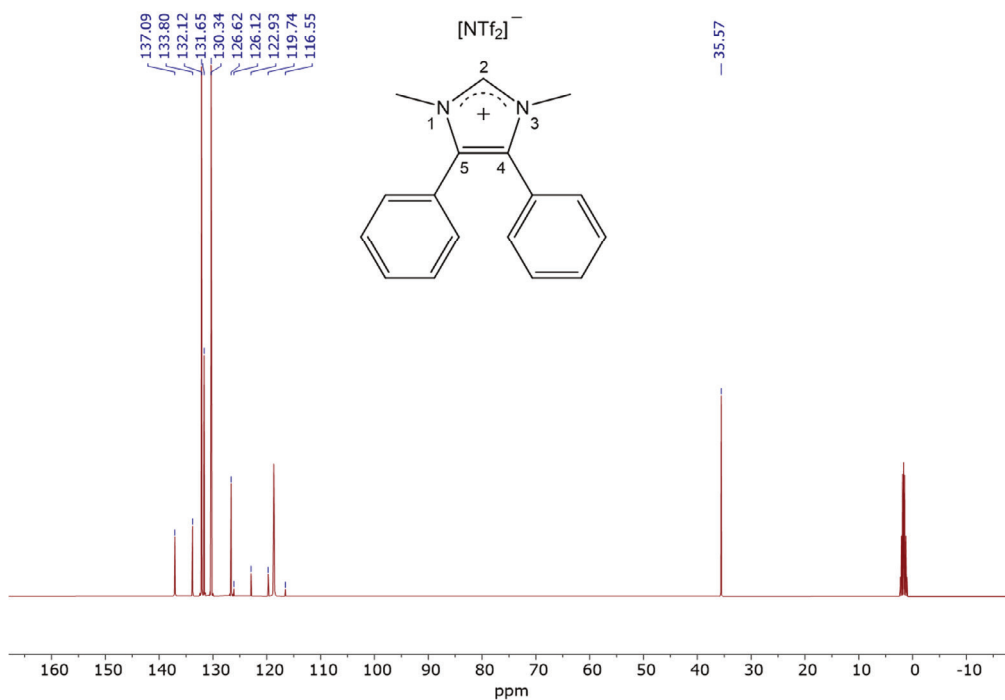


**Figure S4.11.**  $^{13}\text{C}$  NMR spectrum of 1,3-dimethyl-4,5-diphenylimidazolium bis(trifluoromethylsulfonyl)imide in  $\text{CD}_3\text{CN}$ .

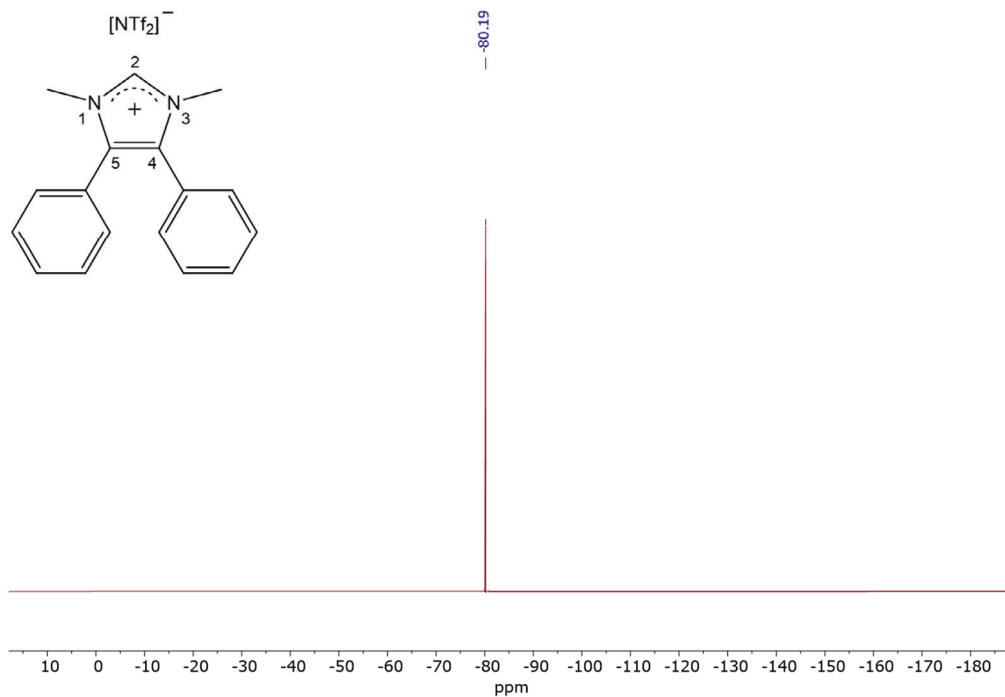


**Figure S4.12.**  $^{19}\text{F}$  NMR spectrum of 1,3-dimethyl-4,5-diphenylimidazolium bis(trifluoromethylsulfonyl)imide in  $\text{CD}_3\text{CN}$ .

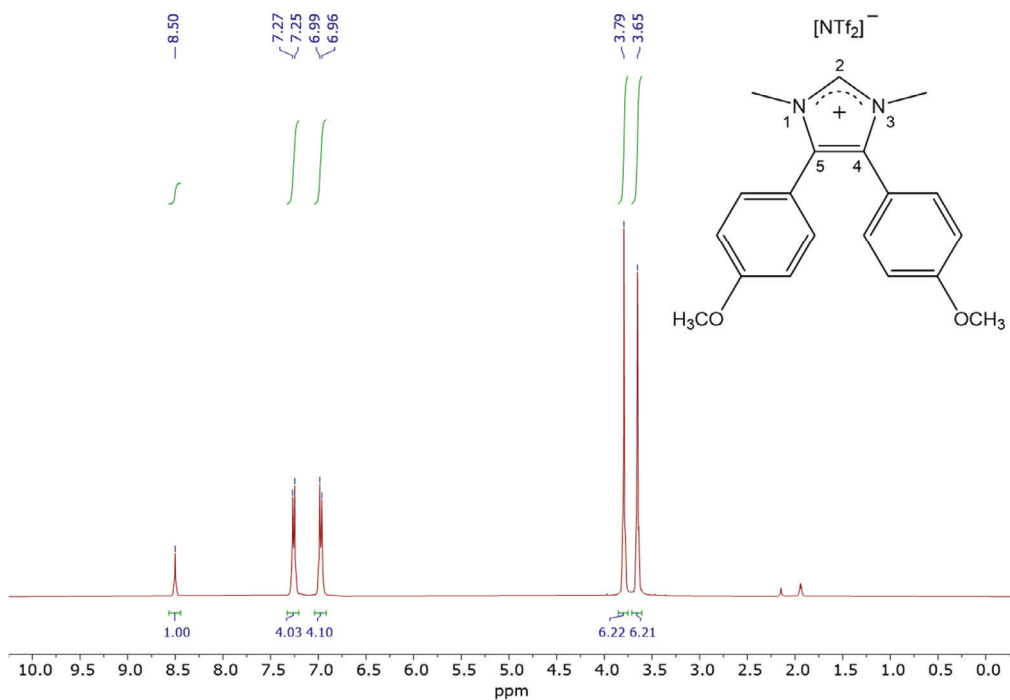


**Figure S4.13.**  $^1\text{H}$  NMR spectrum of 1,3-dimethyl-4,5-bis(4-methoxyphenyl)imidazolium bis(trifluoromethane)sulfonamide in CD<sub>3</sub>CN.

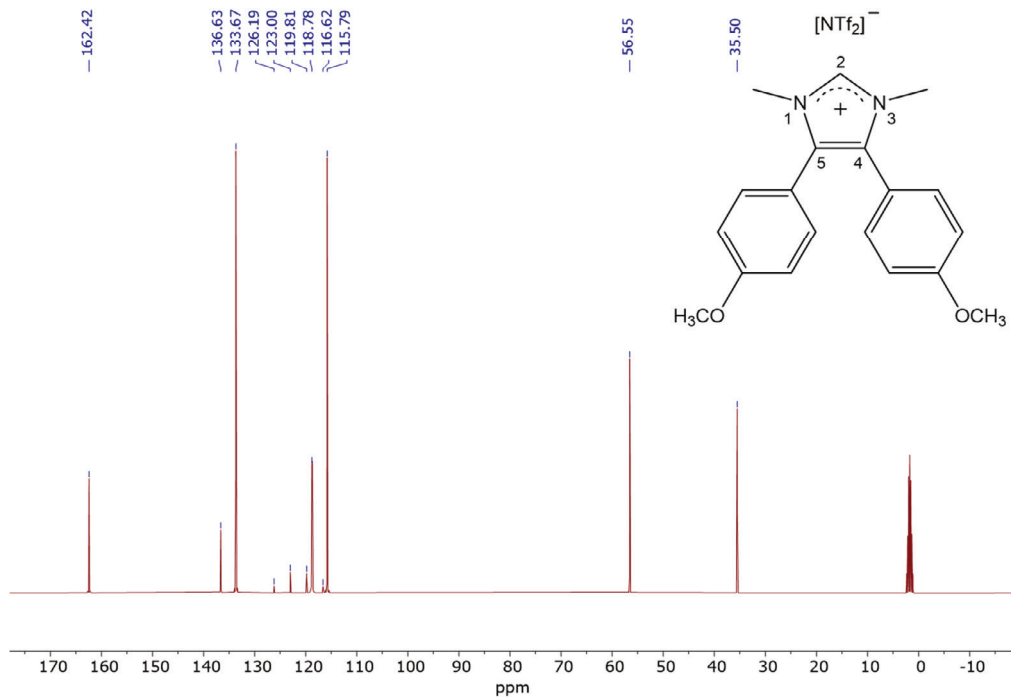


**Figure S4.14.**  $^{13}\text{C}$  NMR spectrum of 1,3-dimethyl-4,5-bis(4-methoxyphenyl)imidazolium bis(trifluoromethane)sulfonamide in CD<sub>3</sub>CN.

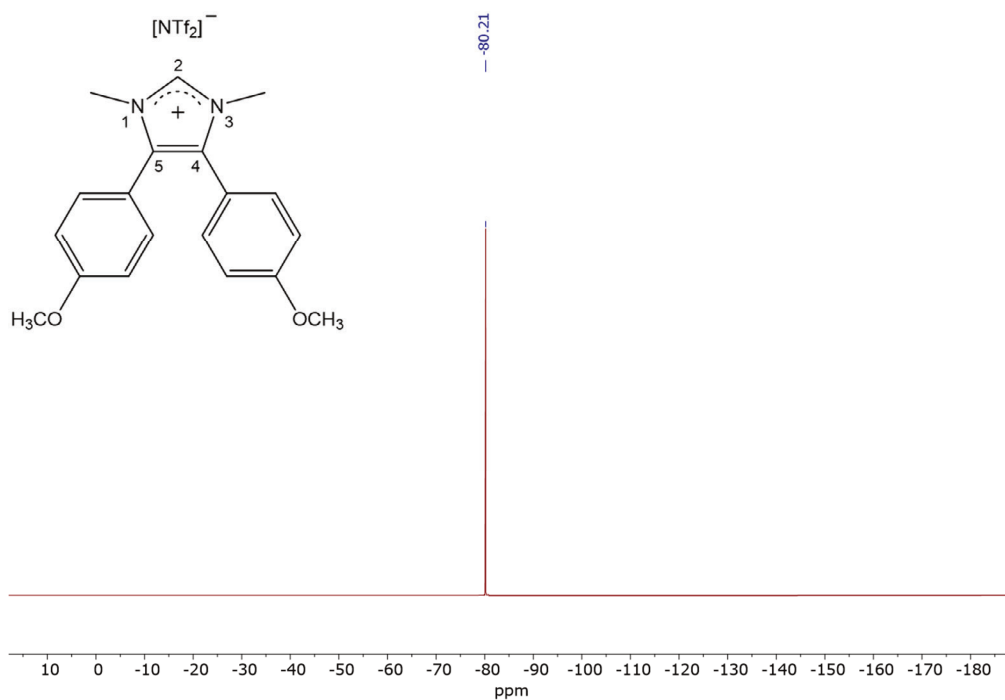


**Figure S4.15.**  $^{19}\text{F}$  NMR spectrum of 1,3-dimethyl-4,5-bis(4-methoxyphenyl)imidazolium bis(trifluoromethane)sulfonamide in  $\text{CD}_3\text{CN}$ .

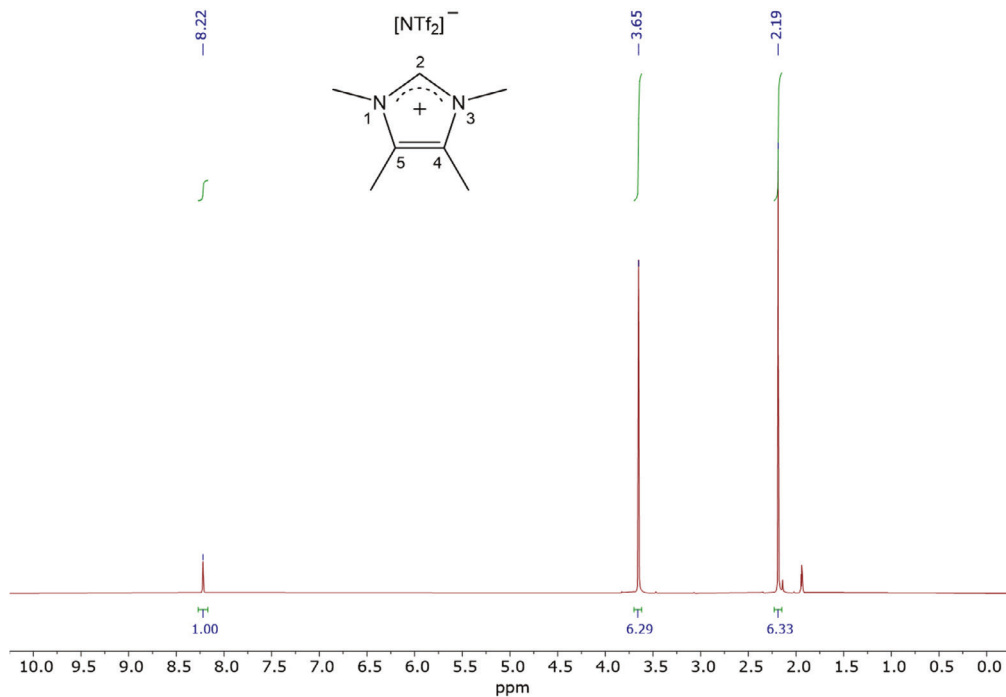


**Figure S4.16.**  $^1\text{H}$  NMR spectrum of 1,3,4,5-tetramethylimidazolium bis(trifluoromethane)sulfonamide in  $\text{CD}_3\text{CN}$ .

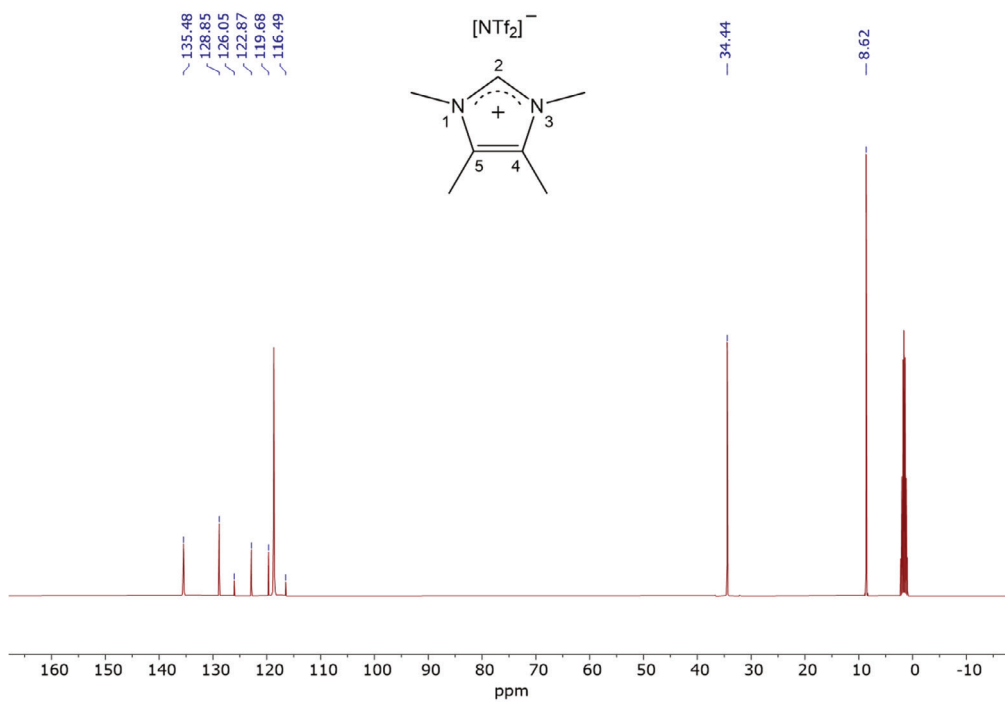


**Figure S4.17.**  $^{13}\text{C}$  NMR spectrum of 1,3,4,5-tetramethylimidazolium bis(trifluoromethane)sulfonamide in  $\text{CD}_3\text{CN}$ .

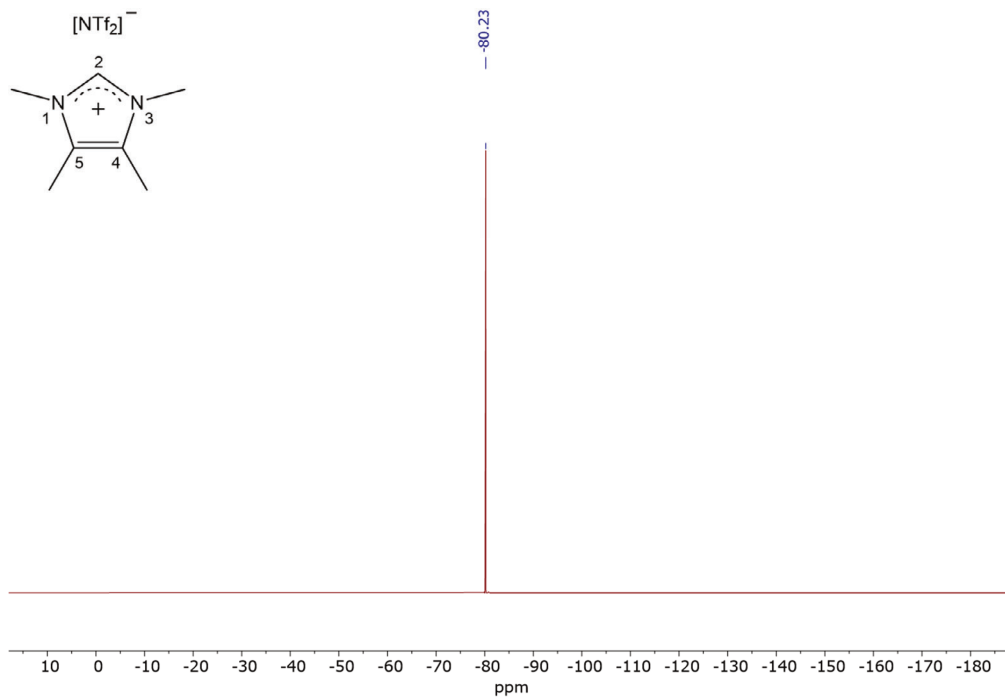


**Figure S4.18.**  $^{19}\text{F}$  NMR spectrum of 1,3,4,5-tetramethylimidazolium bis(trifluoromethane)sulfonamide in  $\text{CD}_3\text{CN}$ .

## II. Computational methods

The computational methods employed for DFT analysis are detailed in Chapter 3. To calculate atomic charges and electron density maps, the Voronoi Deformation Density (VDD) method developed by Matthias Bickelhaupt et al.<sup>95</sup> was utilized. Unlike other charge calculation methods, the VDD method does not rely on explicit basis functions. Instead, it determines the transfer of electronic density to or from specific atoms based on bond formation. This approach has been demonstrated to yield more chemically meaningful charges compared to other methods, such as Bader charges, which can result in extreme values and even exhibit ionic character in covalent bonds.

## III. Materials

Anhydrous acetonitrile (99.8%), acetonitrile (ReagentPlus, 99%), dichloromethane (puriss p.a. ACS reagent  $\geq 99.9\%$ ), diethyl ether (anhydrous, ACS reagent,  $\geq 99.0\%$ ), bis(trifluoromethane)sulfonimide lithium salt (99%), silver trifluoromethanesulfonate ( $\geq 99\%$ ), acetonitrile- $d_3$  ( $\geq 99.8$  atom % D), dimethyl sulfoxide- $d_6$  (99.9 atom % D), iodomethane ( $\geq 99.0\%$ ), 4,5-diphenylimidazole (98%), potassium hydride (30 wt% dispersion in mineral oil) and indene ( $\geq 99\%$ ) were obtained from Sigma-Aldrich. Acetonitrile- $d_3$  (99.8 atom % D) for electrolysis experiments was obtained from Acros Organics. 4,5-Dichloroimidazole ( $>97.0\%$ ) was obtained from TCI Europe N.V. 1,3-Dimethylimidazolium bis(trifluoromethylsulfonyl)imide (99%) was purchased from Iolitec Ionic Liquids Technologies GmbH. Milli-Q water was taken from a Milli-Q Advantage A10 Water Purification System, Millipore. 1,3-Dimethyl-4,5-dichloroimidazolium iodide was prepared according to a published procedure with some modifications<sup>96</sup>. 1,3,4,5-

Tetramethylimidazolium iodide and 1,3,4,5-tetramethylimidazolium bis(trifluoromethane)sulfonimide were prepared according to a published procedure<sup>97</sup>.

#### IV. Synthetic procedures

**NMR Characterization.** 400 MHz <sup>1</sup>H, 101 MHz <sup>13</sup>C and 376 MHz <sup>19</sup>F NMR spectra were recorded on a Bruker Avance III 400 NMR spectrometer in CD<sub>3</sub>CN. Solvent residual signals with chemical shifts of 1.94 ppm (<sup>1</sup>H NMR) and 118.69 ppm (<sup>13</sup>C NMR) were used as reference. For DMSO-d<sub>6</sub>, a chemical shift of 39.52 ppm was taken as a reference in <sup>13</sup>C NMR measurements.

**1,3-Dimethyl-4,5-dichloroimidazolium iodide.** 4,5-Dichloroimidazole (10.67 g, 77.90 mmol) was dissolved in CH<sub>3</sub>CN (150 mL) in a 500 mL round bottom flask equipped with a reflux condenser. Sodium hydrogen carbonate (9.82 g, 116.9 mmol) and excess iodomethane (20 mL, 0.321 mol) were added and the mixture was stirred at 85 °C under N<sub>2</sub> for 48 h. Iodomethane and CH<sub>3</sub>CN were removed using a rotary evaporator. To the solid residue, CH<sub>3</sub>CN (150 mL) was added to redissolve the imidazolium iodide. After stirring, the formed salts were left to settle. The clear solution was transferred to a 1L round bottom flask and the remaining solids were washed with CH<sub>3</sub>CN (3x50 mL). Evaporation of CH<sub>3</sub>CN from the combined solutions yielded 4,5-dichloro-1,3-dimethylimidazolium iodide (22.36 g, 98%). Of this batch, 6.32 g was dissolved in CH<sub>3</sub>CN (50 mL), requiring slight warming (40 °C). Diethyl ether (200 mL) was added under stirring, producing a white precipitate. The solvent was removed by syringe, the solids were washed three times with diethyl ether (3x100 mL) which was also removed and the remaining solid was dried under vacuum. Yield 6.13 g (97%).

<sup>1</sup>H NMR (400 MHz, CD<sub>3</sub>CN): δ 9.29 (s, 1H, 2-H), 3.83 (s, 6H, 1+3-CH<sub>3</sub>). <sup>13</sup>C NMR (101 MHz, CD<sub>3</sub>CN): δ 137.18 (2-C), 121.00 (4+5-C), 36.49 (1+3-C).



**1,3-Dimethyl-4,5-dichloroimidazolium bis(trifluoromethane)sulfonamide.** A conical flask equipped with a stirring bar was charged with 4,5-dichloro-1,3-dimethylimidazolium iodide (6.01 g, 20.52 mmol). Milli-Q water (20 mL) was added, followed by LiNTf<sub>2</sub> (6.48 g, 22.57 mmol, 1.1 eq.) and CH<sub>3</sub>CN (20 mL). After stirring for 24 h, CH<sub>3</sub>CN was removed by a slow flow of N<sub>2</sub>, CH<sub>2</sub>Cl<sub>2</sub> (20 mL) was added to dissolve the imidazolium NTf<sub>2</sub> salt and the layers were transferred to a separation funnel. Some Milli-Q water (20 mL) was added and the aqueous layer was extracted four times with CH<sub>2</sub>Cl<sub>2</sub> (4x100 mL). The combined organic layers were washed with Milli-Q water (20 mL) to remove last traces of LiNTf<sub>2</sub> and dried on Na<sub>2</sub>SO<sub>4</sub>. After evaporation of CH<sub>2</sub>Cl<sub>2</sub> and further drying under vacuum, the product was obtained as a white solid. Yield 8.97 g (98%).

<sup>1</sup>H NMR (400 MHz, CD<sub>3</sub>CN): δ 8.53 (s, 1H, 2-H), 3.79 (s, 6H, 1+3-CH<sub>3</sub>). <sup>13</sup>C NMR (101 MHz, CD<sub>3</sub>CN): δ 136.80 (2-C), 125.98 (NTf<sub>2</sub>), 122.80 (NTf<sub>2</sub>), 121.34 (4+5-C), 119.61 (NTf<sub>2</sub>), 116.43 (NTf<sub>2</sub>), 36.16 (1+3-C). <sup>19</sup>F NMR (376 MHz, CD<sub>3</sub>CN): δ -80.22.

**1,3-Dimethyl-4,5-diphenylimidazolium iodide.** 4,5-Diphenylimidazole (10.0 g, 45.4 mmol) was dissolved in CH<sub>3</sub>CN (150 mL) in a 500 mL round bottom flask equipped with a reflux condenser. Sodium hydrogen carbonate (5.72 g, 68.1 mmol) and excess iodomethane (20 mL, 0.321 mol) were added and the mixture was stirred at 40 °C under N<sub>2</sub> for 7 days. Iodomethane and CH<sub>3</sub>CN were removed using a rotary evaporator. To the solid residue, CH<sub>2</sub>Cl<sub>2</sub> (150 mL) was added to redissolve the imidazolium iodide. After stirring, the formed salts were left to settle. The clear solution was transferred to a 1L round bottom flask and the remaining solids were washed with CH<sub>2</sub>Cl<sub>2</sub> (3x50 mL). The CH<sub>2</sub>Cl<sub>2</sub> solution was dried on Na<sub>2</sub>SO<sub>4</sub>, filtered, and concentrated to 70 mL, then diethyl ether (220 mL) was added under stirring. After settling of the solid imidazolium salt, the liquid layer was removed by syringe. Diethyl ether (150 mL) was added, the suspension was stirred and the ether was removed. The solid imidazolium salt

was washed three times with diethyl ether (3x100 mL) and then dried under vacuum. Yield 16.70 g (98%).

$^1\text{H}$  NMR (400 MHz,  $\text{CD}_3\text{CN}$ ):  $\delta$  8.95 (s, 1H, 2-H), 7.52-7.30 (m, 10H, Ph), 3.71 (s, 6H, 1+3- $\text{CH}_3$ ).  $^{13}\text{C}$  NMR (101 MHz,  $\text{CD}_3\text{CN}$ ):  $\delta$  137.34 (2-C), 133.58, 132.23, 131.56, 130.27, 126.69, 35.84 (1+3-C).

**1,3-Dimethyl-4,5-diphenylimidazolium bis(trifluoromethane)sulfonamide.** A conical flask equipped with a stirring bar was charged with 4,5-diphenyl-1,3-dimethylimidazolium iodide (11.90 g, 31.63 mmol). Milli-Q water (20 mL) was added, followed by  $\text{LiNTf}_2$  (10.0 g, 34.83 mmol, 1.1 eq.) and  $\text{CH}_3\text{CN}$  (20 mL). After stirring for 24 h,  $\text{CH}_3\text{CN}$  was removed by a slow flow of  $\text{N}_2$ ,  $\text{CH}_2\text{Cl}_2$  (20 mL) was added to dissolve the imidazolium  $\text{NTf}_2$  salt and the layers were transferred to a separation funnel. Some Milli-Q water (20 mL) was added and the aqueous layer was extracted four times with  $\text{CH}_2\text{Cl}_2$  (4x100 mL). The combined organic layers were washed with Milli-Q water (20 mL) to remove last traces of  $\text{LiNTf}_2$  and dried on  $\text{Na}_2\text{SO}_4$ . After evaporation of  $\text{CH}_2\text{Cl}_2$  and further drying under vacuum, the product was obtained as a white solid. Yield 16.58 g (99%).

$^1\text{H}$  NMR (400 MHz,  $\text{CD}_3\text{CN}$ ):  $\delta$  8.55 (s, 1H, 2-H), 7.53-7.30 (m, 10H, Ph), 3.68 (s, 6H, 1+3- $\text{CH}_3$ ).  $^{13}\text{C}$  NMR (101 MHz,  $\text{CD}_3\text{CN}$ ):  $\delta$  137.09 (2-C), 133.80, 132.12, 131.65, 130.34, 126.62, 126.12 ( $\text{NTf}_2$ ), 122.93 ( $\text{NTf}_2$ ), 119.74 ( $\text{NTf}_2$ ), 116.55 ( $\text{NTf}_2$ ), 35.57 (1+3-C).  $^{19}\text{F}$  NMR (376 MHz,  $\text{CD}_3\text{CN}$ ):  $\delta$  -80.19.

**1,3-Dimethyl-4,5-bis(4-methoxyphenyl)imidazolium iodide.** 4,5-Bis(4-methoxyphenyl)imidazole (3.31 g, 11.81 mmol) was dissolved in a mixture of  $\text{CH}_3\text{CN}$  (100 mL) and tetrahydrofuran (10 mL) in a 500 mL round bottom flask equipped with a reflux condenser. Sodium hydrogen carbonate (1.488 g, 17.7 mmol) and excess iodomethane (10 mL, 0.16 mol) were added and the mixture was stirred at 40 °C under  $\text{N}_2$  for 7 days. Iodomethane and  $\text{CH}_3\text{CN}$  were removed using a rotary evaporator. To the solid residue,  $\text{CH}_2\text{Cl}_2$  (100 mL)

was added to redissolve the imidazolium iodide. After stirring, the formed salts were left to settle. The clear solution was transferred to a 1L round bottom flask and the remaining solids were washed with CH<sub>2</sub>Cl<sub>2</sub> (3x50 mL). The CH<sub>2</sub>Cl<sub>2</sub> solution was dried on Na<sub>2</sub>SO<sub>4</sub>, filtered, and concentrated to 70 mL, then diethyl ether (220 mL) was added under stirring. After settling of the solid imidazolium salt, the liquid layer was removed by syringe. Diethyl ether (150 mL) was added, the suspension was stirred, and the ether was removed. The remaining imidazolium salt was washed three times with diethyl ether (3x100 mL) and then dried under vacuum. Yield 5.05 g (98%).

<sup>1</sup>H NMR (400 MHz, CD<sub>3</sub>CN): δ 8.90 (s, 1H, 2-H), 7.27 (d, *J* = 8.8 Hz, 4H, Ph), 6.97 (d, *J* = 8.8 Hz, 4H, Ph), 3.79 (s, 6H, OCH<sub>3</sub>), 3.67 (s, 6H, 1+3-CH<sub>3</sub>). <sup>13</sup>C NMR (101 MHz, CD<sub>3</sub>CN): δ 162.13, 136.92 (2-C), 133.70, 133.24, 115.61, 56.63 (OCH<sub>3</sub>), 35.69 (1+3-C).

### **1,3-Dimethyl-4,5-bis(4-methoxyphenyl)imidazolium bis(trifluoromethane)sulfonamide.**

A conical flask equipped with a stirring bar was charged with 4,5-di(4-methoxy)phenyl-1,3-dimethylimidazolium iodide (4.50 g, 10.31 mmol). Milli-Q water (20 mL) was added, followed by LiNTf<sub>2</sub> (3.26 g, 11.35 mmol, 1.1 eq.) and CH<sub>3</sub>CN (20 mL). After stirring for 24 h, CH<sub>3</sub>CN was removed by a slow flow of N<sub>2</sub>, CH<sub>2</sub>Cl<sub>2</sub> (20 mL) was added to dissolve the imidazolium NTf<sub>2</sub> salt and the layers were transferred to a separation funnel. Some Milli-Q water (20 mL) was added and the aqueous layer was extracted four times with CH<sub>2</sub>Cl<sub>2</sub> (4x100 mL). The combined organic layers were washed with Milli-Q water (20 mL) to remove last traces of LiNTf<sub>2</sub> and dried on Na<sub>2</sub>SO<sub>4</sub>. After evaporation of CH<sub>2</sub>Cl<sub>2</sub> and further drying under vacuum, the product was obtained as a viscous amber oil. Yield 6.08 g (100%).

<sup>1</sup>H NMR (400 MHz, CD<sub>3</sub>CN): δ 8.50 (s, 1H, 2-H), 7.26 (d, *J* = 8.8 Hz, 4H, Ph), 6.97 (d, *J* = 8.9 Hz, 4H, Ph), 3.79 (s, 6H, OCH<sub>3</sub>), 3.65 (s, 6H, 1+3-CH<sub>3</sub>). <sup>13</sup>C NMR (101 MHz, CD<sub>3</sub>CN): δ 162.42, 136.63 (2-C),

133.67, 126.19 (NTf<sub>2</sub>), 123.00 (NTf<sub>2</sub>), 119.81 (NTf<sub>2</sub>), 118.78, 116.62 (NTf<sub>2</sub>), 115.79, 56.55 (OCH<sub>3</sub>), 35.50 (1+3-C). <sup>19</sup>F NMR (376 MHz, CD<sub>3</sub>CN):  $\delta$  -80.21.

**1,3,4,5-Tetramethylimidazolium iodide.** <sup>1</sup>H NMR (400 MHz, CD<sub>3</sub>CN):  $\delta$  8.62 (s, 1H, 2-H), 3.69 (s, 6H, 1+3-CH<sub>3</sub>), 2.19 (s, 6H, 4+5-CH<sub>3</sub>). <sup>13</sup>C NMR (101 MHz, DMSO-d<sub>6</sub>):  $\delta$  134.66 (2-C), 126.71 (4+5-C), 33.35 (1+3-C), 7.91 (4+5-CH<sub>3</sub>).

**1,3,4,5-Tetramethylimidazolium bis(trifluoromethane)sulfonamide.** <sup>1</sup>H NMR (400 MHz, CD<sub>3</sub>CN):  $\delta$  8.22 (s, 1H, 2-H), 3.65 (s, 6H, 1+3-CH<sub>3</sub>), 2.19 (s, 6H, 4+5-CH<sub>3</sub>). <sup>13</sup>C NMR (101 MHz, CD<sub>3</sub>CN):  $\delta$  135.48 (2-C), 128.85 (4+5-C), 126.05 (NTf<sub>2</sub>), 122.87 (NTf<sub>2</sub>), 119.68 (NTf<sub>2</sub>), 116.49 (NTf<sub>2</sub>), 34.44 (1+3-C), 8.62 (4+5-CH<sub>3</sub>). <sup>19</sup>F NMR (376 MHz, CD<sub>3</sub>CN):  $\delta$  -80.23.

## V. Determining the pK<sub>a</sub> of DiPh cation

Information on the acidity of imidazolium cations can be obtained by exposing such cations to anions with a known basicity. If its basicity is sufficiently high, the anion will acquire a proton from the imidazolium cation. This process can be monitored using <sup>1</sup>H NMR spectroscopy<sup>70</sup>. Here, the indenyl anion was selected to act as a base and indicator anion. DMSO-d<sub>6</sub> was deprotonated using potassium hydride, and to the resulting potassium dimethyl (CH<sub>3</sub>S(=O)-CH<sub>2</sub>K) solution, indene was added, yielding a green solution of indenylpotassium in DMSO-d<sub>6</sub>. Indene is known to have a pK<sub>a</sub> of 20.1 in DMSO<sup>98</sup>. Treatment of **DiPh** with a 1:1 mixture of indene (1 eq.) and indenylpotassium (1 eq.) led to a rapid color change from green to dark purple, indicating the formation of **DiPh** carbene. A <sup>1</sup>H NMR spectrum of this reaction mixture (**Figure S4.19**, bottom) showed a strong decrease in signal intensity of peaks at  $\delta$  = 5.8, 6.27 and 7.15 ppm, associated with the indenyl anion<sup>99</sup>. This demonstrates that the pK<sub>a</sub> of **DiPh** has a value lower than 20.1. Interestingly, since the DMSO pK<sub>a</sub> value of **MM** is 22.0<sup>70</sup>, we can conclude that the C2-proton acidity of **DiPh** is higher than that of **MM**.

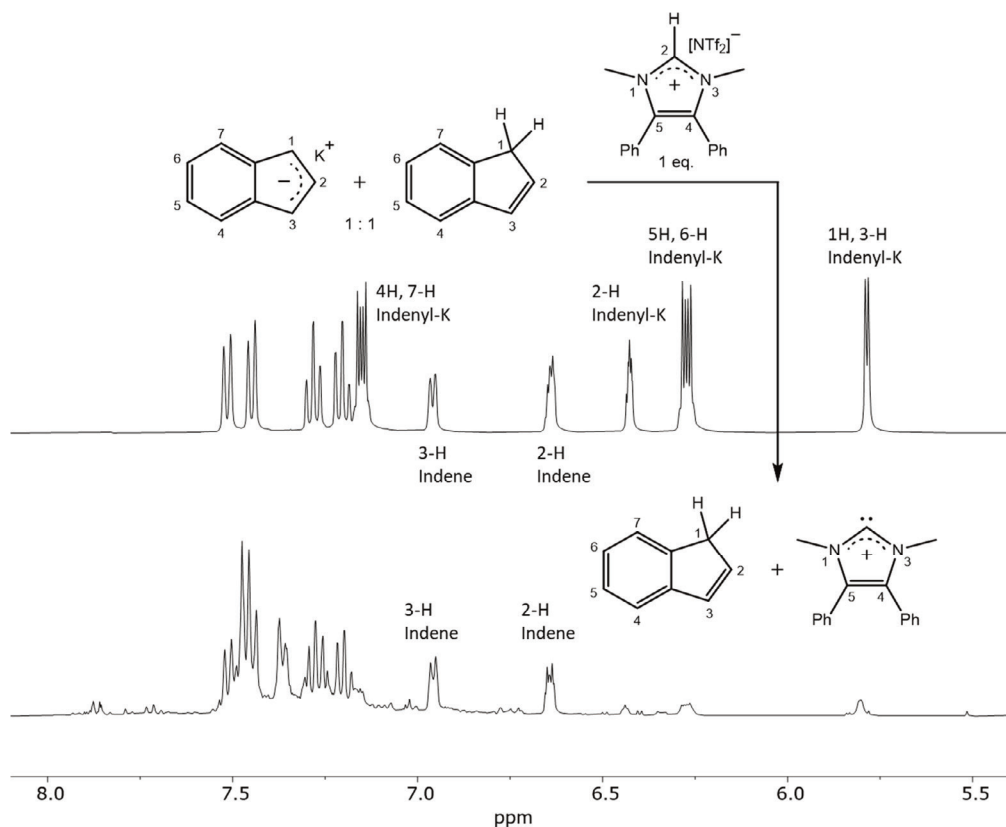


**Figure S4.19.** <sup>1</sup>H NMR spectra of indene and indenyl anion in a 1:1 ratio (top) and after reaction of this mixture with **DiPh** (bottom). The indenyl anion is sufficiently basic to deprotonate **DiPh**, as is evident from the disappearance of the indenyl anion signals in the bottom NMR spectrum.

### Investigation of the C2-proton acidity of DiPh by <sup>1</sup>H NMR spectroscopy

Potassium hydride was washed five times with anhydrous toluene in a glove box containing pre-purified nitrogen to remove mineral oil. The cleaned KH was subsequently dried under vacuum. In the glove box, a vial was charged with KH (0.25 mmol) and DMSO-d<sub>6</sub> (1.0 mL) was added. After H<sub>2</sub> evolution had ceased, indene (0.5 mmol) was added, resulting in a green solution, indicative of indenyl anion formation. After reaction, the solution contained indene (0.25 mmol) and indenyl anion (0.25 mmol). A <sup>1</sup>H NMR spectrum of this solution was recorded. Of the solution, 0.25 mL was taken and added to another vial. To this vial, 0.5 mL of DMSO-

$d_6$  containing  $6.25 \cdot 10^{-5}$  mol of **DiPh** was added, and 0.25 mL of DMSO- $d_6$  to reach a total volume of 1.0 mL. The solution used for  $^1\text{H}$  NMR measurements thus contained 62.5 mM of indene, indenyl anion, and **DiPh** when reaction between the indenyl anion and **DiPh** commenced.

## VI. Discussion of acidity trends in C4, C5-substituted cations

Table S4.1. VDD Atomic Charges of the Imidazolium Ions

Atom	MM	DiCl	DiPh	DiMeOPh	TetraMe
N1, N3	0.020	0.021	0.017		0.012
C2-H	0.135	0.144	0.136		0.127
C2	0.095	0.102	0.092		0.085
C4, C5	-0.007	0.052	0.021		0.016

As mentioned earlier, imidazolium ions are converted into carbenes when treated with a sufficiently strong base. In the corresponding *N*-heterocyclic carbenes, the carbene moiety is stabilized by lone pairs from the adjacent nitrogen atoms. Substituents at the imidazolium ring play an important role in stabilizing the carbene. The first air-stable carbene, 1,3-dimesityl-4,5-dichloroimidazol-2-ylidene, owed its stability to the presence of chlorine atoms at C4 and C5. Its stability was attributed to the inductive electron-withdrawing effect of the chlorine substituents, which reduce electron density on the C2 carbon atom that bears the carbene lone pair<sup>100</sup>. As electron withdrawing substituents stabilize carbenes generated from imidazolium ions, it may be expected that such substituents also facilitate proton removal from the imidazolium C2 and thus lead to more acidic C2 hydrogen atoms. When comparing VDD atomic charges<sup>101</sup> calculated for **MM** and **DiCl**, a higher positive charge is found at C2 of **DiCl** and also its C2 hydrogen atom bears a higher positive charge (**Table S4.1**). This suggests that C2-H of the electron-poor **DiCl** will be more acidic than C2-H of **MM**. **DiPh** shows atomic charges at C2 and at the C2 hydrogen atom that are lower than the charges at **DiCl** and more similar to **MM**, suggesting a closer C2-H acidity for **MM** and **DiPh** cations. Although the overall charge density of the ring, including C4 and C5, displays a larger localized positive charge for **DiPh** compared to **MM** cation (0.266 for **DiPh** versus 0.243 for **MM**) which should

lead to higher acidity as was also discussed in **Section V**. Compared to these imidazolium ions, **TetraMe** has a lower positive charge at C2 and the C2 hydrogen atom, indicating a lower acidity for this more electron-rich imidazolium ion. The acidity order based on VDD atomic charge calculations therefore is **DiCl** > **DiPh** ≥ **MM** > **TetraMe**. <sup>13</sup>C NMR spectroscopy is known to be a valuable tool for investigating charge density distributions in conjugated systems. In **Chapter 3**, we explored the influence of alkyl substituents at the N1 and N3 ring positions of imidazolium ions on the electron density at C2 by comparing <sup>13</sup>C NMR chemical shifts of this atom. Substituents ranging from methyl to tert-butyl led to C2 chemical shifts of 137.85 ppm (**MM**) to 132.88 ppm (**t-Bu t-Bu**), and thus to a range of 5 ppm (**Figure S4.20**). When introducing substituents at C4 and C5, however, the observed range in chemical shifts of the C2 carbon atom is relatively narrow (2.4 ppm), namely from 137.85 ppm (**MM**) to 135.48 ppm (**TetraMe**). This indicates that the more remotely located substituents at C4 and C5 do not have as large an influence on the <sup>13</sup>C chemical shift of C2 as substituents at N1 and N3. Within the same family of substituents, such as phenyl groups, adding a para substituent like methoxy should lead to C2 shift changes that can be rationalized. This is the case, but even here the C2 chemical shift difference induced by the probably weakly withdrawing phenyl- and the strongly donating methoxyphenyl-groups in the imidazolium ions is minimal (0.46 ppm). It must be noted that due to their size, the phenyl groups are not fully in plane with the imidazolium ring, which may limit their influence on its charge distribution. Expectations about C2–H acidity can partly be correlated with the results of the <sup>13</sup>C NMR measurements. For example, the electron-poor **DiCl** is expected to be more acidic than the electron-rich **TetraMe**, which matches with the higher C2 shift value of **DiCl**. The higher chemical shift value of the **DiPh** C2 compared to that of **DiMeOPh** also is in accord with expectations. However, **DiCl** and **DiPh** are both expected to be more electron-poor than **MM**, which is not evident from the <sup>13</sup>C NMR results. Therefore, additional work is needed to establish the (order of) acidity of these imidazolium



cations, for example by exposing these to an anion with a known basicity and using NMR to gauge whether deprotonation occurs or not. Such an experiment was performed with **DiPh**.

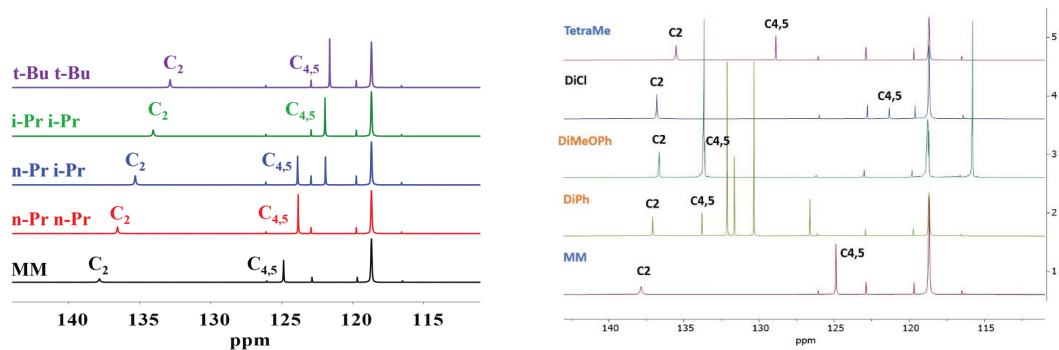
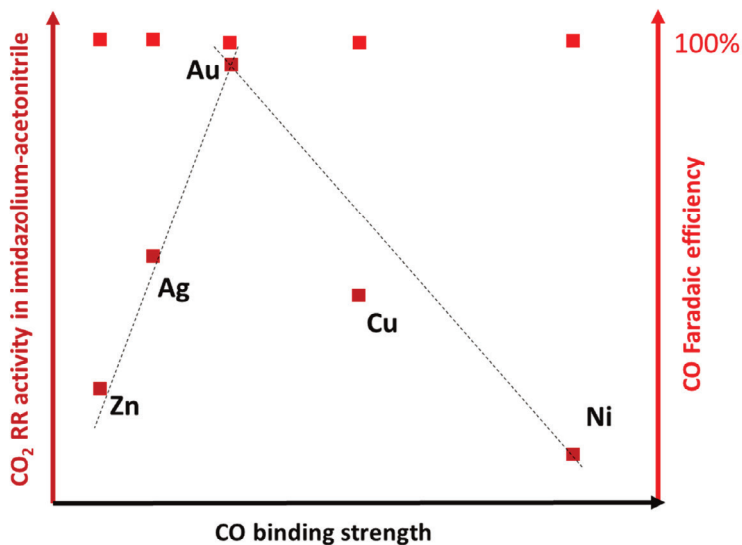


**Figure S4.20.** Comparison of <sup>13</sup>C NMR spectra for 1,3-dialkyl substituted imidazolium cations (left) with those of 4,5-substituted imidazolium cations recorded in CD<sub>3</sub>CN. NTf<sub>2</sub> was the common counter anions used in all measurements.



## Chapter 5:

### Exploring the Structure-Activity Relationship of Late-Transition Metal Catalysts in Imidazolium-Assisted Electrochemical CO<sub>2</sub> Reduction



*This chapter is partially based on: S. Neyrizi, M. A. Hempenius, G. Mul, The Performance of Transition Metals in Imidazolium-Assisted CO<sub>2</sub> Reduction in Acetonitrile. ChemElectroChem. 2023. Accepted.*

## Summary

Electrochemical reduction of CO<sub>2</sub> is extensively studied and trends in the activity of transition metals in aqueous electrolytes have been well established on the basis of differences in CO binding strength. This chapter shows a similar trend (volcano curve) for late-transition metals (Au, Ag, Zn, Cu, and Ni) in dry acetonitrile containing 1,3-dimethyl imidazolium cations, but with smaller performance factors between the late-transition metals and Au than previously determined in aqueous conditions. Moreover, all catalysts exhibit close to 100% selectivity to CO in non-aqueous process conditions. For metals providing a relatively low CO desorption energy in comparison to Au (Ag, Zn), adsorption of CO<sub>2</sub> is proposed to be rate-determining, confirmed by DFT calculations. The high CO desorption energy calculated for Cu and Ni, likely limits the activity observed in reduction of CO<sub>2</sub>. The results of this study imply that metals unsuited for aqueous conditions, hold promise for cost-effective and practically feasible electrochemical conversion of CO<sub>2</sub> to CO in imidazolium containing non-aqueous media. While this study finds that the selectivity remains unchanged under anhydrous MM-acetonitrile electrolyte conditions, it underscores the continued significance of the electronic properties of the catalysts in determining the overall rate of CO<sub>2</sub> reduction

## Introduction

In **Chapter 3**, we investigated the role of imidazolium cation in enhancing the performance of CO<sub>2</sub> reduction in non-aqueous media by highlighting the coordination of the C2-proton to the adsorbed CO<sub>2</sub>, facilitating electron transfer and the first reduction step. It was also demonstrated that the 1,3-dimethyl imidazolium cation (**MM**) showed close to the best performance among cations studied.

Several studies have investigated the performance of electrodes other than Au under non-aqueous conditions. For instance, Vera et al.<sup>47</sup> achieved a high Faradaic efficiency (FE) of up to 90% for oxalic acid formation during CO<sub>2</sub> reduction on a lead electrode in various non-aqueous solvents. Meanwhile, Sacci et al.<sup>102</sup> attempted to improve the performance of CO<sub>2</sub> reduction using CuSn alloys in a mixture of acetonitrile (MeCN) and butyl-methyl imidazolium cation but reported a low FE for CO formation (below 40%), likely due to difficulties in controlling the water content. In situ spectro-electrochemical studies by Koper et al.<sup>21</sup> investigated CO formation on a Cu electrode in MeCN, but the concomitant reduction of water at various overpotentials may have affected the results. Additionally, the analysis did not permit the determination of FEs, limiting the ability to draw conclusions about the reaction efficiency.

To overcome the current limitations and advance our understanding of CO<sub>2</sub> reduction in non-aqueous media, here electrochemical experiments involving different transition metals besides gold are considered, in a carefully controlled acetonitrile solution containing 1,3-dimethyl imidazolium (**MM**) cation as co-catalyst. By examining the catalytic activity of transition metals and utilizing density functional theory (DFT) calculations, insights will be provided into the rate-determining steps and mechanism involved in CO<sub>2</sub> reduction in non-aqueous media. Finally, we compare the observed volcano trend in non-aqueous and aqueous conditions, and

discuss (quantitative) differences on the basis of the role of the imidazolium cations in stimulating reduction of CO<sub>2</sub>.

## Results and discussion

**Figure 5.1** presents the results of CO<sub>2</sub> electrolysis for five polycrystalline electrodes. The chronopotentiometry curves showing the potential vs time are depicted for 0.5 mol% 1,3-dimethylimidazolium bis(trifluoromethylsulfonyl)imide (**MM NTf<sub>2</sub>**) in acetonitrile (MeCN), with anhydrous conditions ensured via a rigorous protocol (for further details, refer to the experimental protocols described in **Chapter 2**). All five metals (Ni, Cu, Au, Ag, and Zn) exhibit close to 100% Faradaic efficiency (FE) to CO.

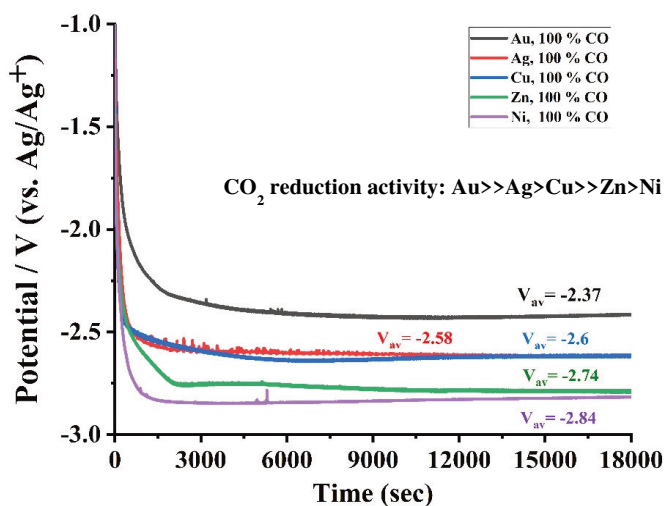


**Figure 5.1.** Electrolysis results for CO<sub>2</sub> reduction at -1 mA/cm<sup>2</sup> for 5 different transition metal catalysts in anhydrous acetonitrile. 0.5 mol% of **MM NTf<sub>2</sub>** was used as both electrolyte and co-catalyst. Additional information regarding gas analysis and evaluation of Faradaic efficiencies can be found in Supporting Information.

We also evaluated the performance of an Fe electrode (**Supporting Information Figure S5.6**).

The Fe electrode is almost inactive for CO<sub>2</sub> reduction in the imidazolium-anhydrous MeCN electrolyte, likely due to \*CO poisoning of the surface<sup>103</sup>. The current observed for Fe electrodes is likely caused by reduction of acetonitrile. A LSV in a similar potential range is

shown for the Zn electrode in **Figure S5.6**. The figure clearly shows a considerable difference in the potential-current profiles under CO<sub>2</sub> and He purge, with a notably larger Faradaic current around -2.0 V vs Ag/Ag<sup>+</sup> under CO<sub>2</sub> atmosphere, exclusively assigned to production of CO. The stability of the Ni electrode was visually assessed as shown in **Figure S5.5**. After 90 mins and after 10 hrs of electrolysis, the Ni surface appears clean and the solution is clear.

Although many studies have reported high FEs for CO formation using Ag and Au catalysts<sup>38, 71, 104</sup>, particularly in aqueous media, to our best knowledge, this is the first study to demonstrate close to 100% FE for CO formation with polycrystalline Ni, Zn, and Cu electrodes (Gas analysis and Faradaic efficiency evaluations can be found in **Supporting Information Section V**). The study also uncovers an intriguing trend in the CO<sub>2</sub> reduction activity of the various transition metal catalysts under near-steady-state conditions for 5 hours. In particular, Au exhibited the highest activity, requiring the lowest potential to achieve the same current density, while Cu and Ag displayed nearly identical potentials. Conversely, Zn and Ni demonstrated the lowest activity. This finding offers valuable insights into the efficacy of different metals as catalysts for CO<sub>2</sub> reduction in non-aqueous media. Jaramillo and co-workers performed a similar study in aqueous media, reporting CO<sub>2</sub> reduction activity for several transition metal catalysts<sup>7</sup>. In their study, Au and Ag were the only catalysts showing a FE greater than 90 percent for CO<sub>2</sub> reduction. Zn and Cu showed, respectively, 80% and 68% FE for products of CO<sub>2</sub> reduction (the remaining FE was assigned to the formation of H<sub>2</sub>), and Ni was reported to display a FE less than 5% for CO<sub>2</sub> reduction with most of the electrons utilized for H<sub>2</sub> evolution. Besides, Au and Ag were the only catalysts displaying FEs for CO formation at maximum levels of around 97% and 89%, respectively, at various potentials. Cu showed a very low FE for CO formation (around 1–2%), with 26% FE for ethylene and 24% FE for methane. In addition, a FE of 9.7% was reported for ethanol and 22.6% for H<sub>2</sub>. These results show that the combination of anhydrous MeCN and imidazolium cation studied in this work can outperform

common aqueous media for CO<sub>2</sub> reduction, in particular for metals active in H<sub>2</sub> formation. The drawback of using anhydrous media is that carbohydrates are not produced, and oxygenated products (such as EtOH) can only be formed in the presence of water.

To support results from electrolysis experiments, **Figure 5.2 (left)** shows the LSV results for all five catalysts under CO<sub>2</sub> atmosphere. Cu shows the lowest overpotential, but shows a distinctively different, shallow i-V curve. To further support the i-V curve of Cu electrode for CO<sub>2</sub> reduction, comparison of LSV results under He and CO<sub>2</sub> purging are also displayed (**Figure 5.2, right**). Although less evident, also for Ni the i-V curve is shallower in comparison to the other metals, with Au clearly showing the highest current densities at equivalent potentials. The shape of the LSV curves of Cu and Ni could suggest a possible difference in the CO<sub>2</sub> reduction mechanism for these two catalysts in comparison to the other metals investigated.

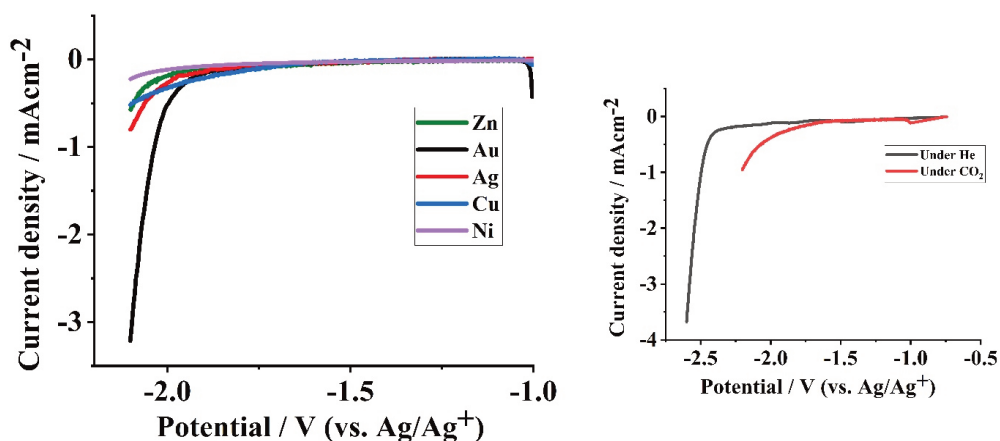


**Figure 5.2. Left:** LSV results for CO<sub>2</sub> reduction for 5 different transition metal catalysts in anhydrous acetonitrile. 0.5 mol% of MM NTf<sub>2</sub> was used as both electrolyte and co-catalyst. **Right:** comparison of LSV results for Cu electrode under He and CO<sub>2</sub> purging.

The results obtained during He purging (**Supporting Information Figure S5.7**) demonstrate a remarkably similar activity for Au, Zn, and Ni electrodes, with onset potentials at approximately



-2.4 V (vs. Ag/Ag<sup>+</sup>). This observation indicates that the reduction of imidazolium is not influenced by the nature of the electrode, suggesting it is most likely a non-catalytic reductive process. This reinforces the notion that the variation in CO<sub>2</sub> reduction activity among different transition metals should be explained by variations in the interaction of the electrode with the CO<sub>2</sub> (reactant) or CO (product) molecules. To further explore these differences, we employed DFT calculations to determine the desorption energies of CO for a range of metals. The results were then compared with CO<sub>2</sub> reduction activities obtained through experiments (as depicted in **Figure 5.3**). Upon analyzing the results presented in **Figure 5.3**, a volcano relationship was discovered between the strength of CO binding and the overall CO<sub>2</sub> reduction activities in anhydrous acetonitrile. Specifically, we observe that Au is located at the apex of the volcano, exhibiting an ideal binding strength for CO and demonstrating the highest CO<sub>2</sub> reduction activity among the catalysts tested. Previous studies have investigated the volcano-shaped activity trend for CO<sub>2</sub> reduction in aqueous media through DFT calculations<sup>15-16</sup>. These studies have shown a similar trend for CO<sub>2</sub> activation, albeit with lower faradaic efficiencies, as demonstrated by Jaramillo's work. One significant difference between this study and previous studies in aqueous media, which will be discussed in detail later, is the relative activities among the different catalysts, which do not align with those observed in previous studies in aqueous media.

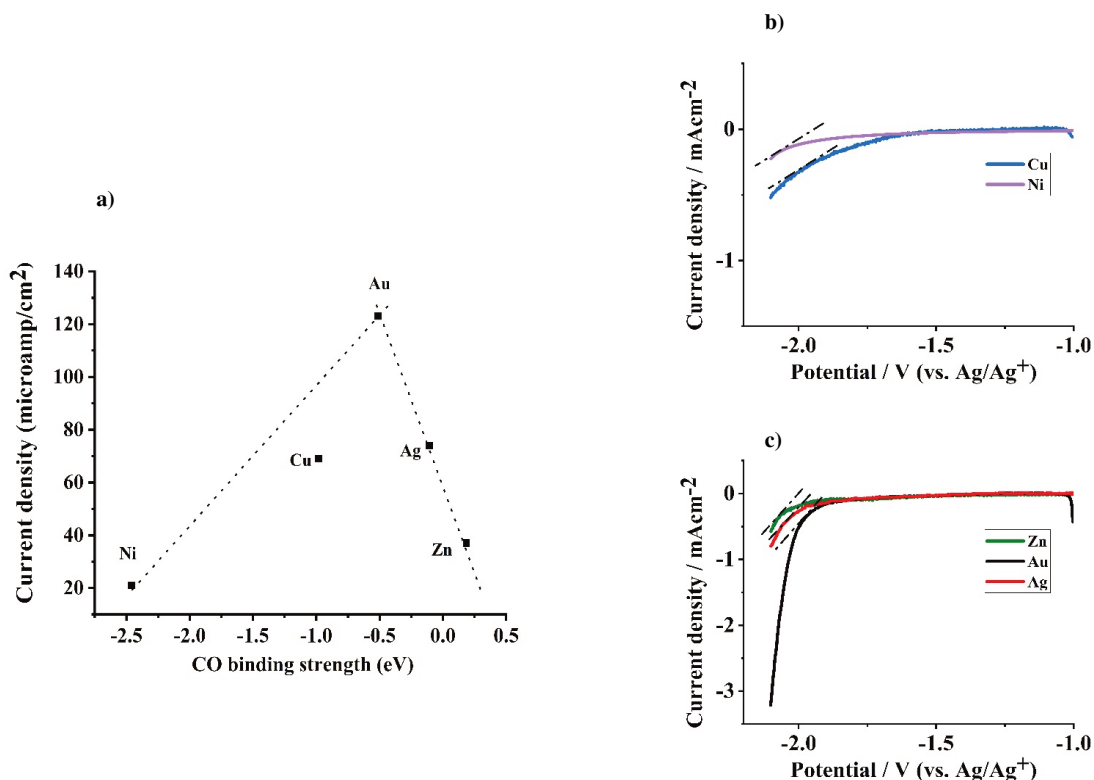


**Figure 5.3.** (a) Volcano plot illustrating current density obtained from chronoamperometry data under stirring conditions for CO<sub>2</sub> reduction at -2 V versus CO binding strength, results are normalized against geometric surface area, (b) LSVs for Ni and Cu electrodes; and (c) LSVs for Zn, Au, and Ag electrodes for CO<sub>2</sub> reduction in anhydrous acetonitrile in quiescent solutions with a CO<sub>2</sub> flow rate of 5 ml/min. In all experiments 0.5 mol% of MM NTf<sub>2</sub> was used as both electrolyte and co-catalyst.

According to **Figure 5.3**, metals such as Ag and Zn, which have lower CO binding energy than Au, demonstrate lower CO<sub>2</sub> reduction activities than Au. Based on this observation, we can infer that for these catalysts, the first electron transfer, which causes the chemical adsorption of CO<sub>2</sub> over the catalyst site<sup>19</sup>, is the rate-determining step for CO<sub>2</sub> reduction. This hypothesis is consistent with our earlier findings in **Chapter 3**, which demonstrated that the electron transfer from the Au electrode to the CO<sub>2</sub> molecule upon its adsorption strongly depends on the composition of the imidazolium cation. **Figure 5.4** provides a visual representation of the charge transfer process from negatively charged Au and Zn metal surfaces to CO<sub>2</sub> molecule.

The figure illustrates the interaction of CO<sub>2</sub> molecule with the metal surfaces, which are located at the same distance from the on-top metal atoms. The analysis shows that the transfer of the partial negative charge to CO<sub>2</sub> molecule is more prominent in the presence of the Au surface compared to the Zn surface.

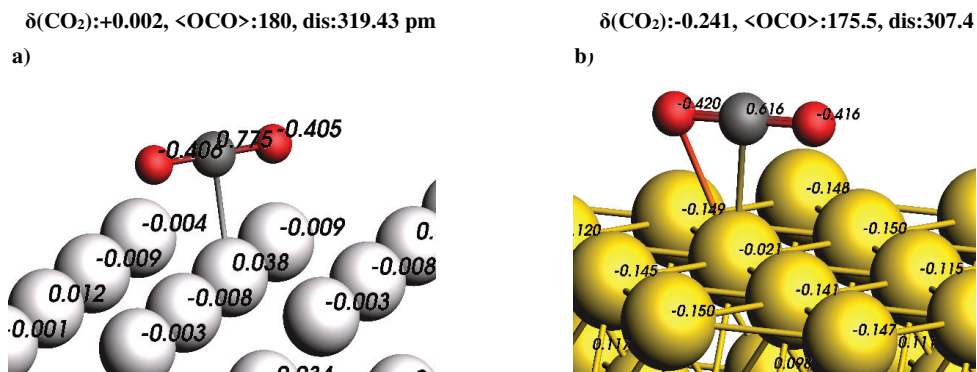


**Figure 5.4.** Mulliken population analysis for CO<sub>2</sub> interacting with negatively charged metal slabs, calculated using single-point BAND calculations. Subfigures (a) and (b) illustrate the results for CO<sub>2</sub> interacting with Zn and Au slabs, respectively. The figure highlights the charge differences between the top metal atom and its surroundings, as well as the negative charges found on oxygen atoms and positive charges found on carbon atoms. The figure highlights the results for charge transfer ( $\delta(\text{CO}_2)$ ) from BAND calculations, along with the CO<sub>2</sub> bond angle ( $\langle \text{OCO} \rangle$ ) and the equilibrium distance from the surface ( $\text{dis}$ : in picometer) from DFTB calculations, which are summarized at the top.

The charge transfer from the negatively charged Zn slab to the CO<sub>2</sub> molecule is found to be rather insignificant and even negative ( $\delta(\text{CO}_2)$ : +0.002) compared to that of Au ( $\delta(\text{CO}_2)$ : -0.241), which can explain the lower activity for CO<sub>2</sub> reduction on Zn. In addition, DFTB calculations were performed to investigate the intrinsic affinity of the two metal slabs with the CO<sub>2</sub> molecule in the absence of negative charge. The results reveal that CO<sub>2</sub> has a stronger interaction with a neutral Au slab compared to a neutral Zn slab, resulting in a shorter equilibrium distance and a smaller OCO bond angle (as summarized at the top of **Figure 5.4**). These findings suggest that the affinity of Zn metal towards CO<sub>2</sub> is noticeably lower than that of Au, which can be attributed to differences in their electronic properties and surface energies<sup>105</sup>. The results presented in **Figure 5.4** lend support to the hypothesis that the initial electron transfer to adsorbed CO<sub>2</sub> represents the rate-determining step for catalysts located on

the left side of the volcano plot, as depicted in **Figure 5.3**. Conversely, metals such as Cu and Ni, which exhibit stronger binding to CO than Au, exhibit slower kinetics. This indicates that for these catalysts with strong CO binding, CO desorption is likely the rate-determining step.

To gain deeper insights into the stronger interaction between Cu and CO compared to Au and CO, DFT calculations were utilized to analyze the Mulliken population of CO and negatively charged Au and Cu slabs (**Figure 5.5**). The results confirm a more robust interaction between CO and the Cu slab, as indicated by a larger partial negative charge transfer from the Cu slab to the CO molecule compared to the Au slab ( $\delta(\text{CO}_2)$ : -0.105 for Cu vs  $\delta(\text{CO}_2)$ : -0.072 for Au).

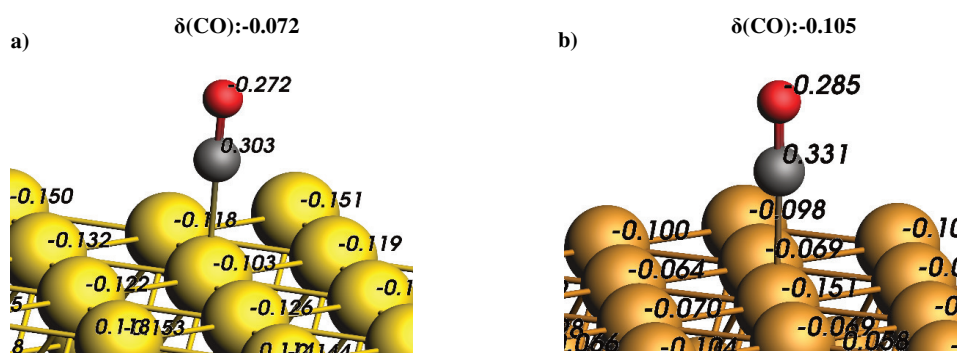


**Figure 5.5.** Mulliken population analysis for CO interacting with negatively charged metal slabs, calculated using single-point BAND calculations. Subfigures (a) and (b) illustrate the results for CO interacting with Au and Cu slabs, respectively. The figure highlights the charge differences between the top metal atom and its surroundings, as well as the negative charges found on oxygen atoms and positive charges found on carbon atoms. Details of charge transfer results are also summarized at the top.

Volcano plot presented in this study serves as a useful tool for predicting the reactivity of transition metal catalysts in non-aqueous CO<sub>2</sub> reduction based on their CO adsorption. Moreover, electronic models, such as the d-band model, which leverage the electronic properties of the metal, particularly the d-band center ( $\epsilon_d$ )<sup>106-107</sup>, have successfully been utilized to predict CO adsorption with transition metals (also see the **Theoretical Appendix** at the end of this chapter). Therefore, combining electronic models with the Volcano plot in this work

should provide a valuable tool for engineering the overall rate of CO<sub>2</sub> reduction in non-aqueous media. However, the observed 100% selectivity towards CO for all the investigated catalysts suggests that altering the reaction conditions, such as the inclusion of a proton source like water or weak acids, should be the primary approach to influence CO<sub>2</sub> reduction selectivity.

Explaining the role of imidazolium cation as a co-promoter is also crucial. Our results in **Chapter 3** demonstrated that imidazolium cation promotes the reaction by reducing the energy of the adsorbed CO<sub>2</sub> intermediate at the Au electrode. However, the question that remains is how imidazolium cation affects the observed volcano trend. To address this, the volcano plot obtained from this study was compared with that from the work of Jaramillo and colleagues<sup>7</sup>, as depicted in **Figure 5.6**. Under aqueous conditions, we observe significant differences in activity when comparing Au to other metals, such as Ag, Cu, and Ni. Specifically, we find ratios of Au/Ag ~ 10 and Cu/Ni ~ 30 for the current density associated with CO<sub>2</sub> reduction at equivalent potential (**Figure 5.6, right**). However, in MeCN-imidazolium-assisted CO<sub>2</sub> reduction, while greater absolute activities are observed for electrodes such as Ni and Cu, the difference between the activities of different electrodes is much smaller (**Figure 5.6, left**). For example, the Au/Ag ratio for the activity reported in our work is only 1.66, compared to the Au/Ag ratio of 10 reported in the work of Jaramillo et al.<sup>7</sup>

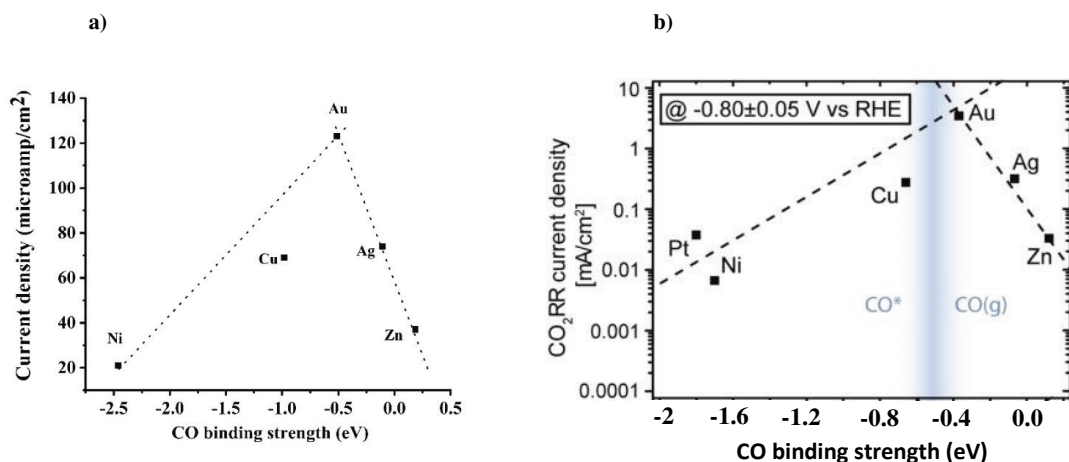


**Figure 5.6.** Volcano plot of CO<sub>2</sub> reduction activity for transition metal catalysts. **(a)** obtained in this work for anhydrous MeCN and 0.5 % mol MM NTF<sub>2</sub> as promoter. **(b)** obtained for aqueous media from work of Jaramillo and co-authors <sup>7</sup>.

In **Chapter 3**, it was demonstrated that imidazolium cation influences the electron density of adsorbed CO<sub>2</sub> by interacting with the C2-proton. This interaction results in a lower energy barrier for the formation of highly polarized adsorbed \*CO<sub>2</sub><sup>-</sup> when imidazolium cations are present. Thus, the primary cause of the modified differences in activity between various transition metal catalysts examined in this study, especially those with high energy barriers for CO<sub>2</sub> adsorption (such as the Zn, Au, and Ag electrodes), is expected to be the reduction of the energy barrier for the formation of polarized intermediates, aided by H-bond formation. The simplified microkinetic model presented in **Supporting Information Section IV** demonstrates that the kinetics of the first electron transfer step leading to chemical adsorption of CO<sub>2</sub> impact the overall reaction rate, even for catalysts where CO desorption is the rate-determining step. Therefore, for catalysts such as Ni and Cu, the primary function of imidazolium cation in stabilizing the CO<sub>2</sub> adsorbed intermediate can still be in effect to modulate the overall reaction rate. However, it is important to note that obtaining the equilibrium constant for CO<sub>2</sub> adsorption, facilitated by imidazolium cation, and accurately quantifying its influence on the overall reaction rate for catalysts with CO desorption as the rate-determining step, necessitates a

detailed kinetic analysis. Furthermore, it is worth noting that while the primary function of imidazolium cation in stabilizing the CO<sub>2</sub> adsorbed intermediate can still modulate the overall reaction rate for catalysts such as Ni and Cu, its impact on the CO desorption process cannot be ruled out. Thus, conducting a dedicated kinetic study is recommended to fully understand the role of imidazolium cation in catalysts where CO desorption is rate-determining.

## **Conclusion**

In summary, this study highlights the promising potential of imidazolium co-catalyzed CO<sub>2</sub> reduction in non-aqueous media using late-transition metal catalysts. The findings reveal several key insights that contribute to the advancement of CO<sub>2</sub> reduction systems. Firstly, the high faradaic efficiency achieved by non-expensive metals such as Zn, Cu, and Ni electrodes in anhydrous acetonitrile, combined with the CO<sub>2</sub> absorption capacity of acetonitrile, presents a cost-effective approach for CO<sub>2</sub> reduction. This opens up new possibilities for developing efficient and economically viable CO<sub>2</sub> conversion technologies. Furthermore, the observation of a volcano relationship among late-transition metals, with Au exhibiting the highest activity trend, provides valuable design principles for optimizing CO<sub>2</sub> reduction efficiency in non-aqueous solvents. Additionally, a noteworthy comparison with aqueous media highlights the advantages of non-aqueous conditions. The uniform selectivity for CO formation in anhydrous conditions contrasts with the more complex selectivity patterns observed in aqueous media. This signifies the greater ease of controlling reaction conditions in non-aqueous media, facilitating more straightforward optimization of selectivity.





# Supporting Information

## Table of Contents

- I. Materials**
- II. Experimental methods**
- III. Computational methods**
- IV. Microkinetic modeling**
- V. GC analysis and faradaic efficiencies**
- VI. Electrochemical data**
- VII. Theoretical Appendix**

## I. Materials

Gold (Au) voltammetry electrodes (3.0 mm diameter, 99.95%) were purchased from Prosense. Gold wire (0.25 mm diameter, 99.99 %), Zn wire (1.0 mm diameter, 99.99 %), Ni wire (0.5 mm diameter, 99.99 %), Fe wire (1.0 mm diameter, 99.99 %), Ag wire (0.25 mm diameter, 99.99 %), and Cu foil (thickness 0.25 mm, 99.98 %) were supplied by Sigma Aldrich. Anhydrous acetonitrile (99.8%), acetonitrile (ReagentPlus, 99%), silver trifluoromethanesulfonate ( $\geq 99\%$ ), acetonitrile-d<sub>3</sub> ( $\geq 99.8$  atom % D) were obtained from Sigma-Aldrich. Acetonitrile-d<sub>3</sub> (99.8 atom % D) for electrolysis experiments was obtained from abcr GmbH, Karlsruhe. 1,3-Dimethylimidazolium bis(trifluoromethylsulfonyl)imide (99%) was purchased from Iolitec Ionic Liquids Technologies GmbH. Milli-Q water was taken from a Milli-Q Advantage A10 Water Purification System, Millipore (18 M $\Omega$ .cm). All chemicals were transferred to the glove box after vacuum drying and were used without further treatment. Additional details can be found in **Chapter 2**.

## II- Experimental methods

The anhydrous electrochemical preparation, reference electrode preparation, and electrochemical measurement procedures followed the protocols outlined in **Chapter 2**. By adhering to these standardized procedures, we ensured that the results obtained were accurate and reproducible. Prior to use, the working electrodes were polished with sandpaper until a shiny surface appeared, washed with Milli-Q water, and sonicated in ethanol for 10 minutes, followed by a final sonication in anhydrous acetonitrile (MeCN) for another 10 minutes.

### III- Computational methods

The Density-Functional based Tight-Binding (DFTB) method was employed to optimize conventional cells for various metals, with lattice vectors being optimized prior to geometry optimization. The optimized conventional cells were used as input data to generate four layers of (111) 2D slabs for different metals. Grimme's GFN1-xTB served as the model Hamiltonian for the DFTB calculations<sup>108</sup>. Subsequently, single-point calculations were performed in the periodic DFT program (BAND)<sup>109-110</sup>. to obtain the formation energies of the slabs. High-quality k-space grids were employed for both DFTB and BAND calculations. The generalized gradient approximation (GGA) with PBE as the default exchange-correlation functional was used for the BAND calculations. A Slater-type basis set of triple- $\zeta$  valence quality with a single polarization function (TZP) was used for all atoms in the calculations<sup>90</sup>. The same settings were used to calculate the formation energy of negatively charged metal slabs. To investigate the interaction between the metal slabs and CO<sub>2</sub>, a single CO<sub>2</sub> molecule that had already been optimized in ADF was introduced to the calculations. The CO<sub>2</sub> molecule was positioned at a distance of 220 picometers from an on-top metallic atom of the slab. A subsequent calculation was then performed using the same settings to obtain the formation energy and charge distribution for a negatively charged slab+CO<sub>2</sub> system. It should be noted that when a negative charge is introduced to the slab+CO<sub>2</sub> system, the engine considers the slab and CO<sub>2</sub> as a whole to obtain the lowest energy charge distribution. The same protocol was also utilized to determine the formation energies of negatively charged slabs+CO systems. The CO desorption energy was subsequently calculated as follows:

$$CO \text{ desorption energy (eV)} = \text{energy of slab} + \text{energy of CO} - \text{energy of (CO + slab)}$$

#### IV- Microkinetic modeling

The microkinetic model we developed assumes that a particular step in the reaction mechanism is rate-determining, and that all other reaction steps are in equilibrium. We also account for the presence of water as an oxygen acceptor and proton donor in the second step of the reaction. It is important to note that if we were to assume CO<sub>2</sub> to be the oxygen acceptor instead of water, we would expect to obtain the same overall reaction rate results. By incorporating these assumptions into our model, we can predict how the presence of imidazolium cation as a promoter affects the rate of the first electron transfer step, and ultimately the overall rate of the reaction. The series of reaction steps for the formation of CO can be described as follows:



Assuming that step **[5.3]** is rate-determining and that **steps 5.2 and 5.1** are in equilibrium, we can write:

$$r_{2+} = k_{2+} \cdot [* CO_2^-] \cdot [H^+]_{sol}^2 = r_{2-} = k_{2-} \cdot [* CO] \cdot [H_2O]_{sol} \quad [5.4]$$

$$[* CO] = \frac{k_{2+}}{k_{2-}} \cdot \frac{[H^+]_{sol}^2}{[H_2O]_{sol}} \cdot [* CO_2^-] = K_{eq2} \cdot \frac{[H^+]_{sol}^2}{[H_2O]_{sol}} \cdot [* CO_2^-] = K_{eq2'} \cdot [* CO_2^-] \quad [5.5]$$

$$r_{1+} = k_{ads_1} \cdot [CO_2]_{sol} = r_{1-} = k_{des_1} \cdot [* CO_2^-] \quad [5.6]$$

$$[* CO_2^-] = \frac{k_{ads_1}}{k_{des_1}} \cdot [CO_2]_{sol} = K_{eq1} \cdot [CO_2]_{sol} \quad [5.7]$$

Combining **equations [5.3] and [5.7]**, we obtain the following expression for the rate of CO desorption:

$$r_{3+} = k_{des_3} \cdot [* CO] = k_{des_3} \cdot K_{eq2'} \cdot K_{eq1} \cdot [CO_2]_{sol} \quad [5.8]$$

with  $K_{eq1}$  from **equation 5.7** we have:

$$K_{eq1} = \frac{k_{ads_1}}{k_{des_1}} = \frac{\kappa \cdot \left(k_b \cdot \frac{T}{h}\right) \cdot \exp\left(-\frac{\Delta G_{ads_1}^\ddagger}{RT}\right)}{\kappa \cdot \left(k_b \cdot \frac{T}{h}\right) \cdot \exp\left(-\frac{\Delta G_{des_1}^\ddagger}{RT}\right)} = \exp(\Delta G_{des_1}^\ddagger - \Delta G_{ads_1}^\ddagger) \quad [5.9]$$

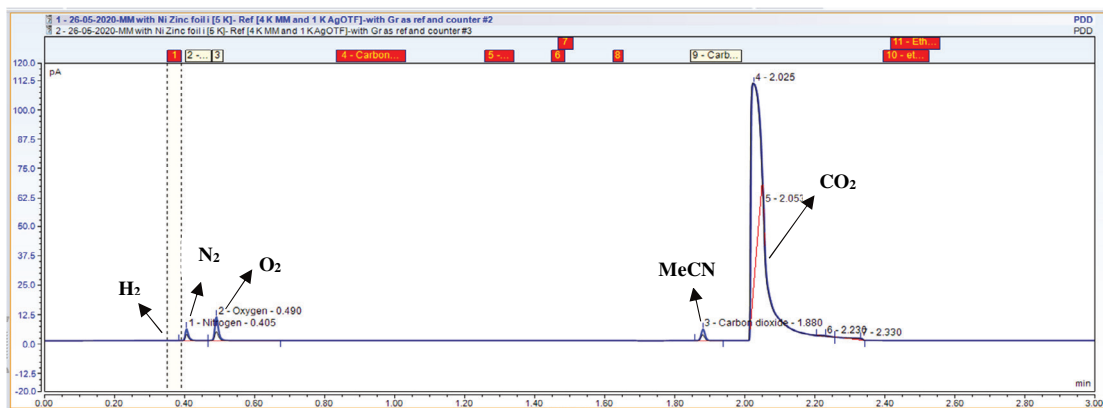
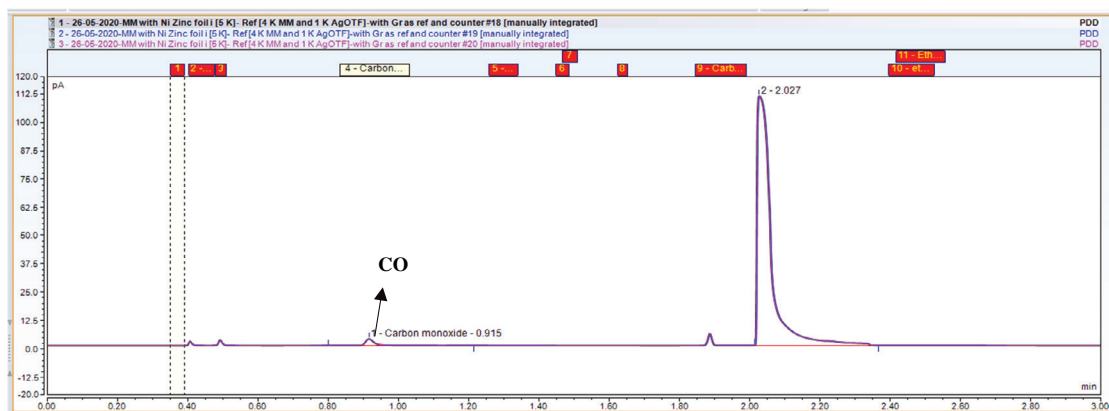
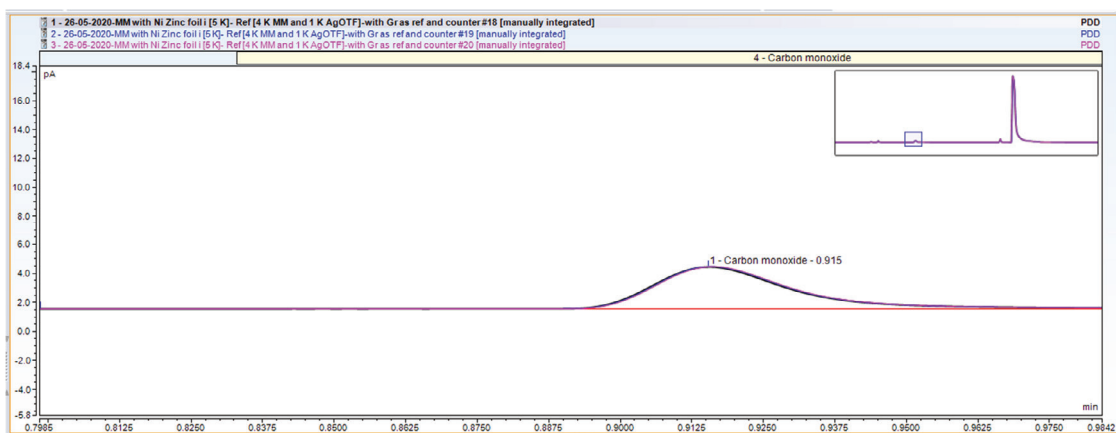
$$r_{3+} = k_{des_3} \cdot [*CO] = k_{des_3} \cdot K_{eq2'} \cdot \exp(\Delta G_{des_1}^\ddagger - \Delta G_{ads_1}^\ddagger) \cdot [CO_2]_{sol} \quad [5.10]$$

where  $\kappa \cdot \left(k_b \cdot \frac{T}{h}\right)$  has the usual meaning in expressions for rate constants.

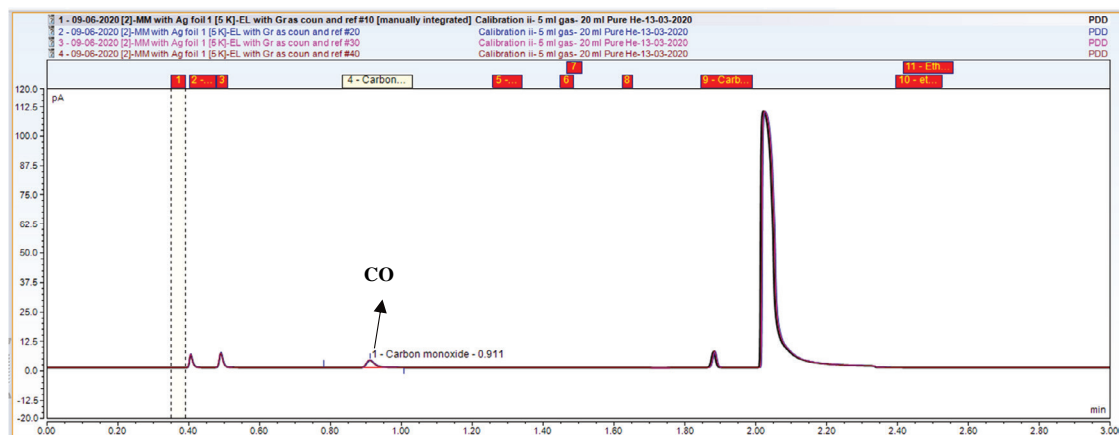
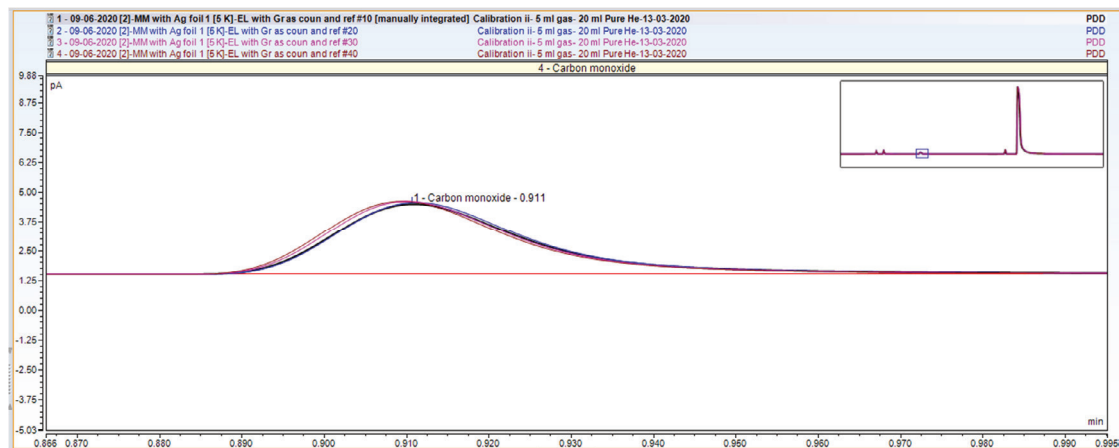
**Equation [5.10]**, as presented above, explains how the activation energy associated with the first electron transfer step ( $\Delta G_{ads_1}^\ddagger$ ) affects the overall reaction rate. A decrease in the activation energy required for the initial step leads to an increase in the reaction rate. As we showed in **Chapter 3**, the presence of imidazolium cations acts as a promoter for the first electron transfer step. Interestingly, even for catalysts where CO desorption is rate-determining, the addition of imidazolium cations improves the overall reaction rate by increasing the equilibrium surface concentration of  $[*CO_2^*]$ . A critical observation is that for catalysts where the first electron transfer is the rate-determining step, the overall reaction rate is determined exclusively by **equation [5.1]**. This underscores the pivotal role played by the imidazolium cation in determining the activity of these catalysts through the modification of the rate constant ( $k_{ads_1}$ ) for the electron-induced CO<sub>2</sub> adsorption step.

## V- GC analysis and faradaic efficiencies

To determine the Faradaic efficiency of the CO<sub>2</sub> reduction reaction, analyses on both the gas and liquid products were conducted. By measuring the quantities of both types of products, one would be able to accurately determine the efficiency of the reaction. Gas products were analyzed using gas chromatography (GC), which was calibrated for the relevant ppm levels of CO and other potential products. Further details on the evaluation of Faradaic efficiencies and GC analysis can be found in **Chapter 2**. Additionally, after electrolysis, the liquid solution was analyzed using nuclear magnetic resonance (NMR) to identify the presence of any other possible products. **Figures S5.1 to S5.4** provide examples of GC sequences used to detect CO and other possible products for all the catalysts studied in this work. It is important to note that the geometric sizes of the electrodes used in our experiments were not uniform, resulting in variations in CO peak intensities in the GC chromatogram. To provide further insight into the behavior of the reactor during electrolysis, **Figure S5.5** presents a series of images taken during and after the electrolysis process.

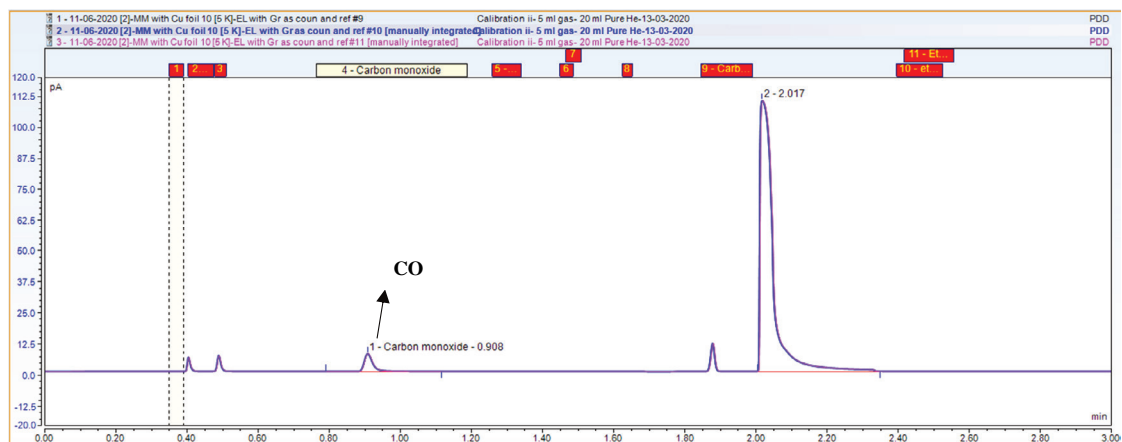
**a****b****c**

**Figure S5.1.** Chromatogram sequences of the GC for detection of the products for CO<sub>2</sub> reduction with Zn electrodes. (a) The background sequences obtained before electrolysis with assignment of the peaks. (b) Sequences with electrolysis at -1 mA/cm<sup>2</sup> showing CO as the only product. (c) Zoomed-in version to highlight the presence of CO from (b). The electrolyte was 0.5 mol% MM NTf<sub>2</sub> in anhydrous MeCN.

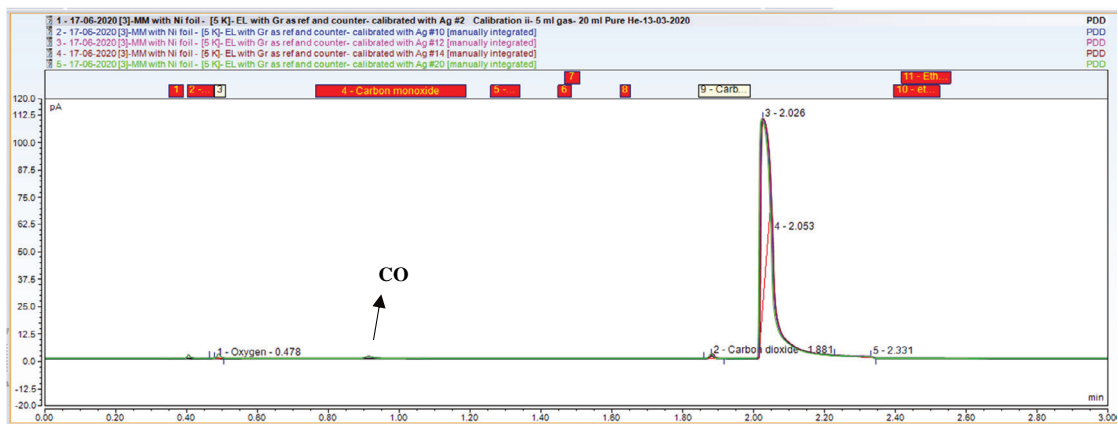
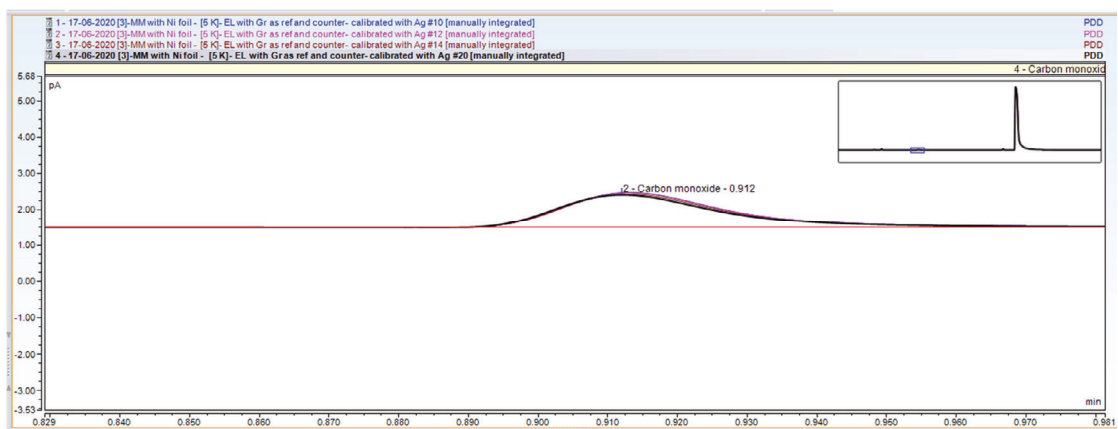
**a****b**

**Figure S5.2.** Sample sequences of the GC for detection of the products for CO<sub>2</sub> reduction with Ag electrode. **(a)** Sequences with electrolysis at -1 mA/cm<sup>2</sup> showing CO as the only product. **(b)** Zoomed-in version to highlight the presence of CO from (a). The electrolyte was 0.5 mol% MM NTf<sub>2</sub> in anhydrous MeCN. Assignments for other peaks are provided in Figure S5.1.





**Figure S5.3.** Sample sequences of the GC for detection of the products for CO<sub>2</sub> reduction with Cu electrode. Sequences with electrolysis at -1 mA/cm<sup>2</sup> showing CO as the only product. The electrolyte was 0.5 mol% MM NTf<sub>2</sub> in anhydrous MeCN. Assignments for other peaks are provided in Figure S5.1.

**a****b**

**Figure S5.4.** Sample sequences of the GC for detection of the products for CO<sub>2</sub> reduction with Ni electrode. **(a)** Sequences with electrolysis at -1 mA/cm<sup>2</sup> showing CO as the only product. **(b)** Zoomed-in version to highlight the presence of CO from (a). The electrolyte was 0.5 mol% MM NTf<sub>2</sub> in anhydrous MeCN. Assignments for other peaks are provided in Figure S5.1.

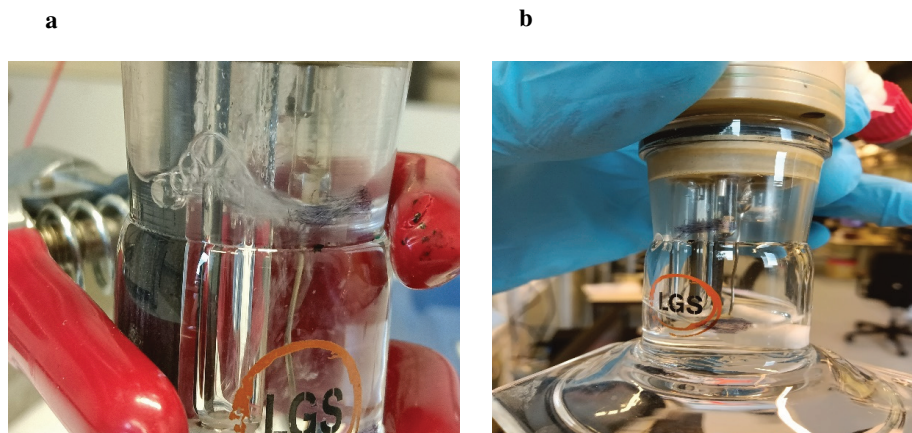


**Figure S5.5.** Images of the reactor used for CO<sub>2</sub> reduction with a Ni electrode are shown above. **(a)** shows the reactor after 90 minutes of electrolysis at -1 mA/cm<sup>2</sup>. and **(b)** shows it after 10 hours of electrolysis. In both images, the Ni surface appears clean and the solution is clear. The electrolyte used was 0.5 mol% MM NTf<sub>2</sub> in anhydrous MeCN.

## VI- Electrochemical data

**Figure S5.6 a** depicts the linear sweep voltammeteries (LSVs) of an iron (Fe) electrode under CO<sub>2</sub> and He purging. We observe that the potential-current profiles under CO<sub>2</sub> and He are remarkably similar, indicating that the Fe catalyst is almost inactive for CO<sub>2</sub> reduction in the imidazolium-anhydrous MeCN electrolyte. This inactivity can be attributed to early catalyst poisoning by CO adsorption<sup>103</sup> and the reduction of the imidazolium cation over the Fe catalyst, as evident from the potential-current profile under He purging. To provide a more comprehensive understanding of this behavior, the same LSV data are included for a Zn electrode in **Figure S5.6 b**. The figure clearly shows a considerable difference in the potential-current profiles under CO<sub>2</sub> and He purging, with a notably larger faradaic current under CO<sub>2</sub> atmosphere, which indicates CO<sub>2</sub> reduction activity. **Figure S5.7** displays the LSV results for Au, Ni and Zn electrodes with MM-acetonitrile electrolyte under He purging

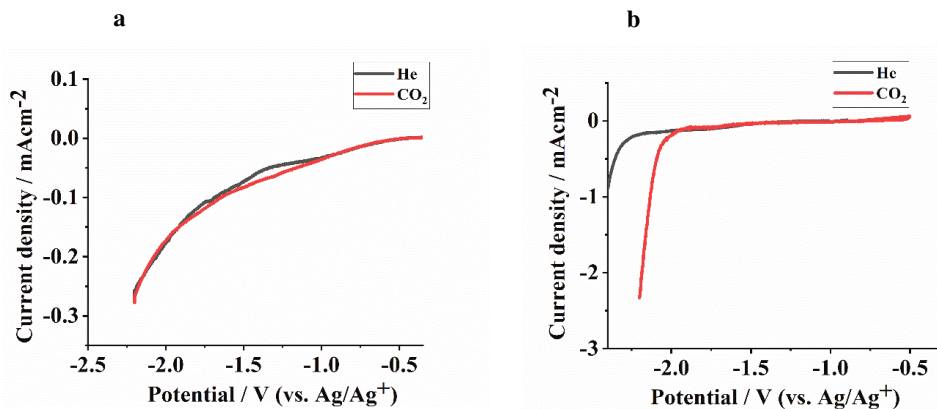


**Figure S5.6.** Linear sweep voltammetry (LSV) results for (a) Fe, and (b) Zn catalysts under CO<sub>2</sub> and He purging in anhydrous MeCN. 0.5 mol% of MM NTF<sub>2</sub> was used as both electrolyte and co-catalyst.

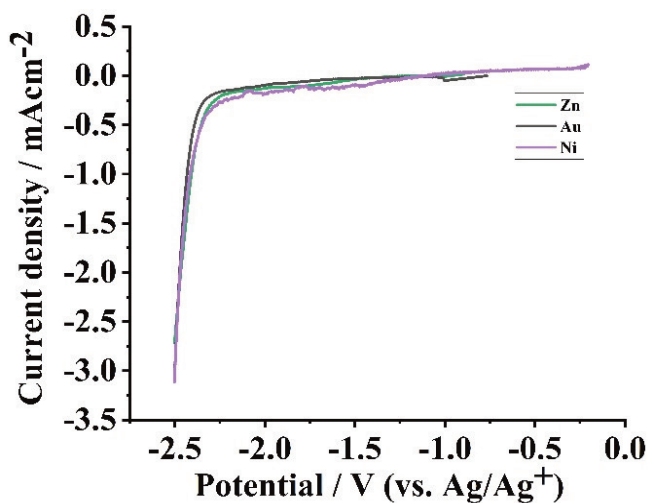


**Figure S5.7.** Linear sweep voltammetry (LSV) results for Au, Ni and Zn catalysts under He purge in anhydrous MeCN, containing 0.5 mol% of MM NTF<sub>2</sub>.

## VII- Theoretical Appendix

A catalytic reaction consists of a series of elementary steps: the adsorption of the reactant on the catalyst surface, diffusion or migration on the surface for recombination, the breaking of some bonds, and the creation of some new ones to form the product molecule. The last step of every heterogeneous catalytic reaction is the desorption of the product molecule from the catalyst surface, which regenerates the catalyst site for the next sequence of the reaction (**Figure S5.8**).

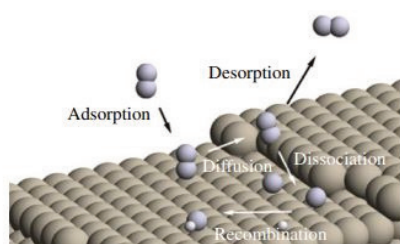


**Figure S5.8.** Schematic illustration of the various elementary steps for a catalytic reaction occurring at a metal surface. The overall rate of the reaction and selectivity towards a specific product is greatly dependent on which of these steps is rate-determining. The figure is adopted from<sup>2</sup>.

In heterogeneous catalysis, the energy barrier for each of these elementary steps is greatly determined by the electronic interaction of the relevant molecule or molecules (reactants, intermediates, or products) with the catalyst surface. These electronic interactions, at their most fundamental levels, consist of a series of complicated quantum phenomena: *the dynamic interaction of orbitals with the electronic states of the metal surface*, whose full understanding is a demanding task and requires a high-level quantum chemical approach. For more details see the monographs from Hoffmann and Van Santen<sup>111-114</sup>. The fundamental question of why some metal catalysts accelerate a specific type of reaction while others do not, can only be answered by decoding these complex electronic effects. Scientists in the field of heterogeneous catalysis have been quite successful in developing models that can relate the trends of catalytic reactions

to some simple electronic structure parameters of the metal catalyst. The *d-band* model developed by Hammer and Norskov<sup>105, 115</sup> relates the adsorption energy of a particular molecule to the *d*-band position of the metal, and by relating the adsorption energies to energy barriers, catalytic trends can be simply explained. The model has been quite successful in describing trends, for example, for N<sub>2</sub>, O<sub>2</sub>, and CO adsorption for various transition metals. Though a full explanation of the *d*-band model is not the intention of this appendix, a brief introduction will turn out to be very useful to understand the experimental results from electrode screening studied in this chapter

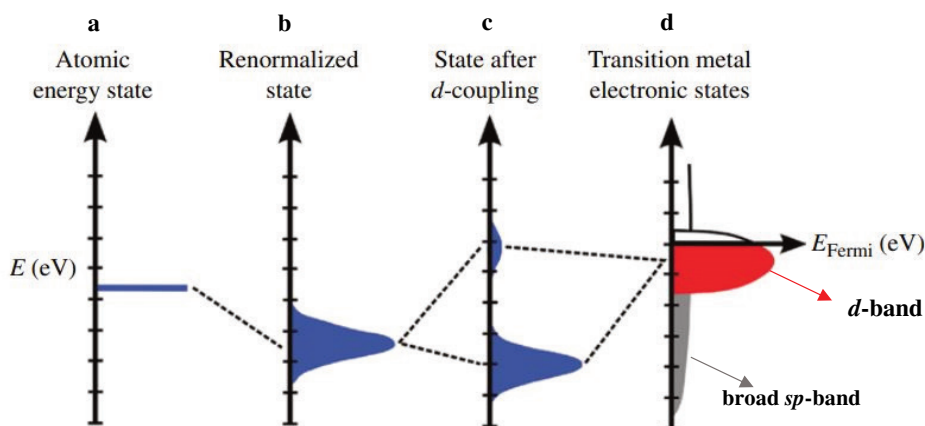


**Figure S5.9.** Schematic illustration of the interaction between the valence level of an adsorbate and the delocalized *sp*-states, followed by a second interaction with the localized *d*-states of a transition metal surface<sup>1</sup>.

**Figure S5.9** illustrates the main idea underlying the *d*-band model. When the adsorbate approaches the surface, its valence state interacts with the broad *sp*-states of the metal surface. After re-normalization (**Figure S5.9 a and b**), we notice that the interaction with the *sp*-state gives rise to a downshift and broadening of the electronic state of the adsorbate. Thus, energy is gained by coupling to the *sp*-state. The *d*-band model assumes that the contribution to the adsorption from the interaction between the low-lying energy *sp*-band and the adsorbate valence state should be the same for all transition metals since they all have the same *sp*-states and the variations in their electronic configuration stem from differences in the *d*-band states. Because

of the weak interactions between very localized electrons, the *d*-band state is narrow and lies very close to the Fermi level of the metal. After renormalization, in the second step, the renormalized *sp*-band interacts with the localized *d*-band states, and because of the narrow nature of the *d*-band, which is like discrete molecular electronic levels, bonding and anti-bonding states are formed as a result of this interaction (**Figure S5.9 c and d**). The formation of these bonding and antibonding states after interaction with the *d*-states is the central idea of the *d*-band model. The relative position of these anti-bonding states to the Fermi level determines how much of the anti-bonding state is filled, which determines the total energy gain for the adsorbate interaction with the metal surface. As a result, we can see that the Fermi level and the relative position of the metal's *d*-band can be used to explain the trend of adsorption at various transition metal surfaces. When the antibonding state lies completely above the Fermi level, no destabilization is expected from the interaction of the *sp*-state with the *d*-band state, and thus a more pronounced adsorption is predicted. However, if antibonding states are below (fully or partially) the Fermi level, a destabilization effect can lower the impact of strong interaction with the *sp*-state.

In this chapter, we observed that the Volcano relation in anhydrous media follows the same relative trend as previously reported in aqueous media. Additionally, we noted that CO adsorption over transition metal catalysts has been well-described using the *d*-band model. From these findings, we can draw two key conclusions:

Firstly, the intrinsic electronic factors that cause the volcano trend in aqueous media have the same impact in anhydrous media. In other words, the intrinsic interactions of transition metals do not change significantly when switching from aqueous to anhydrous media

Secondly, we can apply the principles of the *d*-band model to predict and synthesize efficient catalysts for CO<sub>2</sub> reduction in anhydrous media. By designing catalysts with appropriate electronic properties, we can maximize their activity and selectivity towards desirable products.

These insights have important implications for the development of more effective and sustainable catalytic systems.



## **Chapter 6:**

# **Exploring Electrochemical CO<sub>2</sub> Reduction Catalyzed by 2-Methylated Imidazolium: Insights from ATR-FTIR Spectroscopy**

## Summary

In this chapter we analyze the performance of C2 substituted imidazolium cations in promoting the electrochemical conversion of CO<sub>2</sub>. By using ATR-FTIR, and NMR spectroscopy of a white precipitate formed during the reaction, we demonstrate that reduction of CO<sub>2</sub> takes place according to multiple pathways. On the one hand we provide evidence for the formation of CO and (bi)carbonate, formed by disproportionation of the CO<sub>2</sub> dimer radical anion, and subsequent protonation of the carbonate anion. This is the dominant reaction, since gas chromatography showed a faradaic efficiency of ~80% towards CO. Interestingly, the formation of oxalate, formed by coupling of two CO<sub>2</sub><sup>-</sup> radical anions – is also observed. Oxalate remains in solution, since this is not observed in the NMR analysis of the white precipitate, and therefore likely a minor pathway. Finally, using isotopic labeling for peak assignment – the formation of formate is spectroscopically observed, in agreement with the presence of this anion in the white precipitate – as determined by NMR analysis. This species is formed by protonation of the \*CO<sub>2</sub><sup>-</sup> radical anion. This study shows that contrary to imidazolium cations allowing C2-H coordination to the \*CO<sub>2</sub><sup>-</sup> radical anion (in anhydrous conditions), providing 100% selectivity to the formation of CO, C2-substitution (and likely in the presence of residual water) lowers the reaction selectivity, opening upon channels to formation of other products such as formate and oxalate.

## Introduction

In **Chapters 3 and 4**, we extensively discussed the primary mechanism behind the promotional impact of C2-hydrogenated imidazolium cations. It was concluded that the C2-proton of the cation plays a crucial role in stabilizing the negatively charged intermediate ( $^*CO_2^-$ ). We also demonstrated a higher overpotential recorded with C2-methylated imidazolium compared to C2-hydrogenated cations, signifying reduced co-catalytic performance for the latter. While we discussed 100% faradaic efficiency (FE) for CO formation with C2-hydrogenated cations, we did not extensively discuss the reaction course and selectivity for the C2-methylated cations. Indeed, lower kinetic improvements observed for these cations compared to C2-protonated cations might also entail different selectivity and reaction courses in non-aqueous media. The most referenced work on C2-substituted imidazolium for electrochemical  $CO_2$  reduction in acetonitrile is Lau et al.'s study<sup>8</sup>, which explored modulating C4- and C5-proton donation through the impact of C2-substituents for  $CO_2$  reduction over an Ag electrode. While they mostly reported the formation of CO, information on anhydrous conditions and water content was lacking in their study. Additionally, The use of Ag/AgCl as a supporting salt in the reference capillary in that work is not consistent with our protocol and findings in **Chapter 2**, which demonstrated the significant potential impact of Ag particles in the system in the presence of imidazolium cations. Thus, in this chapter, we aim to gain more insight into the performance of C2-methylated imidazolium using ATR-FTIR studies in combination with our established electrochemical support experiments and ex-situ FTIR and NMR analysis. The chosen imidazolium cation is 1-butyl, 2,3-dimethyl imidazolium (**BMMIM**), which is commercially available, and  $NTf_2^-$  is the common anion.

## Results and discussion

The vibrational spectra of interfacial species were initially examined through in situ ATR-FTIR spectro-electrochemical measurements conducted under an inert atmosphere. **Figure 6.1** illustrates the ATR-FTIR measurements for an Au thin film electrode. These measurements were recorded within the 500-3100  $\text{cm}^{-1}$  range, utilizing a solution of 0.1 M **BMMIM** NTf<sub>2</sub> in acetonitrile. The measurements were taken while purging the system with argon (Ar) and maintaining a constant potential of -2.25 V (versus Fc/Fc<sup>+</sup>). Several negative bands can be attributed to the depletion of the NTf<sub>2</sub> anion from the electronic double layer, spanning the spectral range of 950 to 1400  $\text{cm}^{-1}$ . Specifically, the negative bands at 999  $\text{cm}^{-1}$ , around 1220  $\text{cm}^{-1}$ , and approximately 1320  $\text{cm}^{-1}$  correspond to the asymmetric stretch mode of the -SNS group, the symmetric and asymmetric stretch modes of the -CF<sub>3</sub> group, and the asymmetric stretch mode of SO<sub>2</sub>, respectively<sup>116-118</sup>. It should be noted that the symmetric stretch mode of the SO<sub>2</sub> group, which occurs at approximately 1112  $\text{cm}^{-1}$ , might not have been discernible due

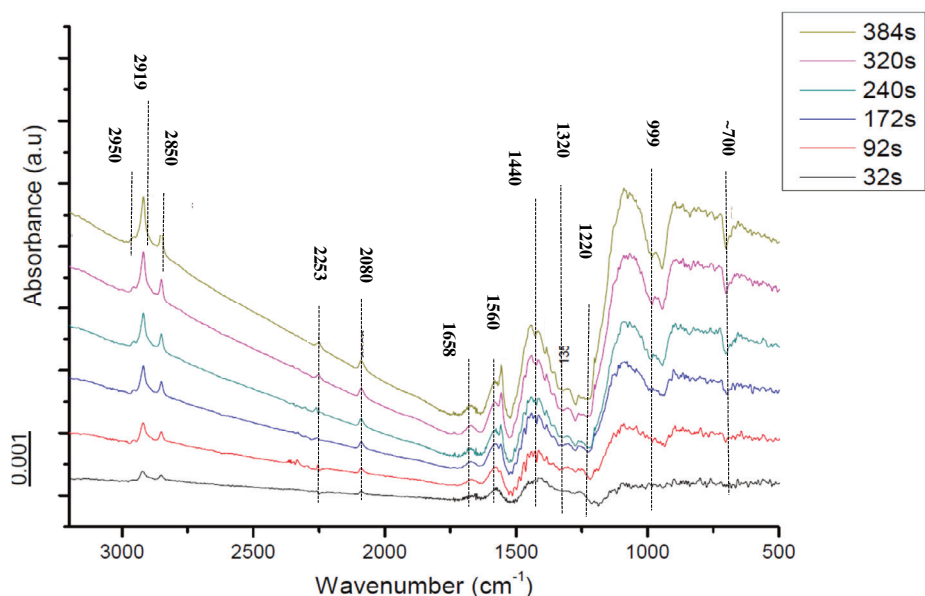


**Figure 6.1.** ATR-FTIR spectra of Au thin film electrode in 0.1 Molar of **BMMIM** NTf<sub>2</sub> in anhydrous MeCN under Ar purging. Spectra were collected at a constant negative potential of -2.25 V vs. Fc/Fc<sup>+</sup>.

to potential artifacts stemming from baseline shifts <sup>119</sup>.

The prominently negative band at approximately  $700\text{ cm}^{-1}$  could potentially be attributed to either the bending vibrational modes of  $-\text{CF}_3$  and  $-\text{SNS}$  groups<sup>118</sup>, or the in-plane symmetrical/asymmetrical bending mode of the imidazolium cation's ring<sup>117</sup>. In the latter scenario, the negative absorption peak indicates a modification in the bending mode of the cation within the electronic double layer. In accordance with Noack et al. <sup>117</sup>, the positive features centered around  $1445\text{ cm}^{-1}$  and  $1430\text{ cm}^{-1}$ , near  $1440\text{ cm}^{-1}$ , can be associated with the asymmetrical stretch of the imidazolium ring in-plane, the  $\text{CH}_3(\text{N})$  stretch, and the symmetrical bending mode of  $\text{NC}(\text{CH}_3)\text{N-HCH}$  within the imidazolium ring. However, it is important to account for potential overlap of these absorbances with those originating from acetonitrile, which might be manifested as peaks at  $1447\text{ cm}^{-1}$  (antisymmetric  $\text{CH}_3$  deformation) and  $1378\text{ cm}^{-1}$  (symmetric  $\text{CH}_3$  deformation) <sup>120</sup>. The positive band observed at  $1580/1590\text{ cm}^{-1}$  can be confidently attributed solely to the symmetrical and asymmetrical in-plane modes of stretch, namely the  $\text{CH}_2(\text{N})$  and  $\text{CH}_3(\text{N})\text{CN}$  modes, occurring within the imidazolium ring. Additionally, the peak at approximately  $1540\text{ cm}^{-1}$  can be associated with the  $\text{C-CH}_3$  bond within the ring and can be attributed to the  $\text{NC}(\text{CH}_3)\text{NCC}$  stretch mode of the cation <sup>2, 3, 6</sup>. The combination of these two peaks results in a composite peak centered around  $1560\text{ cm}^{-1}$  (as depicted in **Figure 6.1**). The prominent positive peaks located at  $2851\text{ cm}^{-1}$  and  $2919\text{ cm}^{-1}$  can be confidently attributed, respectively, to the symmetrical stretching mode of the  $-\text{CH}_2$  group and the symmetrical stretching mode of the  $-\text{CH}_3$  group within the alkyl chain of the cation. Furthermore, the positive feature observed at  $2950\text{ cm}^{-1}$  can be assigned to the asymmetric stretch of the  $-\text{CH}_3$  group in the alkyl chain<sup>1</sup>. The conjunction of positive characteristics corresponding to the imidazolium cation and negative attributes associated with the  $\text{NTf}_2$  anion implies a substitution occurring within the electronic double layer. However, this substitution might not necessarily indicate complete anion depletion. Rather, it suggests a modification in

the relative concentrations when compared to the bulk phase—an occurrence frequently observed at negatively charged electrodes.

The minor positive feature observed around  $\sim 2253\text{ cm}^{-1}$  can be attributed to the CN stretch mode of acetonitrile molecules <sup>121</sup>. This band is similarly present in the FTIR spectra of pure acetonitrile (as depicted in Supporting Information **Figure S6.6**). Moreover, an additional positive feature appears at  $2080\text{ cm}^{-1}$ , which is not evident in the FTIR analysis of bulk acetonitrile. Acetonitrile has the capacity to interact with negatively charged surfaces<sup>122</sup>, leading to the generation of adsorbed acetonitrile or even carbanion  $\text{CH}_2\text{CN}^-$  species. These species might exhibit CN vibrations at wavenumbers lower than those of free acetonitrile molecules <sup>119, 123</sup>. The negative band at  $1658\text{ cm}^{-1}$  can be attributed to the bending mode of residual water molecules that have undergone chemisorption on the surface <sup>121, 124</sup>. It's important to note that the bending frequency of water in its liquid state is typically reported as  $1640\text{ cm}^{-1}$ . The  $18\text{ cm}^{-1}$  blue shift observed could be attributed to the interaction with the negatively polarized Au film electrode, a reasoning also supported by Faguy et al. <sup>121</sup>. It is pertinent to mention that the ATR-FTIR experiment in this study deviates slightly from the protocol detailed in **Chapter 2**. This deviation is due to the specific apparatus used and the challenges encountered in maintaining stringent anhydrous conditions. Consequently, a greater concentration of residual water is to be expected compared to experiments outlined in other chapters.

However, unlike the findings of Figueiredo et al. <sup>21</sup>, we lack any indication of water reduction followed by the subsequent decomposition of acetonitrile into acetamide. This disparity could potentially be attributed to factors such as the inhibitory influence of the imidazolium cation <sup>125</sup>, the meticulous control we have exercised over our water system, and the characteristics of the Au electrode (as discussed in **Chapter 5**).

These spectra recorded in an Ar atmosphere were utilized to obtain time-independent spectra in the presence of CO<sub>2</sub> and using an electrochemical potential, and to study interfacial phenomena under a CO<sub>2</sub> atmosphere. The ATR-FTIR spectra recorded under CO<sub>2</sub> purge are depicted in **Figure 6.2**.

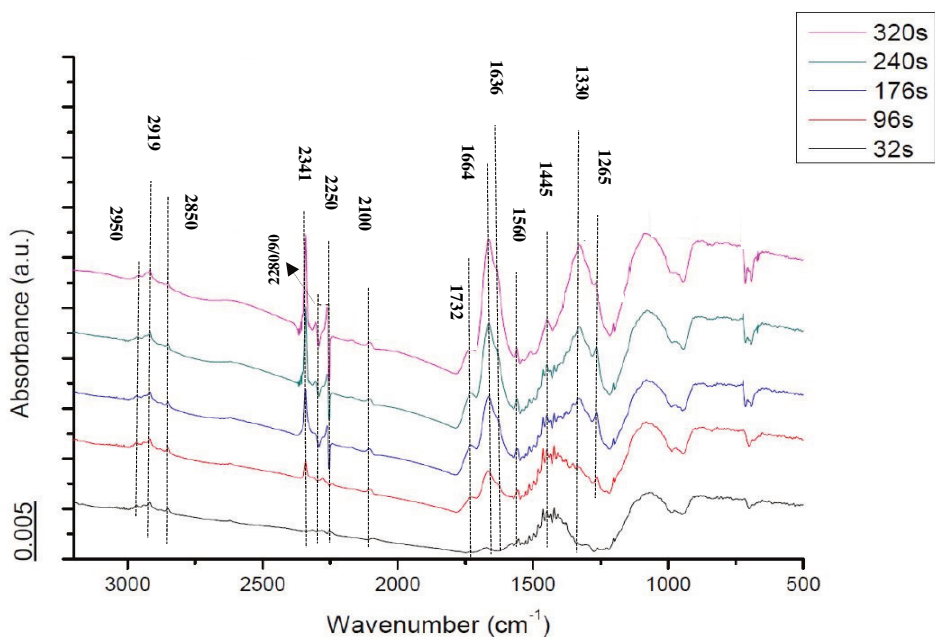


**Figure 6.2.** ATR-FTIR spectra of Au thin film electrode in 0.1 Molar of **BMMIM** NTf<sub>2</sub> in anhydrous MeCN under CO<sub>2</sub> purging. Spectra were collected at a constant negative potential of -2.25 V vs. Fc/Fc<sup>+</sup>. Spectra are displayed relative to a time-independent background spectrum taken under Ar purging.

### Formation of CO and (bi)carbonate

To ensure accurate peak assignment, we conducted electrolysis experiments at a constant potential of -2.25 V (versus Fc/Fc<sup>+</sup>) to assess the distribution of products. A faradaic efficiency of up to 85% was achieved for CO production. In addition to CO, we observed the production of a white solid product at a range of 10-11%. This product was subsequently dissolved in deuterated DMSO and subjected to <sup>13</sup>C and <sup>1</sup>H NMR analysis. Using NMR analysis and comparison with various as-synthesized salts, we established the formation of the bicarbonate

and formate salt of the imidazolium cation (as detailed in **Supporting Information Section III**).

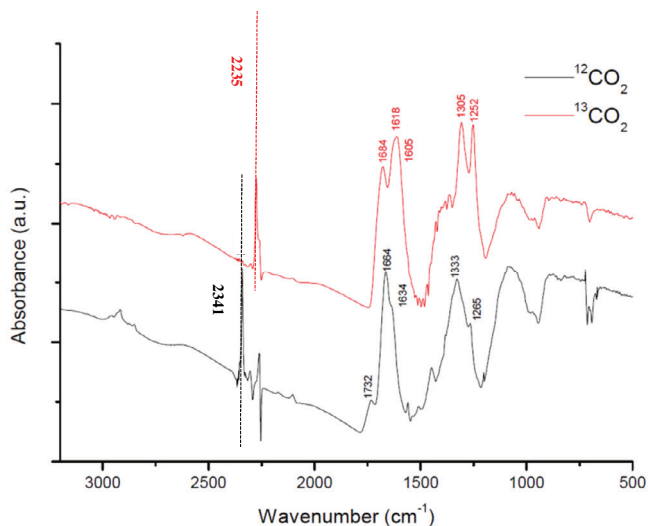


**Figure 6.3.** Comparison of ATR-FTIR Spectra of Au Thin Film Electrode in 0.1 Molar BMMIM NTf<sub>2</sub> in Anhydrous MeCN under <sup>12</sup>CO<sub>2</sub> and <sup>13</sup>CO<sub>2</sub> Purge. The spectra were acquired while maintaining a constant negative potential of -2.25 V (vs. Fc/Fc<sup>+</sup>). Both spectra were recorded after 5 mins of electrolysis.

**Figure 6.3** presents a comparison between spectra obtained using <sup>12</sup>CO<sub>2</sub> and <sup>13</sup>CO<sub>2</sub> in acetonitrile – to corroborate assignments for species formed resulting from CO<sub>2</sub> reduction. Dissolved CO<sub>2</sub> is readily observed by the positively growing band at 2341 cm<sup>-1</sup> assigned to the antisymmetric stretching mode of CO<sub>2</sub><sup>21, 126</sup>. It is accompanied by a negative band situated around ~2250 cm<sup>-1</sup>. This negative band suggests the potential replacement of MeCN molecules with CO<sub>2</sub> at the interface and/or adsorbed on the surface. Importantly, this band does not shift in position in the experiment with <sup>13</sup>CO<sub>2</sub>, which provides additional substantiation for assignment to acetonitrile. The negative band corresponding to the symmetric C-N stretch is accompanied by another negative band at 2280/90 cm<sup>-1</sup>, which can also be assigned to CH<sub>3</sub>CN. These negative bands at these specific wavenumbers were previously reported by Desilvestro and Pons<sup>45</sup> during CO<sub>2</sub> reduction at a Pt electrode under negative potential. The peaks observed



at 2252  $\text{cm}^{-1}$  and 2292  $\text{cm}^{-1}$  within the FTIR spectra of MeCN (as presented in **Supporting Information Section IV**) further corroborate these assignments.

Peaks observed at 2850  $\text{cm}^{-1}$ , 2919  $\text{cm}^{-1}$ , and 2950  $\text{cm}^{-1}$  can be attributed to the imidazolium cation, as discussed in the context of spectra recorded under an Ar atmosphere. These findings suggest that during  $\text{CO}_2$  reduction, imidazolium cations maintain their concentration within the electronic double layer. Simultaneously,  $\text{CO}_2$  likely replaces acetonitrile molecules to engage in the catalytic reaction. In other words, if  $\text{CO}_2$  were to displace imidazolium molecules, we would expect to observe negative bands corresponding to the imidazolium cation. This further implies that imidazolium cations are less likely to be specifically adsorbed at the catalytic sites and are rather present within the electronic double layer. In agreement with the gas phase analysis, the formation of CO is readily observed in our spectra. The recent work by Wang et al.<sup>127</sup> has demonstrated that CO adsorption on Au/ $\text{TiO}_2$  generates a distinct peak at approximately 2100  $\text{cm}^{-1}$ . We also detect a positive band at 2100  $\text{cm}^{-1}$  that persists during  $\text{CO}_2$  reduction (as shown in **Figure 6.2**). Tao et al.<sup>128</sup> have postulated that a band at 2100  $\text{cm}^{-1}$  could be attributed to CO adsorbed on single-fold top sites of the Au electrode. They proposed that CO adsorption on twofold or multifold Au sites would lead to the observation of bands at lower wavenumbers, specifically at 2000  $\text{cm}^{-1}$  and 1940  $\text{cm}^{-1}$ , respectively. This observation substantiates our suggestion that single-fold CO adsorption on Au sites is taking place.

As previously stated for the NMR analysis, to facilitate the identification of other peaks, we conducted the synthesis of various imidazolium complexes, which included  $(\text{BMMIM})_2 \text{CO}_3$ ,  $(\text{BMMIM})_2 \text{C}_2\text{O}_4$ ,  $\text{BMMIM HCO}_3$ , and  $\text{BMMIM HCOO}$ . Notably,  $\text{BMMIM HCO}_3$  and  $(\text{BMMIM})_2 \text{C}_2\text{O}_4$  were observed as white solids, while imidazolium formate and imidazolium carbonate exhibited a distinct behavior, existing as viscous liquids post-anion exchange. Particularly noteworthy is the distinctive change in color observed with imidazolium carbonate.

After these synthetic efforts, we performed FTIR analyses on these imidazolium complexes, and the corresponding spectra are presented in **Supporting Information Section II**.

### **Spectral features of Carbonate and Bicarbonate anions**

An anhydrous carbonate ion exhibits  $D_{3h}$  symmetry and consequently manifests four distinct vibrations, characterized by strong peaks at approximately  $\sim 1420\text{ cm}^{-1}$  (CO symmetric stretch, typically within the range of  $1275\text{-}1590\text{ cm}^{-1}$ ),  $857\text{ cm}^{-1}$  (out-of-plane deformation, typically ranging between  $810\text{-}906\text{ cm}^{-1}$ ), and  $692\text{ cm}^{-1}$  (in-plane deformation, typically ranging between  $670\text{-}756\text{ cm}^{-1}$ ).<sup>129-130</sup> A symmetric CO stretch vibration for the carbonate ion is commonly reported to appear at around  $1040\text{-}1105\text{ cm}^{-1}$ . It has been demonstrated that upon coordination, the original symmetry is diminished, leading to the splitting of certain vibrations and the emergence of new bands in the resulting spectra. When the carbonate ion is coordinated in a bidentate fashion, the CO asymmetric stretch, which initially occurred around  $1420\text{ cm}^{-1}$ , bifurcates into two components: one at approximately  $1270\text{ cm}^{-1}$  and another at the range of  $1520\text{-}1570\text{ cm}^{-1}$ . Bidentate carbonate complexes, such as  $[\text{Co}(\text{en})_2\text{CO}_3]\text{Cl}$ , have exhibited notable absorbances at  $1272$  and  $1281\text{ cm}^{-1}$ , accompanied by an additional feature at  $1577\text{ cm}^{-1}$ .<sup>129, 131</sup> It has also been demonstrated that in the case of hydrogen carbonates, additional splitting of symmetric and asymmetric CO vibrations takes place. The asymmetric stretch shifts towards higher wavenumbers, leading to an absorption within the range of  $1620\text{-}1660\text{ cm}^{-1}$ . This specific asymmetric stretch has been attributed to carbonate groups with their oxygen atoms engaging in interactions with neighboring hydrogen atoms. Thus, it becomes evident that the way carbonates are coordinated and the environment they are solvated in, can give rise to distinct structural arrangements. Consequently, these variations in structure contribute to the observed differences in IR bands. In our FTIR analysis of the synthesized imidazolium carbonate and imidazolium bicarbonate salts, we have observed bands situated within specific

wavenumber ranges. These include the asymmetric stretch in the vicinity of 1630-1670  $\text{cm}^{-1}$ , the symmetric stretch of  $\text{CO}_2$  (pertaining to carbonate) within the range of  $\sim 1295\text{-}1425 \text{ cm}^{-1}$ , the CO stretch between 990-1080  $\text{cm}^{-1}$ , the non-planar rocking motion bands at 830-880  $\text{cm}^{-1}$ , and the  $\text{CO}_2$  bending bands spanning 686-712  $\text{cm}^{-1}$ . Remarkably, these bands are consistent with reported features of alkali metal bicarbonates<sup>129, 131</sup>, such as  $\text{NaHCO}_3$ . However, a distinctive feature emerges at 1281  $\text{cm}^{-1}$ , corresponding to another  $\text{CO}_2$  asymmetric stretch. This feature aligns with bidentate carbonate complexes wherein two oxygen atoms are coordinated with metal centers, as discussed previously<sup>129</sup>. Thus, the presence of this band, coupled with an additional feature found in the 1500-1550  $\text{cm}^{-1}$  range, may suggest a different coordination of a carbonate ion with imidazolium cations, possibly orientated differently than the one with structure resembling monodentate alkali metal bicarbonates. These findings emphasize the need for a careful consideration of various BMMIM- $\text{CO}_3$  complex structures for spectral interpretation in the context of  $\text{CO}_2$  reduction. We also identified a subtle difference in the spectra for imidazolium carbonate and imidazolium bicarbonate. For bicarbonate version, we observed a broad band at around 3100  $\text{cm}^{-1}$ , confidently assignable to the OH vibration of bicarbonate<sup>129</sup>.

### **Formation of (bi)carbonate species in the electrochemical reduction of $\text{CO}_2$**

In the C=O region depicted in **Figure 6.2**, noticeable peaks at 1664 and 1636  $\text{cm}^{-1}$  align well with the transmission spectra of  $[\text{BMMIM}_2 \text{CO}_3]$  and  $[\text{BMMIM HCO}_3]$ . These features can be confidently assigned as vibrations corresponding to the asymmetric CO stretch, as discussed previously. The peak situated at 1445  $\text{cm}^{-1}$  is unique for carbonate, and can be attributed to the CO symmetric stretch and is consistent with the presence of imidazolium carbonate complexes. Additionally, the observed bands at 1265  $\text{cm}^{-1}$  and 1560  $\text{cm}^{-1}$  can be attributed to another set of symmetric and asymmetric vibrations of (bi)carbonate species. Contrasting these result with

the reference spectra, the formation of BMMIM carbonation and BMMIM bicarbonate are evident. However, NMR results from the white precipitate only indicate the formation of bicarbonate and formate species. This suggests that carbonate species are likely to remain soluble in acetonitrile and will play a role in oxidation reaction. The formation of bicarbonate and formate requires the presence of protons. As we did not observe water reduction over Au film, these species can only be formed by interactions with protons resulting from water oxidation over the counter electrode or due to residual water present along with the electrolyte at the cathode electrode.

An intermediate proposed for formation of CO and (bi)carbonate is the  $^*C_2O_4^-$  (Metal-C(=O)COO $^-$ ) – known as the CO<sub>2</sub> dimer radical anion. This intermediate, upon a second electron transfer accompanied by bond cleavage, leads to the formation of CO and carbonate anions, the latter following protonation to form bicarbonate. This mechanism has been proposed for CO<sub>2</sub> reduction at CdS and ZnS nanocrystals, where CO<sub>2</sub> serves as an oxygen acceptor<sup>132-133</sup>. Sheng et al.<sup>132</sup> demonstrated that the presence of such an intermediate would result in the appearance of three bands within the 1000-1700 cm<sup>-1</sup> region, exhibiting a <sup>13</sup>C shift exceeding 30 cm<sup>-1</sup>. However, in our case, we do not observe any new peaks displaying significant <sup>13</sup>C shifts, apart from those assigned to carbonate (**Figure 6.3**). Consequently, the lifetime of this intermediate is apparently that short, that we do not observe this spectroscopically. To observe such intermediate, rapid scan measurements are required (allowing ms time resolution), or even step-scan experiments (allowing microsecond time resolution).

### **Formation of Oxalate**

In addition to the formation of CO and bicarbonate, another significant product of CO<sub>2</sub> reduction previously reported is the creation of oxalate. Our experiment also reveals the presence of this compound, which accounts for the appearance of a band around ~1732 cm<sup>-1</sup> in

our spectra. When comparing reference spectra of different anions, this is the only anion that displays an absorption above  $1700\text{ cm}^{-1}$ . Other notable absorption peaks of oxalate are observed at  $1457$ ,  $1274$ , and  $821\text{ cm}^{-1}$ . While the first two peaks are likely present, their signals might be obscured due to strong overlap with (bi)carbonate peaks. The latter peak is not easily distinguishable in the spectra due to significant baseline attenuation. The formation of oxalate could potentially result from the self-coupling of the adsorbed  $\ast\text{CO}_2^-$  species, a mechanism also proposed by Kamet et al<sup>3</sup> over a lead electrode in acetonitrile.

### **Formation of Formate**

The peak observed around  $1330\text{ cm}^{-1}$  in the in-situ spectra of **Figures 6.2** and **6.3** introduces a novel feature in our analysis. Among the investigated reference compounds, the only one that displayed a somewhat similar absorption near this wavelength was **BMMIM HCOO** (formate). The formation of this compound aligns with the NMR analysis of the solid product, which, in addition to bicarbonate, revealed the presence of formate. While the overlap of several bands assigned to bicarbonate and/or oxalate complicates the assignment of other spectral features expected for formate, the prominence of the  $1330\text{ cm}^{-1}$  peak position and the NMR data provide confidence that formate is indeed generated in the reaction.

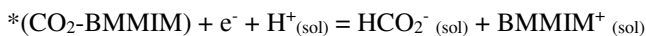
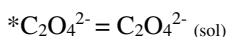
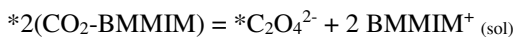
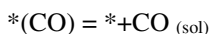
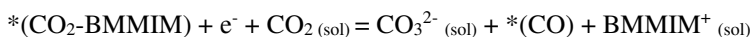
The co-occurrence of oxalate, formate, and CO was also suggested by Amatore and Saveant<sup>23</sup> in aprotic media with limited proton availability. The occurrence of oxalate, formate and CO was also argued by Amatore and Saveant<sup>31</sup> in aprotic media of low proton availability.

## The reactions leading to the (interfacial) products observed

With the discussion above in mind, we propose the following set of equations for CO<sub>2</sub> reduction processes occurring at the Au electrode in the BMMIM-NTf<sub>2</sub>-MeCN electrolyte :



<sup>1</sup>[solvation/hydrogen bonding mediated with imidazolium cation]



## Conclusion

In this chapter, we presented infrared spectroscopic evidence of the formation of various species at the electrode-electrolyte interface. Initially, when CO<sub>2</sub> reduction is conducted in acetonitrile containing 2-methylated imidazolium, both CO and (bi)carbonate species are formed near an Au cathode. Furthermore, the appearance of a novel feature at ~1720 cm<sup>-1</sup> and a robust peak at 1330 cm<sup>-1</sup> suggests the generation of oxalate and formate species, respectively. The identification of formate was also confirmed through NMR analysis of solid products obtained from electrolysis experiments. However, a comprehensive analysis is needed to accurately attribute the observed ATR-FTIR peaks to surface intermediates. This would involve a dedicated investigation, possibly employing other in-situ spectroscopy techniques like Raman

spectroscopy, coupled with DFT calculations to explore the vibrations of such potential intermediates.

The most significant observation in this chapter is the distinct product distribution observed with the C2-methylated imidazolium cation compared to the 100% faradaic efficiency (FE) found with the C2-hydrogenated imidazolium cation in **Chapter 3**. This, combined with the reduced kinetic enhancement observed with the C2-methylated cation, suggests the potential for altering the reaction pathway with imidazolium cations of different functionalities.





# Supporting Information

## Table of Contents

- I. Au thin film for ATR-FTIR experiments
- II. Ion exchange procedure to obtain BMMIM salts with different anions
- III. Electrolysis results
- IV. Additional ATR-FTIR spectra

## I. Au thin film for ATR-FTIR experiments

To amplify the infrared signals, the Au thin film deposited on the Si crystal underwent electrochemical activation before conducting IR experiments. The activation process encompassed three cyclic voltage cycles, alternating between -0.4 and 1.2 V (versus Ag/Ag<sup>+</sup>), utilizing a scan rate of 50 mV/s. Prior to utilization, the Au thin film was characterized by AFM (image shown in **Figure S6.1**) and XPS (data presented in **Table S6.1**). The thickness of the Au film was approximated to be around 20 nm.

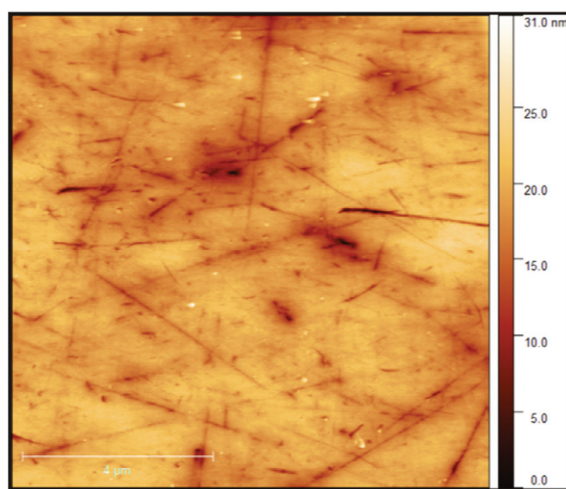


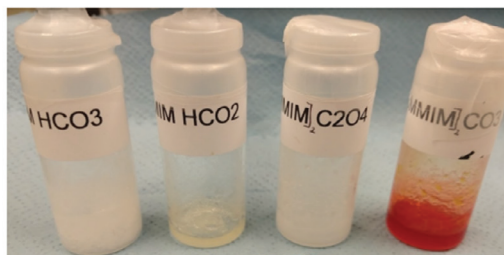
**Figure S6.1.** AFM image of the Au film deposited on an ATR - Si crystal. The area scanned was 10 by 10 micrometer.

**Table S6.1.** XPS analysis of Au thin film deposited on ATR Si crystal.

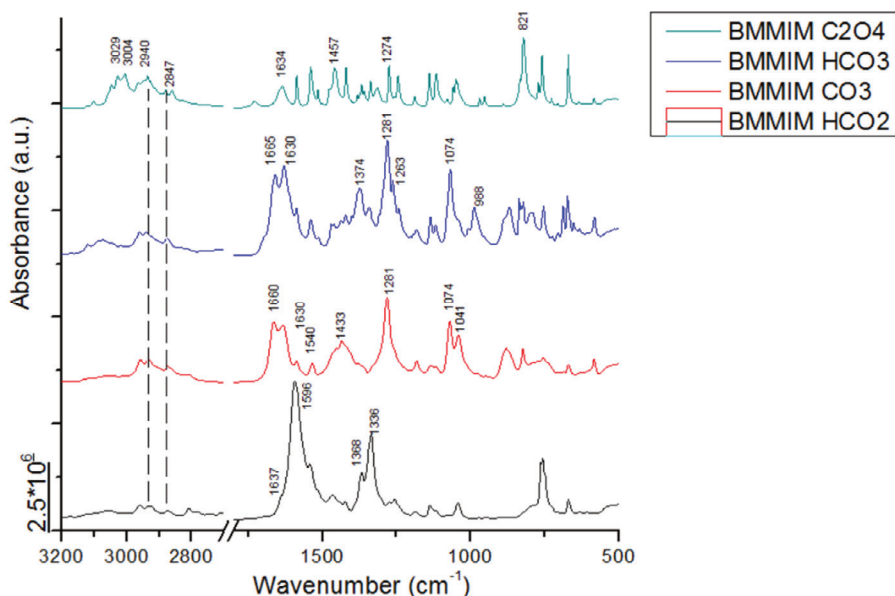
Spectra	Element			
	C	O	Si	Au
Survey spectrum 1	20.81	1.13	7.53	70.54
Survey spectrum 2	27.62	0.42	6.47	65.49
Survey spectrum 3	20.80	4.33	12.05	62.82
Core spectrum	23.21	2.01	7.01	67.77

## II. Ion exchange procedure to obtain BMMIM salts with different anions

[BMMIM] [HCO<sub>3</sub>], [BMMIM]<sub>2</sub> [CO<sub>3</sub>], [BMMIM] HCO<sub>2</sub>, and [BMMIM]<sub>2</sub> [C<sub>2</sub>O<sub>4</sub>] were synthesized using an ion exchange procedure, employing BMMIM Cl and the respective potassium salts (synthesized salts are shown in **Figure S6.2**). Subsequently, IR spectra were recorded (as depicted in **Figure S6.3**) to aid in the understanding of the assignments elucidated in the text.



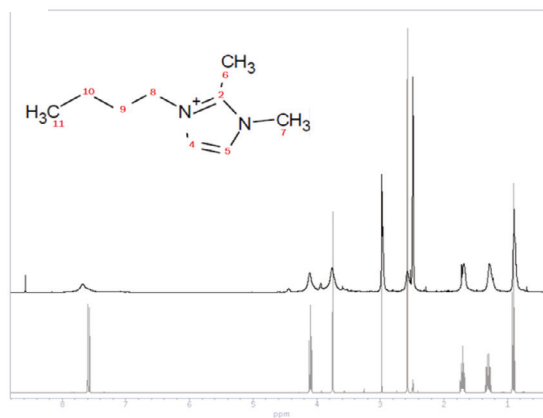
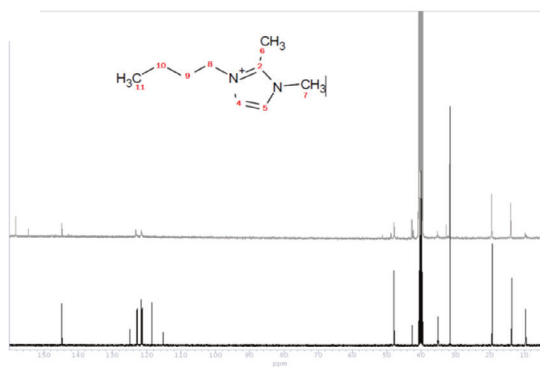
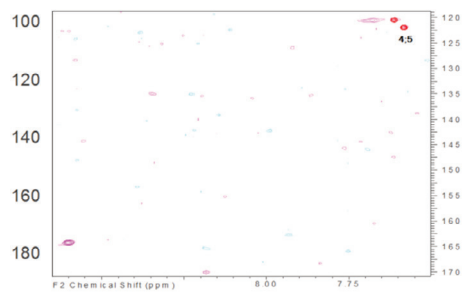
**Figure S6.2.** Synthesized imidazolium products with different counter ions. Imidazolium oxalate and imidazolium bicarbonate appeared as white solids, while imidazolium carbonate and imidazolium formate were obtained in the form of viscous liquids.



**Figure S6.3.** FTIR spectra of the as-synthesized imidazolium salts. All spectra were acquired in atmospheric conditions. A total of 64 scans were recorded and subsequently averaged, employing a resolution of 2 cm<sup>-1</sup>.

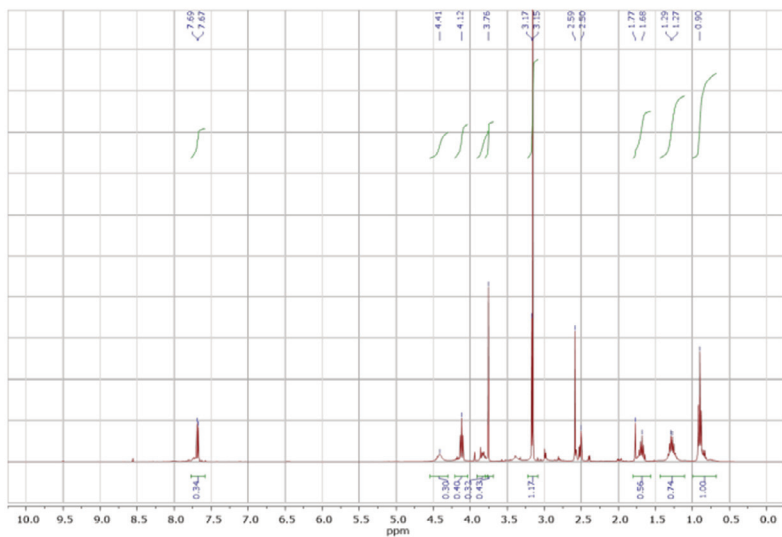
### III. Electrolysis results

After CO<sub>2</sub> electrolysis in acetonitrile, using 2-Methylated Imidazolium cations, a solid (white) precipitate was obtained. This precipitate was filtered from solution, washed with pure acetonitrile, and subsequently dissolved in deuterated DMSO. Following this, comprehensive carbon and proton NMR analyses was conducted (as illustrated in **Figure S6.4 a, b, and c**). Additionally, NMR results derived from the analysis of the synthesized salts are presented in **Figure S6.5 a-d**. The spectra are indicative for a mixture of two compounds. The correspondence between the <sup>1</sup>H NMR peak at 8.57 ppm and the <sup>13</sup>C NMR shift at 165 ppm lends support to the presence of a formate anion. Moreover, an additional <sup>13</sup>C NMR shift, approximately around 160 ppm, suggests the presence of bicarbonate. This observation aligns with the findings of Maton et al.<sup>134</sup>, who also reported a <sup>13</sup>C NMR chemical shift around 160 ppm for the C=O group of imidazolium bicarbonate.

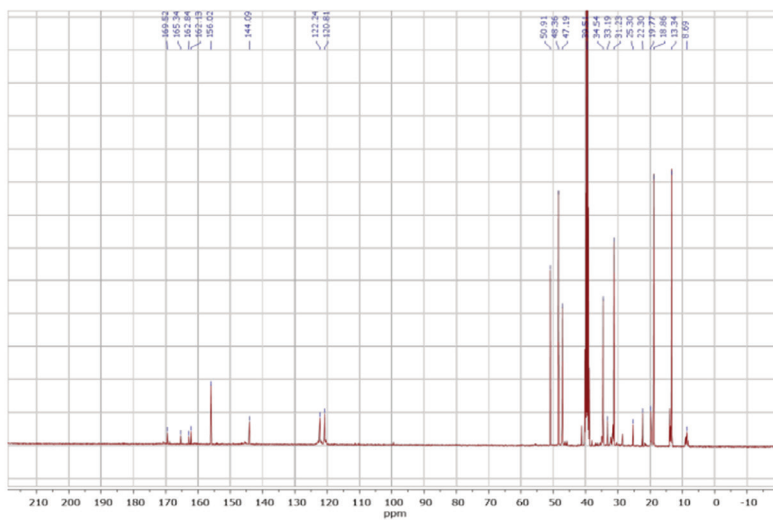
**a****b****c**

**Figure S6.4.** (a)  $^1\text{H}$  NMR and (b)  $^{13}\text{C}$  NMR, and (c) two-dimensional NMR spectra of synthesized imidazolium compounds dissolved in DMSO. The black spectra were recorded before electrolysis, while the gray spectra correspond to the solid products dissolved in deuterated DMSO. 1.5 mol% of dimethyl sulfoxide was used as an internal standard.

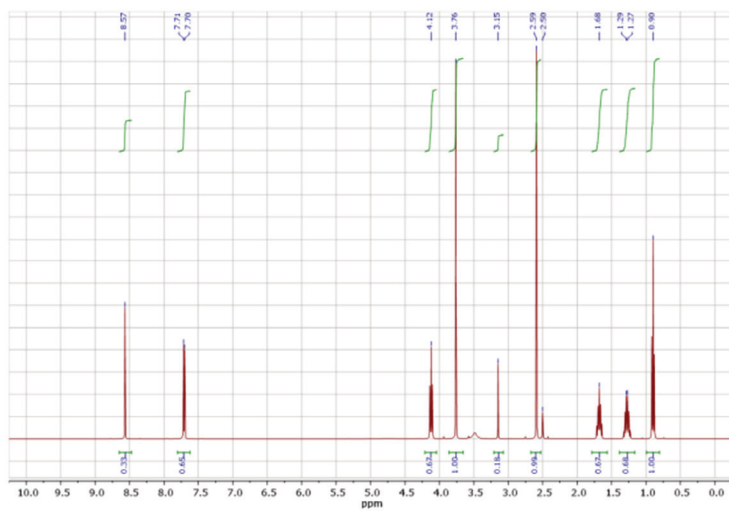
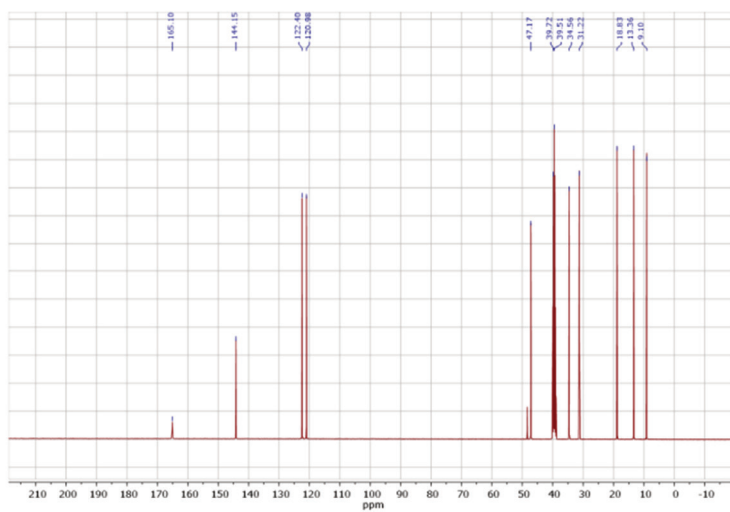
**a**



**b**



**Figure S6.5.a,** <sup>1</sup>H NMR and **b,** <sup>13</sup>C NMR spectra of BMMIM CO<sub>3</sub> in deuterated DMSO.

**c****d**

**Figure S6.5.c,**  $^1\text{H}$  NMR and **d,**  $^{13}\text{C}$  NMR spectra of BMMIM HCO<sub>2</sub> (formate) in deuterated DMSO.

#### IV. Additional FTIR spectra

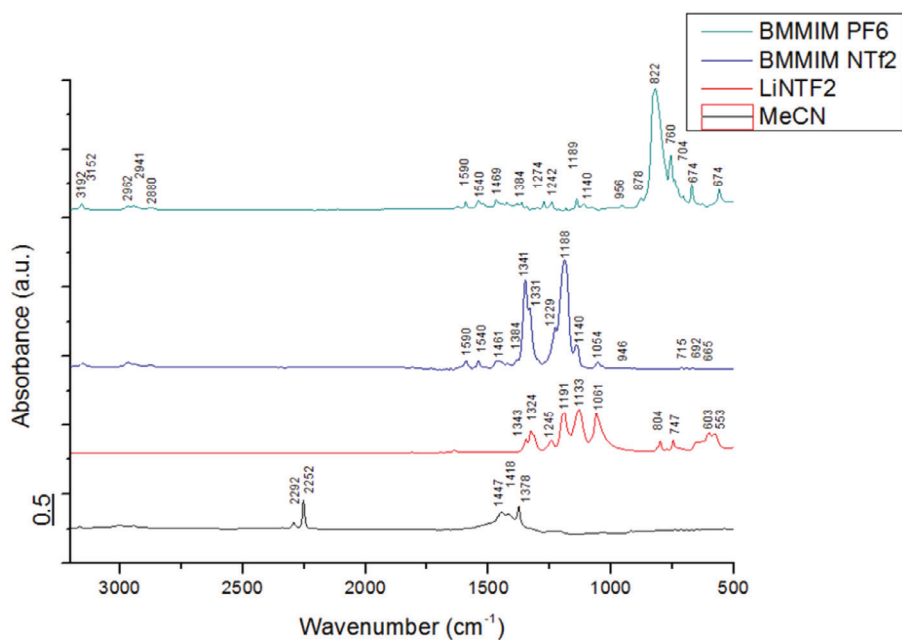
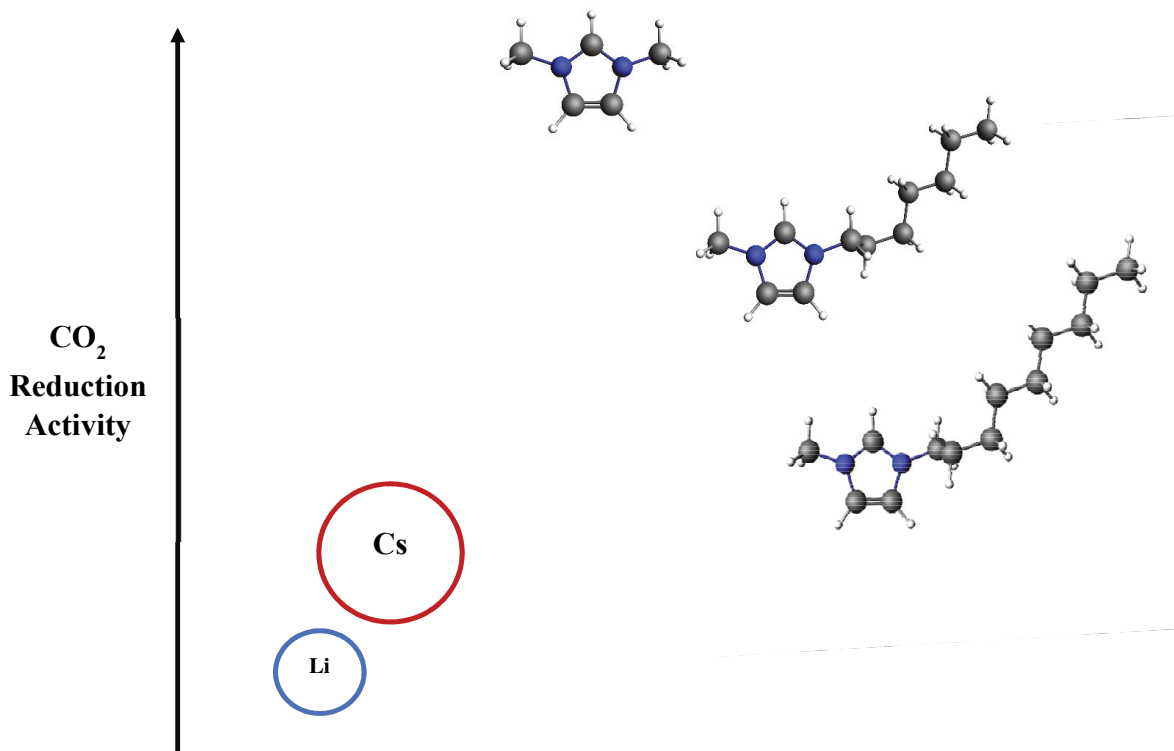


**Figure S6.6.** FTIR Spectra of Various Salts Used for Band Assignment. Additionally, the FTIR spectrum for MeCN is included for comparison.



## Chapter 7:

### Exploring the Influence of Electrolyte Identity on Non-Aqueous CO<sub>2</sub> Reduction: Impact of Alkyl Chain Length and Alkali Metal Cations



## Summary

This **Chapter** examines the influence of alkyl chain length in imidazolium cations on CO<sub>2</sub> reduction and explores the role of alkali metal cations in anhydrous CO<sub>2</sub> reduction. The findings reveal a detrimental effect of longer alkyl chains on CO<sub>2</sub> reduction activity. Moreover, the introduction of alkali metals leads to complete suppression of CO<sub>2</sub> reduction, even in the presence of imidazolium cations. This suppression is likely attributed to the formation of carbonate precipitates on the electrode surface. These results emphasize the importance of alkyl chain length optimization and underscore the challenges associated with alkali metal cations in non-aqueous CO<sub>2</sub> reduction systems.

## Introduction

In the preceding chapters, we explored the fundamental mechanisms underlying the substantial enhancement in performance of Au electrodes in non-aqueous CO<sub>2</sub> reduction through the utilization of the 1,3-dimethyl imidazolium cation. Building upon these findings, **Chapter 7** seeks to broaden our comprehension by investigating two crucial aspects: a) the impact of alkyl chain length within the imidazolium cation, and b) the influence of the nature of alkali metal cations on the non-aqueous CO<sub>2</sub> reduction process. It is worth noting that a comprehensive analysis of these electrolyte effects necessitates dedicated molecular dynamics calculations in conjunction with experimental investigations. However, such computational support lies beyond the scope of this chapter, as our objective here is to establish the foundation for future studies in non-aqueous media.

## Results and Discussion

**Figure 7.1 a** presents the cyclic voltammetry results for three imidazolium cations: 1,3-dimethyl imidazolium NTf<sub>2</sub> (**MM**), 1-methyl-3-heptyl imidazolium NTf<sub>2</sub> (**HM**), and 1-methyl-3-nonyl imidazolium NTf<sub>2</sub> (**NM**), as co-catalysts for CO<sub>2</sub> reduction on an Au electrode in anhydrous acetonitrile. It is evident that an increase in the alkyl chain length leads to a decrease in the activity for CO<sub>2</sub> reduction, especially evident by the high onset potential for the NM imidazolium. In **Figure 7.1 b**, we present the optimized structures of the cations obtained through DFT calculations, along with VDD charge analysis specifically focusing on the C2-H2 bonds. Interestingly, the VDD charge analysis reveals no significant differences in the positive charge densities for the C2 and H2 atoms of the imidazolium rings. Thus, it is unlikely that the variations in charge densities or proton donation from the H2 atoms play a significant role in the observed differences in activities. Instead, we propose that the bulkiness of the cations,

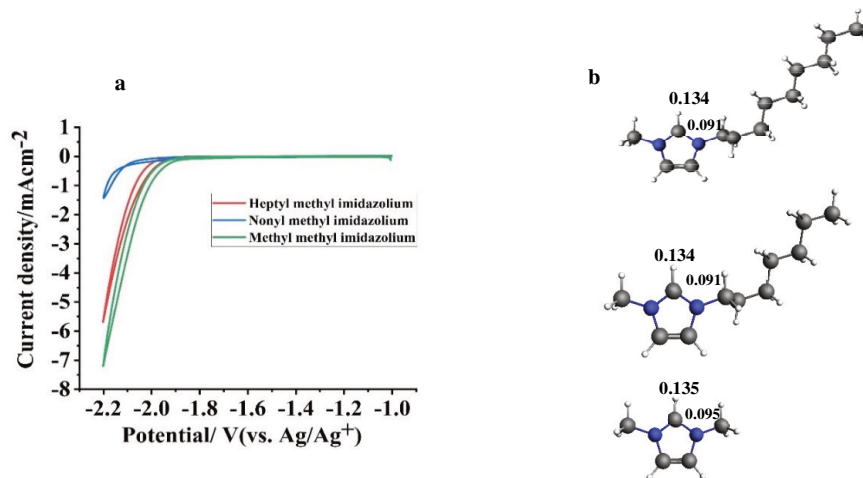


**Figure 7.1.** (a) Cyclic voltammetry results obtained with 0.5 mol% of three different imidazolium cations in CO<sub>2</sub>-saturated anhydrous acetonitrile. The cations investigated include: 1,3-dimethylimidazolium NTf<sub>2</sub> (**MM**), 1-methyl-3-heptyl imidazolium (**HM**), and 1-methyl-3-nonyl imidazolium (**NM**). (b) Comparison of the structures for the three investigated cations in acetonitrile, obtained through DFT calculations. Additionally, the VDD charges of the C2-H2 bonds for each cation are displayed. The B3LYP exchange correlation functional was utilized for all the calculations.

influenced by the flexible and lengthy alkyl chains, may contribute to their co-catalytic effects on CO<sub>2</sub> reduction. Considering the cationic nature of the imidazolium cations and their presence in the double layer, it is plausible that larger cations with more extensive alkyl chains exert their influence on CO<sub>2</sub> reduction through steric effects.

Aldous and Hardwick<sup>135</sup> observed that longer-chain organic cations slow down the rate of electrode kinetics for oxygen reduction on Au electrodes in acetonitrile. They argued that cations with longer alkyl chains reduce the activity of the Au electrode due to competitive adsorption. Similarly, our findings with 1-alkyl-3-methyl cations, including **MM**, **HM**, and **NM** (**Figure 7.1**), demonstrate a decrease in activity when a longer alkyl chain is present at the N1-position. This negative effect of longer alkyl chain length on the kinetics of CO<sub>2</sub> reduction has also been observed on Ag electrodes using different tetra-alkyl ammonium cations<sup>136</sup>. In general, to optimize the performance with imidazolium cations for CO<sub>2</sub> reduction, it is advisable to consider cations with the shortest alkyl chain lengths, to prevent steric hinderance and allow coordination of the C2 proton with adsorbed CO<sub>2</sub>. Further investigations incorporating in situ

electrochemical spectroscopy techniques are required to further examine the adsorption behavior of imidazolium cations and the potential absence of C2-H coordination with surface adsorbed CO<sub>2</sub>. These studies, in combination with molecular dynamics calculations, will provide valuable insights into the dynamics of imidazolium-assisted CO<sub>2</sub> reduction.

We also further explored the impact of alkali metal cations on anhydrous electrochemical CO<sub>2</sub> reduction. **Figure 7.2** presents a comparison of the cyclic voltammetry results obtained in CO<sub>2</sub>-saturated anhydrous acetonitrile using different supporting electrolytes: **MM** NTf<sub>2</sub>, **Li** NTf<sub>2</sub>, **K** NTf<sub>2</sub>, and **Cs** NTf<sub>2</sub>. The results clearly indicate that the activity for CO<sub>2</sub> reduction is significantly higher with **MM** NTf<sub>2</sub> electrolyte compared to the alkali metal cations at the same concentration. In fact, we observed negligible activity with the alkali metal cations under the same experimental conditions. These findings highlight the substantial influence of the electrolyte identity, particularly the presence of the 1,3-dimethyl imidazolium cation, on enhancing the activity for CO<sub>2</sub> reduction in anhydrous conditions.

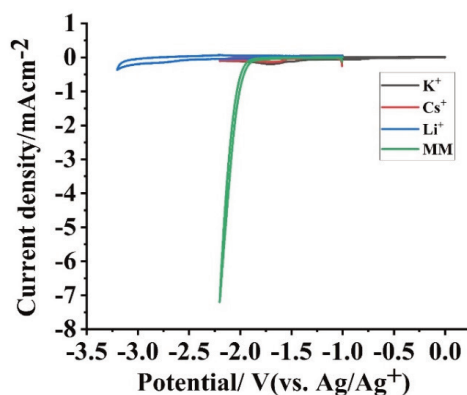


**Figure 7.2.** Cyclic voltammetry results obtained with 0.5 mol% of four different electrolytes in CO<sub>2</sub>-saturated anhydrous acetonitrile. The cations investigated include **MM** NTf<sub>2</sub>, **Li** NTf<sub>2</sub>, **Cs** NTf<sub>2</sub>, and **K** NTf<sub>2</sub>.

**Figure 7.3** illustrates the electrolysis results using **Cs** NTf<sub>2</sub> electrolytes for CO<sub>2</sub> reduction in anhydrous MeCN. We observed a substantial increase in cell voltage over time, indicating an instability in the electrochemical system. Additionally, the faradaic efficiency for CO formation was found to be very poor, with up to 90 percent of electrons consumed for hydrogen production. The observed instability in the potential, which extends beyond the electrochemical window of acetonitrile<sup>137</sup>, is consistent with the inability of Au electrodes to reduce CO<sub>2</sub> in the absence of imidazolium cations. This increasingly higher potential may imply the degradation of acetonitrile<sup>138</sup> which contributes to the current and the formation of H<sub>2</sub>. These observations highlight the inability of alkali metal electrolytes to allow for CO<sub>2</sub> reduction in non-aqueous media.

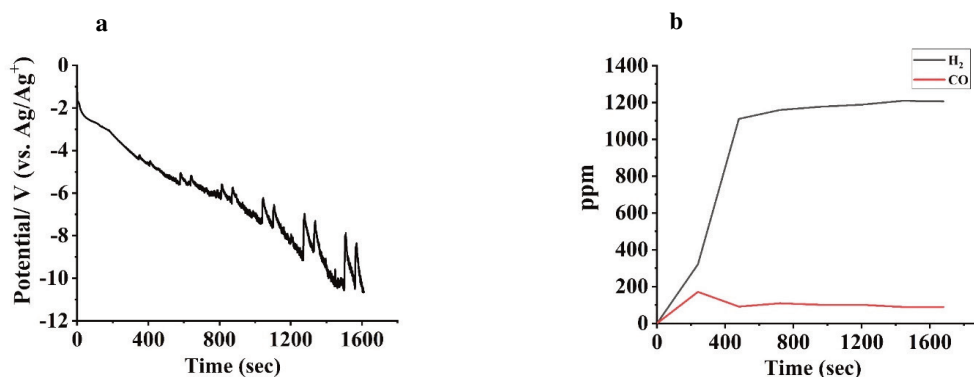


**Figure 7.3.** Electrolysis Results for CO<sub>2</sub> Reduction at -1 mA/cm<sup>2</sup> with 0.5 mol% of **Cs** NTf<sub>2</sub> on Au Working Electrode. **(a)** Time-dependent instability observed in the cell potential profile during electrolysis. **(b)** Limited faradaic efficiency for CO formation, reaching only up to 10%. Additionally, noticeable fluctuations are observed in the potential profile.

The results of this study contrast with the literature findings on the positive impact of alkali metal cations for electrochemical CO<sub>2</sub> reduction in aqueous media<sup>18, 139</sup>. Koper et al.<sup>49</sup> argue that the absence of alkali metal cations prevents CO<sub>2</sub> reduction over Au, Ag, and Cu electrodes in aqueous media. They suggested that partially desolvated alkali metal cations present in the electronic double layer stabilize the high-energy CO<sub>2</sub> radical intermediate through short-range

electrostatic interactions. The argument for CO<sub>2</sub> stabilization through hydrogen bonding with imidazolium cations in anhydrous media, as discussed in this thesis, shares similarities with the role of alkali metal cations in aqueous media. The discrepancy in the role of alkali cations between aqueous and non-aqueous media can be explained by considering the role of solvation in acetonitrile compared to water. According to prior research findings, in aprotic solvents, carbonate species formed during electrochemical reduction tend to precipitate in the presence of alkali metal cations. This phenomenon leads to the passivation of the active electrode surface and the subsequent halt of CO<sub>2</sub> reduction<sup>140-141</sup>. Setterfield-Price and Dryfe<sup>140</sup> demonstrated the presence of deactivating inorganic salts (LiOCO<sub>2</sub> and Li<sub>2</sub>CO<sub>3</sub> were detected via Raman spectroscopy) on the electrode surface (Au and Pt) after CO<sub>2</sub> reduction with 0.1 M LiBF<sub>4</sub> in NMP solvent. The coupling of carbonate species occurs following the second electron transfer, during which alkali metals with higher charge density than organic cations form insoluble inorganic salts. The zoomed-in version of the cyclic voltammetry results from **Figure 7.2** for **K** NTf<sub>2</sub> and **Cs** NTf<sub>2</sub> electrolytes (**Figure 7.4**) reveals an early mass-diffusion limited current reached at negative potentials around -1.8 V (vs. Ag/Ag<sup>+</sup>). This negative peak current can be interpreted as an indirect sign of the formation of a passivation layer over the electrode surface upon CO<sub>2</sub> reduction.

Kash et al.<sup>141</sup>, have demonstrated a potential solution to this issue by introducing acids to aprotic media, such as methanesulfonic acid to dimethyl sulfoxide. This approach led to the formation of CO<sub>2</sub> reduction products with up to 80% faradaic efficiency. Their study highlights the importance of considering alternative electrolyte systems and acid additives to improve the efficiency of CO<sub>2</sub> reduction in aprotic solvents when alkali metals are used as electrolyte.

However, it is important to note that introducing acids to the aprotic solvents alters the composition of the electrolyte. This makes it challenging to directly compare the performance of alkali metal cations and imidazolium cations for non-aqueous CO<sub>2</sub> reduction.

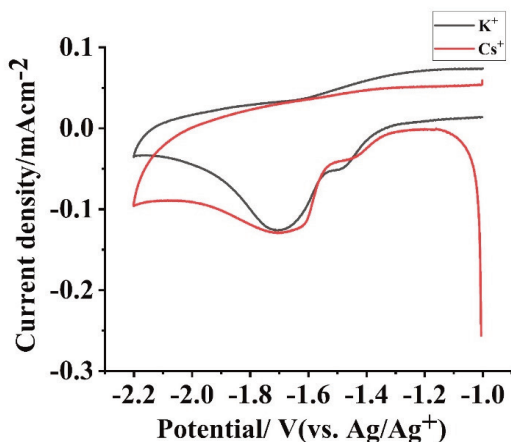


**Figure 7.4.** Cyclic voltammety results obtained with 0.5 mol% of Cs NTF<sub>2</sub> and K NTF<sub>2</sub> electrolytes in CO<sub>2</sub>-saturated anhydrous acetonitrile.

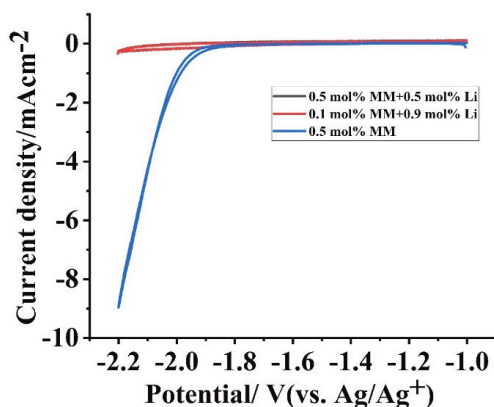


**Figure 7.5.** Cyclic voltammety results for CO<sub>2</sub> reduction in anhydrous acetonitrile obtained with different mixtures of MM and Li cations. NTF<sub>2</sub> was the common anion and total salinity was kept the same. The curves of 0.9 and 0.5 mol% Li overlap.

**Figure 7.5** shows cyclic voltammety results for CO<sub>2</sub> reduction in anhydrous MeCN when Li cations are added to MM in the electrolyte. We notice as soon as Li is introduced to the electrolyte mixture, CO<sub>2</sub> reduction activity is completely suppressed. This observation already implies the stronger impact of alkali metal cations which can be due to their more hydrophilic nature and stronger adsorption on the electrode surface.



## Conclusion

In summary, this chapter investigated the impact of alkyl chain length in imidazolium cations and the influence of alkali metal cations on non-aqueous CO<sub>2</sub> reduction. The results revealed that longer alkyl chain lengths in imidazolium cations did not improve the performance of non-aqueous CO<sub>2</sub> reduction. Instead, smaller cations with higher charge densities showed more favorable electrochemical activities. The introduction of alkali metal cations, which are widely studied electrolytes for aqueous CO<sub>2</sub> reduction, had a negative effect and often led to the complete suppression of CO<sub>2</sub> reduction activity. This phenomenon, as explained by numerous studies, can be attributed to the formation of alkali metal carbonate species, which passivate the active electrode surface and hinder reduction in aprotic solvents. Future research should focus on addressing this challenge to enable a valid comparison between imidazolium cations and alkali metal cations for non-aqueous CO<sub>2</sub> reduction – for example by adding an organic acid to acetonitrile. By overcoming this hurdle, valuable insights can be gained for optimizing the performance of non-aqueous CO<sub>2</sub> reduction systems.



# Supporting Information

## Table of Contents

- I. Materials
- II. Experimental methods
- III. Computational methods
- IV. GC analysis and calculation of faradaic efficiencies

## **I. Materials**

1,3-Dimethylimidazolium bis(trifluoromethylsulfonyl)imide (99%) was purchased from Iolitec Ionic Liquids Technologies GmbH. Potassium bis(trifluoromethanesulfonyl)imide (97%) and Lithium bis(trifluoromethanesulfonyl)imide (98%) were obtained from Alfa Aesar. Cesium bis(trifluoromethanesulfonyl)imide (98%) was obtained from TCI. Milli-Q water was taken from a Milli-Q Advantage A10 Water Purification System, Millipore (18 M $\Omega$ .cm). All chemicals were transferred to a nitrogen-filled MBraun LabMaster glove box via an antechamber that was either evacuated/refilled with nitrogen, or purged with nitrogen gas, and were used without further treatment. Additional details on Materials can be found in **Chapters 2 and 5**.

## **II. Experimental methods**

For details on experimental methods please see **Chapter 2**.

## **III. Computational methods**

Computational methods used in this Chapter are detailed in **Chapter 3**.

## **IV. GC analysis and faradaic efficiencies**

The procedure to analyze gas/liquid products and analyzing faradaic efficiencies are detailed in **Chapter 2**.

# **Chapter 8:**

## **Summary and Perspectives**

## Summary

This thesis has delved into the realm of non-aqueous solvents, specifically focusing on the synergy between imidazolium cations and dry acetonitrile for electrochemical reduction of CO<sub>2</sub>. The initial phase of this work involved the establishment of a universal protocol for conducting electrochemical CO<sub>2</sub> reduction experiments under strictly anhydrous conditions (**Chapter 2**). It became evident that the presence of other metals, whether in the form of counter electrodes or reference electrodes, could significantly impact the experimental outcomes. To mitigate potential artifacts in potential recording, a refined protocol was developed, ensuring the integrity of the obtained results.

In **Chapter 3**, the integration of 0.5 mol% of 1,3-dimethyl imidazolium NTf<sub>2</sub> (**MM** NTf<sub>2</sub>) into acetonitrile was revealed to substantially enhance the reaction kinetics of CO<sub>2</sub> reduction on Au electrodes, as evidenced through comparison with alternative cations such as ammonium types and alkali metals. Notably, among the 1,3-dialkyl imidazolium cations studied, **MM** exhibited superior performance, allowing for the lowest overpotential required for CO<sub>2</sub> reduction at the same current density. Through a combination of DFT calculations, observations of the inverse kinetic isotope effect, and electrochemical studies, a pivotal role of C2-hydrogenated imidazolium cations in promoting reaction kinetics was uncovered. This mechanism revolves around hydrogen bonding donation to the Au-adsorbed CO<sub>2</sub> molecule, thereby facilitating the initial electron transfer. Intriguingly, this phenomenon shares resemblances with low-barrier hydrogen bonds observed in enzyme catalysis..

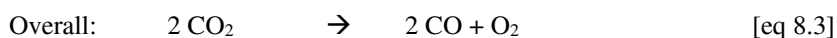
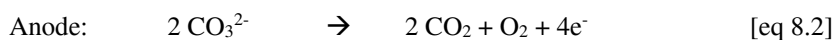
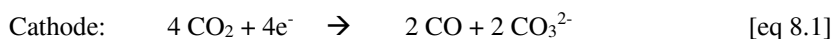
Building on the foundation established in Chapter 3, new avenues for exploration emerged, focusing on the refinement of imidazolium cation performance through modifications in their electronic properties (**Chapter 4**). C4,C5-substituted imidazolium cations were synthesized to investigate their potential in enhancing CO<sub>2</sub> reduction efficiency. However, this endeavor

introduced an additional layer of complexity, primarily stemming from the impact of steric hindrance due to the inclusion of bulkier substituents like phenyl functional groups. This factor could potentially impede CO<sub>2</sub> diffusion to the catalyst site and hinder the coordination of the C2-H to the CO<sub>2</sub> adsorbed on the Au surface. In the case of the most acidic cation, 1,3-dimethyl-4,5-dichloro imidazolium, the lowest overpotential for CO<sub>2</sub> activation was observed. However, the results of electrolysis remained inconclusive, necessitating further investigation. Thus, a delicate equilibrium between steric and electronic effects (the acidity of the C2-H) must be maintained to ensure the cation's electrochemical reactivity falls within the optimal range for CO<sub>2</sub> reduction.

The performance of the anhydrous MM-acetonitrile electrolyte for CO<sub>2</sub> reduction was further highlighted by achieving 100% faradaic efficiency for CO<sub>2</sub> to CO conversion across both noble and non-noble metals, including Zn and Ni, all achieved at relatively low overpotentials (**Chapter 5**). DFT calculations and electrochemical experiments unveiled a volcano plot, positioning the Au electrode at the apex for the highest performance. Zn and Ni electrodes, representing respectively the lowest and highest CO intermediate adsorption capacities, exhibited relatively diminished activity for CO<sub>2</sub> reduction. This volcano plot bore resemblance to the one previously identified in aqueous media. However, the introduction of imidazolium cations appeared to influence the relative catalytic activity between different catalysts, suggesting avenues for future in-depth investigation.

**Chapter 6** was dedicated to an ATR-FTIR study of the performance of C2-methylated imidazolium cations for non-aqueous CO<sub>2</sub> reduction. The main product observed was the formation of CO, with minor byproducts such as formate (likely originating from residual water in these experiments) and oxalate, suggesting the existence of multiple pathways for CO<sub>2</sub> reduction when this cation was employed in our system. The formation of CO as the major product was proposed to be accompanied by the generation of carbonate ions (CO<sub>3</sub><sup>2-</sup>), a

phenomenon also detected through ATR-FTIR measurements. This carbonate species was hypothesized to be formed by the conversion of a second CO<sub>2</sub> molecule, acting as an oxygen acceptor. As for the accompanying anodic reaction, residual water might have undergone conversion to form O<sub>2</sub> (along with protons), or alternatively, carbonate ions could have been oxidized to generate CO<sub>2</sub> and O<sub>2</sub>. If the latter reaction prevailed, the electrochemical cycle concluded as follows:



This hypothesis gained further substantiation through experiments where the degradation of the counter graphite electrode was observed as an alternative sacrificial anodic oxidation upon the introduction of diffusion barriers between the cathode and anode (see **Appendix Section A.II**). This observation supports an oxidation reaction coupled with CO<sub>2</sub> reduction, as was proposed above with carbonate oxidation.

In **Chapter 7**, the investigation focused on examining the impact of alkyl chain length at the C1-position of the C2-hydrogenated cation. It was discovered that longer alkyl chain lengths led to reduced performance in CO<sub>2</sub> reduction. This observation aligned with the adverse effects of steric hindrance observed with bulky substituents at the C4 and C5 positions in Chapter 4. Additionally, experiments involving alkali metal cations were conducted for the purpose of comparison with imidazolium cations. However, the results showed very poor performance and even degradation of the electrolyte due to significant overpotential. This phenomenon was attributed to electrode passivation in experiments involving alkali metal cations within the anhydrous media.

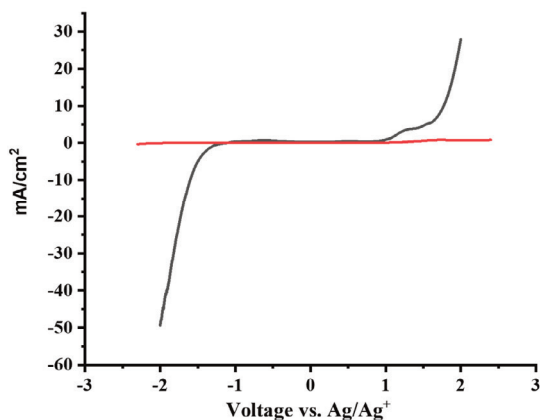


## Perspectives

An intriguing feature that awaits resolution in future investigations is the subtle distinction in the promotional impact of imidazolium cations and alkali metals. Considering the results from this thesis and drawing insights from previous endeavors, we can now propose that both categories of cations play a pivotal role in promoting CO<sub>2</sub> reduction by providing essential solvation/stabilization for the negatively charged \*CO<sub>2</sub><sup>-</sup> intermediate. While this thesis has expounded upon the hydrogen bonding as primary source of the promotional effect for C<sub>2</sub> hydrogenated cations, alkali metals have been argued to promote the reaction through short-range electrostatic interactions. The difference in the nature and the extent to which they efficiently stabilize the \*CO<sub>2</sub><sup>-</sup> intermediate holds theoretical and experimental interest for future study.

Throughout this thesis, we meticulously investigated the performance of imidazolium cations in dry acetonitrile, with occasional deviations due to unavoidable atmospheric exposure. While our efforts maintained relatively dry conditions, which correlated with the observed 100% faradaic efficiency for CO formation, a critical consideration arises when desiring altered selectivity for hydrogenated products. This shift necessitates the presence of proton donors in the system. Remarkably, inadvertent water introduction to the experimental setup led to the unexpected observation of ethanol as a product during experiments with a Ni electrode in the presence of water within MM-acetonitrile electrolytes (see **Appendix Section A.I**). Although requiring further validation, this observation implies the potential manipulation of product outcomes within imidazolium-acetonitrile electrolytes through controlled addition of proton donors. The impact of water on product selectivity has also been highlighted in prior work by Mendieta-Reyes et al.<sup>119</sup> Their findings revealed the emergence of methanol on TiO<sub>2</sub> electrodes in acetonitrile containing 0.5 M water, highlighting the potential role of water as a moderator in the selectivity landscape.

From a process perspective, this thesis discussed the inherent advantages of non-aqueous imidazolium-acetonitrile electrolytes. Among these benefits is the enhancement in CO<sub>2</sub> solubility, reported to be 8 times higher than that of water under atmospheric conditions, accompanied by the concurrent suppression of the competing hydrogen evolution reaction.

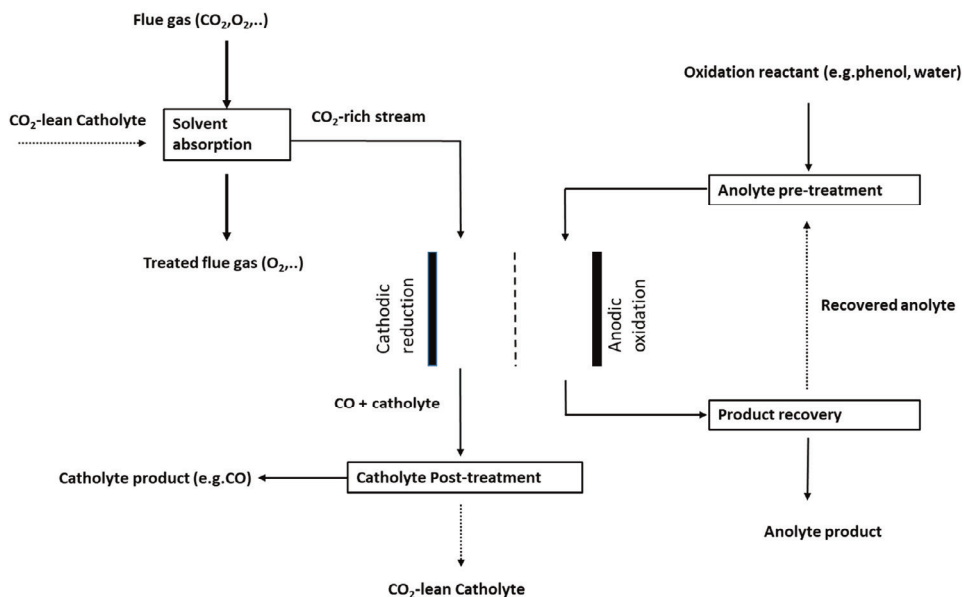


The broad electrochemical window of non-aqueous imidazolium-acetonitrile enables the incorporation of oxidation reactions that possess kinetics distinct from those of water oxidation, which is dominant in aqueous media.

**Figure 8.1.** Electrochemical window of 1,3-dimethyl imidazolium (MM)-acetonitrile vs MM-water. LSVs for Au disk electrode under a purge of He in water with 0.5 mol% of MM Cl (red) and in acetonitrile with 0.5 mol% of MM NTf<sub>2</sub>.

Under conditions of mass transfer control, the heightened CO<sub>2</sub> absorption capacity of MeCN-imidazolium electrolyte facilitates an improved CO<sub>2</sub> conversion rate compared to aqueous media. Another significant characteristic of a non-aqueous imidazolium electrolyte is its wide electrochemical window (as illustrated in **Figure 8.1**). The stability of this electrolyte offers opportunities to integrate desired oxidation reactions with the CO<sub>2</sub> reduction process. For instance, examples include the electrosynthesis of acetophenone<sup>142</sup> and the oxidative dimerization of stilbene in acetonitrile<sup>143</sup>. As long as the reactants and products of the oxidation reaction do not interfere with the CO<sub>2</sub> co-catalyzed reduction reaction, a membrane-free cell can also be envisaged for such a paired electrolysis system.

In conclusion, considering the complexities and challenges associated with aqueous media – despite the environmentally- friendly nature of this electrolyte -, the advantages discussed throughout this thesis of non-aqueous imidazolium electrolytes underscore the potential for using these process conditions for CO<sub>2</sub> reduction. This opens avenues for both fundamental and engineering research in this field. One pivotal question that necessitates exploration is the potential role of imidazolium cations (or azolium types in a more general sense) in stabilizing intermediates within the pathways of C2 and C3 products, particularly on electrodes with higher affinity for CO intermediates. Could this lead to the development of more selective process for C2 and C3 products? This, coupled with the potential influence of proton donors, presents a promising direction for future investigations. These pursuits will demand the utilization of computational studies, modular synthesis techniques, in situ spectroscopy, and comprehensive electrolysis analyses. From a process perspective, numerous opportunities exist to leverage the absorption properties of non-aqueous imidazolium electrolytes and to explore CO<sub>2</sub> reduction under diverse process conditions. As previously suggested, the concept of paired electrolysis holds significant promise, calling for the incorporation of organic electrosynthesis, a burgeoning area of research (**Scheme 8.1**) . Furthermore, it presents an exciting avenue for future industrial trials, particularly in scenarios where oxygen evolution may not be the optimal coupled reaction for CO<sub>2</sub> electrolysis.



**Scheme 8.1. Schematic Illustration of the Integration of CO<sub>2</sub> Solvent Absorption and Paired Organic Electrosynthesis.** A solvent with high CO<sub>2</sub> solubility serves as the absorption medium for the catholyte electrolyte, enabling high CO<sub>2</sub> concentration and, consequently, enhanced conversion rates within a given electrolyte volume and reactor. The choice of the oxidation reaction is dictated by the specific requirements of the cathodic reaction. For instance, in the case of cathodic conversion to hydrogenated products, an oxidation reaction producing protons as byproducts can be envisaged. The coupling should also consider the utilization of side products from cathodic conversion such as carbonate species.

## Appendix

### A.I. Wet experiments with Ni electrode in MeCN-MM electrolyte

CO<sub>2</sub> reduction experiments were conducted with 0.5 mol% of MM NTf<sub>2</sub> in acetonitrile under wet conditions– using a Ni wire electrode. Post-electrolysis NMR analysis revealed the presence of ethanol as one of the products (**Figure A.I.1-2**). To contrast the results obtained under wet conditions, CO<sub>2</sub> reduction experiments were also performed with 0.5 mol% of MM NTf<sub>2</sub> in acetonitrile under dry conditions. Post-electrolysis NMR analysis did not identify the presence of water and ethanol, and only CO was detected as the product (**Figure A.I.3-4**).

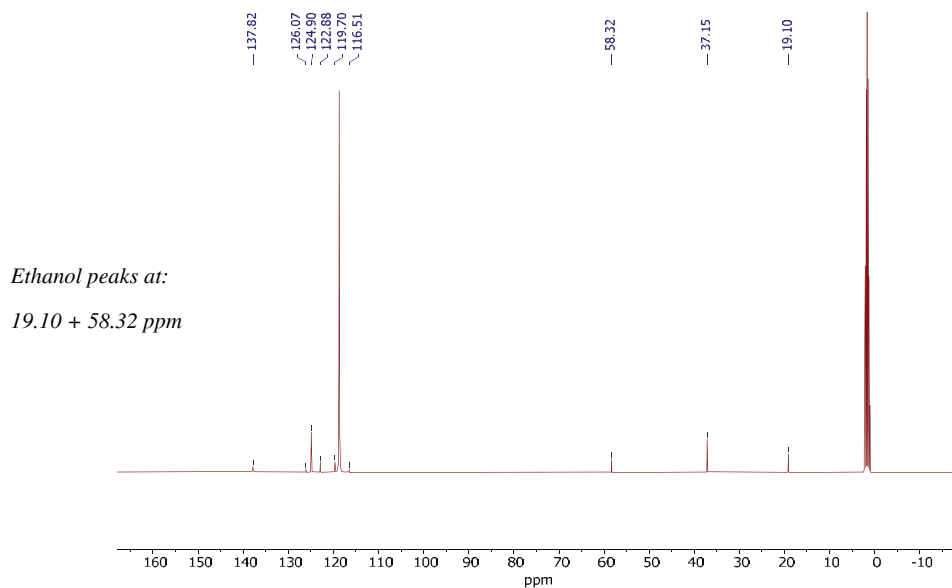


**Figure A.I.1.**  $^{13}\text{C}$  NMR spectrum of 1,3-dimethyl imidazolium bis(trifluoromethylsulfonyl)imide after electrolysis at -1 mA/cm<sup>2</sup> in CD<sub>3</sub>CN on Ni electrode in presence of water. The molar ratio of water to imidazolium was 1:8.8).

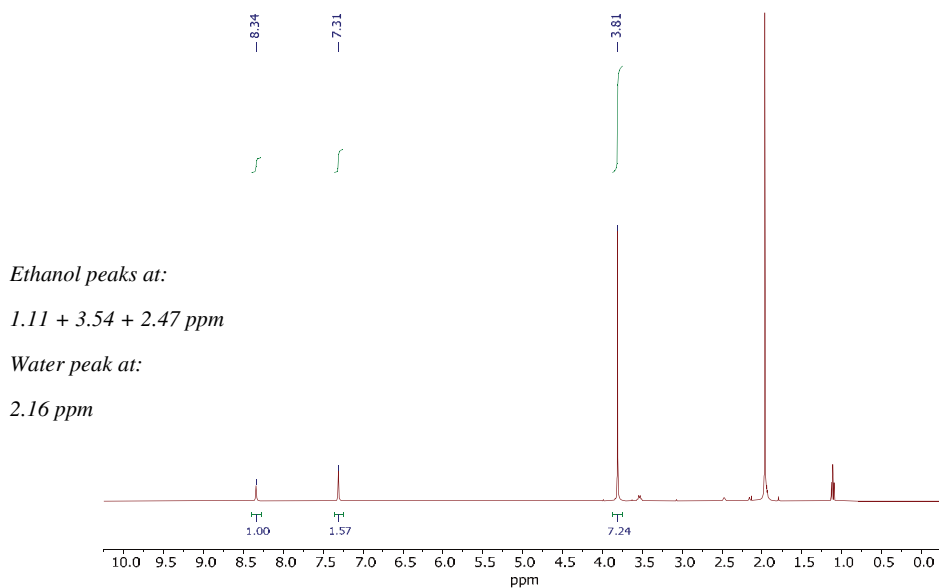


**Figure A.I.2.**  $^1\text{H}$  NMR spectrum of 1,3-dimethyl imidazolium bis(trifluoromethylsulfonyl)imide after electrolysis at -1 mA/cm<sup>2</sup> in CD<sub>3</sub>CN on Ni electrode in presence of water.

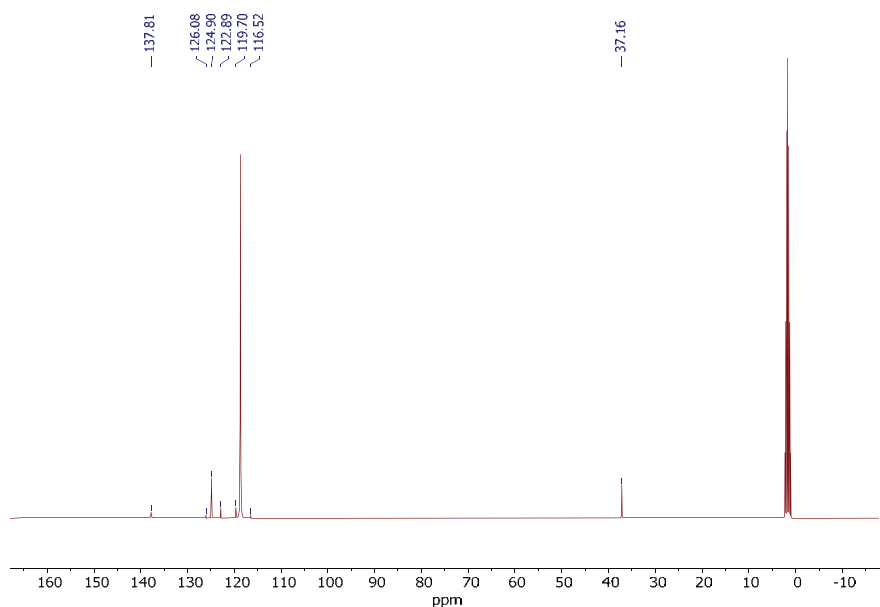


**Figure A.I.3.**  $^{13}\text{C}$  NMR spectrum of 1,3-dimethyl imidazolium bis(trifluoromethylsulfonyl)imide after electrolysis at  $-1\text{ mA/cm}^2$  in  $\text{CD}_3\text{CN}$  on Ni electrode in anhydrous condition.

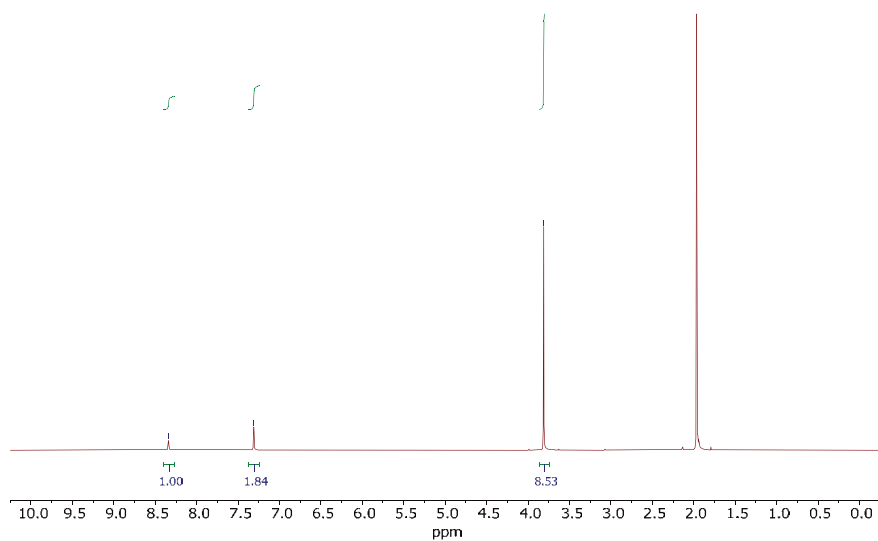


**Figure A.I.4.**  $^1\text{H}$  NMR spectrum of 1,3-dimethyl imidazolium bis(trifluoromethylsulfonyl)imide after electrolysis at  $-1\text{ mA/cm}^2$  in  $\text{CD}_3\text{CN}$  on Ni electrode in anhydrous condition.

## A.II. Experiments with frit between anolyte and catholyte

A supplementary experiment was conducted using a graphite electrode contained within a capillary tube, isolated from the catholyte by a glass frit. **Figure A.II.1(left)** showcases the initial setup of the cell before electrolysis, while **Figure A.II.1 (right)** depicts the same cell after undergoing 30 minutes of electrolysis. Evidently, the experiment exhibited significant degradation and subsequent deposition of graphite at the frit. Despite this degradation, CO continued to be produced with a high faradaic efficiency from the catholyte. However, the deposition of graphite led to the termination of the experiment within 30 minutes. Interestingly, this form of degradation was not observed in our standard experiments where the catholyte and anolyte were not separated. This observation suggests that, in our conventional setup, the CO<sub>2</sub> reduction reaction facilitates the reactants required for the oxidation reaction. As no other discernible product was identified, and in light of our ATR-FTIR study in Chapter 6, we propose the involvement of carbonate as an oxygen carrier in this reaction.

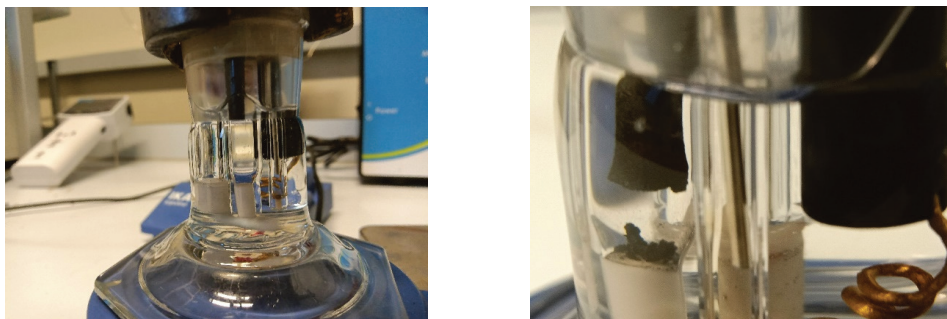


**Figure A.II.1.** Images of the reactor before (left) and after (right) electrolysis with 0.5 molar MM NTF<sub>2</sub> in dry anhydrous acetonitrile. The working electrode is Au wire, and the counter electrode is graphite. The counter electrode is separated from the catholyte with a frit.



# References

1. The Electronic Factor in Heterogeneous Catalysis. In *Fundamental Concepts in Heterogeneous Catalysis*, 2014; pp 114-137.
2. The Potential Energy Diagram. In *Fundamental Concepts in Heterogeneous Catalysis*, 2014; pp 6-25.
3. Sun, L.; Ramesha, G. K.; Kamat, P. V.; Brennecke, J. F., Switching the Reaction Course of Electrochemical CO<sub>2</sub> Reduction with Ionic Liquids. *Langmuir* **2014**, *30* (21), 6302-6308.
4. Wang, Y.; Hatakeyama, M.; Ogata, K.; Wakabayashi, M.; Jin, F.; Nakamura, S., Activation of CO<sub>2</sub> by ionic liquid EMIM-BF<sub>4</sub> in the electrochemical system: a theoretical study. *Physical Chemistry Chemical Physics* **2015**, *17* (36), 23521-23531.
5. Hopkinson, M. N.; Richter, C.; Schedler, M.; Glorius, F., An overview of N-heterocyclic carbenes. *Nature* **2014**, *510* (7506), 485-496.
6. Amit, E.; Dery, L.; Dery, S.; Kim, S.; Roy, A.; Hu, Q.; Gutkin, V.; Eisenberg, H.; Stein, T.; Mandler, D.; Dean Toste, F.; Gross, E., Electrochemical deposition of N-heterocyclic carbene monolayers on metal surfaces. *Nature Communications* **2020**, *11* (1), 5714.
7. Kuhl, K. P.; Hatsukade, T.; Cave, E. R.; Abram, D. N.; Kibsgaard, J.; Jaramillo, T. F., Electrocatalytic Conversion of Carbon Dioxide to Methane and Methanol on Transition Metal Surfaces. *Journal of the American Chemical Society* **2014**, *136* (40), 14107-14113.
8. Lau, G. P. S.; Schreier, M.; Vasilyev, D.; Scopelliti, R.; Grätzel, M.; Dyson, P. J., New Insights Into the Role of Imidazolium-Based Promoters for the Electroreduction of CO<sub>2</sub> on a Silver Electrode. *Journal of the American Chemical Society* **2016**, *138* (25), 7820-7823.
9. Gawel, A.; Jaster, T.; Siegmund, D.; Holzmann, J.; Lohmann, H.; Klemm, E.; Apfel, U.-P., Electrochemical CO<sub>2</sub> reduction - The macroscopic world of electrode design, reactor concepts & economic aspects. *iScience* **2022**, *25* (4), 104011.
10. Gao, S.; Lin, Y.; Jiao, X.; Sun, Y.; Luo, Q.; Zhang, W.; Li, D.; Yang, J.; Xie, Y., Partially oxidized atomic cobalt layers for carbon dioxide electroreduction to liquid fuel. *Nature* **2016**, *529* (7584), 68-71.
11. Roberts, F. S.; Kuhl, K. P.; Nilsson, A., High Selectivity for Ethylene from Carbon Dioxide Reduction over Copper Nanocube Electrocatalysts. *Angewandte Chemie International Edition* **2015**, *54* (17), 5179-5182.
12. Gu, J.; Hsu, C.-S.; Bai, L.; Chen, H. M.; Hu, X., Atomically dispersed Fe<sup>3+</sup> sites catalyze efficient CO<sub>2</sub> electroreduction to CO. *Science* **2019**, *364* (6445), 1091-1094.
13. Liu, K.; Smith, W. A.; Burdyny, T., Introductory Guide to Assembling and Operating Gas Diffusion Electrodes for Electrochemical CO<sub>2</sub> Reduction. *ACS Energy Letters* **2019**, *4* (3), 639-643.
14. Ma, M.; Clark, E. L.; Therkildsen, K. T.; Dalsgaard, S.; Chorkendorff, I.; Seger, B., Insights into the carbon balance for CO<sub>2</sub> electroreduction on Cu using gas diffusion electrode reactor designs. *Energy & Environmental Science* **2020**, *13* (3), 977-985.
15. Higgins, D.; Hahn, C.; Xiang, C.; Jaramillo, T. F.; Weber, A. Z., Gas-Diffusion Electrodes for Carbon Dioxide Reduction: A New Paradigm. *ACS Energy Letters* **2019**, *4* (1), 317-324.
16. Akira, M.; Yoshio, H., Product Selectivity Affected by Cationic Species in Electrochemical Reduction of CO<sub>2</sub> and CO at a Cu Electrode. *Bulletin of the Chemical Society of Japan* **1991**, *64* (1), 123-127.
17. Singh, M. R.; Kwon, Y.; Lum, Y.; Ager, J. W.; Bell, A. T., Hydrolysis of Electrolyte Cations Enhances the Electrochemical Reduction of CO<sub>2</sub> over Ag and Cu. *Journal of the American Chemical Society* **2016**, *138* (39), 13006-13012.
18. Resasco, J.; Chen, L. D.; Clark, E.; Tsai, C.; Hahn, C.; Jaramillo, T. F.; Chan, K.; Bell, A. T., Promoter Effects of Alkali Metal Cations on the Electrochemical Reduction of Carbon Dioxide. *Journal of the American Chemical Society* **2017**, *139* (32), 11277-11287.

19. Birdja, Y. Y.; Pérez-Gallent, E.; Figueiredo, M. C.; Göttle, A. J.; Calle-Vallejo, F.; Koper, M. T. M., Advances and challenges in understanding the electrocatalytic conversion of carbon dioxide to fuels. *Nature Energy* **2019**, *4* (9), 732-745.
20. Sun, Z.; Ma, T.; Tao, H.; Fan, Q.; Han, B., Fundamentals and Challenges of Electrochemical CO<sub>2</sub> Reduction Using Two-Dimensional Materials. *Chem* **2017**, *3* (4), 560-587.
21. Figueiredo, M. C.; Ledezma-Yanez, I.; Koper, M. T. M., In Situ Spectroscopic Study of CO<sub>2</sub> Electroreduction at Copper Electrodes in Acetonitrile. *ACS Catalysis* **2016**, *6* (4), 2382-2392.
22. Blake, J. W.; Padding, J. T.; Haverkort, J. W., Analytical modelling of CO<sub>2</sub> reduction in gas-diffusion electrode catalyst layers. *Electrochimica Acta* **2021**, *393*, 138987.
23. Matsubara, Y., Standard Electrode Potentials for the Reduction of CO<sub>2</sub> to CO in Acetonitrile–Water Mixtures Determined Using a Generalized Method for Proton-Coupled Electron-Transfer Reactions. *ACS Energy Letters* **2017**, *2* (8), 1886-1891.
24. Wakerley, D.; Lamaison, S.; Wicks, J.; Clemens, A.; Feaster, J.; Corral, D.; Jaffer, S. A.; Sarkar, A.; Fontecave, M.; Duoss, E. B.; Baker, S.; Sargent, E. H.; Jaramillo, T. F.; Hahn, C., Gas diffusion electrodes, reactor designs and key metrics of low-temperature CO<sub>2</sub> electrolyzers. *Nature Energy* **2022**, *7* (2), 130-143.
25. Wuttig, A.; Yoon, Y.; Ryu, J.; Surendranath, Y., Bicarbonate Is Not a General Acid in Au-Catalyzed CO<sub>2</sub> Electroreduction. *Journal of the American Chemical Society* **2017**, *139* (47), 17109-17113.
26. Zhu, S.; Jiang, B.; Cai, W.-B.; Shao, M., Direct Observation on Reaction Intermediates and the Role of Bicarbonate Anions in CO<sub>2</sub> Electrochemical Reduction Reaction on Cu Surfaces. *Journal of the American Chemical Society* **2017**, *139* (44), 15664-15667.
27. Goyal, A.; Marcandalli, G.; Mints, V. A.; Koper, M. T. M., Competition between CO<sub>2</sub> Reduction and Hydrogen Evolution on a Gold Electrode under Well-Defined Mass Transport Conditions. *Journal of the American Chemical Society* **2020**, *142* (9), 4154-4161.
28. Ooka, H.; Figueiredo, M. C.; Koper, M. T. M., Competition between Hydrogen Evolution and Carbon Dioxide Reduction on Copper Electrodes in Mildly Acidic Media. *Langmuir* **2017**, *33* (37), 9307-9313.
29. Li, C. W.; Kanan, M. W., CO<sub>2</sub> Reduction at Low Overpotential on Cu Electrodes Resulting from the Reduction of Thick Cu<sub>2</sub>O Films. *Journal of the American Chemical Society* **2012**, *134* (17), 7231-7234.
30. Ren, D.; Wong, N. T.; Handoko, A. D.; Huang, Y.; Yeo, B. S., Mechanistic Insights into the Enhanced Activity and Stability of Agglomerated Cu Nanocrystals for the Electrochemical Reduction of Carbon Dioxide to n-Propanol. *The Journal of Physical Chemistry Letters* **2016**, *7* (1), 20-24.
31. Amatore, C.; Saveant, J. M., Mechanism and kinetic characteristics of the electrochemical reduction of carbon dioxide in media of low proton availability. *Journal of the American Chemical Society* **1981**, *103* (17), 5021-5023.
32. Tomita, Y.; Teruya, S.; Koga, O.; Hori, Y., Electrochemical Reduction of Carbon Dioxide at a Platinum Electrode in Acetonitrile–Water Mixtures. *Journal of The Electrochemical Society* **2000**, *147* (11), 4164.
33. Gong, K.; Fang, Q.; Gu, S.; Li, S. F. Y.; Yan, Y., Nonaqueous redox-flow batteries: organic solvents, supporting electrolytes, and redox pairs. *Energy & Environmental Science* **2015**, *8* (12), 3515-3530.
34. König, M.; Lin, S.-H.; Vaes, J.; Pant, D.; Klemm, E., Integration of aprotic CO<sub>2</sub> reduction to oxalate at a Pb catalyst into a GDE flow cell configuration. *Faraday Discussions* **2021**, *230* (0), 360-374.
35. Tomita, Y.; Teruya, S.; Koga, O.; Hori, Y., Electrochemical Reduction of Carbon Dioxide at a Platinum Electrode in Acetonitrile–Water Mixtures. *Journal of The Electrochemical Society* **2000**, *147* (11), 4164.
36. Christensen, P. A.; Hamnett, A.; Muir, A. V. G.; Freeman, N. A., CO<sub>2</sub> reduction at platinum, gold and glassy carbon electrodes in acetonitrile: An in-situ FTIR study. *Journal of Electroanalytical Chemistry and Interfacial Electrochemistry* **1990**, *288* (1), 197-215.

37. dos Reis, E. A.; da Silva, G. T. S. T.; Santiago, E. I.; Ribeiro, C., Revisiting Electrocatalytic CO<sub>2</sub> Reduction in Nonaqueous Media: Promoting CO<sub>2</sub> Recycling in Organic Molecules by Controlling H<sub>2</sub> Evolution. *Energy Technology* **2023**, *11* (6), 2201367.
38. Hori, Y., Electrochemical CO<sub>2</sub> Reduction on Metal Electrodes. In *Modern Aspects of Electrochemistry*, Vayenas, C. G.; White, R. E.; Gamboa-Aldeco, M. E., Eds. Springer New York: New York, NY, 2008; pp 89-189.
39. Kai, T.; Zhou, M.; Duan, Z.; Henkelman, G. A.; Bard, A. J., Detection of CO<sub>2</sub>•<sup>-</sup> in the Electrochemical Reduction of Carbon Dioxide in N,N-Dimethylformamide by Scanning Electrochemical Microscopy. *Journal of the American Chemical Society* **2017**, *139* (51), 18552-18557.
40. Pei, Y.; Zhong, H.; Jin, F., A brief review of electrocatalytic reduction of CO<sub>2</sub>—Materials, reaction conditions, and devices. *Energy Science & Engineering* **2021**, *9* (7), 1012-1032.
41. Lv, J.-J.; Yin, R.; Zhou, L.; Li, J.; Kikas, R.; Xu, T.; Wang, Z.-J.; Jin, H.; Wang, X.; Wang, S., Microenvironment Engineering for the Electrocatalytic CO<sub>2</sub> Reduction Reaction. *Angewandte Chemie International Edition* **2022**, *61* (39), e202207252.
42. Hahn, C.; Jaramillo, T. F., Using Microenvironments to Control Reactivity in CO<sub>2</sub> Electrocatalysis. *Joule* **2020**, *4* (2), 292-294.
43. Nitopi, S.; Bertheussen, E.; Scott, S. B.; Liu, X.; Engstfeld, A. K.; Horch, S.; Seger, B.; Stephens, I. E. L.; Chan, K.; Hahn, C.; Nørskov, J. K.; Jaramillo, T. F.; Chorkendorff, I., Progress and Perspectives of Electrochemical CO<sub>2</sub> Reduction on Copper in Aqueous Electrolyte. *Chemical Reviews* **2019**, *119* (12), 7610-7672.
44. Gennaro, A.; Isse, A. A.; Severin, M.-G.; Vianello, E.; Bhugun, I.; Savéant, J.-M., Mechanism of the electrochemical reduction of carbon dioxide at inert electrodes in media of low proton availability. *Journal of the Chemical Society, Faraday Transactions* **1996**, *92* (20), 3963-3968.
45. Desilvestro, J.; Pons, S., The cathodic reduction of carbon dioxide in acetonitrile: An electrochemical and infrared spectroelectrochemical study. *Journal of Electroanalytical Chemistry and Interfacial Electrochemistry* **1989**, *267* (1), 207-220.
46. Eneau-Innocent, B.; Pasquier, D.; Francois, R.; Leger, J.-M.; Kokoh, K. B., Electroreduction of carbon dioxide at a lead electrode in propylene carbonate: A spectroscopic study. *Applied Catalysis B Environmental* **2010**, *98*, 65-71.
47. Boor, V.; Frijns, J. E. B. M.; Perez-Gallent, E.; Giling, E.; Laitinen, A. T.; Goetheer, E. L. V.; van den Broeke, L. J. P.; Kortlever, R.; de Jong, W.; Moulto, O. A.; Vlugt, T. J. H.; Ramdin, M., Electrochemical Reduction of CO<sub>2</sub> to Oxalic Acid: Experiments, Process Modeling, and Economics. *Industrial & Engineering Chemistry Research* **2022**, *61* (40), 14837-14846.
48. König, M.; Vaes, J.; Klemm, E.; Pant, D., Solvents and Supporting Electrolytes in the Electrocatalytic Reduction of CO<sub>2</sub>. *iScience* **2019**, *19*, 135-160.
49. Monteiro, M. C. O.; Dattila, F.; Hagedoorn, B.; García-Muelas, R.; López, N.; Koper, M. T. M., Absence of CO<sub>2</sub> electroreduction on copper, gold and silver electrodes without metal cations in solution. *Nature Catalysis* **2021**, *4* (8), 654-662.
50. Rosen, B. A.; Salehi-Khojin, A.; Thorson, M. R.; Zhu, W.; Whipple, D. T.; Kenis, P. J. A.; Masel, R. I., Ionic Liquid-Mediated Selective Conversion of CO<sub>2</sub> to CO at Low Overpotentials. *Science* **2011**, *334* (6056), 643-644.
51. Atifi, A.; Boyce, D. W.; DiMeglio, J. L.; Rosenthal, J., Directing the Outcome of CO<sub>2</sub> Reduction at Bismuth Cathodes Using Varied Ionic Liquid Promoters. *ACS Catalysis* **2018**, *8* (4), 2857-2863.
52. Sung, S.; Kumar, D.; Gil-Sepulcre, M.; Nippe, M., Electrocatalytic CO<sub>2</sub> Reduction by Imidazolium-Functionalized Molecular Catalysts. *Journal of the American Chemical Society* **2017**, *139* (40), 13993-13996.
53. Lim, H.-K.; Kwon, Y.; Kim, H. S.; Jeon, J.; Kim, Y.-H.; Lim, J.-A.; Kim, B.-S.; Choi, J.; Kim, H., Insight into the Microenvironments of the Metal-Ionic Liquid Interface during Electrochemical CO<sub>2</sub> Reduction. *ACS Catalysis* **2018**, *8* (3), 2420-2427.
54. Rosen, B. A.; Haan, J. L.; Mukherjee, P.; Braunschweig, B.; Zhu, W.; Salehi-Khojin, A.; Dlott, D. D.; Masel, R. I., In Situ Spectroscopic Examination of a Low Overpotential Pathway for Carbon Dioxide Conversion to Carbon Monoxide. *The Journal of Physical Chemistry C* **2012**, *116* (29), 15307-15312.

55. Kemna, A.; García Rey, N.; Braunschweig, B., Mechanistic Insights on CO<sub>2</sub> Reduction Reactions at Platinum/[BMIM][BF<sub>4</sub>] Interfaces from In Operando Spectroscopy. *ACS Catalysis* **2019**, *9* (7), 6284-6292.
56. Kuhl, K. P.; Cave, E. R.; Abram, D. N.; Jaramillo, T. F., New insights into the electrochemical reduction of carbon dioxide on metallic copper surfaces. *Energy & Environmental Science* **2012**, *5* (5), 7050-7059.
57. Snook, G. A.; Best, A.; Pandolfo, A. G.; Hollenkamp, A. F., Evaluation of a Ag|Ag<sup>+</sup> reference electrode for use in room temperature ionic liquids. *Electrochemistry Communications* **2006**, *8*, 1405-1411.
58. Pavlishchuk, V. V.; Addison, A. W., Conversion constants for redox potentials measured versus different reference electrodes in acetonitrile solutions at 25°C. *Inorganica Chimica Acta* **2000**, *298* (1), 97-102.
59. Joshi, P. B.; Karki, N.; Wilson, A. J., Electrocatalytic CO<sub>2</sub> Reduction in Acetonitrile Enhanced by the Local Environment and Mass Transport of H<sub>2</sub>O. *ACS Energy Letters* **2022**, *7* (2), 602-609.
60. Díaz-Duque, Á.; Sandoval-Rojas, A. P.; Molina-Osorio, A. F.; Feliu, J. M.; Suárez-Herrera, M. F., Electrochemical reduction of CO<sub>2</sub> in water-acetonitrile mixtures on nanostructured Cu electrode. *Electrochemistry Communications* **2015**, *61*, 74-77.
61. Oh, Y.; Vrabel, H.; Guidoux, S.; Hu, X., Electrochemical reduction of CO<sub>2</sub> in organic solvents catalyzed by MoO<sub>2</sub>. *Chemical Communications* **2014**, *50* (29), 3878-3881.
62. Garrison, J. C.; Youngs, W. J., Ag(I) N-Heterocyclic Carbene Complexes: Synthesis, Structure, and Application. *Chemical Reviews* **2005**, *105* (11), 3978-4008.
63. Zhukhovitskiy, A. V.; Mavros, M. G.; Van Voorhis, T.; Johnson, J. A., Addressable Carbene Anchors for Gold Surfaces. *Journal of the American Chemical Society* **2013**, *135* (20), 7418-7421.
64. Lara, P.; Rivada-Wheelaghan, O.; Conejero, S.; Poteau, R.; Philippot, K.; Chaudret, B., Ruthenium nanoparticles stabilized by N-heterocyclic carbenes: ligand location and influence on reactivity. *Angewandte Chemie (International ed. in English)* **2011**, *50* (50), 12080-4.
65. Shen, H.; Tian, G.; Xu, Z.; Wang, L.; Wu, Q.; Zhang, Y.; Teo, B. K.; Zheng, N., N-heterocyclic carbene coordinated metal nanoparticles and nanoclusters. *Coordination Chemistry Reviews* **2022**, *458*, 214425.
66. Ratschmeier, B.; Braunschweig, B., Cations of Ionic Liquid Electrolytes Can Act as a Promoter for CO<sub>2</sub> Electrocatalysis through Reactive Intermediates and Electrostatic Stabilization. *The Journal of Physical Chemistry C* **2021**, *125* (30), 16498-16507.
67. Zeng, S.; Zhang, X.; Bai, L.; Zhang, X.; Wang, H.; Wang, J.; Bao, D.; Li, M.; Liu, X.; Zhang, S., Ionic-Liquid-Based CO<sub>2</sub> Capture Systems: Structure, Interaction and Process. *Chemical Reviews* **2017**, *117* (14), 9625-9673.
68. Park, Y.; Lin, K.-Y. A.; Park, A.-H. A.; Petit, C., Recent Advances in Anhydrous Solvents for CO<sub>2</sub> Capture: Ionic Liquids, Switchable Solvents, and Nanoparticle Organic Hybrid Materials. *Frontiers in Energy Research* **2015**, *3*.
69. Magill, A. M.; Cavell, K. J.; Yates, B. F., Basicity of Nucleophilic Carbenes in Aqueous and Nonaqueous Solvents Theoretical Predictions. *Journal of the American Chemical Society* **2004**, *126* (28), 8717-8724.
70. Chu, Y.; Deng, H.; Cheng, J.-P., An Acidity Scale of 1,3-Dialkylimidazolium Salts in Dimethyl Sulfoxide Solution. *The Journal of Organic Chemistry* **2007**, *72* (20), 7790-7793.
71. Hori, Y.; Wakebe, H.; Tsukamoto, T.; Koga, O., Electrocatalytic process of CO selectivity in electrochemical reduction of CO<sub>2</sub> at metal electrodes in aqueous media. *Electrochimica Acta* **1994**, *39*, 1833-1839.
72. Wuttig, A.; Yaguchi, M.; Motobayashi, K.; Osawa, M.; Surendranath, Y., Inhibited proton transfer enhances Au-catalyzed CO<sub>2</sub>-to-fuels selectivity. *Proceedings of the National Academy of Sciences* **2016**, *113* (32), E4585-E4593.
73. Parada, G. A.; Goldsmith, Z. K.; Kolmar, S.; Rimgard, B. P.; Mercado, B. Q.; Hammarström, L.; Hammes-Schiffer, S.; Mayer, J. M., Concerted proton-electron transfer reactions in the Marcus inverted region. *Science* **2019**, *364* (6439), 471-475.

74. Bourrez, M.; Steinmetz, R.; Ott, S.; Gloaguen, F.; Hammarström, L., Concerted proton-coupled electron transfer from a metal-hydride complex. *Nature Chemistry* **2015**, *7* (2), 140-145.
75. Chalkley, M. J.; Garrido-Barros, P.; Peters, J. C., A molecular mediator for reductive concerted proton-electron transfers via electrocatalysis. *Science* **2020**, *369* (6505), 850-854.
76. Inayeh, A.; Groome, R. R. K.; Singh, I.; Veinot, A. J.; de Lima, F. C.; Miwa, R. H.; Crudden, C. M.; McLean, A. B., Self-assembly of N-heterocyclic carbenes on Au(111). *Nature Communications* **2021**, *12* (1), 4034.
77. Vermeeren, P.; van der Lubbe, S. C. C.; Fonseca Guerra, C.; Bickelhaupt, F. M.; Hamlin, T. A., Understanding chemical reactivity using the activation strain model. *Nature Protocols* **2020**, *15* (2), 649-667.
78. Deng, L.; Ziegler, T.; Fan, L., A combined density functional and intrinsic reaction coordinate study on the ground state energy surface of H<sub>2</sub>CO. *The Journal of Chemical Physics* **1993**, *99* (5), 3823-3835.
79. Deng, L.; Ziegler, T., The determination of intrinsic reaction coordinates by density functional theory. *International Journal of Quantum Chemistry* **1994**, *52* (4), 731-765.
80. te Velde, G.; Bickelhaupt, F. M.; Baerends, E. J.; Fonseca Guerra, C.; van Gisbergen, S. J. A.; Snijders, J. G.; Ziegler, T., Chemistry with ADF. *Journal of Computational Chemistry* **2001**, *22* (9), 931-967.
81. Barton Cole, E.; Lakkaraju, P. S.; Rampulla, D. M.; Morris, A. J.; Abelev, E.; Bocarsly, A. B., Using a One-Electron Shuttle for the Multielectron Reduction of CO<sub>2</sub> to Methanol: Kinetic, Mechanistic, and Structural Insights. *Journal of the American Chemical Society* **2010**, *132* (33), 11539-11551.
82. Costentin, C.; Savéant, J.-M.; Tard, C., Catalysis of CO<sub>2</sub> Electrochemical Reduction by Protonated Pyridine and Similar Molecules. Useful Lessons from a Methodological Misadventure. *ACS Energy Letters* **2018**, *3* (3), 695-703.
83. Reece, S. Y.; Nocera, D. G., Proton-coupled electron transfer in biology: results from synergistic studies in natural and model systems. *Annual review of biochemistry* **2009**, *78*, 673-99.
84. Mayer, J. M., PROTON-COUPLED ELECTRON TRANSFER: A Reaction Chemist's View. *Annual Review of Physical Chemistry* **2004**, *55* (1), 363-390.
85. Cleland, W. W., Low-barrier hydrogen bonds and enzymatic catalysis. *Archives of biochemistry and biophysics* **2000**, *382* (1), 1-5.
86. Northrop, D. B., Follow the Protons: A Low-Barrier Hydrogen Bond Unifies the Mechanisms of the Aspartic Proteases. *Accounts of Chemical Research* **2001**, *34* (10), 790-797.
87. Fernandez, P. L.; Murkin, A. S., Inverse Solvent Isotope Effects in Enzyme-Catalyzed Reactions. *Molecules* **2020**, *25* (8), 1933.
88. Stephens, P. J.; Devlin, F. J.; Chabalowski, C. F.; Frisch, M. J., Ab Initio Calculation of Vibrational Absorption and Circular Dichroism Spectra Using Density Functional Force Fields. *The Journal of Physical Chemistry* **1994**, *98* (45), 11623-11627.
89. Grimme, S.; Ehrlich, S.; Goerigk, L., Effect of the damping function in dispersion corrected density functional theory. *Journal of Computational Chemistry* **2011**, *32* (7), 1456-1465.
90. Van Lenthe, E.; Baerends, E. J., Optimized Slater-type basis sets for the elements 1-118. *Journal of computational chemistry* **2003**, *24* (9), 1142-56.
91. Levens, A.; An, F.; Breugst, M.; Mayr, H.; Lupton, D. W., Influence of the N-Substituents on the Nucleophilicity and Lewis Basicity of N-Heterocyclic Carbenes. *Organic Letters* **2016**, *18* (15), 3566-3569.
92. Bi, S.; Wang, R.; Liu, S.; Yan, J.; Mao, B.; Kornyshev, A. A.; Feng, G., Minimizing the electroadsorption of water from humid ionic liquids on electrodes. *Nature Communications* **2018**, *9* (1), 5222.
93. Chen, L. D.; Urushihara, M.; Chan, K.; Nørskov, J. K., Electric Field Effects in Electrochemical CO<sub>2</sub> Reduction. *ACS Catalysis* **2016**, *6* (10), 7133-7139.
94. Ringe, S.; Clark, E. L.; Resasco, J.; Walton, A.; Seger, B.; Bell, A. T.; Chan, K., Understanding cation effects in electrochemical CO<sub>2</sub> reduction. *Energy & Environmental Science* **2019**, *12* (10), 3001-3014.

95. Fonseca Guerra, C.; Handgraaf, J. W.; Baerends, E. J.; Bickelhaupt, F. M., Voronoi deformation density (VDD) charges: Assessment of the Mulliken, Bader, Hirshfeld, Weinhold, and VDD methods for charge analysis. *Journal of computational chemistry* **2004**, *25* (2), 189-210.
96. Hindi, K. M.; Siciliano, T. J.; Durmus, S.; Panzner, M. J.; Medvetz, D. A.; Reddy, D. V.; Hogue, L. A.; Hovis, C. E.; Hilliard, J. K.; Mallet, R. J.; Tessier, C. A.; Cannon, C. L.; Youngs, W. J., Synthesis, Stability, and Antimicrobial Studies of Electronically Tuned Silver Acetate N-Heterocyclic Carbenes. *Journal of Medicinal Chemistry* **2008**, *51* (6), 1577-1583.
97. Fumino, K.; Peppel, T.; Geppert-Rybczyńska, M.; Zaitsau, D. H.; Lehmann, J. K.; Verevkin, S. P.; Köckerling, M.; Ludwig, R., The influence of hydrogen bonding on the physical properties of ionic liquids. *Physical Chemistry Chemical Physics* **2011**, *13* (31), 14064-14075.
98. Bordwell, F. G.; Bausch, M. J., Methyl effects on the basicities of cyclopentadienide and indenide ions and on the chemistry of their transition metal complexes. *Journal of the American Chemical Society* **1983**, *105* (19), 6188-6189.
99. Edlund, U.; Eliasson, B.; Kowalewski, J.; Trogen, L., The electronic structure of the s-indacenyldianion. Structural assessment by nuclear magnetic resonance spectroscopy and molecular orbital calculations. *Journal of the Chemical Society, Perkin Transactions 2* **1981**, (9), 1260-1263.
100. Arduengo, A. J.; Davidson, F.; Dias, H. V. R.; Goerlich, J. R.; Khasnis, D.; Marshall, W. J.; Prakasha, T. K., An Air Stable Carbene and Mixed Carbene "Dimers". *Journal of the American Chemical Society* **1997**, *119* (52), 12742-12749.
101. Fonseca Guerra, C.; Handgraaf, J.-W.; Baerends, E. J.; Bickelhaupt, F. M., Voronoi deformation density (VDD) charges: Assessment of the Mulliken, Bader, Hirshfeld, Weinhold, and VDD methods for charge analysis. *Journal of Computational Chemistry* **2004**, *25* (2), 189-210.
102. Sacchi, R. L.; Velardo, S.; Xiong, L.; Lutterman, D. A.; Rosenthal, J., Copper-Tin Alloys for the Electrocatalytic Reduction of CO<sub>2</sub> in an Imidazolium-Based Non-Aqueous Electrolyte. *Energies* **2019**, *12* (16), 3132.
103. Akhade, S. A.; Luo, W.; Nie, X.; Bernstein, N. J.; Asthagiri, A.; Janik, M. J., Poisoning effect of adsorbed CO during CO<sub>2</sub> electroreduction on late transition metals. *Physical Chemistry Chemical Physics* **2014**, *16* (38), 20429-20435.
104. Gao, D.; Zhang, Y.; Zhou, Z.; Cai, F.; Zhao, X.; Huang, W.; Li, Y.; Zhu, J.; Liu, P.; Yang, F.; Wang, G.; Bao, X., Enhancing CO<sub>2</sub> Electroreduction with the Metal-Oxide Interface. *J Am Chem Soc* **2017**, *139* (16), 5652-5655.
105. Hammer, B.; Nørskov, J. K., Theoretical surface science and catalysis—calculations and concepts. In *Advances in Catalysis*, Academic Press: 2000; Vol. 45, pp 71-129.
106. Nørskov, J. K.; Abild-Pedersen, F.; Studt, F.; Bligaard, T., Density functional theory in surface chemistry and catalysis. *Proceedings of the National Academy of Sciences* **2011**, *108* (3), 937-943.
107. Hammer, B.; Morikawa, Y.; Nørskov, J. K., CO Chemisorption at Metal Surfaces and Overlayers. *Physical Review Letters* **1996**, *76* (12), 2141-2144.
108. Grimme, S.; Bannwarth, C.; Shushkov, P., A Robust and Accurate Tight-Binding Quantum Chemical Method for Structures, Vibrational Frequencies, and Noncovalent Interactions of Large Molecular Systems Parametrized for All spd-Block Elements (Z = 1–86). *Journal of Chemical Theory and Computation* **2017**, *13* (5), 1989-2009.
109. Franchini, M.; Philipsen, P. H. T.; van Lenthe, E.; Visscher, L., Accurate Coulomb Potentials for Periodic and Molecular Systems through Density Fitting. *Journal of Chemical Theory and Computation* **2014**, *10* (5), 1994-2004.
110. Wiesenecker, G.; Velde, G. t.; Baerends, E. J., Analytic quadratic integration over the two-dimensional Brillouin zone. *Journal of Physics C: Solid State Physics* **1988**, *21* (23), 4263.
111. Hoffmann, R., A chemical and theoretical way to look at bonding on surfaces. *Reviews of Modern Physics* **1988**, *60* (3), 601-628.
112. Basic Quantum-Chemical Concepts, The Chemical Bond Revisited (Jointly Written with I. Tranca). In *Modern Heterogeneous Catalysis*, 2017; pp 173-207.
113. Chemical Bonding and Reactivity of Transition Metal Surfaces. In *Modern Heterogeneous Catalysis*, 2017; pp 209-291.

114. Mechanisms of Transition Metal Catalyzed Reactions. In *Modern Heterogeneous Catalysis*, 2017; pp 293-343.
115. Hammer, B.; Norskov, J. K., Why gold is the noblest of all the metals. *Nature* **1995**, *376* (6537), 238-240.
116. Kenta, M.; Naoya, N.; Yuki, I.; Kazuya, M.; Tetsuo, S.; Masatoshi, O., Potential-induced restructuring dynamics of ionic liquids on a gold electrode: Steric effect of constituent ions studied by surface-enhanced infrared absorption spectroscopy. *Journal of Electroanalytical Chemistry* **2017**, *800*, 126-133.
117. Noack, K.; Schulz, P. S.; Paape, N.; Kiefer, J.; Wasserscheid, P.; Leipertz, A., The role of the C2 position in interionic interactions of imidazolium based ionic liquids: a vibrational and NMR spectroscopic study. *Physical Chemistry Chemical Physics* **2010**, *12* (42), 14153-14161.
118. Kiefer, J.; Fries, J.; Leipertz, A., Experimental vibrational study of imidazolium-based ionic liquids: Raman and infrared spectra of 1-ethyl-3-methylimidazolium bis(trifluoromethylsulfonyl)imide and 1-ethyl-3-methylimidazolium ethylsulfate. *Appl Spectrosc* **2007**, *61* (12), 1306-11.
119. Mendieta-Reyes, N. E.; Cheuquepán, W.; Rodes, A.; Gómez, R., Spectroelectrochemical Study of CO<sub>2</sub> Reduction on TiO<sub>2</sub> Electrodes in Acetonitrile. *ACS Catalysis* **2020**, *10* (1), 103-113.
120. Venkateswarlu, P., The Rotation-Vibration Spectrum of Methyl Cyanide in the Region 1.6 $\mu$ –20 $\mu$ . *The Journal of Chemical Physics* **2004**, *19* (3), 293-298.
121. Faguy, P. W.; Fawcett, W. R.; Liu, G.; Motheo, A. J., A study of the adsorption of acetonitrile on a gold electrode from aqueous solutions using in situ vibrational spectroscopy. *Journal of Electroanalytical Chemistry* **1992**, *339* (1), 339-353.
122. Briega-Martos, V.; Costa-Figueiredo, M.; Orts, J. M.; Rodes, A.; Koper, M. T. M.; Herrero, E.; Feliu, J. M., Acetonitrile Adsorption on Pt Single-Crystal Electrodes and Its Effect on Oxygen Reduction Reaction in Acidic and Alkaline Aqueous Solutions. *The Journal of Physical Chemistry C* **2019**, *123* (4), 2300-2313.
123. Morterra, C.; Peñarroya Mentrut, M.; Cerrato, G., Acetonitrile adsorption as an IR spectroscopic probe for surface acidity/basicity of pure and modified zirconias. *Physical Chemistry Chemical Physics* **2002**, *4* (4), 676-687.
124. Elderderi, S.; Leman-Loubière, C.; Wils, L.; Henry, S.; Bertrand, D.; Byrne, H. J.; Chourpa, I.; Enguehard-Gueiffier, C.; Munnier, E.; Elbashir, A. A.; Boudesocque-Delaye, L.; Bonnier, F., ATR-IR spectroscopy for rapid quantification of water content in deep eutectic solvents. *Journal of Molecular Liquids* **2020**, *311*, 113361.
125. Feaster, J. T.; Jongorius, A. L.; Liu, X.; Urushihara, M.; Nitopi, S. A.; Hahn, C.; Chan, K.; Nørskov, J. K.; Jaramillo, T. F., Understanding the Influence of [EMIM]Cl on the Suppression of the Hydrogen Evolution Reaction on Transition Metal Electrodes. *Langmuir* **2017**, *33* (37), 9464-9471.
126. Herzberg, G.; Crawford, B. L., Jr., Infrared and Raman Spectra of Polyatomic Molecules. *The Journal of Physical Chemistry* **1946**, *50* (3), 288-288.
127. Wang, X.; Rosspeintner, A.; Ziarati, A.; Zhao, J.; Bürgi, T., Insight into the transient inactivation effect on Au/TiO<sub>2</sub> catalyst by in-situ DRIFT and UV-vis spectroscopy. *Nature Communications* **2022**, *13* (1), 5458.
128. Tao, Z.; Pearce, A. J.; Mayer, J. M.; Wang, H., Bridge Sites of Au Surfaces Are Active for Electrocatalytic CO<sub>2</sub> Reduction. *Journal of the American Chemical Society* **2022**, *144* (19), 8641-8648.
129. Gatehouse, B. M.; Livingstone, S. E.; Nyholm, R. S., 636. The infrared spectra of some simple and complex carbonates. *Journal of the Chemical Society (Resumed)* **1958**, (0), 3137-3142.
130. Bishop, J. L.; King, S. J.; Lane, M. D.; Brown, A. J.; Lafuente, B.; Hiroi, T.; Roberts, R.; Swayze, G. A.; Lin, J. F.; Sánchez Román, M., Spectral Properties of Anhydrous Carbonates and Nitrates. *Earth and Space Science* **2021**, *8* (10), e2021EA001844.
131. Miller, F. A.; Wilkins, C. H., Infrared Spectra and Characteristic Frequencies of Inorganic Ions. *Analytical Chemistry* **1952**, *24* (8), 1253-1294.
132. Sheng, H.; Oh, M. H.; Osowiecki, W. T.; Kim, W.; Alivisatos, A. P.; Frei, H., Carbon Dioxide Dimer Radical Anion as Surface Intermediate of Photoinduced CO<sub>2</sub> Reduction at Aqueous Cu and CdSe

Nanoparticle Catalysts by Rapid-Scan FT-IR Spectroscopy. *Journal of the American Chemical Society* **2018**, *140* (12), 4363-4371.

133. Fujiwara, H.; Hosokawa, H.; Murakoshi, K.; Wada, Y.; Yanagida, S., Surface Characteristics of ZnS Nanocrystallites Relating to Their Photocatalysis for CO<sub>2</sub> Reduction. *Langmuir* **1998**, *14* (18), 5154-5159.

134. Maton, C.; Van Hecke, K.; Stevens, C. V., Peralkylated imidazolium carbonate ionic liquids: synthesis using dimethyl carbonate, reactivity and structure. *New Journal of Chemistry* **2015**, *39* (1), 461-468.

135. Aldous, I. M.; Hardwick, L. J., Influence of Tetraalkylammonium Cation Chain Length on Gold and Glassy Carbon Electrode Interfaces for Alkali Metal–Oxygen Batteries. *The Journal of Physical Chemistry Letters* **2014**, *5* (21), 3924-3930.

136. Dongfang, N.; Haiyang, W.; Huicheng, L.; Xincheng, Z., The effect of the alkyl chain length of the tetraalkylammonium cation on CO<sub>2</sub> electroreduction in an aprotic medium. *Electrochemistry Communications* **2015**, *52*, 58-62.

137. Buzzeo, M. C.; Hardacre, C.; Compton, R. G., Extended Electrochemical Windows Made Accessible by Room Temperature Ionic Liquid/Organic Solvent Electrolyte Systems. *ChemPhysChem* **2006**, *7* (1), 176-180.

138. Foley, J.; Korzeniewski, C.; Pons, S., Anodic and cathodic reactions in acetonitrile/tetra-n-butylammonium tetrafluoroborate: an electrochemical and infrared spectroelectrochemical study. *Canadian Journal of Chemistry* **2011**, *66*, 201-206.

139. Ikemiya, N.; Natsui, K.; Nakata, K.; Einaga, Y., Effect of alkali-metal cations on the electrochemical reduction of carbon dioxide to formic acid using boron-doped diamond electrodes. *RSC Advances* **2017**, *7* (36), 22510-22514.

140. Setterfield-Price, B. M.; Dryfe, R. A. W., The influence of electrolyte identity upon the electro-reduction of CO<sub>2</sub>. *Journal of Electroanalytical Chemistry* **2014**, *730*, 48-58.

141. Gomes, R. J.; Birch, C.; Cencer, M. M.; Li, C.; Son, S.-B.; Bloom, I. D.; Assary, R. S.; Amanchukwu, C. V., Probing Electrolyte Influence on CO<sub>2</sub> Reduction in Aprotic Solvents. *The Journal of Physical Chemistry C* **2022**, *126* (32), 13595-13606.

142. Ballini, R.; Barboni, L.; Fiorini, D.; Giarlo, G.; Palmieri, A., One pot synthesis of 3,5-alkylated acetophenone and methyl benzoate derivatives via an anionic domino process. *Chemical Communications* **2005**, (20), 2633-2634.

143. Hong, F.-J.; Low, Y.-Y.; Chong, K.-W.; Thomas, N. F.; Kam, T.-S., Biomimetic Oxidative Dimerization of Anodically Generated Stilbene Radical Cations: Effect of Aromatic Substitution on Product Distribution and Reaction Pathways. *The Journal of Organic Chemistry* **2014**, *79* (10), 4528-4543.



## Acknowledgements

I am profoundly grateful for the invaluable support and contributions that made this work possible.

First, I owe a great debt of gratitude to Professor **Guido Mul**, my promoter. Guido, your unwavering support over the past six years, spanning both my master's and PhD, has been instrumental in my academic journey. Your ability to keep my spirits high, even in moments of disappointment, and your guidance towards my goals have been indispensable.

I also extend my deep appreciation to Dr. **Mark Hempenius**, who has been my primary research collaborator throughout this journey. Mark, I have learned two critical lessons from you that have shaped my approach to research. The first is your unwavering commitment to conducting meticulous experimental work and the precise reporting of data. The second is your resilience in the face of research challenges, a quality I now consider paramount for conducting high-quality research. I am particularly grateful for your dedication, often extending to weekends, when you selflessly supported me in the lab!

I would also like to express my heartfelt thanks to my two former master's students, **Joep Kiewiet** and **Maarten Buitelaar**. Your dedication and hard work significantly contributed to the progress of this study. Without your valuable input, the quality of this research would not have reached its current level. I wish both of you immense success in your future careers. On the technical side, I must acknowledge the great help provided by our group's technician, **Robert Meijer**. Robert, your patience in accommodating my constant requests and interruptions in the lab was greatly appreciated. I also want to express my gratitude to the colleagues from mechanical workshop whose contributions were invaluable. I also need to extend my thanks to all other group members who have made direct or indirect contributions to my research work.

I would also like to thank **Hannah Thuijs** from CBBC office for her support and for facilitating my research across the consortium. I also need to express my gratitude to Dr. **Paul J Corbett**, my industrial supervisor from Shell, for his constant support over these years.

I am also deeply indebted to my dear friends, **Amir Hossein, Meisam**, and **Shri**, who have consistently been my primary motivators and sources of support. Your role in my journey cannot be overstated. Meisam and Shri, I wish you both the very best as you navigate the final stages of your own Ph.D. journeys.

I extend my deepest appreciation to my beloved mother, **Tahereh**, whose unwavering support has been the cornerstone of my journey and has positioned me where I stand today. To my family, my brothers **Saied** and **Masoud**, and my sister **Saiedeh**, I offer my profound thanks for their unwavering support and dedication. Lastly, I want to express my immense gratitude to my dear wife, **Faranak**. This work owes a great debt to your support and boundless motivation. I've always promised to repay your support with the best performance I can muster, and I wholeheartedly remain committed to that promise

## Publications

1. S. Neyrizi, J. Kiewiet, M. A. Hempenius, G. Mul, What It Takes for Imidazolium Cations to Promote Electrochemical Reduction of CO<sub>2</sub>. ACS Energy Lett. 2022, 7, 3439–3446. Front cover of the Journal. <https://doi.org/10.1021/acsenergylett.2c01372>. (Chapter 3 of this thesis)
2. S. Neyrizi, M. A. Hempenius, G. Mul, The Performance of Transition Metals in Imidazolium-Assisted CO<sub>2</sub> Reduction in Acetonitrile. ChemElectroChem. 2023. Accepted. (Chapter 5 of this thesis)



